

A Model-based Understanding of Reversible Oxide-ion-conducting and Proton-conducting Solid Oxide Fuel Cells (SOFCs)

Zur Erlangung des akademischen Grades
Doktor der Ingenieurwissenschaften
der Fakultät für Maschinenbau
Karlsruher Institut für Technologie (KIT)

genehmigte
Dissertation
von

Vikram Menon, M.S.
geb. in Chennai, Indien

Tag der mündlichen Prüfung: 06.03.2015

Hauptreferent: Prof. Dr. rer. nat. habil. Ulrich Maas

Korreferent: Prof. Dr. rer. nat. habil. Olaf Deutschmann

"Somewhere, something incredible is waiting to be known."

- Carl Sagan

*"I don't know anything, but I do know that everything
is interesting if you go into it deeply enough."*

- Richard P. Feynman

Acknowledgements

I would like to express my deepest gratitude to the following people who have always supported me since the inception of my work:

- Prof. Olaf Deutschmann, for giving me the opportunity to work in his research group and honing my ideas through his immense knowledge, support, and patience.
- Prof. Vinod M. Janardhanan, for sharing his enthusiasm and understanding of the subject matter despite working in another continent.
- Prof. Ulrich Maas, who accepted to be my co-supervisor and was very understanding of all the nuances of my path ahead.
- Prof. Robert J. Kee and Dr. Huayang Zhu (Colorado School of Mines, USA) for all the fruitful discussions on the vanguard developments in the field of batteries and fuel cells.
- Prof. Wolfgang Bessler, for taking the time off to invite me to DLR, Stuttgart and explain the SOFC models used in his group.
- Dr. Steffen Tischer, whose general and technical advice made things easier during my PhD. I am grateful to Dr. Lubow Maier for sharing her insight on reaction kinetics. I would also like to thank Dr. Matthias Hettel and Dr. Günter Schoch for creating a very conducive work environment.
- Dr. Julian Dailly and Dr. Qingxi Fu (EIFER) for providing experimental data, and being motivated as collaborators on various state-of-the-art ideas.
- Members within the research group - Sivaram Kannepalli, Henning Stotz, Tobias Kimpel, Karla Herrera Delgado, and Aayan Banerjee for the constant debates on topics pertaining to chemical technology. This definitely helped in bringing new perspectives into various models and techniques being used. I am also thankful for their support during all the tough mo-

ments of my PhD. I would also like to thank Ursula Schwald and Leonhard Rutz for their helpful contribution towards the administrative and IT services offered in the group, respectively.

- My family, friends and fiancée. I am indebted to my parents for striving to give me the best at all stages of my life. I am grateful to my close friends in India and the USA, who never fail to get a laugh out of me, for being there at all costs and at all times. I thank my fiancée Sneha for her priceless moral support and love, and for being the answer to a part of my life.

Finally, I appreciate Steinbeis GmbH für Technologietransfer (STZ 240 Reaktive Strömungen) for giving me a cost free academic license of DETCHEM™. Financial support by the Helmholtz Research School *Energy-Related Catalysis* is gratefully acknowledged.

Kurzfassung

Reversible Festoxidbrennstoffzellen (SOFCs) stehen gegenwärtig im Fokus der Forschung als effiziente Bauteile zur Energieumwandlung. Die Kombination der Vorteile wie schnelle Reaktionskinetik, Beständigkeit gegenüber Vergiftungen, preiswerte Katalysatormaterialien, hohe Energiedichte, Flexibilität der eingesetzten Brennstoffe und geringe Schadstoffemissionen bietet vielfältige Anwendungsmöglichkeiten in Bereichen der Automobilindustrie, chemischer Anlagen bzw. stationärer und dezentraler Kraftwerke.

Das vorgestellte numerische Modell besteht auf Ebene der elementaren Brennstoffzelle aus einem detaillierten, 42 Reaktionen umfassenden heterogenen Reaktionsmechanismus für die Anode (Ni-basierter Katalysator), modifizierten Butler-Volmer-Gleichungen für die Chemie des Ladungstransfers, dem Dusty-Gas-Modell (DGM) für den Stofftransport im porösen Medium, einem Pfropfenströmungsmodell für den Gastransport in den Kanälen sowie einem eindimensionalen Wärmeleitungsmodell für den Festkörper. Auf Ebene des SOFC-Stacks wird ein neues hierarchisches Modell verwendet, um das instationäre 2-D- bzw. 3-D-Wärmeleitungsproblem durch Entkopplung der Temperaturen für die feste und die gasförmige Phase zu lösen. Ein Cluster-Agglomerations-Algorithmus wird angewandt, um die Elementarzellen anhand ihrer lokalen Temperaturprofile in Gruppen einzuteilen. Es wird angenommen, dass sich die Zellen einer Gruppe identisch verhalten, so dass jeweils für eine repräsentative Zelle eine detaillierte Simulation ausgeführt wird. Dadurch wird die benötigte Rechenzeit signifikant reduziert.

Numerische Simulationen werden für verschiedene Konfigurationen vorgestellt: von elementaren 1-D elektrochemischen Zellen, über quasi-2-D planare Zellen, bis zu komplexen 3-D Stack-Anordnungen, um die Programmeffizienz und die Effektivität bei der Designoptimierung zu testen. Das Gesamtpaket wird eingesetzt zur Untersuchung: (i) des transienten Verhaltens von SOFC-Stacks, (ii) von Festoxidelektrolysezellen (SOECs) zur elektrolytischen Wasserstoffproduktion, (iii) von SOECs zur Synthesegasproduktion durch Koelektrolyse von H_2O und CO_2 sowie (iv) des Massen- und Wärmetransports in protonenleitenden SOFCs.

In allen Fällen wurden 1-D Knopfzellen-Simulationen verwendet, um aus experimentellen Daten die elektrochemischen Parameter abzuleiten. Aufbauend auf diesen Parametern wurden die quasi-2-D planaren Zellen und die 3-D SOFC-Stacks untersucht. Im Fall (i) werden die Ergebnisse für einen Stack präsentiert, der mit einem vorreformierten Kohlenwasserstoff betrieben wird. Transiente Temperaturänderungen auf Strom- bzw. Spannungs-Lastwechsel werden analysiert. Auch der Einfluss der Randbedingungen auf die Ansprechzeit und die interne Wärmeverteilung im Stack werden betrachtet. Für Fall (ii) werden Ergebnisse bezüglich der chemischen Prozesse in der Brennstoffelektrode, der elektrochemischen Vorgänge sowie der irreversiblen Energieverluste im SOEC-Betrieb präsentiert. Darüber hinaus wird das SOEC-System einer Leistungsanalyse unterzogen. Im Fall (iii) werden der Einfluss der mikrostrukturellen Eigenschaften, des Einlass-Brenngasstromes sowie der Temperatur auf die Leistungsparameter der SOEC diskutiert. Eine Reaktionsfluss-Analyse wird unter Leerlaufbedingungen ausgeführt, um Kennlinien und die Reaktionskinetik der Methanproduktion bei der Koelektrolyse zu bestimmen. Abschließend wird im Fall (iv) das Verhalten einer adiabatisch betriebenen planaren Zelle im Gleichstrombetrieb untersucht. Numerische Simulationen werden ausgeführt, um den Einfluss verschiedener Betriebsbedingungen auf Temperaturverteilung, Stofftransport und Elektrochemie zu betrachten. Der Effekt, den eine Einteilung der Anode in vier Zonen mit unterschiedlichen spezifischen katalytischen Oberflächen auf die makroskopischen Leistungsparameter hat, wird untersucht.

Abstract

Reversible solid oxide fuel cells (SOFCs) have gained substantial interest in recent time as high efficiency sources for energy conversion. A unique combination of advantages such as fast reaction kinetics, poison tolerance, utilization of inexpensive catalysts, high power density, fuel flexibility and low emissions have helped SOFCs find application in the automobile industry, chemical plants, and stationary/distributed power plants.

In this thesis, a unified framework to model and analyze the dynamics of solid oxide cells (SOCs) is described. The computational framework, at the unit-cell level, covers a detailed 42-step reaction mechanism for heterogeneous chemistry in the anode structure (Ni-based catalysts), modified Butler-Volmer equations to represent charge transfer chemistry, the Dusty Gas Model (DGM) for multi-component diffusion in porous media, a plug flow model for flow through the gas channels, and a 1-D solid-phase heat balance model. At the SOFC stack level, a novel hierarchical approach is employed to solve the unsteady 2-D or 3-D heat conduction problem by decoupling the solid-phase temperature from that of the fluid-phase. A cluster agglomeration algorithm is used that divides unit cells into clusters according to the differences in their local temperature profiles, and is based on the assumption that all cells with similar temperature profiles behave identically. All unit cells of one cluster are then represented by one cell, for which in depth simulation is carried out. This approach significantly reduces computation time. Simulations are performed for configurations ranging from simple 1-D button cells to quasi-2-D planar cells to complex 3-D stacks, to elucidate the effectiveness of the tool for performance and design optimization. The unified numerical framework is then employed to study: (i) the transient behavior of SOFC stacks, (ii) solid oxide electrolysis cells (SOECs) for hydrogen production by H_2O electrolysis, (iii) SOECs for synthesis gas production by $\text{H}_2\text{O}/\text{CO}_2$ co-electrolysis, and (iv) mass and heat transport in proton-conducting SOFCs.

In all cases, 1-D button cell simulations are carried out to reproduce the experiments and deduce electrochemical fit parameters. The obtained fit parameters are extended to the quasi-2-D planar cell and 3-D SOFC stack models for further analysis. For case (i), results are presented for a stack running on a pre-reformed hydrocarbon fuel composition. Transient thermal response to load changes is analyzed by introducing step changes in cell potential and current. Also, the impact of boundary

conditions on thermal response time and internal temperature distribution of the stack is examined. For case (ii), results pertaining to detailed chemical processes within the fuel electrode, electrochemical behavior and irreversible losses during SOEC operation are presented. Furthermore, efficiency analysis of the SOEC system is also carried out. In case (iii), the influence of microstructural properties, inlet gas velocity at the fuel channel, and temperature on SOEC performance parameters are discussed. Reaction flow analysis is performed, at OCV, to study methane production characteristics and kinetics during co-electrolysis. Finally, for case (iv), the performance of the cell is analyzed by assuming the co-flow planar cell to be adiabatic. Simulations are carried out to understand the influence of various operating conditions on temperature distribution, species transport, and electrochemistry in the cell. The effect of dividing the anode into four zones, with different specific catalytic areas, on macroscopic performance parameters is investigated.

Keywords

Solid oxide fuel cell (SOFC), solid oxide electrolysis cell (SOEC), SOFC stacks, proton-conducting, oxide-ion-conducting, steam electrolysis, co-electrolysis, hydrogen production, syngas production, direct internal reforming, numerical modeling, reaction kinetics, transient three dimensional modeling

Contents

Acknowledgements	V
Kurzfassung	VII
Abstract	IX
Keywords.....	X
Contents.....	XI
Nomenclature	XV
Chapter 1 Introduction	1
1.1 Objectives.....	3
1.2 Brief outline of the thesis	4
Chapter 2 Modeling fundamentals	7
2.1 Operating principle	7
2.2 Common SOFC membrane-electrode assembly (MEA) materials	9
2.3 Prospects and challenges of the technology.....	13
2.4 Thermo-catalytic and gas-phase chemistry.....	13
2.4.1 Reaction pathways in a SOFC anode	14
2.4.2 Mean-field approximation.....	17
2.4.3 Gas-phase chemistry	21
2.5 Electrochemistry and charge transfer.....	22
2.5.1 Electrochemical model for reversible oxide-ion-conducting SOFCs	23
2.5.2 Electrochemical model for proton-conducting SOFCs.....	32
2.6 Porous media transport	33
2.7 Flow in the gas channels	36
2.8 Thermal transport.....	38
2.8.1 Quasi-2-D single co-flow planar SOFC	38
2.8.2 3-D SOFC stacks	39
2.9 Solution algorithm.....	41
2.9.1 1-D button cell	41
2.9.2 Quasi 2-D single co-flow planar SOFC	43
2.9.3 3-D SOFC stacks	45
Chapter 3 A novel approach to understand the transient behavior of high-density SOFC stacks	51

3.1	Step change in constant current.....	55
3.1.1	Adiabatic boundary condition	55
3.1.2	Neumann boundary condition	60
3.2	Step change in constant voltage	62
3.2.1	Adiabatic boundary condition	62
3.2.2	Neumann boundary condition	64
3.3	Summary.....	67
Chapter 4	On the production of hydrogen in SOECs by steam electrolysis	69
4.1	Model validation.....	71
4.2	Thermal characteristics of the SOEC during isothermal operation.....	74
4.3	Effect of operating temperature on the SOEC	75
4.4	Effect of steam content and current density on the SOEC	76
4.5	Adsorbed surface species distribution within the cathode.....	78
4.6	Efficiency analysis of the SOEC.....	81
4.7	Diffusion limitation behavior vs. micro-structural properties	83
4.8	Summary.....	84
Chapter 5	On the production of synthesis gas in SOECs by co-electrolysis of steam/carbon dioxide	87
5.1	Experimental setup	89
5.2	1-D electrochemical model.....	90
5.2.1	Model validation.....	90
5.2.2	Effect of operating temperature on the SOEC	93
5.2.3	Effect of micro-structural properties on the SOEC	95
5.3	1-D + 1-D co-flow planar SOEC.....	96
5.3.1	Effect of temperature and electrode thickness on the exit gas composition.....	96
5.3.2	Effect of inlet gas velocity on the exit gas composition	98
5.3.3	Type of electrolysis vs. species composition in the cathode and fuel channel	99
5.4	Possible methane production reaction pathways.....	101
5.5	Summary.....	105
Chapter 6	Investigating mass and heat transport in proton-conducting SOFCs	107
6.1	Model validation and parametric analysis	109
6.2	Summary.....	122
Chapter 7	Summary and outlook.....	125
7.1	Accomplished results.....	125
7.2	Future work	128
Appendix.....		129
A. Surface reaction mechanism over Ni-based electrodes.....		129

B. Modified B-V equation derivation for H-SOFCs	130
References.....	135
Curriculum Vitae.....	149

Nomenclature

A_{act}	active anode surface area for electrochemistry (m^2)
A_c	area of cross section of flow channels (m^2)
A_i	pre-exponential factor for the Arrhenius expression (order dependent)
A_s	area of the solid MEA (m^2)
A_{sp}	specific catalytic area (m^{-1})
B_g	permeability (m^2)
C_p	specific heat ($J\ kg^{-1}K^{-1}$)
d_p	particle diameter (m)
d_{pore}	pore diameter (m)
D_h	hydraulic diameter (m)
\mathcal{D}	diffusivity ($m^2\ s^{-1}$)
D_{kl}^e	effective binary diffusion ($m^2\ s^{-1}$)
D_h	hydraulic diameter (m)
$D_{k,Kn}^e$	effective Knudsen diffusion ($m^2\ s^{-1}$)
E_{cell}	cell voltage (V)
E_{CO}^{des}	desorption energy for CO ($J\ mol^{-1}$)
$E_{CO_2}^{des}$	desorption energy for CO ₂ ($J\ mol^{-1}$)
E_{el}	activation energy for ion transport across the electrolyte ($J\ mol^{-1}$)
E^{eq}	equilibrium potential (V)
E_f^{act}	activation energy for the forward reaction ($J\ mol^{-1}$)
$E_{H_2}^{des}$	desorption energy for H ₂ ($J\ mol^{-1}$)
$E_{O_2}^{des}$	desorption energy for O ₂ ($J\ mol^{-1}$)
E_{rev}	reversible cell potential (V)
E_r^{act}	activation energy for the reverse reaction ($J\ mol^{-1}$)
F	Faraday constant ($C\ mol^{-1}$)
Gz	Graetz number
h	heat transfer coefficient ($J\ m^{-2}K^{-1}s^{-1}$); specific enthalpy ($J\ kg^{-1}$)
H_c	channel height (m)
H^0	standard state enthalpy ($J\ mol^{-1}$)
ΔH	enthalpy change ($J\ mol^{-1}$)
\dot{H}	mixture enthalpy ($J\ mol^{-1}$)
i	current density ($A\ cm^{-2}$)
i_0	exchange current density ($A\ m^{-2}$)
J_k	species molar flux ($mol\ m^{-2}s^{-1}$)
k_f	forward rate constant
k_r	reverse rate constant
K_b	total number of bulk species
K_c	equilibrium constant in terms of concentration
K_g	total number of gas-phase species

K_p	equilibrium constant in terms of pressure
K_s	total number of surface species
Kn	Knudsen number
l	thickness (m)
N	number of charge transferred
\dot{n}	molar flow rate (mol s^{-1})
p	pressure (Pa)
p^0	standard state pressure (Pa)
p_{amb}	ambient pressure (bar)
p_k	partial pressure of species k
p^*	equilibrium partial pressure
P_e	MEA electrochemically active perimeter (m)
Pr	Prandtl number
\dot{Q}	heat source term ($\text{J m}^{-3}\text{s}^{-1}$)
R	gas constant ($\text{J mol}^{-1}\text{K}^{-1}$)
R_{ct}	charge transfer resistance ($\Omega \text{ cm}^2$)
R_{tot}	total area specific ohmic resistance ($\Omega \text{ cm}^2$)
Re	Reynolds number
\dot{s}_k	molar production rate of species k due to surface reactions ($\text{mol m}^{-2}\text{s}^{-1}$)
S^0	sticking coefficient; standard state entropy (J K^{-1})
ΔS	entropy change (J K^{-1})
t	time (s)
T	temperature (K)
V	volume (m^3)
V_{OC}	open-circuit voltage (V)
V_{th}	thermo-neutral voltage (V)
W_k	molecular weight of species k (kg mol^{-1})
X	mole fraction
$[X]$	concentration (mol m^{-3})
x, y, z	co-ordinate direction (m)
Y	mass fraction

Greek letters

β	temperature exponent in the Arrhenius expression
β_a	anode charge transfer coefficient (O-SOFCs)
β_c	cathode charge transfer coefficient (O-SOFCs)
γ	normalization factor
δ	Kronecker delta symbol; thickness (m)
ε	emissivity
ε_{ki}	coverage dependency of the activation energy in the forward rate constant expression for species k in the i^{th} reaction
η	overpotential (V)
η_{elec}	electrical power generation efficiency
η_{leak}	leakage overpotential (V)
$\eta_{overall}$	hydrogen production efficiency
η_{O-P}	oxygen production factor
η_{R-U}	reactant utilization factor
η_{th}	thermal utilization efficiency
$\eta_{voltage}$	voltage efficiency

λ	thermal conductivity ($\text{J m}^{-1}\text{Ks}^{-1}$)
λ_m	mean free path of specified species in the mixture (m)
θ	surface coverage fraction
μ	viscosity ($\text{kg m}^{-1}\text{s}^{-1}$)
μ_{ki}	order dependency of the surface coverage in the forward rate constant expression for species k in the i^{th} reaction
ν'	stoichiometric coefficient of reactants
ν''	stoichiometric coefficient of products
ρ	density (kg m^{-3})
σ	conductivity (S m^{-1}); Stefan-Boltzmann constant
σ_k	co-ordination number of species k
τ	tortuosity
v	velocity (m s^{-1})
φ	porosity
χ	species symbol
$\dot{\omega}$	molar production rate of species k due to gas-phase reactions ($\text{mol m}^{-3}\text{s}^{-1}$)
Γ	surface site density (mol m^{-2})
Φ	solution vector for the DAE system
Ψ	heat flux ($\text{J m}^{-2}\text{s}^{-1}$)

Subscripts

ac	air channel
el	electrolyte
f	fluid
fc	air channel
fe	fuel electrode
i	reaction index
k	species index
oe	oxidant electrode
s	solid (porous media - MEA)

Abbreviation

<i>APU</i>	auxiliary power units
<i>ASR</i>	area-specific resistance
<i>B-V</i>	Butler-Volmer
<i>CHP</i>	combined heat and power
<i>DFFC</i>	direct flame type solid oxide fuel cell
<i>DGM</i>	dusty-gas model
<i>H-SOFC</i>	proton-conducting solid oxide fuel cell
<i>LHV</i>	lower-heating value
<i>MEA</i>	membrane electrode assembly
<i>OCV</i>	open-circuit voltage
<i>O-SOFC</i>	oxide-ion-conducting solid oxide fuel cell
<i>RWGS</i>	reverse water-gas shift
<i>SOC</i>	solid oxide cell
<i>SOEC</i>	solid oxide electrolysis cell
<i>SOFC</i>	solid oxide fuel cell
<i>TPB</i>	three-phase boundary
<i>WGS</i>	water-gas shift

Chapter 1 Introduction

Electrochemical cells offer an efficient way to directly convert chemical energy into electrical energy. A fuel cell, in particular, is an electrochemical device that uses reactants such as hydrogen and air to produce electricity, steam and heat. In the case of high temperature fuel cells, the supply of fuels other than pure hydrogen is feasible. Among the low temperature fuel cells, direct methanol fuel cells use methanol as fuel. Thus, depending on the type of fossil fuel fed into these high-temperature fuel cells, carbon monoxide and other lower hydrocarbons pose as potential by-products. Unlike conventional combustion engines, NO_x is not produced as reactants in the gas channels do not directly mix for energy conversion to take place. Nevertheless, sulphur is a common poison to all fuel cells and should be removed from the gas stream. Attributes such as low pollutant formation, relatively silent operation, high modularity, high energy efficiency, and lack of 'memory effect' like batteries have made fuel cells a formidable option to counter the dependence on conventional energy sources. Moreover, fuel cells are not limited by Carnot efficiency. The schematic diagram of classically available fuel cells is shown in Fig. 1.1.

In this work, the primary focus is on solid oxide fuel cells (SOFCs). Typically, SOFCs have an operating temperature of 600–1000 °C. This paves way for high fuel flexibility, though at such high temperatures less active catalysts can be used. The catalysts are more stable, and less sensitive to impurities in the fuel. Thereby, carbon monoxide, which is a poison for low temperature fuel cells, can be used as fuel for high temperature fuel cells like the SOFC. These fuel cells also produce high-grade process heat, apart from electricity, that finds application in co-generation or combined heat and power (CHP) plants. High temperature also enhances kinetics and reduces the resistivity of the solid electrolyte, leading to highly efficient energy conversion and power production. Another advantage is the viability of direct internal reforming, which reduces complexity at the systems level by eliminating the need for an external reformer. Some of the major challenges facing this technology are (i) cost and innovation of materials, (ii) coking on nickel-based catalysts, and (iii) non-linear temperature gradients that cause mismatch in the variable thermal expansion rates of the anode, cathode and electrolyte, leading to delamination.

There is a great deal of extant literature on the modeling of SOFCs. They mainly emphasize on understanding the interplay of diverse multi-physics phenomena at work, in order to characterize and optimize electrochemical performance. Thus, to facilitate the development of a robust model, one has to consider the strong coupling between various detailed aspects of porous media transport, fluid mechanics, energy transport, thermodynamics, heterogeneous and gas-phase chemical reactions, electrochemistry, and mass transport in the cell. Hence, numerical modeling becomes a challenging task to address. Until recently, most models covered in literature to predict experimental data with reasonable accuracy made questionable assumptions in the areas of heterogeneous chemistry and/or charge transfer. Some of the research groups doing pioneering work in SOC modeling belong to Prof. Robert J. Kee (Colorado School of Mines, USA), Prof. Wolfgang G. Bessler (Hochschule Offenburg, Germany), Prof. David G. Goodwin (Caltech, USA), Dr. Yixiang Shi (Tsinghua University, China) and Prof. Vinod M. Janardhanan (IIT Hyderabad, India). Nevertheless, an attempt has been made to conduct a detailed study of SOFCs for configurations ranging from simple 1-D electrochemical cells to quasi-2-D unit cells to complex 3-D stacks, to elucidate the effectiveness of the computational tool for performance prediction and optimization.

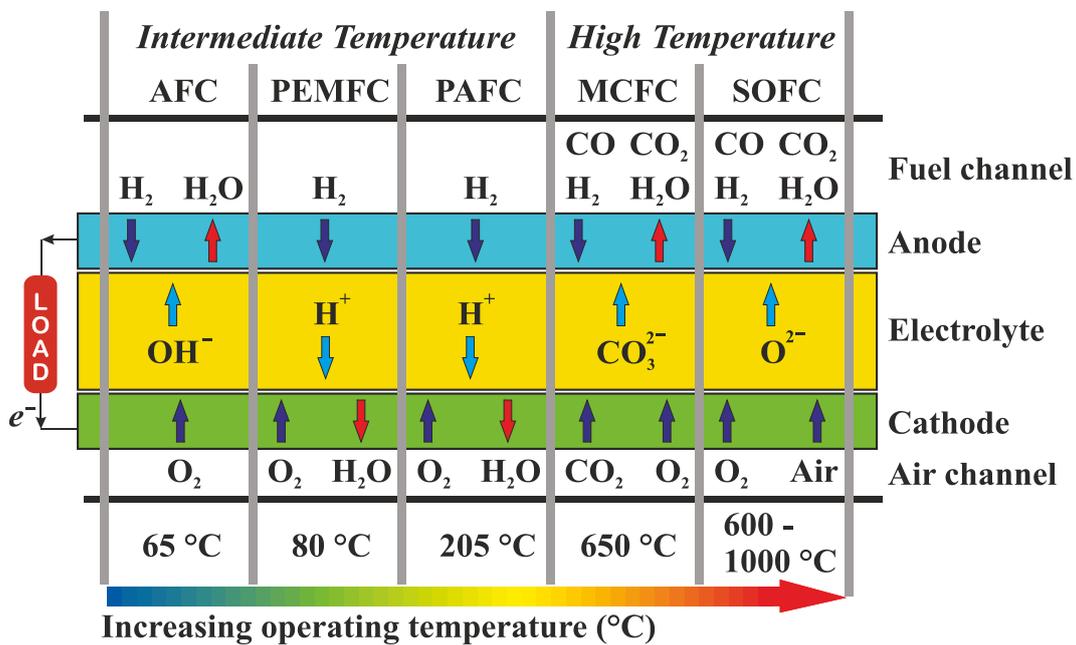


Figure 1.1: Basic operation differences in major fuel cell types (AFC - alkaline fuel cell, PEMFC - proton exchange membrane fuel cell, PAFC - phosphoric acid fuel cell, MCFC - molten carbonate fuel cell, SOFC - solid oxide fuel cell).

1.1 Objectives

The overall aim of this thesis is to develop a unified modeling framework for oxide-ion-conducting and proton-conducting SOFCs, in order to clearly understand its physico-chemical dynamics. In general, numerical models help in (i) reducing cost by cutting down on rigorous experiments, and (ii) providing insight into detailed system operation and performance parameters at every nodal position of the grid. Information on the latter could then be used to improve the trade-off between fuel utilization rate and cell efficiency. The computational framework is essentially applied to investigate the following systems:

- 3-D modeling of high channel density SOFC stacks.
- Solid oxide electrolysis cells (SOECs) for hydrogen production by H_2O electrolysis.
- Solid oxide electrolysis cells (SOECs) for syngas production by $\text{H}_2\text{O}/\text{CO}_2$ co-electrolysis.
- Proton-conducting SOFCs.

Although several 3-D SOFC stack models have been proposed in literature, none of them taken into account the detailed interactions between micro-scale elementary kinetics and performance parameters at the macro-scale. All reported models involved the simulation of every cell in the stack, which makes them computationally expensive. The goal of our model was to drastically reduce computation time by the usage of a cluster-agglomeration algorithm, without significant compromise in accuracy. Then, the model was used to study response times of the stack to step-changes in load, along with the impact of adiabatic and Neumann boundary conditions on temperature distributions in the system. Unlike batteries which need to be recharged or disposed after they are used up, fuel cells will produce electricity as long as there is fuel supply. Thus, fuel supply becomes the limiting step towards achieving continuous power production.

Traditional methods for producing hydrogen or syngas include steam reforming of natural gas or liquid hydrocarbons, coal/biomass gasification etc. The hydrogen is usually separated from CO_2 via pressure swing adsorption (PSA), chemical scrubbing or membrane reactors. Besides these established methods, SOECs deliver an efficient way to convert steam and/or carbon dioxide to hydrogen or syngas, via the simultaneous usage of heat and electricity. In this thesis, emphasis is laid on understanding various loss mechanisms involved in the high temperature electrolysis of H_2O for hydrogen production. Apart from the electrochemical analysis of SOECs, an efficiency analysis re-

veals the optimal operating conditions for the specific cell. In the case of co-electrolysis in SOECs, operating conditions and micro-structural properties of the electrodes play a key role in determining the functioning of the system. The computational model aims at giving useful instructions in optimizing system parameters, and understanding heterogeneous chemistry in the cell. Also, reaction flow analysis is carried out in a perfectly mixed batch reactor, at OCV, to elucidate on plausible sources of methane formation in the cell and confirm/clear uncertain results in literature. Throughout the modeling work in this thesis, it was noticed that temperature and its gradient played a pivotal role in inhibiting the use of desired membrane electrode assembly (MEA) materials, by controlling their stability. Therefore, lowering the operating temperature is imperative for practical applications. Also, unlike Carnot engines, the theoretical efficiencies of fuel cells increase with decreasing operating temperature. Proton-conducting SOFCs provide a possible solution to this problem by the fact that they possess higher theoretical energy efficiencies than their oxide-ion-conducting counterpart, as they yield higher average reversible cell potentials under the same conditions. Hence, these systems could be foreseen to produce higher electrochemical performance at lower temperatures. Thus, the study of thermal management/cell temperature distribution becomes all the more necessary, and is addressed in this work for proton conducting SOFCs.

1.2 Brief outline of the thesis

The general synopsis of the work presented in this thesis is laid out in Chapter 1. The following chapters form the crux of the thesis:

- Chapter 2 presents fundamentals that are specific to SOFCs and the detailed description of the employed computational framework. The solution algorithm and methods used in solving the coupled partial differential equations (PDEs), and differential algebraic equations (DAEs), are also elaborated.
- Chapter 3 elucidates on the novel approach used to describe the transient behavior of SOFC stacks. The approach shows a strong reduction in computation time, along with its ability to predict temperature time constants that conform to experimental findings.
- Chapter 4 reports the complex fundamental and functional interactions within a SOEC during hydrogen production by H_2O electrolysis. The dependence of electrochemical performance and losses on cell operating conditions is described. Furthermore, optimal operating voltage is determined using an efficiency analysis.

- Chapter 5 illustrates the study of SOECs for syngas production via H₂O/CO₂ co-electrolysis. The outcome of this analysis was an in-depth understanding of the multi-physics of the system, and its potential sources of carbon and methane formation.
- Chapter 6 demonstrates the working of a proton-conducting SOFC undergoing non-isothermal operation. Simulations are carried out to evaluate temperature distribution and species transport in the cell.
- Chapter 7 describes the brief summary of the thesis and outlook on future work that is relevant to the trajectory of the developed modeling framework.

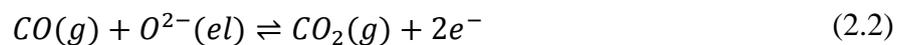
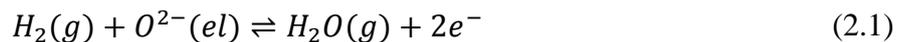
It should to be noted that all models were evaluated with relevant experiments from literature in chapters 3–6.

Chapter 2 Modeling fundamentals

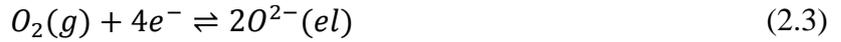
Investigation into fuel cells dates back to the description provided by German physicist C. F. Schönbein, and Welsh physicist and barrister W. R. Grove [1-4]. They described the basis of a primitive fuel cell. These systems have come a long way since its inception, from being used in space-based applications to conventional stationary/mobile power units. This chapter gives a comprehensive coverage of the operating principles, potential and challenges associated with the technology, and the modeling framework employed in the subsequent chapters.

2.1 Operating principle

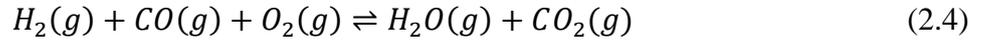
Fuel cells are electrochemical energy conversion devices that directly convert chemical energy into electrical energy. They are categorized based on (i) fuel supplied, and (ii) electrolyte material used. A typical fuel cell consists of an anode-electrolyte-cathode assembly (MEA), interconnect plates next to the gas channels, and gas seals. The basic structure and working principle of a fuel cell are illustrated in Fig. 2.1. The fuel enters the cell through the inlet manifold at the fuel channel, while the oxidant enters through the inlet manifold at the oxidant channel. In the case of oxide-ion-conducting SOFCs, the most commonly used electrolyte is 8–10 mol % Y_2O_3 stabilized ZrO_2 (YSZ). At sufficiently high operating temperatures (600–1000 °C), the Y^{3+} replaces a Zr^{4+} in the lattice. This frees an O^{2-} ion for conduction from the cathode to the anode via the electrolyte. This is depicted by the negative ion travelling towards the anode in the figure. The product gases leave the fuel channel from its exit manifold. The half-cell oxidation reaction at the anode is given by



The half-cell reduction reaction at the cathode is



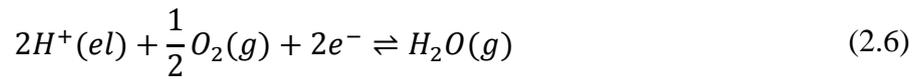
The net reaction for oxide-ion-conducting SOFCs is



In the case of proton-conducting fuel cells, the positive ion travels towards the cathode via the electrolyte. With regard to proton-conducting SOFCs, the charge transfer pathways within the electrolyte are not well understood. The half-cell oxidation reaction at the anode is given by



The half-cell oxygen reduction reaction at the cathode is



The net reaction for proton-conducting SOFCs reduces to

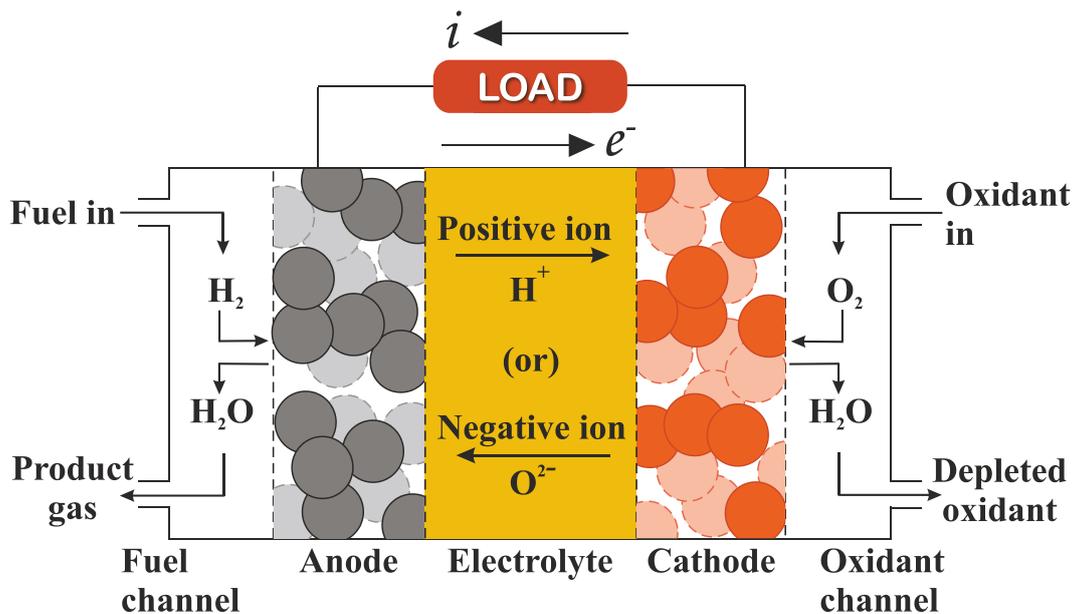


Figure 2.1: Working principle of a general SOFC. Adapted from Ref. [5].

It is important to note that SOFCs can also operate in "reverse" mode as SOECs, for the production of H_2 or syngas (H_2/CO) via H_2O electrolysis or H_2O/CO_2 co-electrolysis, respectively. In this thesis, we only consider the case of oxide-ion-conducting SOECs. The global charge transfer reactions, in these systems, are the reverse of Eqs. 2.1–2.4. For more information on other fuel cell fundamentals, concerned readers can refer to a fuel cell handbook [6].

2.2 Common SOFC membrane-electrode assembly (MEA) materials

The MEA is composed of an electrolyte layer that is in contact with the cathode and anode on either side. It is widely accepted that charge transfer chemistry occurs at the three-phases boundaries (TPB), which are basically interfaces formed by the electrocatalyst, electrolyte and gas-phase boundaries. The desired properties of the MEA depend on the operational conditions and its influence on the coupled interactions between various physico-chemical phenomena in the cell. Recent trends in MEA material development are detailed in Refs. [5, 7, 8].

Electrolytes form the interface between the cathode and anode in the MEA and are expected to be good ionic/protonic conductors. The most common oxide-ion conducting electrolyte is 8–10 mol % Y_2O_3 stabilized ZrO_2 (YSZ). This polycrystalline ceramic exhibits good stability and ionic conductivity at 650–1000 °C. The choice of an electrolyte is a strong function of the operating temperature of the system. Detailed reviews about conventional and novel ionic conductors have been carried out in literature [9]. Proton-conducting electrolytes promise enhanced performance at lower operating temperatures. Typical proton-conductors employed in SOFCs belong to the $Ba(Zr,Ce,Ln)O_{3-\delta}$ perovskite family and have relatively lower resistivities at 600–700 °C [10, 11].

Traditionally, SOFC anodes utilize a cermet of nickel and YSZ (usually the same material as the electrolyte depending on the ion conducted). Nickel is an electronic conductor, while YSZ is an ionic conductor. It is important for the anode to possess high electronic conductivity, enhanced activity, high thermal and mechanical stability, and a large TPB area. These requirements also vary based on the type of fuel used. As the carbon number in hydrocarbon fuels increases, the propensity of these materials towards coking increases [12]. Coking blocks active sites in the catalyst, leading to lower electrochemical performance. Hence, Ni-based cermets become increasingly incompatible for such applications. Some of the other challenges include sensitivity to sulphur, loss in material strength due to cyclic changes in volume due to oxidation/reduction intolerance, and much larger thermal expansion coefficient of the anode compared to the electrolyte and cathode. One way to

suppress coke formation is by using ceria-based anodes, during operation with hydrocarbon fuels having low steam to carbon ratios [13]. Typically, Yttrium doped ceria (YDC), Gadolinium doped

Table 2.1: Impact of MEA and fuel on peak power density for O-SOFCs [14]

Reference	MEA (anode/electrolyte/cathode)	T (°C)	Fuel	P_{peak} (W/cm ²)
[15]	Ni-YSZ/YSZ-SDC/LSC-SDC	800	Pure H ₂	1.8
			Pure CO	0.7
[16]	Ni-YSZ/YSZ/LSM-YSZ	800	CH ₄ + 3% H ₂ O	0.96
[17]	Ni-YSZ/YSZ/LSCF-GDC	800	H ₂ + 3% H ₂ O	1.44
			CH ₄ + 3% H ₂ O	1.27
[18]	Ni-SDC/SDC/SDC-BSCF ^a	787	18.8% CH ₄ + 16.2% O ₂ + 65% He (by vol.)	0.76
[19]	Ru-Ni-GDC/GDC/SSC ^b	600	H ₂ + 2.9% H ₂ O	0.769
			Dry CH ₄	0.750
			Dry C ₂ H ₆	0.716
			Dry C ₃ H ₈	0.648
[20]	Cu-CeO ₂ -YSZ/YSZ/LSM-YSZ ^c	800	Pure H ₂	0.31
			n-C ₄ H ₁₀	0.18
[21]	NiO-YSZ/YSZ/LSCF-GDC ^d	770	5% <i>iso</i> -C ₈ H ₁₈ + 9% air + 86% CO ₂	0.6
[22]	NiO-SDC/SDC/LSCF-SDC ^e	600	H ₂ + 3% H ₂ O	1.00
		590	6% <i>iso</i> -C ₈ H ₁₈ + 94% air	0.6
[23]	(BaO/Ni-YSZ)/YSZ/SDC-LSCF	750	Dry C ₃ H ₈	0.88
			CO + 3% H ₂ O	0.7
		850	96% CO + 1% H ₂ ^f	1.08

^a Single chamber cell.

^b SSC - Sm_{0.5}Sr_{0.5}CoO₃.

^c Electrolyte-supported cell.

^d With an anode catalyst layer of Ru-CeO₂/PSZ/Ru-CeO₂.

^e With an anode catalyst layer of Ru-CeO₂/PSZ-CeO₂/Ru-CeO₂.

^f Remaining 3% comprises of H₂O, CO₂, and CH₄.

ceria (GDC) or Samarium doped ceria (SDC) are used, i.e., ceria is doped with the one of the cations - Gadolinium (Gd^{3+}), Samarium (Sm^{3+}) or Yttrium (Y^{3+}). In order to circumvent drawbacks posed by Ni-based catalysts, perovskite-type structures with similar electrical and catalytic properties have been proposed [24]. Due to their flexibility in doping and substitution of cations, desired electrode properties can be achieved. Nevertheless, the test of this material lies in finding out whether oxygen-ion conduction or surface diffusion of adsorbed oxygen intermediates is the rate-determining step. Table 2.1 shows a few examples of the trend in materials, fuels and performance of oxide-ion-conducting SOFCs.

In SOFCs, cathodes provide a pathway for (i) the electrons involved in the half cell reduction reaction, and (ii) oxygen transport from the bulk gas stream to the TPB. In general, most cathodes belong to the family of lanthanum-based perovskite materials (structure ABO_3). They have proven to be cost-effective, compared to the historical usage of noble metals. Selected examples of cathode materials in SOFCs include strontium-doped lanthanum manganite (LSM - $La_{1-x}Sr_xMnO_3$), strontium-doped lanthanum cobalt ferrite (LSCF - $La_{1-x}Sr_xCo_{1-y}Fe_yO_{3-\delta}$), strontium-doped lanthanum cobaltite (LSC - $La_{1-x}Sr_xCoO_{3-\delta}$), and strontium-doped lanthanum ferrite (LSF - $La_{1-x}Sr_xFeO_{3-\delta}$) [25]. The interfacial properties at the cathode-electrolyte interface is a factor in determining activation overpotentials. Some important factors in choosing cathodes are electronic and ionic conductivity, thermal, chemical and mechanical stability, and high activity. Cathodes also suffer from interdiffusion with the interconnects that are made of chromium alloys. Chromium vapors tend to poison the cathode by forming precipitates, which are highly dependent on oxygen partial pressure, at the TPB [26]. This decreases electrochemical performance of the cell by enhancing charge transfer resistance and cathode overpotential. Another novel cathode material that has gained attention is $Ba_{1-y}Sr_yCo_{1-x}Fe_xO_3$ (BSCF), for intermediate temperature and 'single chamber' fuel cell operation [27]. It has been found to have a high rate of oxygen diffusion to the TPB, which in turn controls the magnitude of area-specific resistance (ASR). This material is also used in proton-conducting SOFCs. Table 2.2 gives a comparison between different MEA materials and their corresponding maximum power outputs for proton-conducting SOFCs. A review of this can be found in Ref. [28].

Interconnects are electrical conductors that are used to connect multiple individual cells in series or parallel in a stack. They also serve as gas barriers between adjacent fuel and oxidant channels of consecutive cells. In most cases, ceramic perovskite materials are used as interconnects for high temperature operation, i.e., doped lanthanum and yttrium chromites (dopants may be Mg, Sr, Ca, Ca/Co). Dopant concentrations govern thermo-mechanical and electrical properties. The geometric

configuration of these materials mainly depend on the stack design and operating conditions. An ideal interconnect would have very good electrical conductivity, corrosion resistance, and good contact properties at the interface. In recent times, metallic alloys (typically high-chrome alloys) have also been used as interconnects, due to superior performance at lower temperatures and more focus on reducing operating temperatures of SOFCs [29]. Nevertheless, the corrosion resistant oxides that are formed on exposure to highly oxidizing conditions have very low conductivity, and are a challenge to this technology. Also, varying temperature cycles tend to cause fatigue and reduce the strength of these materials. Along with interconnects, gas seals play an important role in preventing mixing of fuel and oxidant, providing electrical insulation, and in mechanical bonding between two different components. Different types of seals exist, and are broadly divided into bonded seals and compressed seals. Interested readers are directed to a fuel cell handbook for more information [30].

Table 2.2: Impact of MEA and fuel on peak power density for H-SOFCs

Reference	MEA (anode/electrolyte/cathode)	T (°C)	Fuel	P_{peak} (mW/cm ²)
[31]	3 wt % Pd-loaded FeO/BCY25/Ba _{0.5} Pr _{0.5} CoO ₃ ^a	600	H ₂	134
[32]	Ni-BCSO/BCSO/BCSF-BCSO ^b	600	97% H ₂ + 3% H ₂ O	132
		700		340
[33]	Ni-BCGO/BCGO/LSCO-BCGO ^c	700	NH ₃	355
		750		384
		700	H ₂	371
[28]	Ni-BCY10/BCY10/BSCF ^d	600	H ₂	380
		700		550
[34]	Ni-BCY10/BCY10/Pr ₂ NiO _{4+δ} ^e	600	97% H ₂ + 3% H ₂ O	96
		650		132
[35]	Ni-BCY10/BCY10/Pr ₂ NiO _{4+δ} ^f	600	H ₂	180

^a BCY25 - 25 mol % Y³⁺ - doped BCY (~ 0.5 mm thick). Oxidant - air.

^b BCSO - BaCe_{0.8}Sm_{0.2}O_{2.90} (~ 50 μm thick). Oxidant - oxygen.

^c Electrolyte (BCGO) - BaCe_{0.8}Gd_{0.2}O_{2.90} (~ 50 μm thick), cathode (LSCO) - La_{0.5}Sr_{0.5}CoO_{3-δ}. Oxidant - oxygen.

^d Electrolyte (BCY10) - BaCe_{0.9}Y_{0.1}O_{2.95} (~ 50 μm thick), cathode (BSCF) - Ba_{0.5}Sr_{0.5}Co_{0.8}Fe_{0.2}O_{3-δ}. Oxidant - air.

^e BCY10 - BaCe_{0.9}Y_{0.1}O_{3-δ} (~ 85 μm thick). Oxidant - air.

^f Electrolyte - ~ 50 μm thick. Oxidant - compressed air.

2.3 Prospects and challenges of the technology

SOFCs have shown tremendous potential on the road to commercialization. Some of the applications of these systems include auxiliary power units (APUs), portable and stationary power, and commercial and residential CHPs. Apart from the traditional geometric configurations - button, planar and tubular, several innovative designs have been proposed. Single chamber solid oxide fuel cells avoid the problem of sealing, which is critical for high temperature fuel cells, as both fuel and air are mixed before being fed into the cell [36]. Nonetheless, the electrodes need to be highly selective and chemically stable during thermo-catalytic conversion of the fuel. Monolithic-type SOFCs have gained considerable attention. Due to its structural complexity, the process of identifying major sources of irreversibility to enhance system efficiency becomes all the more necessary [37]. Segmented-in-series SOFCs offer a promising route towards enhancing electrochemical performance by reducing lateral electrical resistance (using optimal cell widths), and decreasing cost by employing lesser amount of catalyst (Ni) as well as cheap fabrication techniques [38]. In general, prospects of SOFC technology can also be found in extant literature [39].

The major challenges to the market of SOFCs involve reducing cost and increasing durability. These arise out of certain technical aspects related to cell operation. The fundamental reason for high cost, and reduced cell lifetime, is the operating temperature. These high operating temperatures lead to the usage of more expensive materials that need to be resistant to thermal degradation [40]. But, one must bear in mind the trade-off between temperature and its effect on electrolyte resistivity and chemical kinetics in the cell, which has adverse consequences on the overall efficiency. Hence, this represents a major obstacle towards producing compatible materials [41, 42]. Another barrier is that the response times to changes in load, and the operational start-up time, are strongly dependent on temperature in these systems. Nonetheless, thermal insulators and shields have to be provided for minimization of heat losses and protection. Therefore, current efforts are directed towards lowering operating temperature, and the development of novel materials and stack designs.

2.4 Thermo-catalytic and gas-phase chemistry

Chemical reactions take place by breaking chemical bonds of reactants and simultaneously forming new bonds of products via absorption or release of energy, respectively. The difference between a catalyzed and a non-catalyzed reaction is the magnitude of the activation energy barrier. A catalyzed reaction has lower activation energy. The general Arrhenius expression gives the relationship

between the rate of a reaction and its dependence on temperature and activation energy (Eq. 2.8). It can be seen that the rate of a reaction decreases with an increase in activation energy, although the free energy and enthalpy are unchanged. Operating conditions such as temperature and pressure are adjusted to lower the free energy, to facilitate the reaction by making it thermodynamically favorable [43].

$$k = AT^\beta \exp\left(\frac{-E_a}{RT}\right) \quad (2.8)$$

In general, the chemical and physical steps involved in a heterogeneous catalytic reaction are [44]:

1. Mass transfer of reactant(s) from the bulk fluid to the external surface of the catalyst pellet.
2. Pore diffusion of the reactant from the external surface, through the catalyst pores, to the internal catalytic surface.
3. Surface reactions on the catalyst surface involving (i) adsorption of reactant, (ii) reaction on the surface to form products, and (iii) desorption of products from the surface.
4. Pore diffusion of products from the internal catalytic surface to the external pore surface on the pellet.
5. Mass transfer of the product(s) from the external pellet surface to the bulk fluid.

It is crucial to understand these steps in order to determine which one is rate-determining. This will help postulate rate laws for various catalytic mechanisms. If step 3 is found to be rate-limiting, the adsorption and kinetic models are usually described by the Langmuir-hinshelwood approach, Freundlich isotherm, Eley-Rideal mechanism, BET isotherm etc. Each of these models have questionable assumptions involved in formulating rate laws. In this thesis, we use the mean-field approximation for the micro-kinetic model.

2.4.1 Reaction pathways in a SOFC anode

The heterogeneous chemical reactions occurring in the anode of a SOFC are mainly directly towards providing hydrogen/syngas as fuel for electrochemical reactions. The internal reforming process can take place either directly or indirectly. In the former mode of operation, the reforming process occurs directly within the cell to produce electrochemical reactants. In the case of indirect internal reforming, the fuel is additionally reformed with the help of an external reformer that is integrated with the SOFC system [45]. Direct internal reforming tends to be advantageous from the

perspective of effective utilization of heat, which is generated by chemical reactions within the anode. Nevertheless, degradation of cell performance by coke formation is a hurdle unless optimal operating conditions and anode properties are considered. Traditionally, reforming of hydrocarbons has been the most common route towards producing synthesis gas or syngas [46]. The product yields of such processes are enhanced by catalysts. The most common SOFC anode catalyst is nickel, due to it being inexpensive and readily available compared to other noble metals. However, it is well established that nickel promotes coking, which leads to its deactivation [47]. In this work, only thermo-catalytic reactions pertaining to methane are considered. The reactions specifying the conversion of methane to syngas, along with carbon formation, is described globally in Table 2.3.

Table 2.3: Global reactions in a Ni-based SOFC anode [48]

Methane steam reforming	
$CH_4(g) + H_2O(g) \rightleftharpoons CO(g) + 3H_2(g)$	$\Delta H_{298}^0 = +206.2 \text{ kJ/mol}$
$CH_4(g) + 2H_2O(g) \rightleftharpoons CO_2(g) + 4H_2(g)$	$\Delta H_{298}^0 = +164.7 \text{ kJ/mol}$
Methane dry reforming	
$CH_4(g) + CO_2(g) \rightleftharpoons 2CO(g) + 2H_2(g)$	$\Delta H_{298}^0 = +247.2 \text{ kJ/mol}$
Methane partial oxidation	
$CH_4(g) + \frac{1}{2}O_2(g) \rightleftharpoons CO(g) + 2H_2(g)$	$\Delta H_{298}^0 = -35.6 \text{ kJ/mol}$
Methane total oxidation	
$CH_4(g) + 2O_2(g) \rightleftharpoons CO_2(g) + 2H_2O(g)$	$\Delta H_{298}^0 = -802 \text{ kJ/mol}$
Water-gas shift (WGS)	
$CO(g) + H_2O(g) \rightleftharpoons CO_2(g) + H_2(g)$	$\Delta H_{298}^0 = -41.1 \text{ kJ/mol}$
Methanation	
$CO(g) + 3H_2(g) \rightleftharpoons CH_4(g) + H_2O(g)$	$\Delta H_{298}^0 = -206 \text{ kJ/mol}$
$2CO(g) + 2H_2(g) \rightleftharpoons CH_4(g) + CO_2(g)$	$\Delta H_{298}^0 = -247.2 \text{ kJ/mol}$
Boudouard reaction	
$2CO(g) \rightleftharpoons C(s) + CO_2(g)$	$\Delta H_{298}^0 = -172.4 \text{ kJ/mol}$
Methane cracking	
$CH_4(g) \rightleftharpoons C(s) + 2H_2(g)$	$\Delta H_{298}^0 = +74.9 \text{ kJ/mol}$
Gasification of Carbon	
$C(s) + H_2O(g) \rightleftharpoons CO(g) + H_2(g)$	$\Delta H_{298}^0 = +131.3 \text{ kJ/mol}$
$C(s) + O_2(g) \rightleftharpoons CO_2(g)$	$\Delta H_{298}^0 = -393.5 \text{ kJ/mol}$

Apart from the thermo-catalytic processes that lead to carbon formation, carbon might also undergo electrochemical oxidation via



The global rate laws that are formulated for these reactions have varying fit parameters reported in literature [49-51]. They usually have limited validity, in terms of the operating conditions they can be employed at. This mainly arises due to the intrinsic variation in the pre-exponential factor based on the assumed reaction molecularity and order. Also, this factor is highly dependent on temperature and properties of the catalyst material. In order to avoid this problem of dubious fit parameters used as pre-exponential factors and activation energies, a 42-step elementary surface reaction mechanism is employed throughout this thesis.

The detailed multi-step heterogeneous reaction mechanism, used in this study, consists of 42 reactions and 6 gas-phase species. It takes into account the adsorption/desorption of H_2 , O_2 , CH_4 , CO , CO_2 and H_2O from the surface of Ni [52]. Also, it encompasses the global aspects of the water-gas shift reaction, formation of carbon monolayer, methanation reactions, steam reforming, dry reforming, partial and total oxidation of C_1 species. It was made thermodynamically consistent and extended to temperatures between 220 and 1700 °C. However, the initial mechanism was validated only at 800 °C [53]. Furthermore, the extended mechanism was validated and tested with experimental data obtained from methane reforming over nickel/alumina monoliths in the temperature range of 900-1350 K, and with additional data from literature. Comparison with equilibrium calculations demands further work to predict surface carbon deposition rates. The carbon coverage varies as a strong function of operating temperature and steam/carbon (S/C) ratio. Moreover, the prediction of carbon deposition using the thermodynamic properties of graphite is questionable. It has been argued that carbon nanofibers (CNF) are more likely to form in the SOFC anode, and they possess different thermodynamic properties as compared to graphite [54]. However, the predicted Nernst potentials are independent of the carbon type. Unlike the case involving higher hydrocarbons, gas-phase reactions in the fuel channel can be neglected [55]. Also, the mechanism used in this work does not account for bulk-phase Ni oxidation, which is one of the most important causes for cell degradation. The reaction mechanism scheme for the oxidation and reforming of methane is shown in Fig. 2.2, while the reactions are listed in the Appendix. Nevertheless, other elementary reaction mechanisms have also been proposed in literature [56]. The computational framework used in modeling these reactions via the mean-field approximation is described in the next sub-section.

species), K_b is number of the bulk species that form in the inner solid catalyst, v'_{ki} and v''_{ki} are the stoichiometric coefficients of the k^{th} species in the i^{th} reaction, and χ_k denotes the species k involved in the reaction.

A modified Arrhenius expression, based on mean field approximation, is used for the calculation of the forward reaction rate constant for the i^{th} thermo-catalytic reaction in the cathode according to

$$k_{fi} = A_i \left(\frac{T}{T^0}\right)^{\beta_i} \exp\left(-\frac{E_{ai}}{RT}\right) \prod_{k=K_g+1}^{K_g+K_s} \theta_k^{\mu_{ki}} \exp\left(-\frac{\varepsilon_{ki}\theta_k}{RT}\right) \quad (2.11)$$

Here, A_i is the pre-exponential factor, E_{ai} is the activation energy, μ_{ki} and ε_{ki} are parameters modeling the order and activation energy dependency on surface coverage, respectively, for the i^{th} reaction, β_i is the temperature exponent, θ_k is the surface coverage, R the gas constant, and T is the temperature. The rate constant of the reverse reaction is calculated from thermodynamic data, i.e.,

$$K_{ci} = \frac{k_{fi}}{k_{ri}} = K_{pi} \left(\frac{p^0}{RT}\right)^{\sum_{k=1}^{K_g} \nu_{ki}} \prod_{k=K_g+1}^{K_g+K_s} \frac{\sigma_k^{\nu'_k}}{\sigma_k^{\nu''_k}} \quad (2.12)$$

Here, p^0 is the pressure at standard conditions and K_{pi} is the equilibrium constant. Also, $\nu_k = \nu''_k - \nu'_k$. K_{pi} is calculated from

$$K_{pi} = \exp\left(-\frac{\Delta G_i^0}{RT}\right) = \exp\left(\frac{\Delta S_i^0}{R} - \frac{\Delta H_i^0}{RT}\right) \quad (2.13)$$

The change in entropy ΔS^0 and enthalpy ΔH^0 are calculated from the thermodynamic properties of the concerned species as,

$$\frac{\Delta S_i^0}{R} = \sum_{k=1}^{K_g+K_s} \nu_{ki} \frac{S_k^0}{R} \quad (2.14)$$

$$\frac{\Delta H_i^0}{RT} = \sum_{k=1}^{K_g+K_s} \nu_{ki} \frac{H_k^0}{RT} \quad (2.15)$$

The definition of K_{ci} and K_{pi} lead to Eq. 2.12, and are given by

$$K_{ci} = \prod_{k=1}^{K_g+K_s} [X]_k^{v_{ki}}, K_{pi} = \prod_{k=1}^{K_g} \left(\frac{p_k}{p^0}\right)^{v_{ki}} \prod_{k=K_g+1}^{K_g+K_s} \theta_k^{v_{ki}} \quad (2.16)$$

From the relation $\theta_k = \frac{[X]_k \sigma_k}{\Gamma}$, the temporal variations of surface coverage θ_k are given by

$$\frac{d\theta_k}{dt} = \frac{\dot{s}_k \sigma_k}{\Gamma}, \quad k = K_g + 1, \dots, K_g + K_s \quad (2.17)$$

where σ_k is the co-ordination number (number of sites required for a species for adsorption), Γ is the surface site density that represents the maximum number of adsorption sites on a unit catalytic surface area (a value of 2.66×10^{-9} mol/cm² is considered in this study) and \dot{s}_k is the molar production rate of a gaseous or surface species k due to heterogeneous reaction, which is equal to

$$\dot{s}_k = \sum_{i=1}^{K_r} v_{ki} k_{fi} \prod_{k=1}^{K_g+K_s+K_b} [X]_k^{v'_{ki}} \quad (2.18)$$

Here, K_r is the number of surface reactions, $[X]_k$ is the concentration of species k , v_{ki} is the net stoichiometric coefficient of the species in the i^{th} reaction (positive for products, negative for reactants), and v'_{ki} are the stoichiometric coefficients of reactants. At steady-state, $\dot{s}_k = 0$ in Eq. 2.17 for surface species, implying no variation in surface coverage with time (although varying spatially). The lateral interaction of surface species between different locations of the catalytic surface is neglected. The sum of all the coverages on the mono-layer catalyst surface follows the condition

$$\sum_{k=1}^{K_s} \theta_k = 1 \quad (2.19)$$

The rate constants for adsorption reactions are conveniently described using sticking coefficients. Sticking coefficients represent the probability of adsorption for a particle hitting the catalyst surface, whose magnitudes lie between [0, 1]. This probability is nothing but the ratio of the number of atoms that adsorb to the total number of atoms that impinge on the same surface at a given time interval. It depends on the surface temperature, kinetic energy of the atoms, surface coverage and the number of active sites available. Experimentally, numerous methods exist for the study of gas-surface collision dynamics. Some of them are molecular beam techniques involving "King and

Wells" approach and single crystal adsorption calorimetry, X-ray photoelectron spectroscopy (XPS), scanning tunneling microscopy (STM) etc. Theoretically, the collision frequency needs to be calculated from the kinetic theory of gases to determine the sticking coefficient. From this, the reaction rate is given by

$$\dot{s}_k = S_k^{eff} \sqrt{\frac{RT}{2\pi W_k}} [X]_k \quad (2.20)$$

where W_k is the molecular weight of species k . The local adsorption probability S_k^{eff} is given by

$$S_k^{eff} = S_k^0 \prod_{k=1}^{K_s} \theta_k^{v'_{ki}} \quad (2.21)$$

$$\prod_{k=1}^{K_s} \theta_k^{v'_{ki}} = \theta_{free}^\tau \text{ and } \tau = \sum_{k=1}^{K_s} v'_{ki} \quad (2.22)$$

Where, θ_{free} is the available free catalytic surface coverage. As $\theta_k = \frac{[X]_k \sigma_k}{\Gamma}$, the reaction rate in Eq. 2.20 reduces to

$$\dot{s}_k = k_{fi}^{ads} [X]_k [X]_{free}^\tau \quad (2.23)$$

and,

$$k_{fi}^{ads} = \frac{S_k^0}{\Gamma^\tau} \sqrt{\frac{RT}{2\pi W_k}} \quad (2.24)$$

The initial sticking coefficient of the uncovered surface is S_k^0 . This assumes Boltzmann distribution of molecular velocities near the surface. This assumption is not valid when the sticking probability approaches unity, due to which the effective sticking coefficient has to be corrected by [58]

$$S_k^{eff'} = \frac{S_k^{eff}}{1 - \frac{1}{2} S_k^{eff}} \quad (2.25)$$

In the case of elementary reactions, it is important to note that the reaction mechanism is constructed in such a way so as to ensure thermodynamic consistency. This means that the chemical kinetic parameters of the forward reaction are determined independently, while the kinetic parameters for the reverse reaction are derived from the following constraints

$$E_f^{act} - E_r^{act} = \Delta H \quad (2.26)$$

$$\frac{A_f}{A_r} = \exp\left(\frac{\Delta S}{R}\right) \quad (2.27)$$

where ΔH is the reaction enthalpy and ΔS is the reaction entropy. In developing the reaction mechanism, the rate constants are usually determined from a combination of surface science experiments as well as theoretical studies such as Unity Bond Index-Quadratic Exponential Potential (UBIQEP), Density Functional Theory (DFT), Monte Carlo (MC) and Molecular Dynamics (MD) simulations. In reality, formulation of thermodynamic consistency is more complex. It involves a detailed algorithm to produce thermodynamic consistent rate coefficients and surface potentials [59].

2.4.3 Gas-phase chemistry

The developed model can also handle gas-phase reactions occurring in the fuel channel of the SOFC, which becomes prominent in the case of operation with higher hydrocarbons, and at very high temperatures and elevated pressures. These non-catalytic homogeneous reactions are taken into account mathematically via the appropriate inclusion of a source term in the fluid flow model. The general chemical reaction employing only gas-phase species is the same as Eq. 2.10, apart from the fact that $K_s = K_b = 0$. The rate expression k_{fi} takes an Arrhenius form similar to Eq. 2.8, i.e.,

$$k_{fi} = A_i T^{\beta_i} \exp\left(\frac{-E_{ai}}{RT}\right) \quad (2.28)$$

The reaction rate of each gas-phase species is

$$\dot{\omega}_k = \sum_{i=1}^{K_{gr}} \nu_{ki} k_{fi} \prod_{k=1}^{K_g} [X]_k^{\nu_{ki}'} \quad (2.29)$$

where $\dot{\omega}_k$ is the molar production rate of a gaseous species k due to homogeneous reactions and K_{gr} is the number of non-catalytic reactions. As elementary reactions are reactions that appear in the molecular level in a way that is exactly similar to what is described by the reaction equation, the reaction orders are equal to the stoichiometric coefficients. This is the reason behind using ν'_{ki} in Eq. 2.29. Gas-phase reactions are not considered in any of the simulations in this thesis.

2.5 Electrochemistry and charge transfer

This section revolves around models describing charge transfer chemistry in both oxide-ion-conducting and proton-conducting SOFCs. Charge transfer occurs at the three-phases boundaries (TPB), which are basically interfaces formed by the electro-catalyst, electrolyte and gas-phase boundaries [60]. In reality, the TPB is highly characterized by the micro-structure properties of the anode, and form very complex pathways for the transport of ions and electrons. In this study, we only consider charge transfer occurring at the electrode-electrolyte interface (interfacial charge transfer) and not across the utilization region of the electrodes (distributed charge transfer). In general, charge transfer in a SOFC is not well understood. The basic operation of a fuel cell is governed by various electrochemical losses. In order to maximize the output of a SOFC, it is important to understand the origin and factors affecting these overpotentials. The major losses/irreversibilities can be categorized as follows:

- **Activation overpotential (η_a)** - this loss occurs when a part of the input energy is lost in overcoming the slowness with which the charge transfer reactions occur at the anode and cathode TPBs. Analogous to catalytic and non-catalytic reactions, the charge transfer process consists of a series of reaction steps. The slowest reaction step determines the overall rate of the electrochemical charge transfer process. The electrons need to overcome an activation barrier to travel from a region of higher potential (electrolyte) to a region of lower potential (anode). The amount of energy required to do this depends on the relative potential difference between the anode and the electrolyte. The activation overpotential is the potential difference above the equilibrium value between the anode and the electrolyte, required to produce a current, i.e., $\eta_a = (\phi_a - \phi_e) - (\phi_a^{eq} - \phi_{el}^{eq}) = E_a - E_a^{eq}$. This applies to the electron transfer process between the cathode and the electrolyte as well. This is determined from the global or modified Butler-Volmer (B-V) equation. Some of the factors that affect this overpotential η_a are materials, interface properties, surface roughness, temperature, pressure, current density etc.

- **Concentration overpotential (η_{conc})** - these losses arise due to mass transport limitations within the electrode. It is the potential difference caused by the differences in concentration of the electrochemically active species between the bulk solution and the TPBs, as described by the Nernst equation. In simple terms, it is the difference between the reversible potentials in the channel- and the electrolyte-electrode interfaces. These are dominant at high current densities due to excessive product build-up at the TPB, leading to a shortage in supply of electrochemical reactants. This can be optimized by controlling the micro-structural parameters of the anode, i.e., by increasing porosity and pore diameter, and reducing tortuosity.
- **Ohmic overpotential (η_{ohm})** - as the name suggests, these resistances arise due to the intrinsic electrical and ionic conductivities of the electrode and electrolyte materials, respectively. In modern fuel cells, the major source of ohmic overpotential is the electrolyte itself. The resistance offered by this material can be lowered by reducing its thickness. In reality, ohmic resistance should also take into account the contact resistances caused at the interfaces. However, we assume good adherence between different MEA materials in order to neglect these resistances.

2.5.1 Electrochemical model for reversible oxide-ion-conducting SOFCs¹

This sub-section will give an overview of the mathematical basis behind the electrochemical model. Three main charge transfer pathways have been proposed in literature for SOFCs: (i) hydrogen spillover, (ii) oxygen spillover and (iii) interstitial hydrogen transfer [61]. A spillover reaction involves the transfer of one species that is either adsorbed or formed on a first surface onto a second surface, in order to either adsorb or react with other adsorbed species. Chapters 3 and 4, of this thesis, are pretty straightforward in assuming H₂-H₂O as the only electrochemically active charge transfer pathway. In this case, potential balance equations pertaining to only H₂-H₂O are considered, while any equation containing CO-CO₂ is neglected. Chapter 5 assumes both H₂-H₂O and CO-CO₂ to be electrochemically active charge transfer pathways as it involves syngas production by co-electrolysis of H₂O and CO₂. This segment gives a unified electrochemical model that accounts for both H₂-H₂O and CO-CO₂ as charge transfer pathways. Fig. 2.3 shows the electrochemical reactions occurring in the MEA of a typical oxide-ion-conducting SOFC. The electrochemical model holds valid irrespective of whether the cell is operating in the fuel cell mode or the electrolysis mode. This will further be investigated in detail.

¹ Parts of this section are taken from Menon et al. [62]. Copyright (2014), with permission from Elsevier.

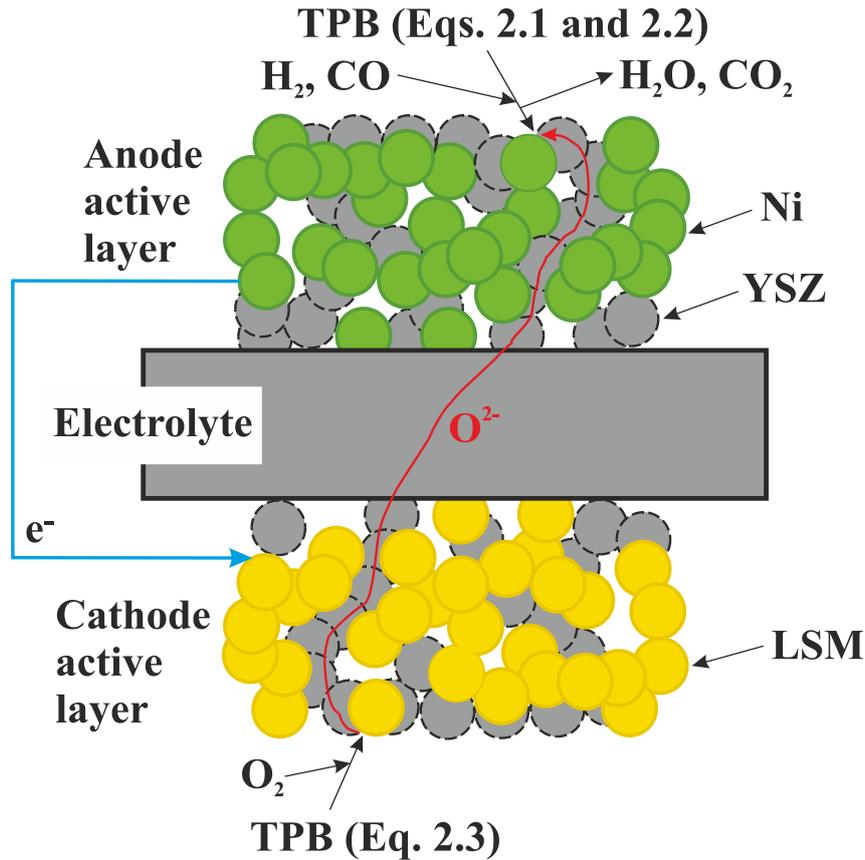


Figure 2.3: Electrochemical reactions occurring in the MEA of a typical oxide-ion-conducting SOFC.

In the fuel cell mode of operation, it is sufficient to consider H_2 oxidation kinetics as the dominant pathway, even in the presence of gases such as CO and CH_4 [63]. In the electrolysis mode of operation, it is still unclear as to whether CO is produced due to only the reverse water-gas shift reaction (RWGS) or due to a combination of both RWGS and electrolysis of CO_2 [64, 65]. This is determined by comparing the ASR values, obtained during AC and DC characterization of the cell, between H_2O electrolysis, CO_2 electrolysis, and co-electrolysis operations. The net current density, with respect to electrochemically active species H_2O - H_2 and CO_2 - CO , is computed as the normalized sum of currents - i_{H_2} and i_{CO} through two parallel pathways of charge transfer. Here, symbols with the subscript ' H_2 ' correspond to the pathway involving H_2 - H_2O oxidation/reduction, while those with the subscript ' CO ' correspond to the accompanying parallel pathway involving CO - CO_2 oxidation/reduction. The two analogous electro-chemical reactions normalize to a single value of current density via charge and mass conservation equations. In the electrolysis mode of operation, the potential balance equation in each pathway is formulated after taking into account all the irreversibilities (resistances) that occur during operation and is related to the current density by

$$E_{cell} = E_{rev,H_2} + \left| \eta_{a,fe(i_{H_2})} \right| + \eta_{a,oe(i_{H_2})} + \eta_{ohm(i_{H_2})} + \eta_{conc(i_{H_2})} \quad (2.30)$$

$$E_{cell} = E_{rev,CO} + \left| \eta_{a,fe(i_{CO})} \right| + \eta_{a,oe(i_{CO})} + \eta_{ohm(i_{CO})} + \eta_{conc(i_{CO})} \quad (2.31)$$

where as in the fuel cell mode of operation,

$$E_{cell} = E_{rev,H_2} - \eta_{a,fe(i_{H_2})} - \left| \eta_{a,oe(i_{H_2})} \right| - \eta_{ohm(i_{H_2})} - \eta_{conc(i_{H_2})} \quad (2.32)$$

$$E_{cell} = E_{rev,CO} - \eta_{a,fe(i_{CO})} - \left| \eta_{a,oe(i_{CO})} \right| - \eta_{ohm(i_{CO})} - \eta_{conc(i_{CO})} \quad (2.33)$$

where $\eta_{a,fe}$ and $\eta_{a,oe}$ are the activation overpotentials at the fuel electrode and oxidant electrode respectively, η_{ohm} is the ohmic overpotential, and η_{conc} is the concentration overpotential. The concentration overpotential is not treated explicitly as porous media transport is modeled in detail, i.e., the reversible potential is calculated using gas-phase concentrations at the electrode-electrolyte interface. E_{rev} is the ‘reversible’ cell voltage, which is the maximum possible potential that can be derived from a cell operating reversibly, and is given by the Nernst equation as

$$E_{rev,H_2} = E_{H_2}^0 + \frac{RT}{2F} \ln \left(\frac{p_{H_2,fe} p_{O_2,oe}^{1/2}}{p_{H_2O,fe}} \right) \quad (2.34)$$

$$E_{rev,CO} = E_{CO}^0 + \frac{RT}{2F} \ln \left(\frac{p_{CO,fe} p_{O_2,oe}^{1/2}}{p_{CO_2,fe}} \right) \quad (2.35)$$

where E^0 is the electromotive force (EMF) at standard pressure, p_i represents the partial pressures of H_2 , H_2O , CO , CO_2 (at the fuel electrode TPB) and O_2 (at the oxidant electrode TPB). The subscripts ‘oe’ and ‘fe’ stand for oxidant electrode and fuel electrode, respectively. The temperature dependent E^0 is calculated from thermodynamic data ($\Delta G(T)/2F$). The source of all the thermodynamic species data is the JANAF tables. The ohmic overpotential in Eqs. 2.30 - 2.33 is given by

$$\eta_{ohm} = R_{tot}i \quad (2.36)$$

where R_{tot} is given by

$$R_{tot} = R_{el} + R_c + R_{oe} + R_{fe} \quad (2.37)$$

The magnitudes of these resistances depend on the type of material used and the micro-structure of the porous electrode. In modern cells, the electronic resistances of both electrodes R_{oe} , R_{fe} and the contact resistances between solid-solid interfaces R_c are negligible compared to the ionic resistance of the electrolyte R_{el} , which is given by

$$R_{el} = \frac{l_{el}}{\sigma_{el}} \quad (2.38)$$

where l_{el} is the thickness of the electrolyte, and σ_{el} is the electrolyte conductivity, with the SI unit - S/m, which varies as a strong function of temperature as

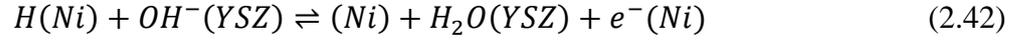
$$\sigma_{el} = \sigma_0 T^{-1} \exp\left(\frac{-E_{el}}{RT}\right) \quad (2.39)$$

Here, E_{el} is the activation energy for ion transport and σ_0 is the pre-exponential factor. The global charge transfer reaction for the H₂-H₂O pathway can be seen as a series of elementary steps, considering hydrogen spillover to be the most probable mechanism [66-68].

1. Adsorption/desorption of H₂ on the Ni surface



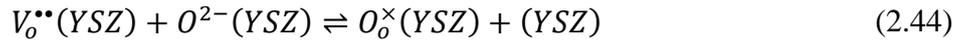
2. Single electron charge transfer reactions at the TPB region



3. H₂O adsorption/desorption on the Ni surface



4. Transfer of oxygen ions between the bulk and YSZ



Here, H(Ni) represents the hydrogen atom attached to the Ni surface, $V_o^{\bullet\bullet}(YSZ)$ is an oxygen vacancy and $O_o^{\times}(YSZ)$ is a lattice oxygen. The symbols in the brackets stand for the specific surface to which the corresponding species is attached. The modified B-V equation is used to describe the functional relationship between the activation losses and current density by considering Eq. 2.42 to be the rate-limiting step, and the others to be in equilibrium [66]. For the charge transfer pathway H₂-H₂O, this takes the form

$$i_{H_2} = i_{0,H_2} \left[\exp\left(\frac{(1 + \beta_a)F\eta_{a,fe}}{RT}\right) - \exp\left(-\frac{\beta_c F\eta_{a,fe}}{RT}\right) \right] \quad (2.45)$$

For a single electron transfer reaction, the charge transfer coefficients $\beta_a + \beta_c = 1$. The exchange current density is expressed as a function of temperature, and partial pressure of products and reactants (obtained due to its coupling with the micro-kinetic model) participating in the charge transfer chemistry, although it makes more physical sense to express it as a function of open surface coverage and surface coverage of electrochemically active species. The exchange current density i_{0,H_2} (when $\beta_a = \beta_c = 0.5$) is expressed as

$$i_{0,H_2} = i_{H_2}^* \frac{(p_{H_2}/p_{H_2}^*)^{1/4} (p_{H_2O})^{3/4}}{1 + (p_{H_2}/p_{H_2}^*)^{1/2}} \quad (2.46)$$

The equilibrium partial pressure $p_{H_2}^*$ is given by [66]

$$p_{H_2}^* = p_{H_2} \left(\frac{\theta_{Ni}}{\theta_H} \right)^2 = A_{H_2} \exp\left(\frac{-E_{H_2}^{des}}{RT}\right) \frac{\Gamma^2}{S_{H_2}^0} \sqrt{2\pi W_{H_2} RT} \quad (2.47)$$

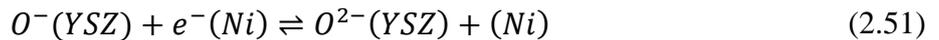
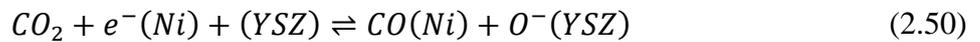
where $\Gamma = 2.6 \times 10^{-9}$ mol/cm², the pre-exponential factor $A_{H_2} = 5.59 \times 10^{19}$ cm² mol⁻¹s⁻¹, sticking coefficient for H₂ adsorption $S_{H_2}^0 = 0.01$, and the activation energy $E_{H_2}^{des} = 88.12$ kJ/mol. These parameters are equal to the ones used in the surface reaction mechanism described in Refs. [53, 66].

In case of the charge transfer pathway CO-CO₂, a similar approach is followed where the global charge transfer equation is divided into a series of elementary steps [69]. These are

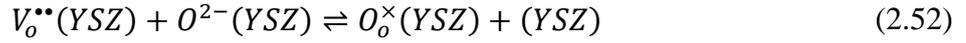
1. Adsorption/desorption of CO₂ and CO on Ni surface



2. Single electron charge transfer reactions at the TPB region



3. O²⁻ ion incorporation into the bulk YSZ



Eq. 2.51 is assumed to be rate limiting [70], through which a modified B-V equation is derived. For the charge transfer pathway CO-CO₂, this takes the form

$$i_{CO} = i_{0,CO} \left[\exp\left(\frac{\beta_a F \eta_{a,fe}}{RT}\right) - \exp\left(-\frac{(1 + \beta_c) F \eta_{a,fe}}{RT}\right) \right] \quad (2.53)$$

The exchange current density $i_{0,CO}$ (when $\beta_a = \beta_c = 0.5$) is [69]

$$i_{0,CO} = i_{CO}^* \frac{(p_{CO_2}/p_{CO})^{1/4}}{1 + (p_{CO}/p_{CO}^*) + (p_{CO_2}/p_{CO_2}^*)} \quad (2.54)$$

The formulae for calculating the equilibrium partial pressures p_{CO}^* and $p_{CO_2}^*$ are as follows [69]

$$p_{CO_2}^* = p_{CO_2} \left(\frac{\theta_{Ni}}{\theta_{CO_2}} \right) = A_{CO_2} \exp\left(\frac{-E_{CO_2}^{des}}{RT}\right) \frac{\Gamma}{S_{CO_2}^0} \sqrt{2\pi W_{CO_2} RT} \quad (2.55)$$

$$p_{CO}^* = p_{CO} \left(\frac{\theta_{Ni}}{\theta_{CO}} \right) = A_{CO} \exp\left(\frac{-E_{CO}^{des}}{RT}\right) \frac{\Gamma}{S_{CO}^0} \sqrt{2\pi W_{CO} RT} \quad (2.56)$$

Here, $\Gamma = 2.66 \times 10^{-9}$ mol/cm², $A_{CO_2} = 6.447 \times 10^7$ s⁻¹, $A_{CO} = 3.56 \times 10^{11}$ s⁻¹, $E_{CO_2}^{des} = 25.98$ kJ/mol, $E_{CO}^{des} = 111.27$ kJ/mol, $S_{CO_2}^0 = 1 \times 10^{-5}$, and $S_{CO}^0 = 0.5$. These values are similar to the adsorption/desorption reactions of the corresponding species in the heterogeneous reaction mechanism (listed in the Appendix) [52, 71].

At the oxidant electrode, the charge transfer reactions are divided into multiple steps [66]. These are

1. Adsorption/desorption of oxygen on the oxidant electrode surface



2. Diffusion to the TPB region



3. Charge transfer and incorporation into the electrolyte



The charge transfer step Eq. 2.59 is considered to be rate limiting, which gives the modified B-V equation [66]

$$i_i = i_{0,O_2} \left[\exp\left(\frac{\beta_a F \eta_{a,oe}}{RT}\right) - \exp\left(-\frac{\beta_c F \eta_{a,oe}}{RT}\right) \right] \quad (2.60)$$

where i is the current, i_0 is the exchange current density, η is the activation overpotential, F is the Faraday constant, T is the temperature and β is the asymmetric charge transfer coefficient. The subscript index i refers to either H₂ or CO, as Eq. 2.60 involves two anode activation overpotentials for each charge transfer pathway: H₂-H₂O and CO-CO₂. The exchange current density i_{0,O_2} (when $\beta_a = \beta_c = 0.5$) is expressed as

$$i_{0,O_2} = i_{O_2}^* \frac{(p_{O_2}/p_{O_2}^*)^{1/4}}{1 + (p_{O_2}/p_{O_2}^*)^{1/2}} \quad (2.61)$$

where the equilibrium pressure $p_{O_2}^*$ is

$$p_{O_2}^* = A_{O_2} \exp\left(\frac{-E_{O_2}^{des}}{RT}\right) \quad (2.62)$$

For the LSM/YSZ interface, $A_{O_2} = 4.9 \times 10^9$ atm and $E_{O_2}^{des} = 200$ kJ/mol [72].

An Arrhenius expression is used to describe the temperature dependence of the exchange current density which takes form of i_i^* in Eqs. 2.46, 2.54 and 2.61, and is given by

$$i_i^* = k_i \exp\left(-\frac{E_i}{RT}\right) \quad (2.63)$$

where the subscript index i refers to either H_2 , CO or O_2 . The parameters k_i and E_i are the electrochemical fit parameters, which are deduced by reproducing experimental data. To summarize, the electrochemical branches used in chapters 3–5 are shown in Fig. 2.4.

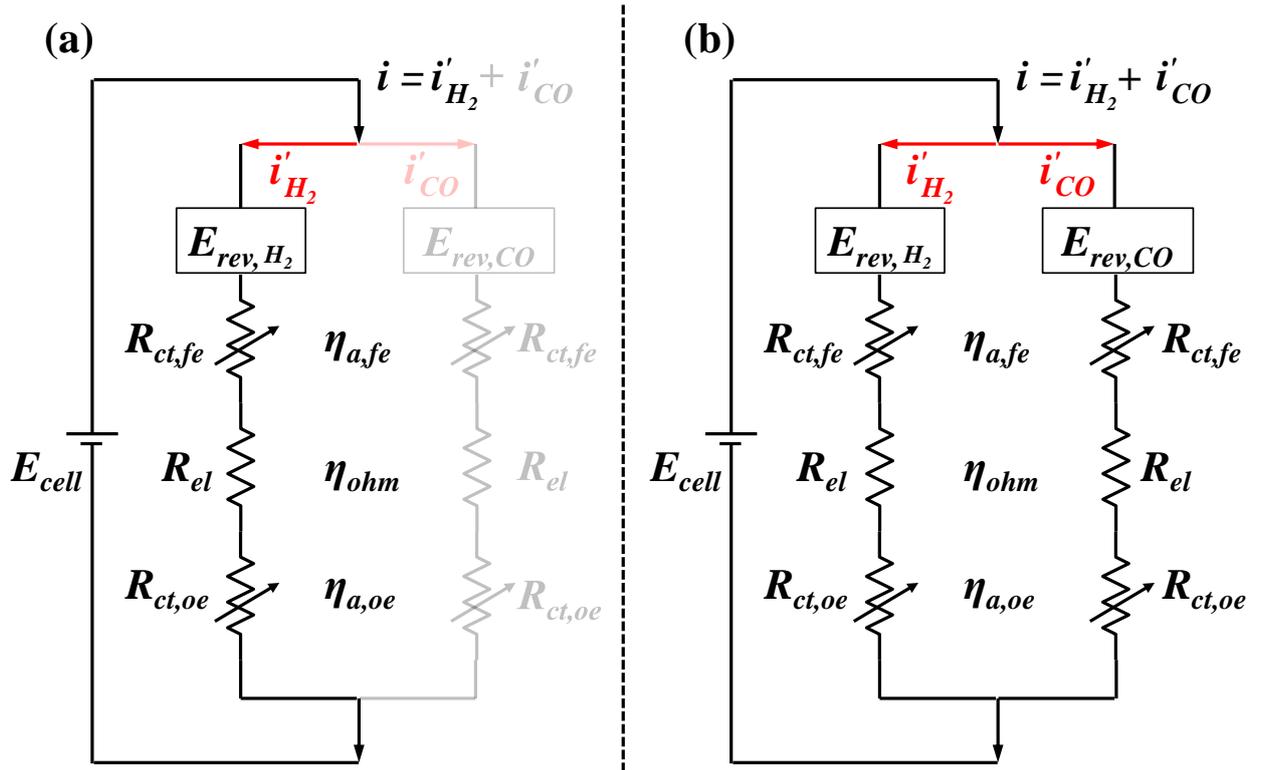


Figure 2.4: Electrochemical models used in chapters 3–5: (a) Chapters 3 and 4 only employ equations for the i'_{H_2} branch of the circuit; (b) Chapter 5 employs equations for both i'_{H_2} and i'_{CO} branches of the circuit. Adapted from Ref. [73].

In the case of co-electrolysis of H_2O and CO_2 , due to the fact that the TPB sites are shared by both H_2O and CO_2 , a factor γ is introduced to normalize the net current density and account for the relative percentages of H_2O and CO_2 at the electrode-electrolyte interface. Therefore, the net current density reduces to

$$i = i'_{H_2} + i'_{CO} = \gamma i_{H_2} + (1 - \gamma) i_{CO} \quad (2.64)$$

where,

$$\gamma = \frac{Y_{H_2O}^{TPB}}{(Y_{H_2O}^{TPB} + Y_{CO_2}^{TPB})} \quad (2.65)$$

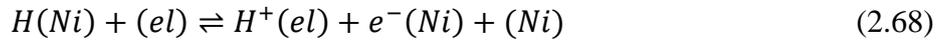
This normalization factor approach has been established and validated [73, 74]. However, it is independent of certain factors affecting the TPB such as ratio of ionic to electronic particles, coordination number of ionic and electronic particles, fraction overlap between these particles, volume fraction of these constituents, foreign impurities in the TPB and degradation effects on the Ni catalyst.

2.5.2 Electrochemical model for proton-conducting SOFCs

The difference between the electrochemical models, used in this work, for oxide-ion-conducting and proton-conducting solid oxide cells (SOCs) is detailed here. The Nernst equation is given by

$$E_{rev} = E^0 + \frac{RT}{2F} \ln \left(\frac{p_{H_2,fe} p_{O_2,oe}^{1/2}}{p_{H_2O,oe}} \right) \quad (2.66)$$

where E^0 is the electromotive force (EMF) at standard pressure, p_i represents the partial pressures of O_2 , H_2O (at the oxidant electrode TPB) and H_2 (at the fuel electrode TPB). The multi-step reactions that are considered for the derivation of the modified B-V equation are [61, 68]



Eq. 2.68 is considered to be rate limiting [75]. The activation overpotential at the electrode-electrolyte interfaces is related to the current density, in implicit form, by the non-linear B-V equation. For the electrochemical oxidation of H_2 , the modified B-V equation is used (detailed derivation is listed in the Appendix). The relationship is given by

$$i = i_{0,a} \left[\exp \left(\beta_a \frac{Fn_e}{RT} \eta_{a,fe} \right) - \exp \left(-(1 - \beta_a) \frac{Fn_e}{RT} \eta_{a,fe} \right) \right] \quad (2.69)$$

where i is the current, i_0 is the exchange current density, n_e is the number of electrons involved per reaction (equal to 1 since a single electron transfer reaction is considered), η_a is the activation overpotential, F is the Faraday constant, T is the temperature and β is the asymmetric charge transfer coefficient. At OCV, the rate of charge transfer in the anodic direction is equal to the rate of charge transfer in the cathodic direction. For the electrochemical reduction of O_2 , a global B-V equation is used because the kinetic parameters needed to calculate the partial equilibrium pressure of O_2 were not available in literature for the specific material being considered. This takes the form

$$i = i_{0,c} \left[\exp\left(\beta_a \frac{Fn_e}{RT} \eta_{a,oe}\right) - \exp\left(-(1 - \beta_a) \frac{Fn_e}{RT} \eta_{a,oe}\right) \right] \quad (2.70)$$

Here, $n_e = 2$ (from Eq. 2.6). The temperature dependent exchange current densities can be expressed in Arrhenius form as

$$i_{0,a} = k_{H_2} \exp\left(-\frac{E_{H_2}}{RT}\right) \frac{(p_{H_2}/p_{H_2}^*)^{1/4}}{1 + (p_{H_2}/p_{H_2}^*)^{1/2}} \quad (2.71)$$

$$i_{0,c} = k_{O_2} \exp\left(-\frac{E_{O_2}}{RT}\right) \left(\frac{p_{O_2,c}}{p_{amb}}\right)^{1/4} \quad (2.72)$$

where k_{H_2} , E_{H_2} , k_{O_2} and E_{O_2} are electrochemical fit parameters, and $p_{H_2}^*$ is described by Eq. 2.47. The order dependency of the oxygen partial pressure is obtained by assuming surface diffusion of oxygen intermediates to be the rate limiting step, rather than the charge transfer reaction [76-78].

2.6 Porous media transport^{1, 2}

Mass transport within porous media is strongly influenced by pore size. Typically, three fundamental diffusion phenomena exist: bulk or molecular diffusion, Knudsen diffusion and surface diffusion. Molecular diffusion arises from the kinetic energy of gas molecules and are dominant in large pores whose sizes are significantly greater than the mean free path of a gas molecule. Knudsen diffusion arises when the mean free path exceeds the characteristic length of the pores. In this case, the probability of gas molecules colliding with the pore walls is higher than it colliding with other gas

¹ Parts of this section are taken from Menon et al. [79]. Copyright (2013), with permission from Elsevier.

² Parts of this section are taken from Menon et al. [62]. Copyright (2014), with permission from Elsevier.

molecules. This is characterized by the Knudsen number ($Kn = \lambda_m/d_{\text{pore}}$), where λ_m is the mean free path. $Kn \ll 1$ implies molecular diffusion is dominant, while $Kn \gg 1$ means Knudsen diffusion is dominant. Surface diffusion occurs in micro-pores when adsorbed species hop along the pore walls [8, 57]. Due to geometrical considerations, i.e., since the electrode thickness is much smaller than its length, species transport through the porous media is assumed to be one-dimensional along its thickness, transverse to the direction of axial flow in the channel. This reaction-diffusion equation is given by

$$\frac{\partial(\phi\rho_f Y_k)}{\partial t} = -\frac{\partial(J_k W_k)}{\partial y} + \dot{s}_k W_k A_{\text{sp}}, \quad k = 1, \dots, K_g \quad (2.73)$$

The total density of the fluid within the porous structure can be computed from

$$\frac{\partial(\phi\rho_f)}{\partial t} = -\sum_{k=1}^{K_g} \frac{\partial(J_k W_k)}{\partial y} + \sum_{k=1}^{K_g} \dot{s}_k W_k A_{\text{sp}} \quad (2.74)$$

Here, \dot{s}_k is the heterogeneous molar production rate of the chemical species k , y is the independent spatial variable along the thickness, and A_{sp} is the specific catalytic area available for surface reactions. The species molar flux J_k in the porous bed is evaluated using the dusty-gas model (DGM) equation as [66]

$$J_k = -\left[\sum_{l=1}^{K_g} D_{kl}^{DGM} \nabla[X]_l + \left(\sum_{l=1}^{K_g} \frac{D_{kl}^{DGM} [X]_l}{D_{l,\text{Kn}}^e} \right) \frac{B_g}{\mu} \nabla p \right] \quad (2.75)$$

The DGM is written as an implicit relationship between the pressure gradients, concentration gradients, molar fluxes, binary diffusion coefficients and Knudsen diffusion coefficients. It neglects the effect of external forces and thermo-diffusion. The porous medium is considered to be a stationary component of the mixture in which the Chapman-Enskog kinetic theory is used to estimate the binary diffusivities, while the pressure variations are proportional to the variations in gas concentrations [80, 81]. The species molar flux J_k is derived by inverting the following equation

$$\sum_{l \neq k} \frac{[X]_l J_k - [X]_k J_l}{[X]_T D_{kl}^e} + \frac{J_k}{D_{k,Kn}^e} = -\nabla[X]_k - \frac{B_g [X]_k}{\mu D_{k,Kn}^e} \nabla p \quad (2.76)$$

where $[X]_T = p/RT$ is the total molar concentration. Although DGM is computationally more complex than the Stefan-Maxwell (SMM) or Fick's model (FM) to represent porous media transport, it was found to be the most appropriate for H₂-H₂O and CO-CO₂ systems based on the effect of three factors: current density, pore size and reactant concentration. For low H₂ concentrations (in systems with H₂-H₂O-Ar inlet gas mixtures), the superiority of the models varied as DGM > SMM > FM. However, DGM is recommended for multi-component H₂-H₂O-CO-CO₂ systems [82]. Since the flux ratios among gas species become complicated for multi-component H₂-H₂O-CO-CO₂ systems, the equimolar counter diffusion assumption is no longer valid. In this scenario, the DGM is recommended, over the Fick's model (FM) or the Stefan-Maxwell model (SMM), to resolve flux ratios using Graham's law of diffusion in parallel with fluxes occurring due to local current densities. The first term on the right-hand side of Eq. 2.75 represents the diffusive flux (molecular diffusion acting in series with Knudsen diffusion) and the second term represents the viscous flux (Darcy flow arising due to pressure gradients). D_{kl}^{DGM} is defined as the DGM diffusion coefficients and is formulated as

$$D_{kl}^{DGM} = \mathcal{H}^{-1} \quad (2.77)$$

where the elements of the \mathcal{H} matrix are

$$h_{kl} = \left[\frac{1}{D_{k,Kn}^e} + \sum_{j \neq k} \frac{X_j}{D_{kj}^e} \right] \delta_{kl} + (\delta_{kl} - 1) \frac{X_k}{D_{kl}^e} \quad (2.78)$$

The permeability B_g in Eq. 2.75 is given by the Kozeny-Carman relationship [83]

$$B_g = \frac{\phi^3 d_p^2}{72\tau(1-\phi)^2} \quad (2.79)$$

Here, d_p is the particle diameter and τ is the tortuosity. The effective Knudsen diffusion coefficient $D_{k,Kn}^e$ in Eq. 2.76 is given by

$$D_{k,Kn}^e = \frac{\phi d_{\text{pore}}}{\tau} \frac{1}{3} \sqrt{\frac{8RT}{\pi W_k}} \quad (2.80)$$

The effective binary diffusivity D_{kl}^e in Eq. 2.76 is given by

$$D_{kl}^e = \frac{\phi}{\tau} \mathcal{D}_{kl} \quad (2.81)$$

where \mathcal{D}_{kl} is the binary diffusion coefficient of species k in l . Solution of Eq. 2.73 requires the reaction source terms \dot{s}_k and boundary conditions at the electrode-gas chamber and electrode-electrolyte interfaces. At the electrode-gas chamber interface the inlet mass fractions serve as the boundary condition, while at the electrode-electrolyte interface the chemical species fluxes are zero. The electrochemical reaction source terms, for electrochemically active species, are calculated from the current density and enter as fluxes at the electrode-electrolyte interface.

2.7 Flow in the gas channels^{1, 2}

A quasi-two-dimensional model reported previously is used for the simulation of the gas channels, i.e., the planar single channel model is not a full 2-D model. The species composition is resolved in 1-D in the gas channels (along the direction of axial flow) as well as in the porous media (transverse to the direction of axial flow). For each axial position in the flow channel, the porous media is resolved across its thickness, i.e., even though the governing equations have only one independent space coordinate, it generates an overall 2-D effect [45, 66, 84, 85]. The quasi-two-dimensional co-flow planar model solves for the gas channels by assuming plug flow. The axial diffusion is negligible compared to the axial convective transport. The radial variation in species composition is neglected as diffusive mixing is assumed to be predominant [86]. Since the channel dimensions considered are quite small (~ 1 mm), the plug flow assumption is adequate to represent species transport in the channels. Thus, the model has a fixed number of cells/nodes in the axial direction, and no radial meshing. This obviously tends to have an impact on the accuracy of the computed solution, compared to the boundary layer and Navier-Stokes models. The plug flow equation for species continuity in the channels is given by

¹ Parts of this section are taken from Menon et al. [79]. Copyright (2013), with permission from Elsevier.

² Parts of this section are taken from Menon et al. [62]. Copyright (2014), with permission from Elsevier.

$$\frac{\partial(\rho_f Y_k)}{\partial t} = -\frac{\partial(\rho_f v Y_k)}{\partial z} + \frac{P_e}{A_c} J_k W_k + W_k \dot{\omega}_k, \quad k = 1, \dots, K_g \quad (2.82)$$

In this thesis, gas-phase reactions are not considered, i.e., $\dot{\omega}_k = 0$. The velocity in the gas channel can be calculated from the momentum equation,

$$\frac{\partial(\rho_f v)}{\partial t} = -\frac{\partial(\rho_f v v)}{\partial z} + v \sum_{k=1}^{K_g} \frac{P_e}{A_c} J_k W_k \quad (2.83)$$

where P_e is the perimeter associated with the electrochemically active membrane electrode assembly (MEA), ρ_f is the fluid density, Y_k is the species mass fraction of species k , v is the velocity, z is the axial position, W_k is the species molecular weight, and A_c is the cross-sectional area of the channel. Assuming constant pressure in the channels, the density is calculated from the ideal gas equation

$$p\bar{W} = \rho_f RT \quad (2.84)$$

with \bar{W} represented as

$$\bar{W} = \sum_{k=1}^{K_g} X_k W_k \quad (2.85)$$

In Eqs. 2.82 and 2.83, J_k is the flux at the electrode-channel interface, which is calculated using the dusty-gas model (DGM). These species molar fluxes depend on the heterogeneous chemistry within the porous-electrode structure and local current density $i(z)$. The energy balance equation for the flow channels is given by

$$\frac{\partial(\rho_f C_{pf} T_f)}{\partial t} = -\frac{\partial(v \rho_f C_{pf} T_f)}{\partial z} + \frac{4}{D_h} h(T_s - T_f) \quad (2.86)$$

Here, C_{pf} is the specific heat capacity of the fluid. T_f and T_s are the temperatures of the fluid stream and solid phase, respectively. The geometry dependent Nusselt number Nu , which is used to calculate the heat transfer coefficient h at every axial position, is represented as an empirical formula [87]

$$Nu = \frac{hD_h}{\lambda} \quad (2.87)$$

$$Nu = 3.095 + 8.933 \left(\frac{1000}{Gz} \right)^{-0.5386} \exp \left(-\frac{6.7275}{Gz} \right) \quad (2.88)$$

where D_h is the hydraulic diameter, λ is the thermal conductivity of the fluid, Gz is the Graetz number which is given in terms of the Reynolds number, Re , and Prandtl number, Pr , as

$$Gz = \frac{D_h}{z} Re Pr \quad (2.89)$$

2.8 Thermal transport^{1, 2}

2.8.1 Quasi-2-D single co-flow planar SOFC

In this solid-phase energy balance model, the solid-phase refers to the combined thickness of the anode, electrolyte and cathode. The variation of temperature along the thickness is neglected because the length of the porous media is much greater than its thickness. Hence, the equation in 1-D is given as

$$\rho_s C_{ps} \frac{\partial T_s}{\partial t} = \frac{\partial}{\partial z} \left(\lambda_{eff,s} \frac{\partial T_s}{\partial z} \right) + \frac{A_c}{A_s} \dot{Q} - \frac{A_{act}}{V_s} P_{out} \quad (2.90)$$

where t is the time, T_s is the temperature, ρ_s is the density, C_{ps} is the heat capacity, $\lambda_{eff,s}$ is the effective heat conductivity, A_{act} is the electrochemically active anode surface area, V_s is the volume of the solid, P_{out} is the power density output and \dot{Q} is the heat source term arising from the interaction

¹ Parts of this section are taken from Menon et al. [85]. Copyright (2012), with permission from Elsevier.

² Parts of this section are taken from Menon et al. [75].

with the channels (this changes along the channel axis with species composition and by means of heat exchange with the solid-phase). Subscript 's' refers to the solid-phase or combined porous media. Here, A_c and A_s are the areas of cross section of the channel and solid-phase, respectively. As the channels experience negligible pressure change, \dot{Q} can be expressed in terms of an enthalpy flux as

$$\dot{Q} = - \sum_{k=1}^{K_g} \frac{\partial(\rho_f v h_k Y_k)}{\partial z} \quad (2.91)$$

In 1-D, effective solid thermal conductivity $\lambda_{eff,s}$ is obtained from the harmonic mean (decreases the influence of larger values and strongly tends towards smaller values in the element set) of the effective thermal conductivities of the three different porous-media materials. The effective thermal conductivity for each material is averaged by the number of its radial nodes (y-axis), before the harmonic mean is taken. The effective conductivity at each radial node is given by [88]

$$\lambda_{eff} = \phi \lambda_{fluid} + (1 - \phi) \lambda_{solid} \quad (2.92)$$

where λ_{fluid} is the thermal conductivity of the gas and λ_{solid} is the solid thermal conductivity. The inlet boundary conditions at time $t = 0$, are the initial conditions. At the exit of the reactor channels, adiabatic Neumann boundary conditions are used,

$$\left. \frac{dT_f}{dz} \right|_{z=L} = 0 \quad (2.93)$$

Similarly, for the solid-phase temperature (Eq. 2.90) adiabatic boundary conditions are used at both ends, i.e., at $z=0$ and $z=L$,

$$\left. \frac{dT_s}{dz} \right|_{z=0} = 0, \quad \left. \frac{dT_s}{dz} \right|_{z=L} = 0 \quad (2.94)$$

2.8.2 3-D SOFC stacks

The timescales of various processes such as kinetics, diffusion, and heat transfer occurring in an SOFC stack are different from each other, and the heat transfer process has a higher time constant

compared to the rest of the processes. Therefore, it is quite rational to assume all processes but heat transfer to be in steady-state. In the method adopted here, the solid phase temperature is decoupled from the fluid phase to develop the transient stack model, which solves the transient two- or three-dimensional heat conduction equation. While solving the heat conduction equation, the stack is assumed to be a porous media consisting of straight channels.

$$\rho_s C_{ps} \frac{\partial T_s}{\partial t} = \frac{\partial}{\partial x_i} \left(\lambda_{ij} \frac{\partial T_s}{\partial x_j} \right) + \dot{Q} \quad (2.95)$$

where t is the time, T_s is the solid structure temperature, ρ_s is the density, C_{ps} is the heat capacity, λ_{ij} is the tensor of heat conductivity, \dot{Q} is the heat source term from the interaction with the channels. Time integration is carried out for the solid phase heat balance. At every axial position, solid phase temperature is obtained and subsequently used to calculate the reaction rates and gas phase temperature. The MEA is collectively considered as porous media by the solid structure (subscript 's').

Solving the partial differential equations requires the specification of boundary conditions at the borders of the simulation domain. Depending on the operating conditions, Dirichlet boundary conditions

$$T|_{wall} = const \quad (2.96)$$

or Neumann conditions

$$k \frac{\partial T}{\partial n} \Big|_{wall} = \Psi \quad (2.97)$$

may be used. In the above equations, the heat flux Ψ in the normal direction of the border n may consist of a linear heat condition term, a bi-quadratic radiation term and a constant term

$$\Psi = h(T_s - T_{surr}) + \varepsilon \sigma (T_s^4 - T_{surr}^4) + \Psi_{const} \quad (2.98)$$

Here, σ is the Stefan-Boltzmann constant. The heat transfer coefficient h , the emissivity ε , and the temperature of the surroundings T_{surr} have to be specified as model parameters. Nevertheless, the

stack model may easily be coupled with an arbitrary combination of user-defined Dirichlet or Neumann boundary conditions. The initial condition used in this case refers to the initial temperature of the solid structure/stack. Physically, it is the operating temperature to which the stack is heated up before usage, as SOFCs operate at a range of temperatures from 600 to 1000 °C.

The heat source term is derived from the simulation of individual cells. For systems with nearly constant pressure, the energy conservation can be expressed in terms of enthalpy. Constant pressure is assumed while modeling the individual channels. Then, the enthalpy flux in the channel $\dot{H}_{channel}$ can only be changed along the channel axis by means of heat exchange with the stack. If the channel density is γ (channels per unit area of the cross-section), the source term can be expressed as

$$\dot{Q} = -\gamma \frac{\partial \dot{H}_{channel}}{\partial x} + Q_{ohmic} \quad (2.99)$$

Here, Q_{ohmic} is the heat release due to ohmic heating within the electrolyte. By inclusion of enthalpy of formation into its definition, $\dot{H}_{channel}$ does not change due to electrochemical oxidation.

2.9 Solution algorithm^{1, 2}

2.9.1 1-D button cell

Figure 2.5 portrays a three-dimensional schematic representation of the button-cell configuration. The solution procedure for this system is well documented [71]. In short, the button cell model solves for the reaction diffusion equation (Eq. 2.73) along its discretized axi-symmetric line. This model does not solve for gas flow in the channels. The molar flux is calculated using the DGM, with the provision of two boundary conditions. The first boundary condition at the electrode-gas chamber interface is given by the inlet mass fractions in the gas channel. The second boundary condition equates to species fluxes that are calculated based on the local current density at the electrode-electrolyte interface. Time integration of Eqs. 2.73 and 2.74 is performed, until steady-state, to yield species mass fractions in the porous media. Differential algebraic equation (DAE) solver LIMEX is used to solve the equation system [89]. Fig. 2.6 summarizes these boundary conditions. For oxide-ion conducting SOFCs, the boundary condition at the fuel electrode-electrolyte interface is given by the molar fluxes of the electrochemically active species.

¹ Parts of this section are taken from Menon et al. [85]. Copyright (2012), with permission from Elsevier.

² Parts of this section are taken from Menon et al. [75].

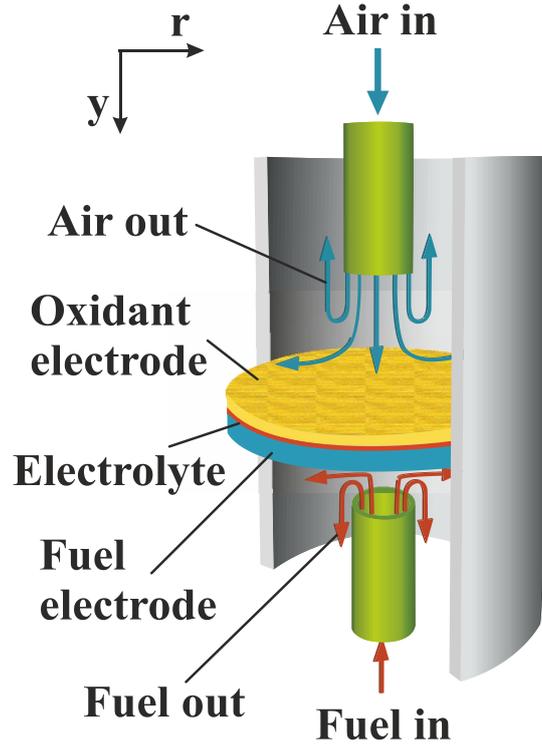


Figure 2.5: Three-dimensional illustration of the button-cell configuration. Blue arrows refer to the air feed, while red arrows represent the fuel feed.

These fluxes are related to the current density by

$$J_{H_2O} = -J_{H_2} = \frac{i'_{H_2}}{2F}, J_{CO_2} = -J_{CO} = \frac{i'_{CO}}{2F} \quad (2.100)$$

while at the oxidant electrode-electrolyte interface, the boundary condition is

$$J_{O_2} = -\frac{(i'_{H_2} + i'_{CO})}{4F} \quad (2.101)$$

For proton-conducting SOFCs, the fluxes of all species but hydrogen are zero at the anode-electrolyte interface, and is given by

$$J_{H_2} = -\frac{i}{2F} \quad (2.102)$$

At the cathode-electrolyte interface, the electrochemical fluxes amount to

$$J_{H_2O} = \frac{i}{2F}, J_{O_2} = -\frac{i}{4F} \quad (2.103)$$

These are standard boundary conditions that are required to solve the reaction-diffusion equation and are independent of geometry type.

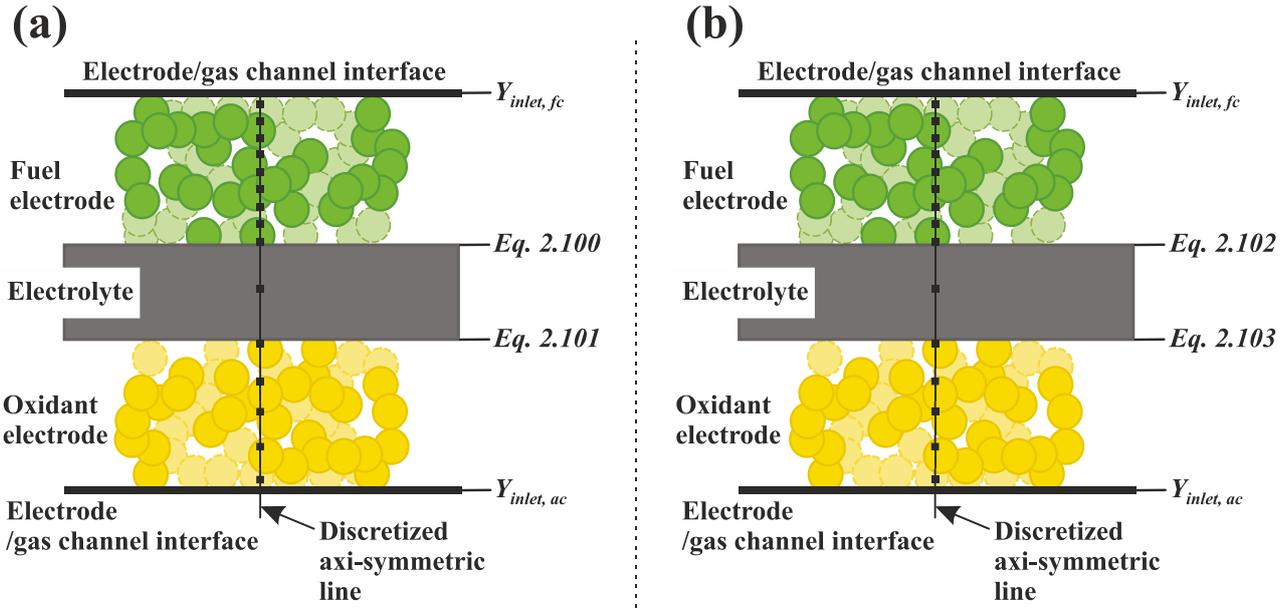


Figure 2.6: Boundary conditions needed to solve the reaction-diffusion equation for (a) oxide-conducting SOCs, and (b) proton-conducting SOFCs.

2.9.2 Quasi 2-D single co-flow planar SOFC

Eqs. 2.30–2.33, 2.73, 2.74, 2.82–2.84, 2.86, and 2.90 form a system of coupled non-linear equations, which can be treated as a differential-algebraic system mathematically. Their residual form can be written as

$$F(\Phi) = 0 \quad (2.104)$$

where the vector Φ is given by

$$\Phi = [(Y, \dot{m}, T)_{fc}, (Y, \rho, T, \theta)_{fe,1} \dots (Y, \rho, T, \theta)_{fe,n}, (T)_{el}, (Y, \rho, T)_{oe,1}, \dots (Y, \rho, T)_{oe,m}, (Y, \dot{m}, T)_{ac}]^T \quad (2.105)$$

Here, the indices (fc) , $(fe,1)$, (fe,n) , (el) , $(oe,1)$, (oe,m) , (ac) stand for fuel channel, first discretized cell in the fuel electrode, n^{th} discretized cell in the fuel electrode, cell in the electrolyte, first discretized cell in the oxidant electrode, m^{th} discretized cell in the oxidant electrode, and air channel, respectively. This is shown in Fig. 2.7. In this thesis, the number of discretized nodes in the electrodes and electrolyte is the same for every chapter.

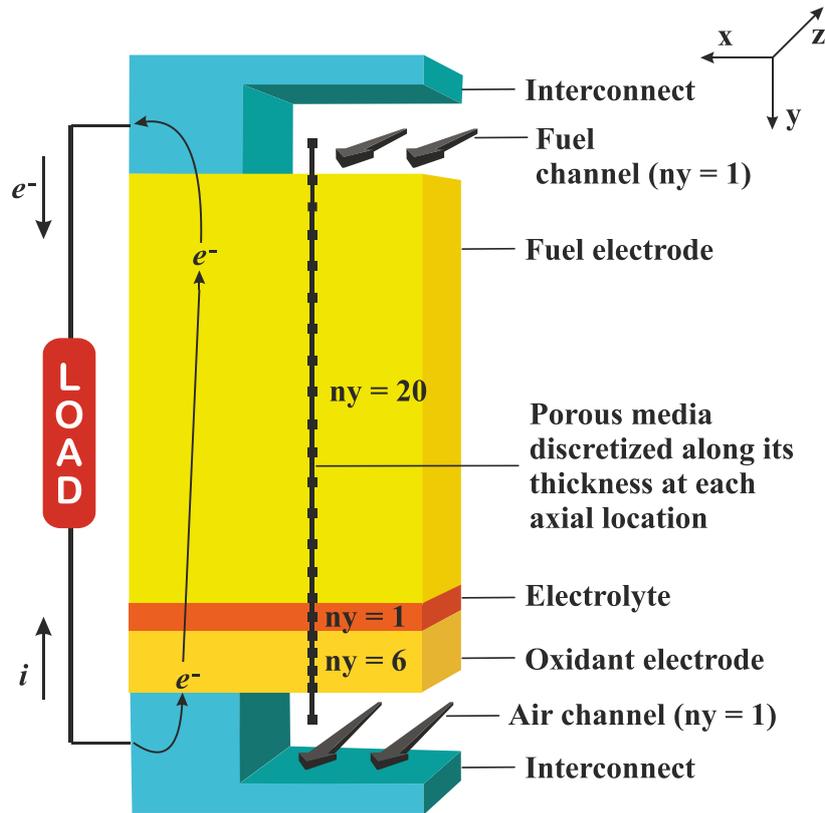


Figure 2.7: Cross-sectional view of a co-flow planar SOFC depicting the discretization along the thickness of the porous media. 'ny' represents the number of nodes along the y axis.

They are first cast in finite-volume form, with the specification of required number of axial and transverse nodes/cells. The entire solution procedure follows a space marching algorithm: at each axial position the transient system of equations is solved until a steady-state solution is obtained. The initial condition at each axial position assumes the converged solution from the previous finite volume cell. The solid-phase temperature is decoupled from that of the fluid-phase, due to the fact that heat transfer has a higher time constant compared to mass transfer, diffusion and kinetics. At every time step of the solid-phase temperature calculation, space marching of the entire channel is carried out. At every axial position, the solid phase temperature is obtained, and subsequently used to calculate the reaction rates and gas phase temperature. The equation system is solved using the differential algebraic equation (DAE) solver LIMEX [89]. A damped Newton iteration algorithm is

employed to solve the system of algebraic model equations (Eqs. 2.30–2.33, 2.45, 2.53, 2.60 for oxide-ion-conducting cells, and Eqs. 2.32, 2.33, 2.69, 2.70 for proton-conducting cells) to obtain the current density [45, 62, 66, 71, 79, 84, 85]. The entire program is written in FORTRAN and is a part of the software package DETCHEM™ [90]. The flow chart illustrating the implementation of the solution algorithm is shown in Fig. 2.8.

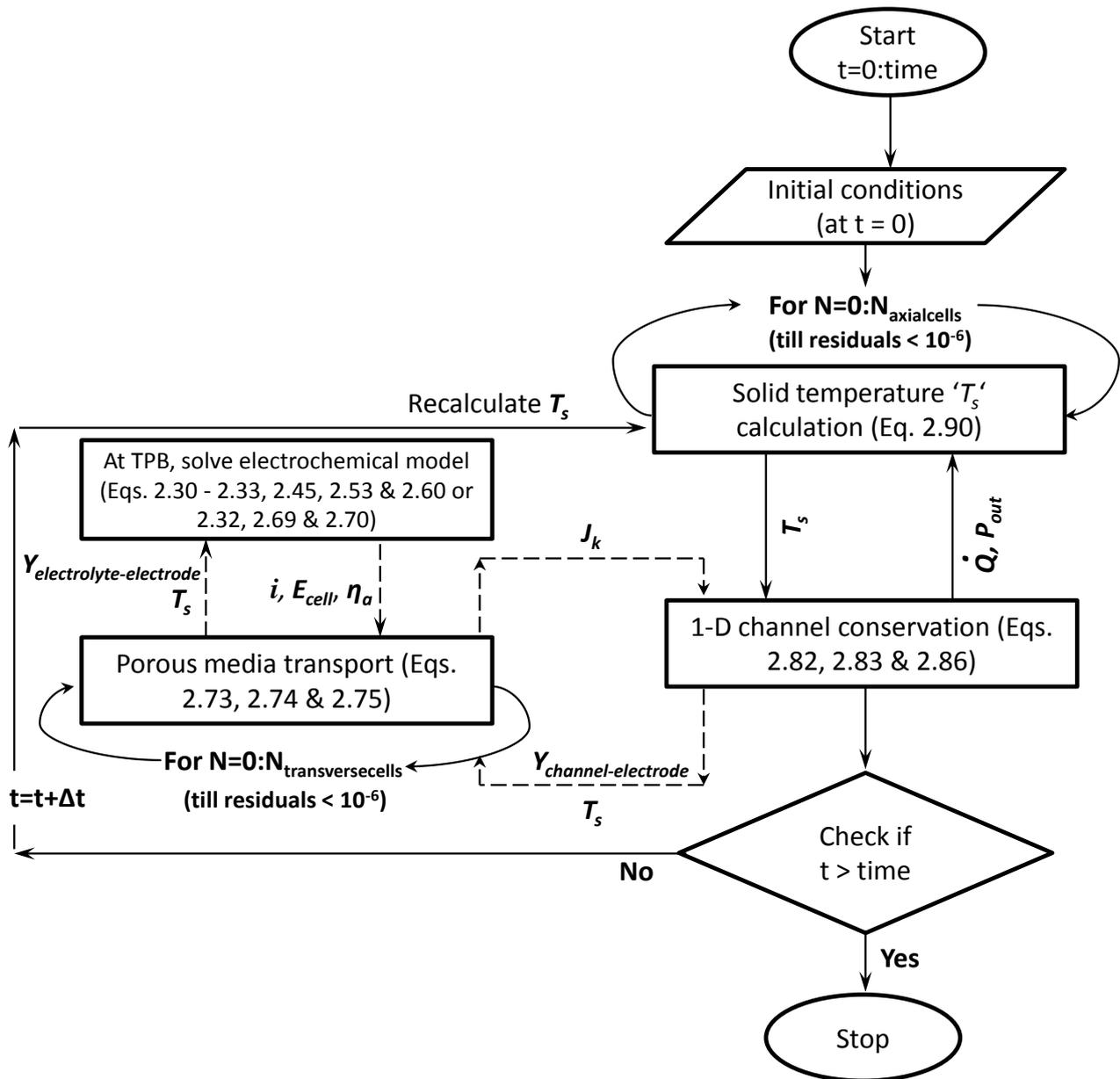


Figure 2.8: Schematic representation of the overall solution algorithm via a flowchart.

2.9.3 3-D SOFC stacks

Discretization of the PDE - The stack is assumed to be a continuum, whose transient temperature field is described by the heat conduction equation Eq. 2.95. This differential equation shall be

solved for the two- and three-dimensional cases. We assume that all channels of the unit cells within the stack are parallel, denoted by the direction of the x-axis.

The two- or three-dimensional fields need to be discretized in order to solve the differential equations. Here, we chose a finite volume method. For the two-dimensional case, we always use an orthogonal grid. In case of three dimensions, the grid in the yz-plane can be unstructured and consisting of arbitrarily shaped triangles and quadrilaterals. This grid is extended orthogonally into the x-direction. Thus, the finite volume elements are three- or four-sided prisms.

Due to the orthogonality of the grid with respect to the direction of the unit cell channels, it is easy to distinguish between the axial and radial direction for the heat conduction. In order to account for structure dependent differences, separate heat conductivity coefficients in the axial and the radial directions are applied, λ_{axial} and λ_{radial} , respectively.

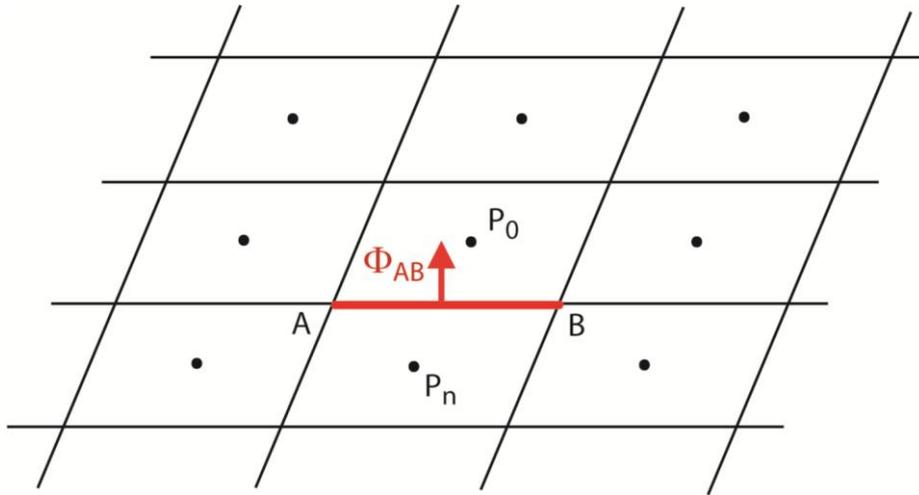


Figure 2.9: Depiction of gradient approximation in radial direction by specified temperatures.

The heat source term \dot{Q} is obtained from the simulations of individual cells. Each row of grid cells in the axial direction defines a temperature profile that is used as the boundary condition for the channels crossing these grid cells. Thus, the number of cells of the grid in the y-direction or in the xz-plane defines the maximum number of different temperature profiles for the unit cell simulations.

In order to resolve the heat field, Eq. 2.95 is discretized by the finite volume method. For a partial differential equation (PDE) of the form

$$\rho_s C_{ps} \frac{\partial T_s}{\partial t} = \frac{\partial}{\partial x_i} \left(\lambda \frac{\partial T_s}{\partial x_j} \right) \quad (2.106)$$

we integrate over a channel and apply Stokes' integral theorem to get

$$V \cdot \rho_s C_{ps} \frac{\partial T_s}{\partial t} = \sum_{faces} \Phi_{face} \quad (2.107)$$

Here, Φ_{face} is the heat flow through a face of the channel. The channel itself shall be denoted by index 0 and its neighbor by index n . In the axial direction, we can directly use a finite difference approximation of the temperature gradient because of the orthogonality of the grid

$$\Phi_{ax} = -\lambda A_{face} \left(\frac{T_0 - T_n}{x_0 - x_n} \right) \quad (2.108)$$

In radial direction, the gradient can be approximated by the temperatures T_0, T_n, T_A, T_B , as shown in Fig. 2.9. The heat flow then becomes

$$\Phi_{rad} = \Phi_{AB} \cdot \Delta x \quad (2.109)$$

with

$$\Phi_{AB} = \lambda \cdot \left(\frac{\partial T}{\partial y} \right) \cdot \left(\frac{-(z_B - z_A)}{(y_B - y_A)} \right) \quad (2.110)$$

This expression can be simplified into

$$\Phi_{AB} = -\lambda (\alpha(T_0 - T_n) + \beta(T_B - T_A)) \quad (2.111)$$

with

$$\alpha = \frac{\overline{AB}^2}{|\overline{AB} \times \overline{P_n P_0}|} \quad (2.112)$$

$$\beta = \frac{\overline{AB} \cdot \overline{P_n P_0}}{|\overline{AB} \times \overline{P_n P_0}|} \quad (2.113)$$

The parameters α and β only have to be calculated once for the grid. As a result of finite volume approximation, these grid based parameters depend on P_0 , P_n , which refer to centers of adjacent cells, and A , B , which are nodes of the same cell. With them, the right-hand side of the PDE is transformed into a system of algebraic equations.

Choosing representative channels - Calculating individual channel flow fields is the most time consuming step in a stack simulation. In order to reduce the computational cost, only representative channels are chosen for detailed simulation [91]. Due to the representation of the stack by a discrete grid, there is a unique channel boundary temperature profile for each axial row of grid points. A finite number of variables (for instance, only temperature T is considered in this case) completely define the parameters for a channel simulation, i.e., the calculation of source terms can be viewed as a mapping from the input vector

$$x^k = (T_{wall,1}^k, \dots, T_{wall,n}^k) \quad (2.114)$$

of the k^{th} discretized channel to an output vector containing the heat source terms \dot{Q} of the respective grid points. This mapping can be expected to be continuous; channels with similar input vectors shall be similar in source terms. For the identification of similar channels, an agglomerative cluster algorithm is applied.

A weight w^k can be assigned to each vector x^k that accounts for the absolute number of channels represented by x^k , which is proportional to the size of the corresponding stack area. In addition, a distance function $d(x^i, x^j)$ is necessary, for which a normalized maximum norm is chosen:

$$d(x^i, x^j) = \max(d_T(T_{wall,1}^i, T_{wall,1}^j), \dots, d_T(T_{wall,n}^i, T_{wall,n}^j)) \quad (2.115)$$

with distance function

$$d_T(T^i, T^j) = \frac{|T^i - T^j|}{\delta T} \quad (2.116)$$

i.e., temperatures are normalized with respect to a temperature difference δT . The agglomerative cluster algorithm, illustrated in Fig. 2.10, can be sketched as follows:

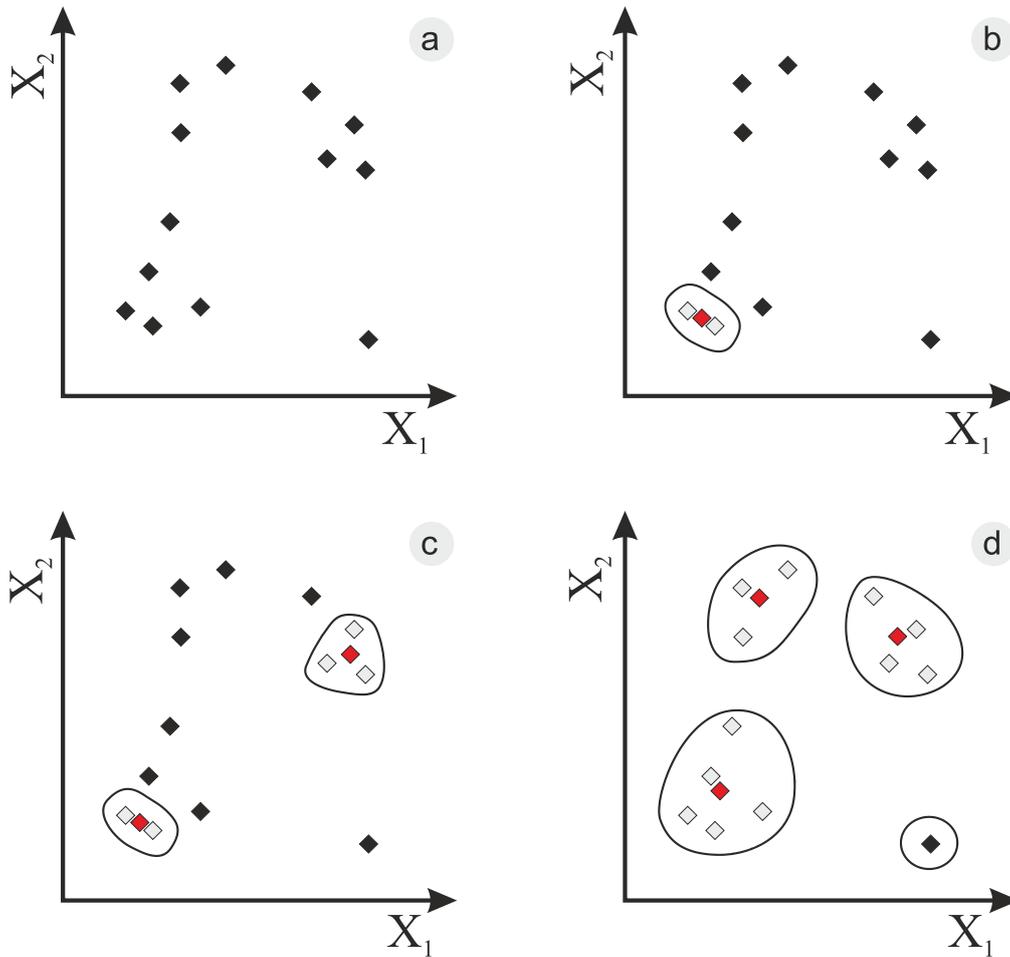


Figure 2.10: Agglomerative cluster algorithm. (a) Given set of data points. (b) Join two data points into one cluster. (c) After the third agglomeration step, two clusters have been formed. (d) Final representation of the data by four clusters. Adapted from Ref. [91].

1. Find the minimum $d^* = d(x^{i^*}, x^{j^*}) = \min_{i \neq j} (d(x^i, x^j))$.
2. Stop if $d^* > 1$, .

3. Let $x^* = (w^{i^*}x^{i^*} + w^{j^*}x^{j^*})/(w^{i^*} + w^{j^*})$ and $w^* = w^{i^*} + w^{j^*}$.
4. Eliminate $(x^{i^*}, w^{i^*}), (x^{j^*}, w^{j^*})$ and replace by (x^*, w^*) .
5. Go to 1.

The remaining x^k are the input vectors for representative channels. All input vectors in one cluster are associated with the same output source terms. Since the channel equations are not explicitly time-dependent, the number of channel calculations can be further reduced by including the x^k of previously calculated channels into the clustering, and reusing their results. A schematic representation of the coupling between the solid section and the individual channel is shown in Fig. 2.11. The stack code is available as a part of DETCHEMTM software [90].

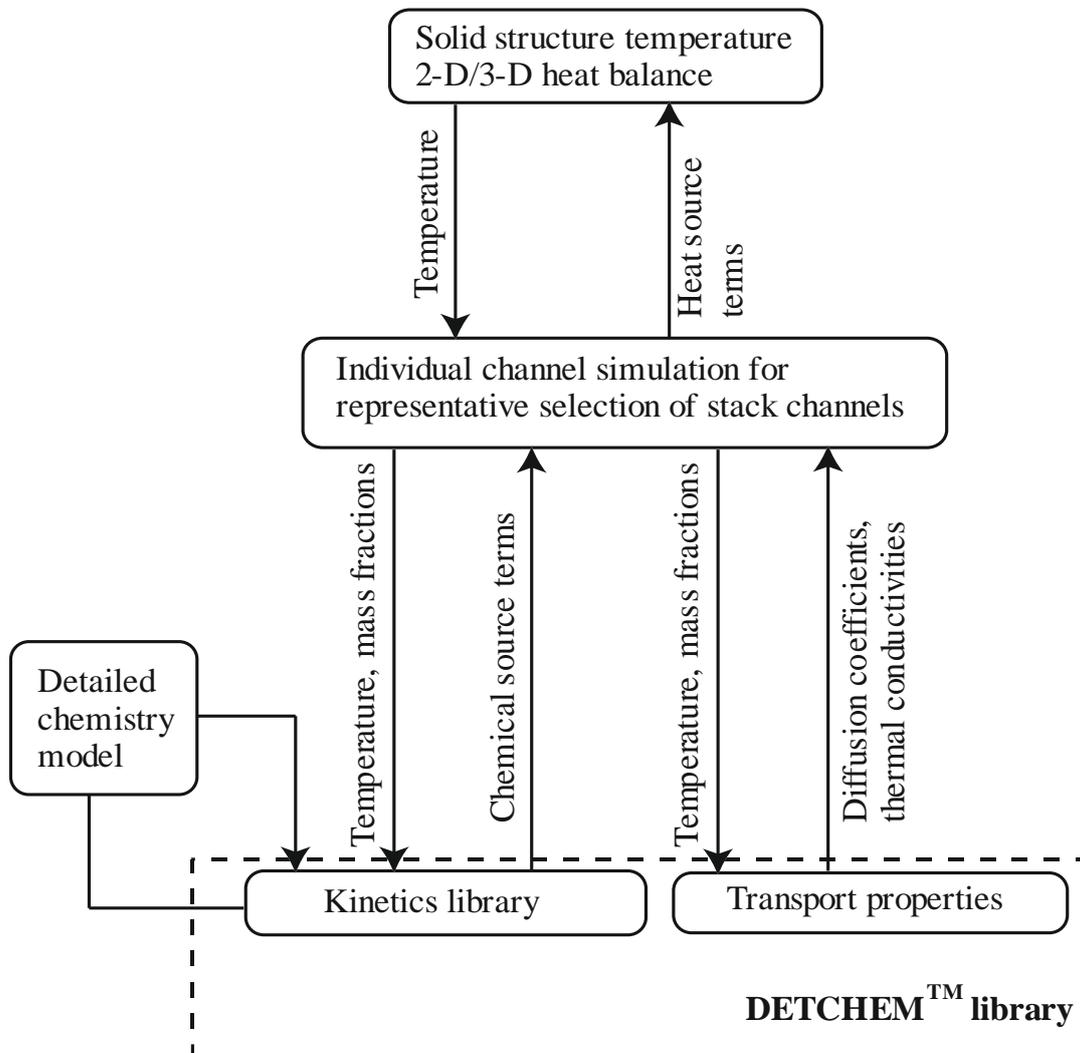


Figure 2.11: Illustration of the coupling between the solid structure and the channel. Adapted from Refs. [85, 90].

Chapter 3 A novel approach to understand the transient behavior of high-density SOFC stacks

¹Solid Oxide Fuel Cells (SOFCs) are efficient power sources for distributed or stationary power plants, and mobile applications. Their wide usability is due to their modularity, high electrical efficiency, low environmental pollution, fuel flexibility, and tolerance to fuel pollutants. A typical unit cell in a planar SOFC stack is composed of a positive electrode-electrolyte-negative electrode (PEN) assembly, interconnect plates on both sides and gas seals. In practical applications of SOFCs, multiple cells are assembled to form a stack and a serial connection in an electric loop to generate high voltage and power.

An attractive feature of SOFCs is the possibility of it being combined with other power generation systems (e.g., gas turbines) to achieve high electrical power generation efficiencies, due to their high working temperatures [92-96]. One such application domain that draws considerable interest from the automobile industry is the use of SOFCs as auxiliary power units (APUs), because of their advantages. For SOFC-based APUs, it is not trivial to operate the cells on pure hydrogen. Nevertheless, operating the cells on reformat fuels from gasoline or diesel may be more attractive because these fuels are available on-board and can be reformed before usage as fuel. The reforming can be carried out inside or outside the stack. Furthermore, the APUs are subjected to frequent load changes which cannot be pre-determined. The control strategy and the power electronics associated with these applications may be quite complex [97-100]. Understanding the response time of a system is particularly important because of the frequently fluctuating nature of demand for electrical power.

In this chapter, we present the application of the new stack model and its solution algorithm. The model is demonstrated with a pragmatic fuel composition for APUs. A number of issues, such as (i) required power rating of the APU, (ii) start-up time, (iii) response to load changes, (iv) control strategies, (v) fuel choice, (vi) fuel utilization, (vii) stack degradation, and (viii) stack volume, need

¹Parts of this chapter are taken from Menon et al. [85]. Copyright (2012), with permission from Elsevier.

to be considered when addressing the application of SOFC as APUs. However, as a first step, the focus is only on the development of the numerical algorithm, stack simulation, and transient response to load changes. In the present analysis, we report the modeling of a SOFC stack with a channel density of $25/\text{cm}^2$, made up of co-flow configuration. The fuel composition employed is 31.81% H_2 , 36.56% N_2 , 13.19% CO , 13.19% CH_4 , 2.23% CO_2 , and 3.02% H_2O . This fuel composition essentially results from mixing 3% H_2O to the fuel obtained from the partial oxidation of methane with air [101].

This chapter presents the application of a novel model to study the transient behavior of SOFC stacks in two and three dimensions. A hierarchical model is developed by decoupling the temperature of the solid phase from the fluid phase, as shown in Fig. 3.1 [102]. The information supplied by the DETCHEM library is shown in Fig. 2.11.

Structure of DETCHEM™ (Detailed Chemistry)

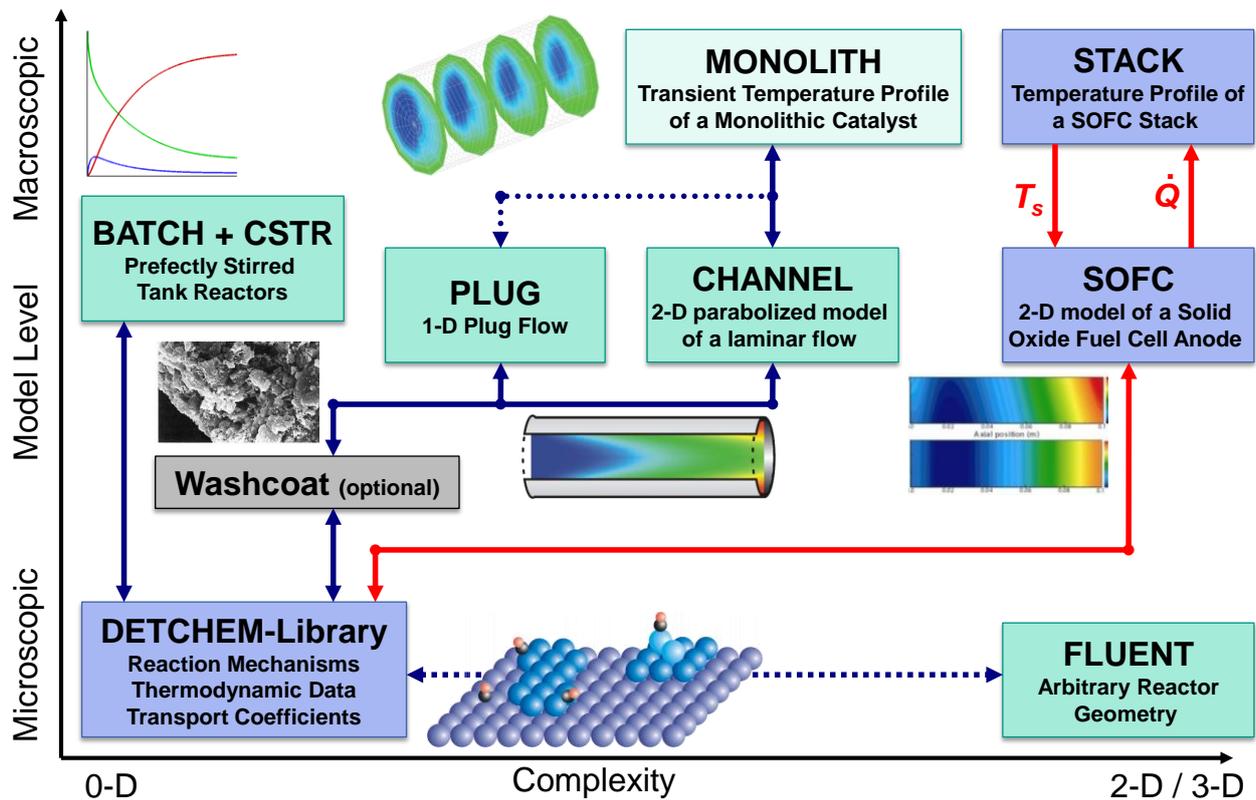


Figure 3.1: Structure of the DETCHEM™ software package. Red arrows are the pathways that are relevant to this study. The information exchanged between a single cell and the solid stack structure is shown. T_s - temperature of the solid-structure and \dot{Q} - heat source term.

For demonstration purposes, we consider a stack having an active area of $10 \text{ cm} \times 10 \text{ cm}$. The fuel and air channels are assumed to be of 1 mm^2 cross-sectional area. All the physical parameters and thermal properties used to describe the stack are given in Table 3.1. The electrochemical model parameters used for the calculations are shown in Table 3.2. However, the exchange current density parameters are adjusted to produce $\sim 0.72 \text{ V}$ at 300 mA/cm^2 . Adiabatic and Neumann boundary conditions are implemented for the present calculation. It should be noted that the time constants pertaining to electrochemistry, diffusion, internal impedance, mass transfer and temperature dynamics are specific to the model parameters used in this study.

Table 3.1: Stack component parameters and properties

Physical properties	
Flow channels	
Length (m)	0.1
Height (m)	1×10^{-3}
Width (m)	1×10^{-3}
Anode	
Thickness (μm)	750
Porosity (%)	35
Tortuosity	3.5
Particle diameter (μm)	2.5
Pore diameter (μm)	1.0
Specific area (m^{-1})	1.080×10^5
Cathode	
Thickness (μm)	30
Porosity (%)	35
Tortuosity	3.5
Particle diameter (μm)	2.5
Pore diameter (μm)	1.0
Specific area (m^{-1})	1.080×10^5
Electrolyte	
Thickness (μm)	15
Thermal properties	
Solid/Stack	
Specific heat capacity (J/kg K)	440
Density (kg/m^3)	5940
Thermal conductivity (J/m s K)	1.86
Insulator	
Specific heat capacity (J/kg K)	1047
Density (kg/m^3)	480
Thermal conductivity (J/m s K)	0.059
Thermal emissivity	0.09
Convective coefficient between insulator/surrounding ($\text{W m}^{-2}\text{K}^{-1}$)	2

Table 3.2: Electrochemical model/input parameters

Anode asymmetry factor (β_a)	0.5
Cathode asymmetry factor (β_c)	0.5
Exchange current density parameters	
Pre-exponential for H ₂ oxidation (k_{H_2}) (A/cm ²)	1.07×10^4
Pre-exponential for O ₂ reduction (k_{O_2}) (A/cm ²)	5.19×10^3
Activation energy for H ₂ oxidation (E_{H_2}) (J/mol)	87.8×10^3
Activation energy for O ₂ reduction (E_{O_2}) (J/mol)	88.6×10^3
Ionic conductivity (σ_0) (S/cm)	3.6×10^5
Ionic conductivity (E_{el}) (J/mol)	80.0×10^3

As described in the previous chapter, either the voltage or the current is fixed to estimate the rest of the electrochemical parameters. Therefore, two different transient responses following load changes are studied here: (i) load change at constant current and (ii) load change at constant voltage. For both cases, the stack is initially assumed to be at 800°C. Fig. 3.2 describes the grid structure used in the simulation of the 3-D SOFC stack.

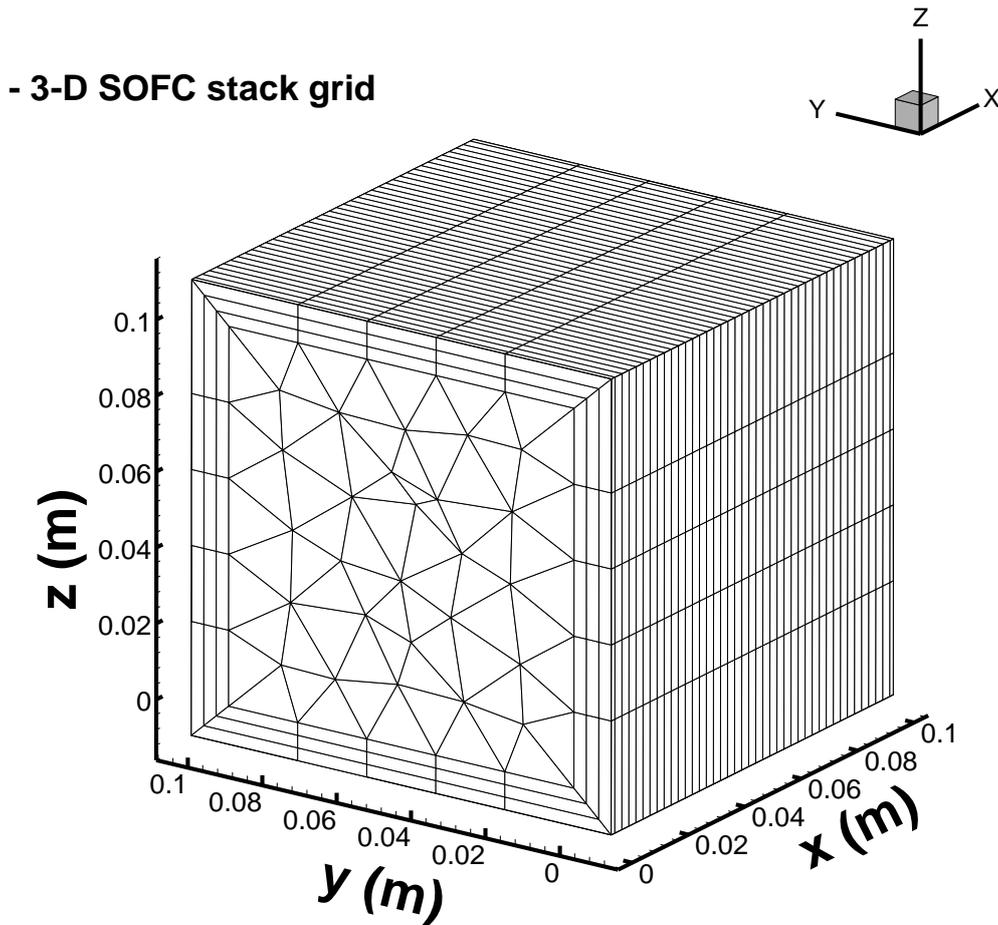


Figure 3.2: Structure of the grid used in the 3-D simulations, consisting of arbitrarily shaped triangle and quadrilateral volume elements.

3.1 Step change in constant current

3.1.1 Adiabatic boundary condition

Figure 3.3 displays the transient response in the stack temperature for cells operating at constant current. From the initial state, the temperature distribution in the stack reaches steady-state after ~ 14.5 minutes. At $t = 80$ min, a step change in current from 0.3 A/cm^2 to 0.4 A/cm^2 is introduced. As expected, the stack temperature increases with the step increase in current and reaches steady-state after another ~ 17 minutes. These response times correspond well with the values reported by Ivers-Tiffée et al. [103]. The corresponding changes in cell voltage and reversible voltage are shown in Figs. 3.4a and 3.4b. The reversible potential decreases following the step change in current due to the increase in temperature.

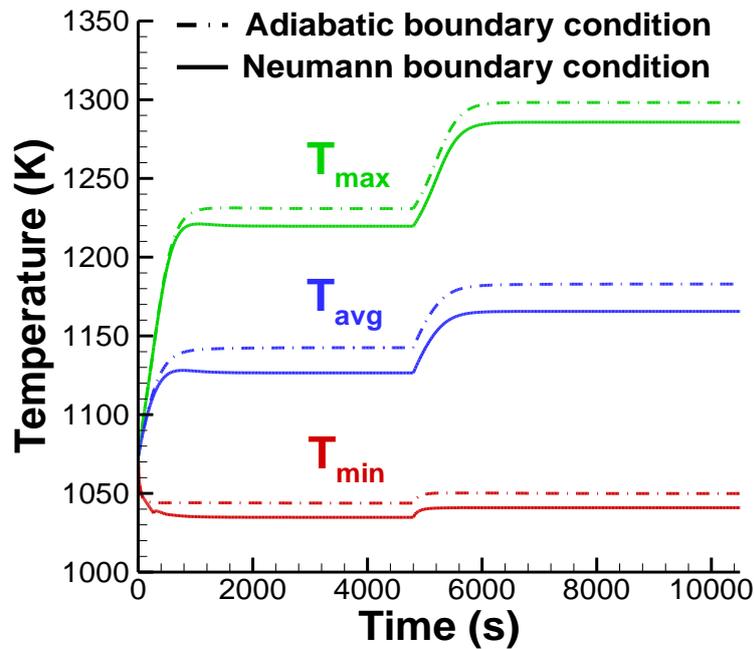


Figure 3.3: Maximum, minimum, and average temperature in the stack for a step change in current from 0.3 A/cm^2 to 0.4 A/cm^2 .

However, subsequent to the step change in current from 300 mA/cm^2 to 400 mA/cm^2 , the cell voltage first decreases before reaching steady-state. The initial decrease in cell potential occurs due to the following reasons:

- An increase in current leads to an increase in overpotential losses, because the stack temperature at the time of step change still corresponds to the steady-state temperature at 300 mA/cm^2 .

- The activation losses gradually decrease as the temperature approaches the new steady-state. In short, the under-shoot in cell potential originates from the over-shoot in activation losses following the step-change. The corresponding transient response of activation losses at the anode and cathode are displayed in Figs. 3.5 and 3.6, respectively. It is important to remember that the fuel electrode (represented by the subscript '*fe*') is the anode, while the oxidant electrode (represented by the subscript '*oe*') is the cathode.

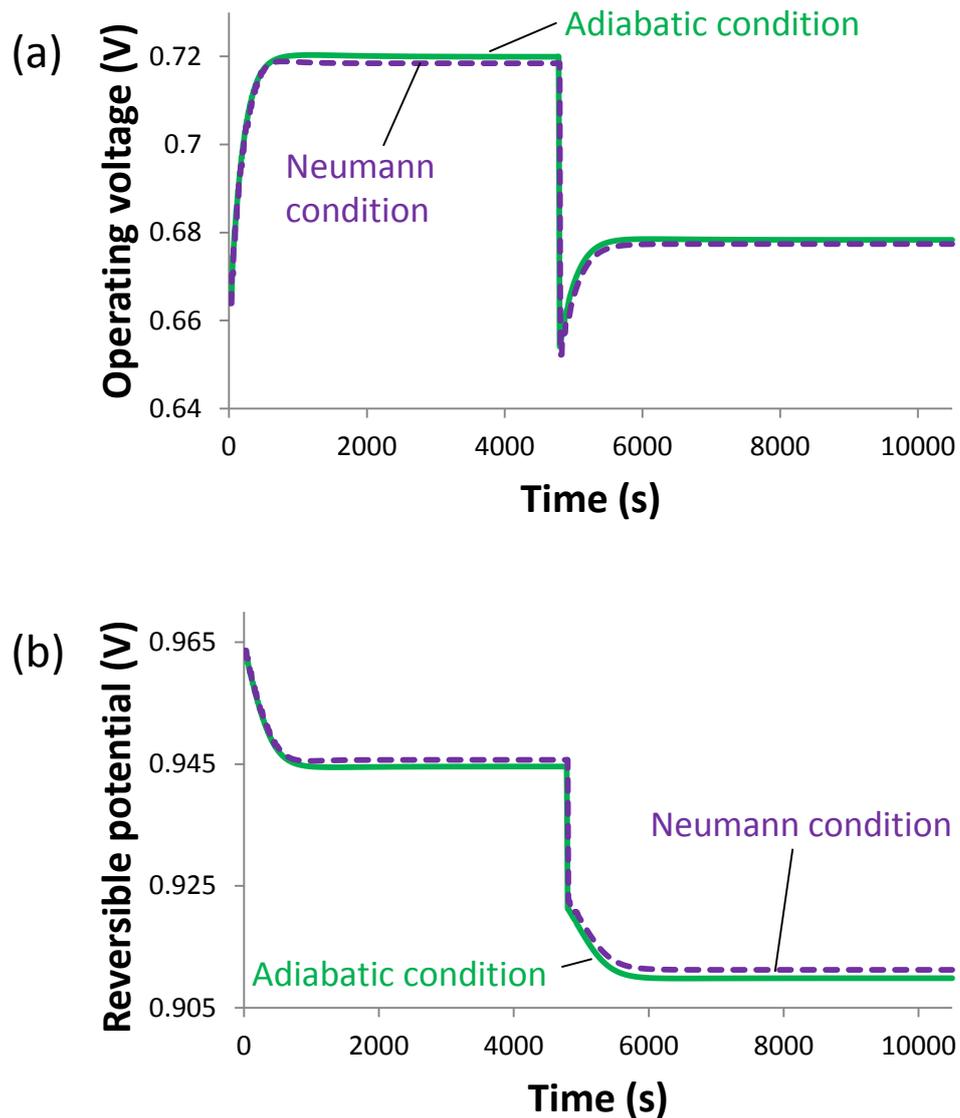


Figure 3.4: The effect of step change in current from 0.3 A/cm² to 0.4 A/cm² on: (a) Cell potential, and (b) reversible potential.

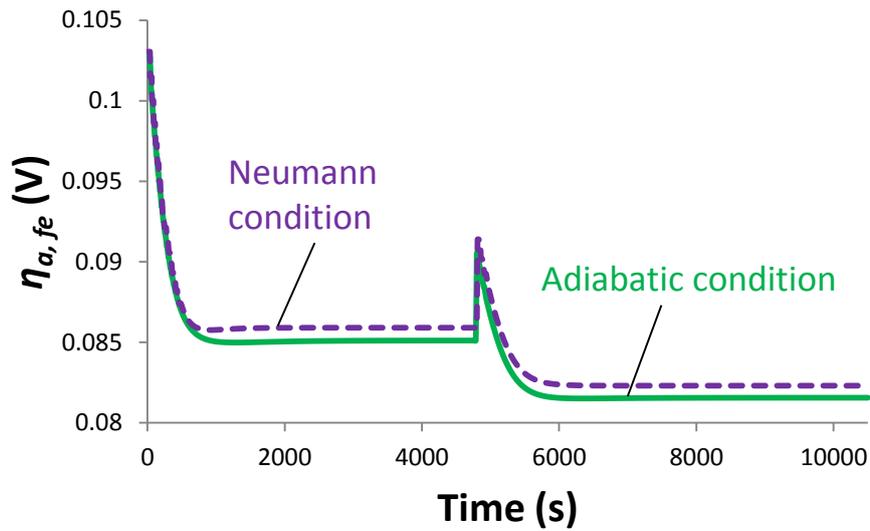


Figure 3.5: Anode activation overpotential following a step change in current from 0.3 A/cm^2 to 0.4 A/cm^2 .

In Figure 3.7, we see the response of the stack temperature to step changes in current density from 0.3 A/cm^2 and 0.5 A/cm^2 to a new steady-state value of 0.4 A/cm^2 . The response times of the system, after the respective step changes are introduced, are the same and equate to ~ 17 minutes. Thus, we observed that the response times remain independent of the magnitude of load introduced. This phenomenon was also observed by Achenbach [104].

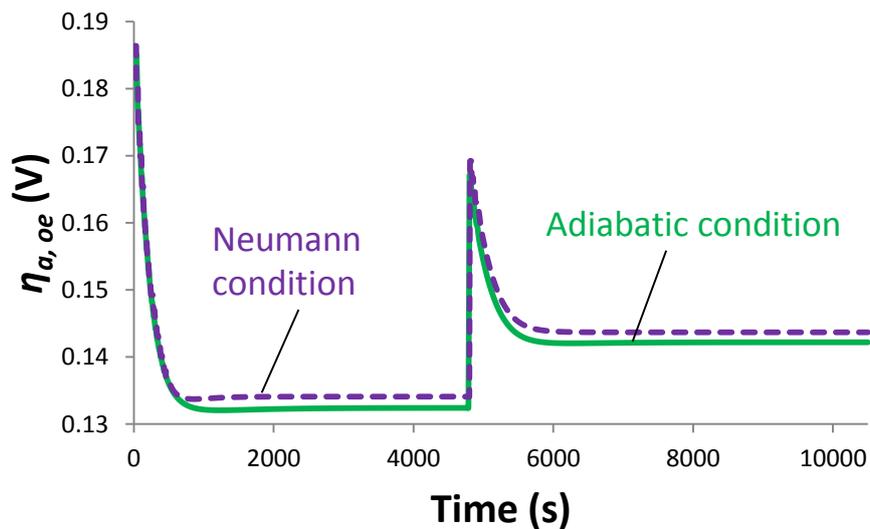


Figure 3.6: Cathode activation overpotential following a step change in current from 0.3 A/cm^2 to 0.4 A/cm^2 .

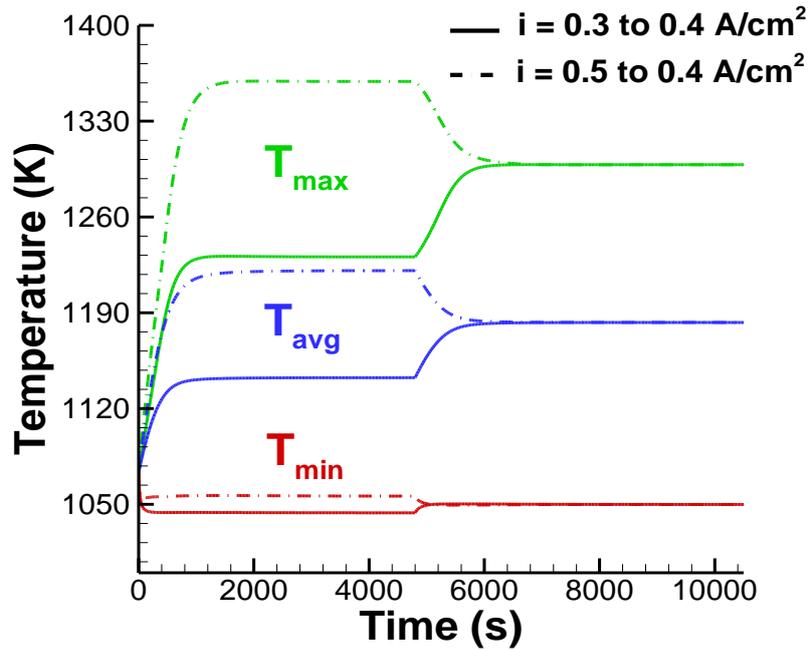


Figure 3.7: Transient temperature distribution during load change from $i = 0.3 \text{ A/cm}^2$ or $i = 0.5 \text{ A/cm}^2$ to $i = 0.4 \text{ A/cm}^2$.

The temperature distribution in the stack at different planes along and across the flow direction, after the first steady-state, is displayed in Fig. 3.8. As expected, the temperature in the stack increases in a monotonic manner along the flow direction due to the combined effect of exothermic cell reactions and the current consumed by the internal cell resistance. Uniform profiles are observed across the direction of flow because of the relatively thin PEN structure, and the fact that the radial and axial solid thermal conductivities are equal. However, at the single cell level, the temperature profiles are non-linear and vary based on location in the stack [105]. Also, the insulator seems to have minimal effect on the internal temperature distribution of the system. It should be noticed that the model has a limitation that it does not account for individual mechanical components in the stack. It is a lumped parameter model as far as individual mechanical components are concerned, and therefore, it is assumed that the entire stack has the same thermal properties.

Li et al. have studied the dynamic response of the cell to changes in fuel flow rates [106]. Even though Achenbach and Li et al. simulated cross flow cells, the time constant reported by Li et al. is in the order of hours and that reported by Achenbach is in the order of a few minutes. Achenbach [104, 107] examined the transient cell voltage performance due to temperature changes and perturbations in current density. Furthermore, Li et al. reported that the time constants for different parts of the cell to reach steady-state are different. Although both these studies are done for internal re-

forming, the fuel compositions used differ slightly from each other. Nevertheless, the time constant reported by Li et al. differs largely from that reported by Achenbach. Therefore, it must be assumed that the time constant for the cell processes depends largely on the model parameters used. Unfortunately, it is not possible to make a direct comparison as the aforementioned literature does not provide a comprehensive list of material properties and electrochemical model parameters.

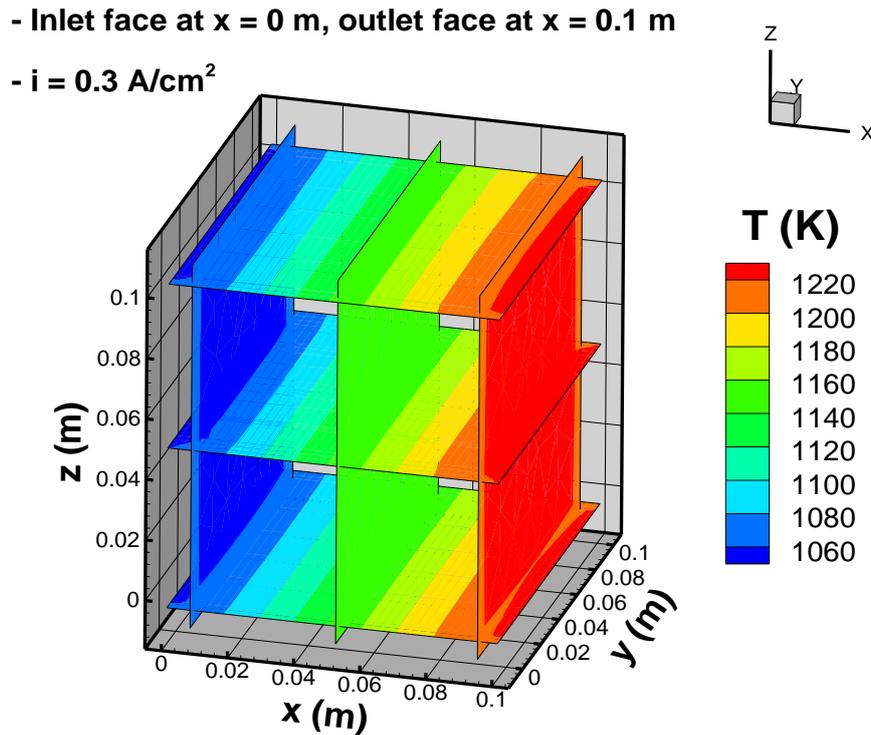


Figure 3.8: Temperature distribution in the 3-D stack (solid phase) at different surface planes, along and across the flow direction, at $t = 60$ minutes during adiabatic operation.

During the simulations, we observed that the time constants for the dynamic responses are strongly dependent on thermal diffusivity ($\lambda/\rho_s C_{ps}$). Lower thermal diffusivity led to a faster response or to a shorter time constant, which can be attributed to mass transfer dynamics. This is due to the fact that higher thermal diffusivity implies faster spread of heat from one part of the stack to the other. Thus, thermal fluctuations travel faster forcing the single cells at different locations to adapt their temperature dependent electrochemical parameters. These electrochemical parameters in turn have an effect on the concentration gradients in the cell, via the fluxes. This was also observed by Achenbach [104]. It might be possible that Li et al. [106] used high thermal diffusivity for their model calculations, which led to very high response times. This phenomenon is depicted in Fig. 3.9, with the corresponding solid stack structure properties listed in Table 3.3. A number of other stack

operating conditions, such as convection and radiation losses, and the effect of re-circulation zones at the inlet and outlet faces/manifolds are not discussed here.

Table 3.3: Solid structure/stack material properties

Material	Thermal conductivity ($\lambda - \text{W/mK}$)	Thermal diffusivity ($\alpha - \text{mm}^2/\text{s}$)
α_1	1.86	0.716
α_2	5.86	2.466
α_3	27	6.923

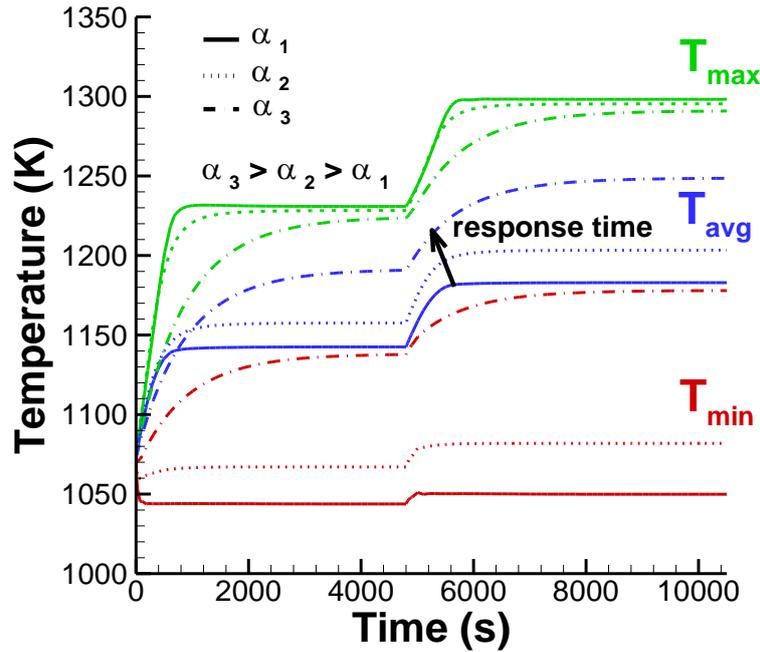


Figure 3.9: Illustration of solid structure material property vs. response time for a step change in current from 0.3 A/cm^2 to 0.4 A/cm^2 .

3.1.2 Neumann boundary condition

The Neumann condition, as described in Table 3.1, is applied at the four faces of the stack, barring the inlet and outlet face which are kept adiabatic. As shown in Fig. 3.3, the temperature distribution reaches steady-state from the initial value after ~ 15 minutes. A step change in current from 0.3 A/cm^2 to 0.4 A/cm^2 at $t = 80$ min is introduced, due to which the temperature distribution in the stack reaches a new steady-state value in ~ 18.5 minutes. This is due to the dependence of response time on operating conditions.

The heat loss at the surface of the stack results in a decrease in the magnitude of its temperature distribution, which leads to the production of relatively low amount of waste heat. This causes the average cell temperature to decrease, which manifests itself as an increase in ohmic polarization,

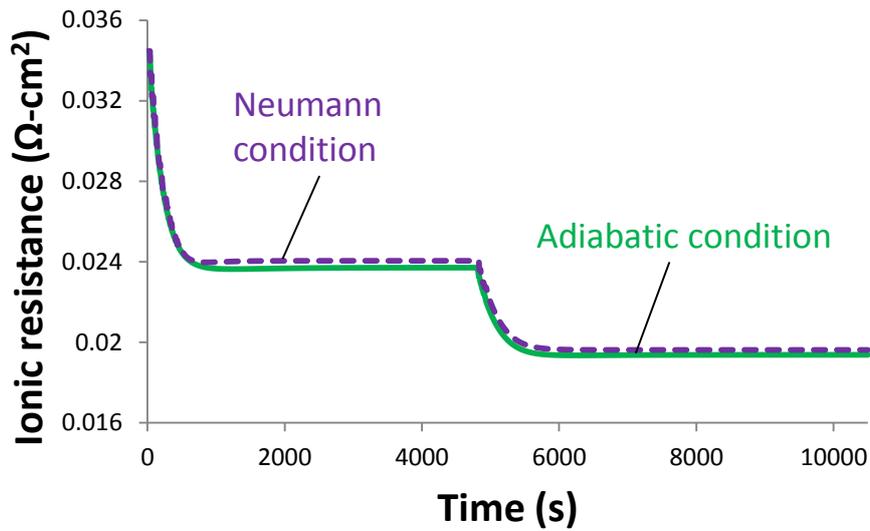


Figure 3.10: Ohmic polarization following a step change in current from 0.3 A/cm² to 0.4 A/cm².

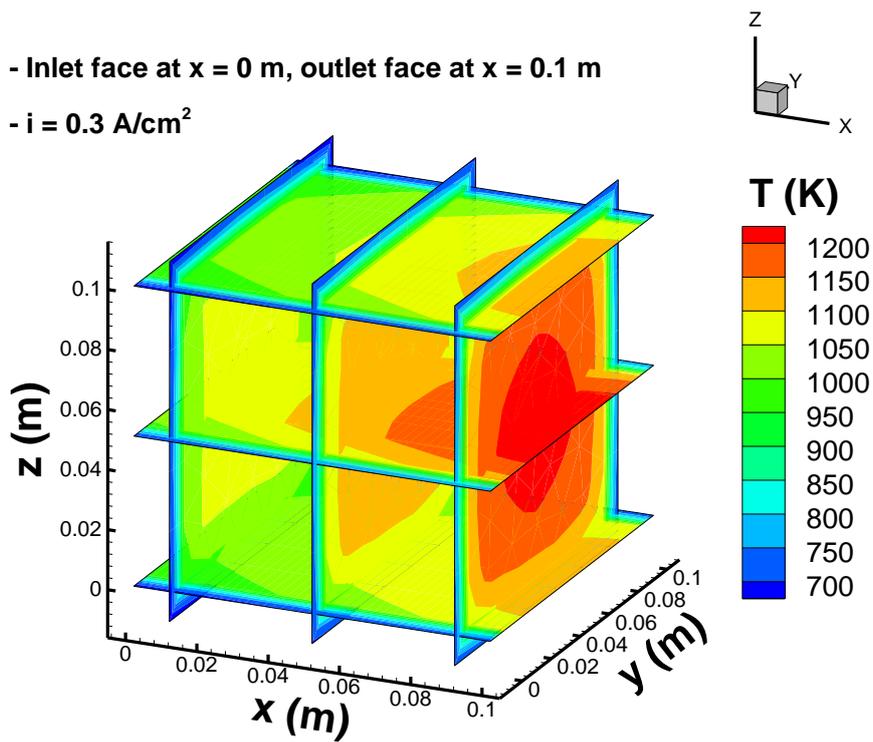


Figure 3.11: Temperature distribution in the 3-D stack (solid phase) at different surface planes, along and across the flow direction, at t = 60 minutes during computation with an imposed Neumann condition.

resulting in a lower operating cell voltage as described in Fig. 3.10. The reversible potential, which is obtained from the Nernst equation, is higher due to lower amount of heat generated by the cell

($T\Delta S$) that operates reversibly. This increases the amount of free energy available to the system. This phenomenon is shown in Fig. 3.4.

The internal temperature distribution in the stack, at different planes, after the attainment of the first steady-state is shown in Fig. 3.11. These temperature profiles form a pre-dominant factor in determining variations in induced thermal stresses in the materials positioned at different locations of the system. Furthermore, as a result of heat loss/flux at the boundaries, distinct temperature contours are formed due to the increase in temperature gradients in the Y and Z directions. This shows the importance of 3-D modeling in determining how temperature dynamics play an important role in the transient responses of a SOFC system.

3.2 Step change in constant voltage

3.2.1 Adiabatic boundary condition

Figure 3.12 describes the transient response in temperature for cells operating at constant voltage. Here, the initial steady-state is achieved in ~ 15 minutes, and at $t = 80$ min, a step change in voltage from 0.7 to 0.8 V is introduced. The increase in cell potential decreases the average current obtained from the stack, and hence, the stack temperature reaches a new lower steady-state in ~ 18 minutes.

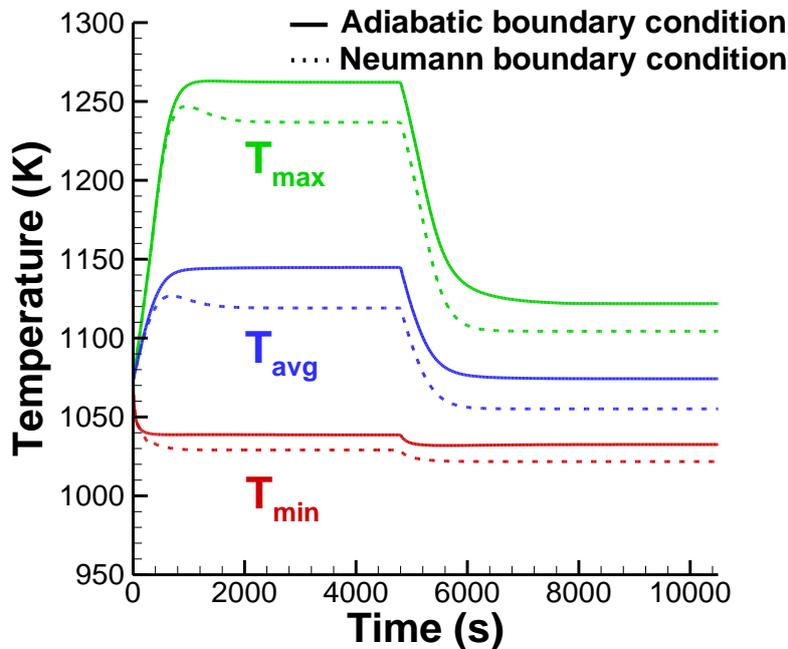


Figure 3.12: Maximum, minimum, and average temperature in the stack for step change in voltage from 0.7 V to 0.8 V.

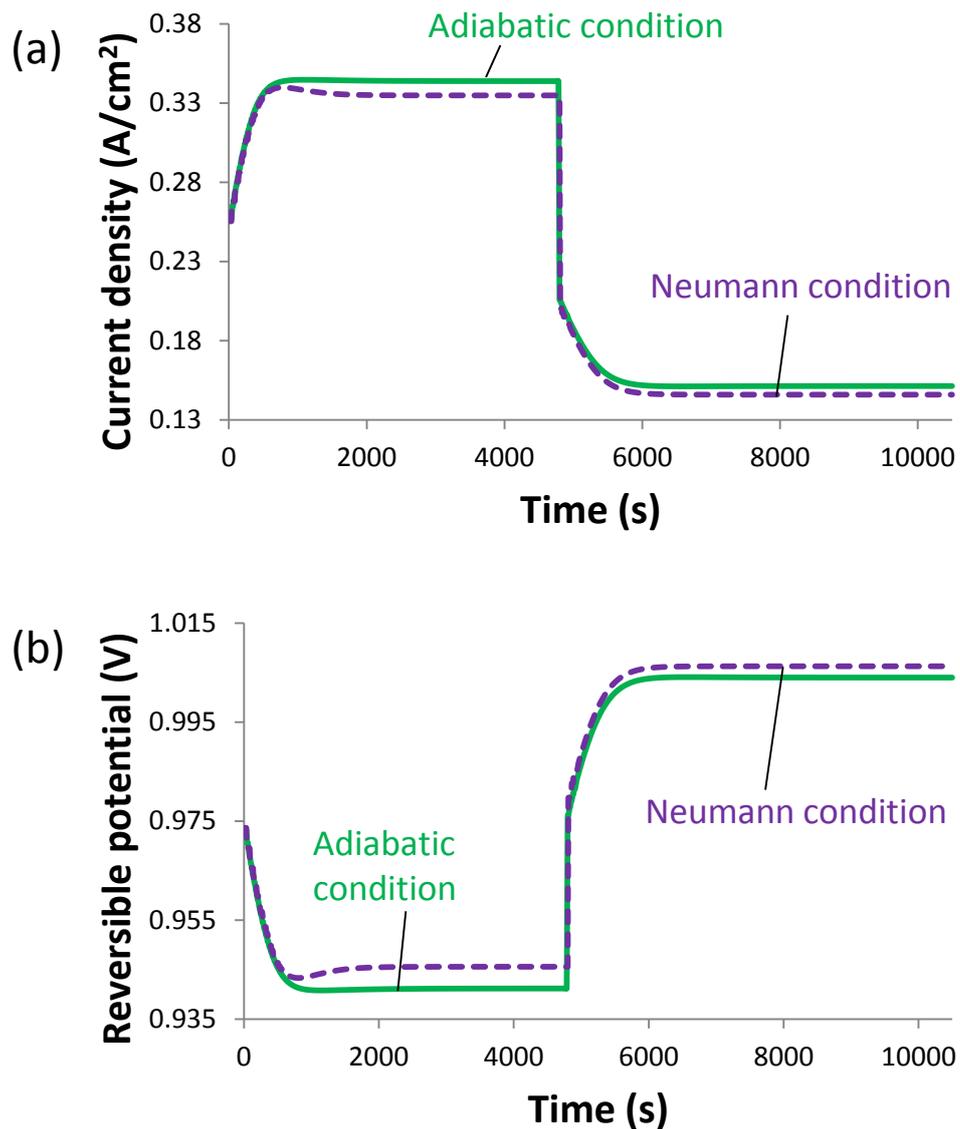


Figure 3.13: The effect of step change in voltage from 0.7 V to 0.8 V on: (a) Average current density, and (b) Reversible cell potential.

The corresponding transient responses in current and reversible potential are displayed in Figs. 3.13a and 3.13b, respectively. As usual, the decrease in temperature following the step increase in voltage leads to an increase in the reversible potential. The current density drops from ~ 340 mA/cm² following the step change in voltage, and then gradually assumes a new steady-state value of ~ 150 mA/cm². Nevertheless, the step change in voltage leads to an under-shoot in activation losses. At the time of step change, the temperature in the stack corresponds to that of ~ 340 mA/cm²; however, the drop in current density at higher stack temperature leads to lower activation losses, which in turn corresponds to the point of under-shoot. Nonetheless, as the stack temperature

assumes a new lower steady-state value, the activation losses increase and asymptotically reach a new steady-state value. The anode and cathode activation losses are displayed in Figs. 3.14a and 3.14b, respectively.

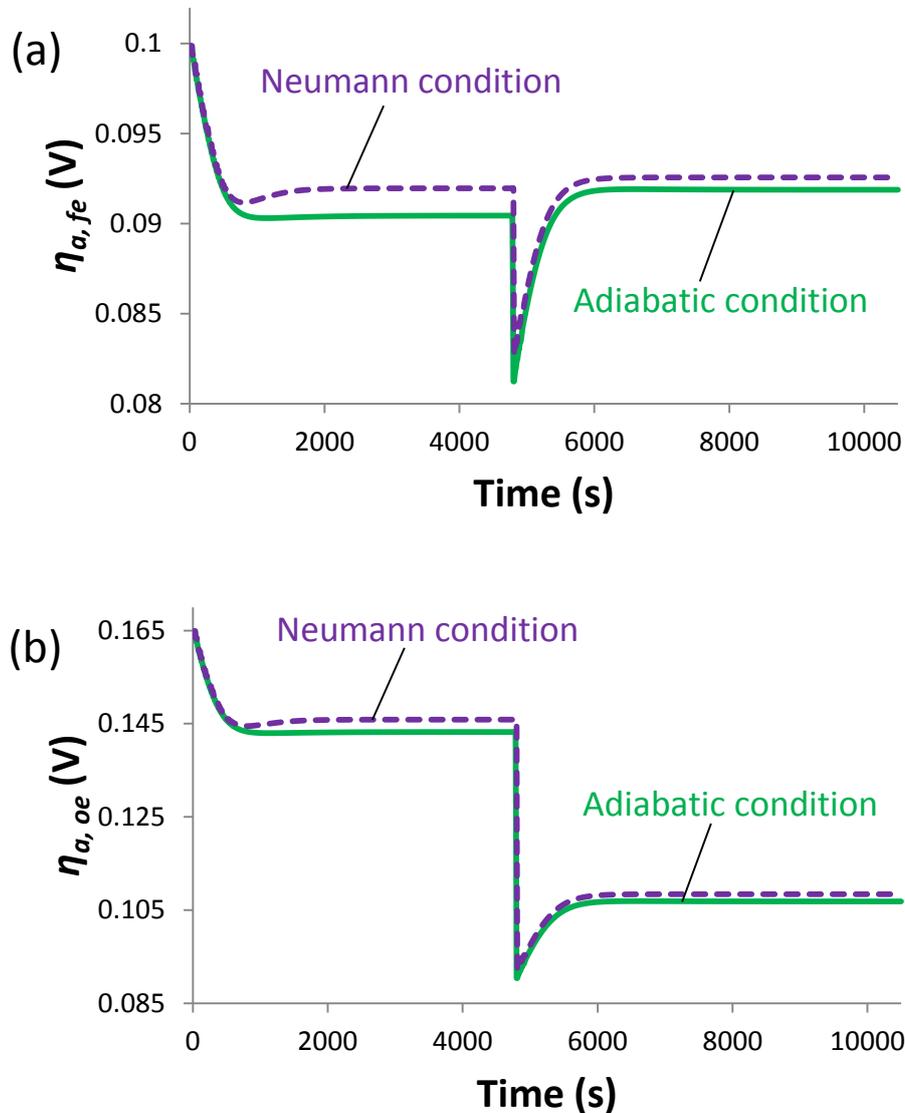


Figure 3.14: The effect of step change in voltage from 0.7 V to 0.8 V on: (a) Anode activation overpotential, and (b) Cathode activation overpotential.

3.2.2 Neumann boundary condition

The thermal properties of the insulator and the choice of the Neumann condition at the stack surface are described in Ref. [108]. Fig. 3.12 shows that the time taken to reach steady-state from the initial condition is ~ 17 minutes. At $t = 80$ min., a step change in voltage from 0.7 to 0.8 V is introduced,

causing the stack temperature to attain a new steady-state value in about ~ 17 minutes. The ohmic polarization increases as the operating temperature decreases, which results in the decrease of current density at a given cell voltage, as shown in Fig. 3.13a. Consequently, the reversible potential increases as shown in Fig. 3.13b.

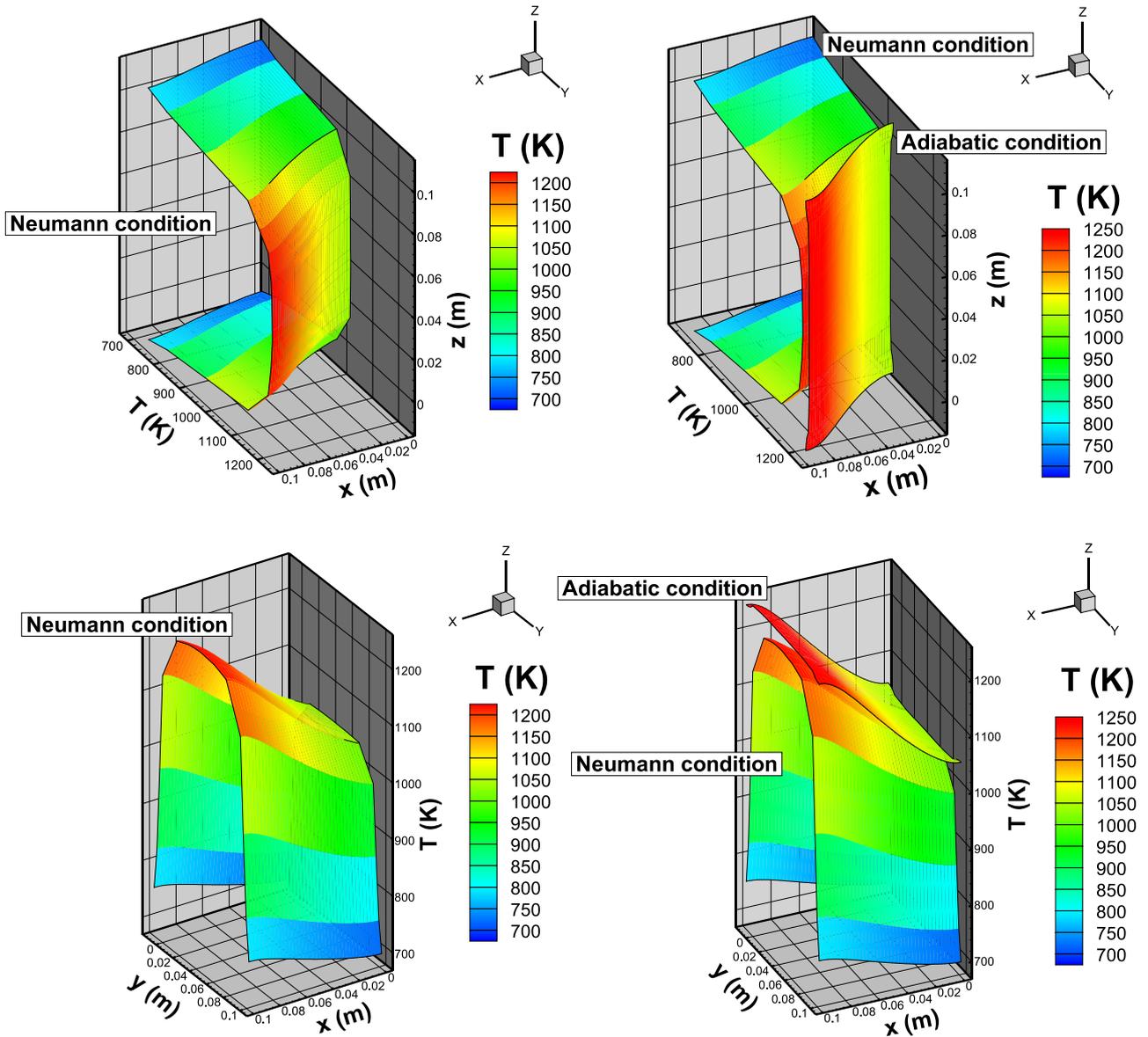


Figure 3.15: Internal steady-state temperature distribution of the stack before step change in voltage from 0.7 V to 0.8 V.

The 3-D contour plots of the SOFC stack describe the steady-state internal temperature distributions before and after the step change in voltage is introduced, which are shown in Figs. 3.15 and 3.16, respectively. These figures represent the temperature profiles of the cell located at the center of the stack. A comparison with the adiabatic case provides a comprehensive idea about the differences in

the magnitudes of temperature gradients for the same model input parameters. It can be seen that the adiabatic condition results in a smaller temperature gradient at the boundaries compared to the case involving heat loss at the boundaries.

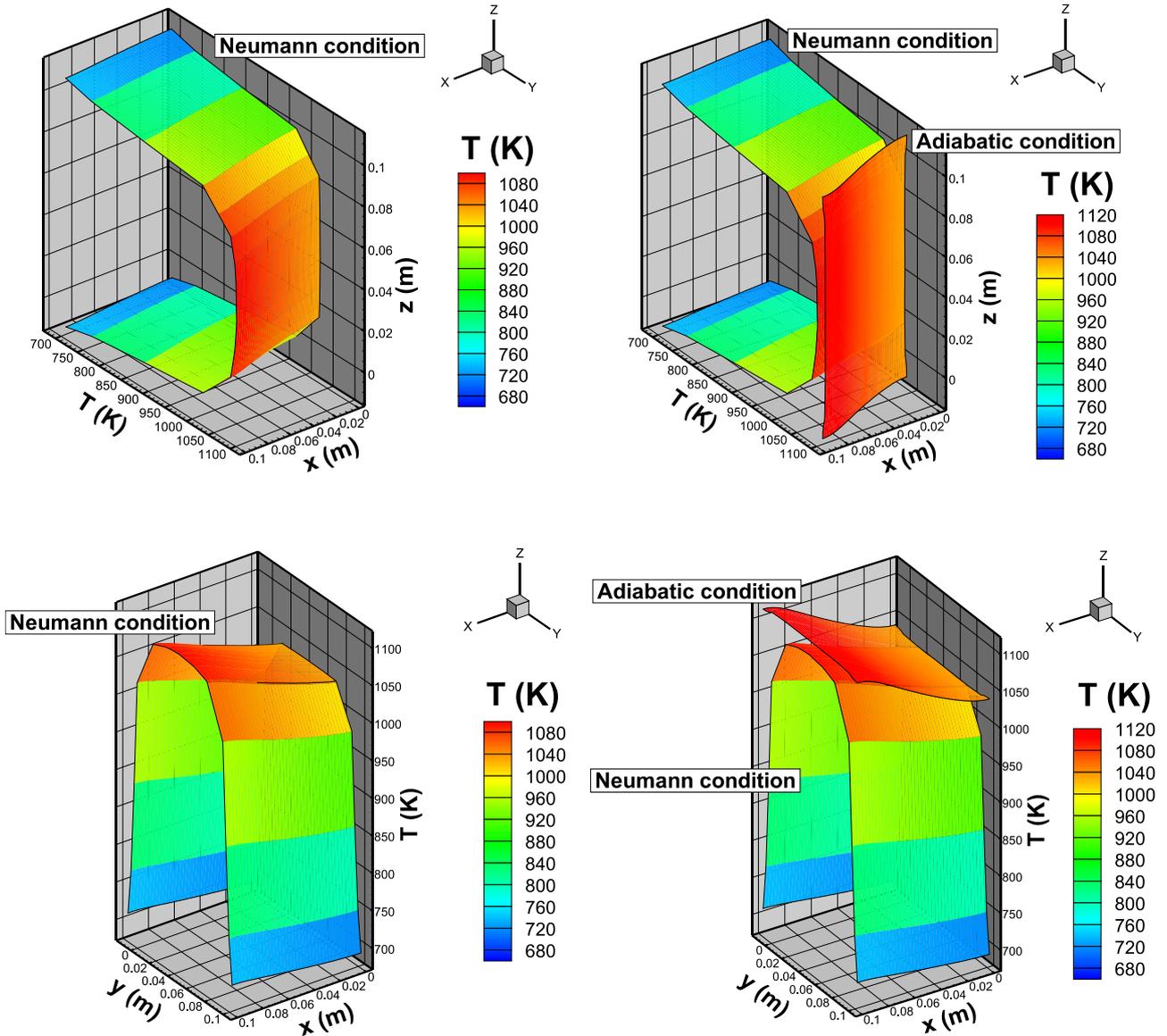


Figure 3.16: Internal steady-state temperature distribution of the stack after step change in voltage from 0.7 V to 0.8 V.

The resulting temperature distribution arises due to the net effect of heat absorbed or released as a result of heterogeneous chemical reactions, heat release due to the electrochemical reactions at the TPB, resistive heating within the electrolyte, convective heat transfer to and from the channels, radiation heat transfer with the interconnects, and also heat loss at the stack boundaries in the case of an imposed Neumann condition. The temperature decline at the inlet is attributed to endothermic

reforming reactions [45]. It is evident that the temperature increases in the axial direction due to exothermic cell reactions, along with the air and fuel channel temperature. This in turn reflects in the gradual increase of insulator temperature from the inlet to the outlet face. Each cell's temperature distribution also depends on its position within the stack. This affects the dynamics of almost all other mechanisms. During our simulations, when considering different materials for insulation at the stack surface, we observed that the choice of insulation layer was mainly responsible for controlling the surface temperature of the system that determined the amount of heat available for transfer to the surroundings.

3.3 Summary

A novel numerical algorithm for the modeling of 3-D/2-D SOFC stacks is developed. The model is demonstrated with a reformat fuel composition for a co-flow cell configuration. Instead of simulating every individual cell in the stack, only representative ones based on the cluster agglomeration algorithm are chosen for detailed simulation. This approach dramatically reduces the computation time required for stack simulation. Furthermore, the dynamics of the stack during two different transient responses to load changes: constant current and constant voltage, was studied. It was observed that the adiabatic/Neumann conditions at the borders of the simulation domain yielded almost the same response times between the two steady-states, for both types of load changes. The limitation of the model is the higher level of abstraction related to the individual mechanical components of the stack. Nevertheless, the novel model and computational tool can assist in a better understanding of heat balances in SOFC stacks, even when operated with fuels other than pure hydrogen.

Chapter 4 On the production of hydrogen in SOECs by steam electrolysis

¹Solid Oxide Electrolysis Cells (SOECs) have emerged in recent time as high efficiency sources for hydrogen production, in the midst of pressing demands for change from fossil fuel dependency. Hydrogen offers itself as a promising alternative, via electrolysis of renewable water source, making it a useful energy carrier. Solid Oxide Fuel Cells (SOFCs) can be operated in “reverse” mode at high temperatures as solid oxide electrolysis cells (SOECs) for production of H₂ by means of steam electrolysis [109-111]. For high temperature electrolyzers, the major interest lies in the fact that the Gibbs free energy change or the electrical energy demand of the system decreases with increasing temperature, while the product of temperature and entropy change or the heat energy demand increases. Hence, a fraction of the total energy demand can be supplied in the form of heat. Also, high temperature operation is favorable from the viewpoint of kinetics and electrolyte conductivity.

The basic principle of a SOEC is the inverse of that of a SOFC, having an overall electrochemical reaction given by Eq. 4.3. The representation of the planar SOEC under consideration, in this study, is shown in Fig. 4.1. The water reduction (Eq. 4.1) and oxygen production (Eq. 4.2) take place through the following reactions:

At the cathode-electrolyte interface,

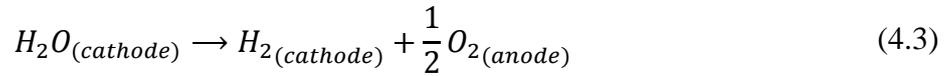


At the anode-electrolyte interface,



¹ Parts of this chapter are taken from Menon et al. [79]. Copyright (2013), with permission from Elsevier.

The net reaction reduces to,



where, the cathode is the fuel electrode and the anode is the oxidant electrode (opposite to the that of a SOFC). A parameter that often comes in handy to determine the theoretical point of operation, at thermal equilibrium, is the thermo-neutral voltage as given by Eq. (4). It is defined as the voltage at which no heat exchange with the surrounding occurs, i.e., all the input energy for the electrolysis process comes only from the electrical input energy.

$$V_{th} = \frac{\Delta H}{nF} \quad (4.4)$$

Here, ΔH is the lower heating value (LHV)/higher heating value (HHV) of hydrogen, n is the number of electrons involved in the reaction and F is the Faraday constant. The electrolysis reaction absorbs heat when operating below the thermo-neutral voltage and gives off heat when operating above it. It is important in designing electrolyzers, since all electricity supplied beyond this point is converted to heat, which must be removed to maintain cell temperature.

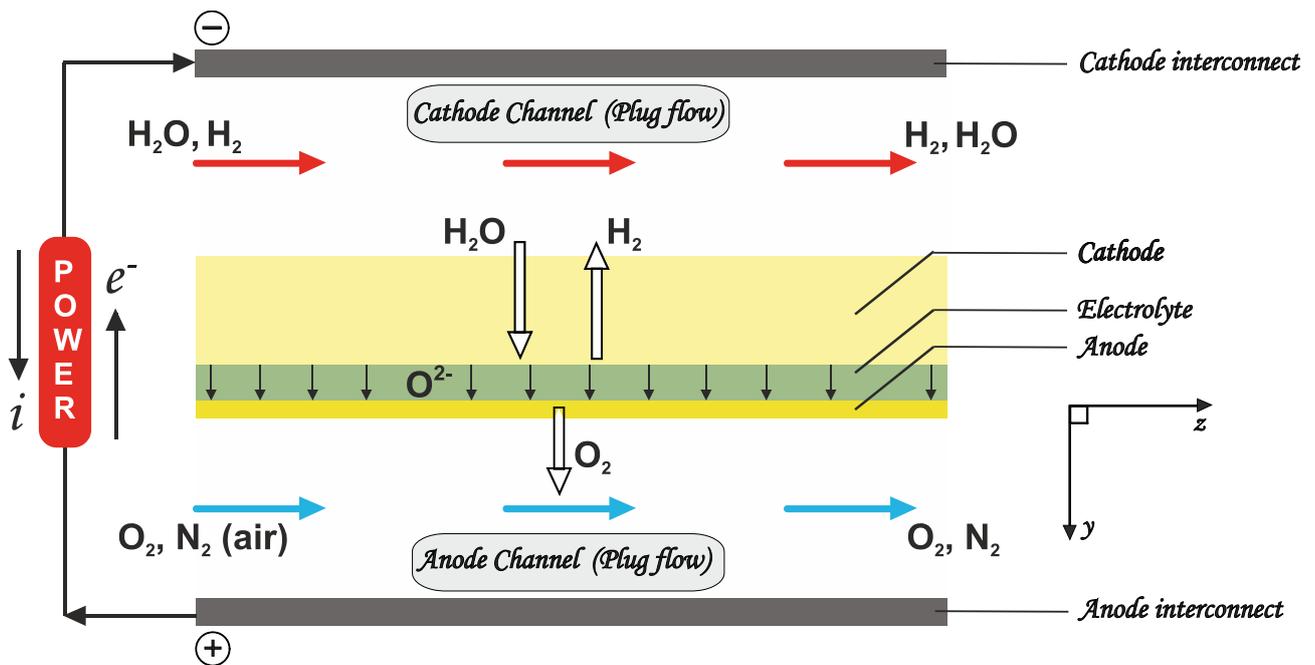


Figure 4.1: Schematic representation of a planar co-flow Solid Oxide Electrolysis Cell (SOEC).

In the present analysis, we report an in-house model that utilizes an approach to study complex phenomena at micro- and macro-scales. The simulation applies detailed models for electrochemical conversion at the three-phase boundary, an elementary heterogeneous reaction mechanism for the thermo-catalytic fuel electrode chemistry, dusty-gas model to account for multi-component diffusion through porous media, and a plug flow model for flow through the channels [66, 85]. The present work mainly focuses on the parametric analysis of detailed chemical processes within the H₂ electrode, electrochemical behavior, efficiency and irreversible losses during SOEC operation. The source code is available as a part of DETCHEMTM software package [90].

4.1 Model validation

The model is validated with experiments performed by Jensen et al. [112]. In the experiments, they demonstrated H₂O electrolysis with a new SOEC that resulted in the attainment of a record breaking current density of -3.6 A/cm^2 . The thicknesses of the NiO/YSZ porous support layer, NiO/YSZ hydrogen electrode, YSZ electrolyte and LSM/YSZ oxygen electrode were 300 μm , 10 μm , 10 μm and 10 μm respectively. Fig. 4.2 shows good agreement between numerical simulation results and experiment data, measured at 750°C and 850°C with an inlet steam composition of 50% H₂O in H₂, and at 950°C with an inlet steam composition of 70% H₂O in H₂. For the former inlet gas composition, the inlet flow rate to the Ni/YSZ electrode was 25 l/h while air to LSM/YSZ electrode was supplied at 140 l/h. At 950°C, the inlet gas - 70% H₂O + 30% H₂ to the Ni/YSZ electrode had a rate of 45 l/h alongside the supply of pure O₂ to the LSM/YSZ electrode.

Table 4.1: Electrochemical model/input parameters

Anode asymmetry factor (β_a)	0.5
Cathode asymmetry factor (β_c)	0.5
Exchange current density parameters	
Pre-exponential for H ₂ electrode (k_{H_2}) (A/cm ²)	3.50428×10^{4f}
Pre-exponential for O ₂ electrode (k_{O_2}) (A/cm ²)	1.69850×10^{4f}
Activation energy for H ₂ electrode (E_{H_2}) (J/mol)	87.4×10^{3f}
Activation energy for O ₂ electrode (E_{O_2}) (J/mol)	88.75×10^{3f}
Ionic conductivity (σ_0) (S/cm)	3.6×10^5
Ionic conductivity (E_{el}) (J/mol)	80.0×10^3

^f Fitted parameter

Leakage overpotentials could be considered in the potential balance equation if the difference between cell voltages, throughout experiment and simulation, at open-circuit is evident. The electrochemical model input parameters used for reproducing the experimental data are listed in Table 4.1. The values of thicknesses of the electrodes, electrolyte, and cell properties used in the model valida-

tion are also listed in Table 4.2. It is important to note that micro-structural properties are assumed to be within a reasonable realistic range for modern day cells due to its unavailability in the aforementioned article. A case for its importance will be explained shortly. The electrochemical button cell model (discretized along the axi-symmetric line) was used to reproduce experimental data. All figures depicting electrochemical characteristics of the cell are 1-D button cell simulations (Figs. 4.2, 4.4, 4.6, 4.7 & 4.13). Every other figure refers to the co-flow planar configuration.

Table 4.2: Cell parameters and properties used for model validation/analysis

Parameter	Model Validation	Parametric analysis
Fuel electrode		
Thickness (μm)	310	310
Porosity (%)	35	35
Tortuosity	3.0	3.0
Particle diameter (μm)	1.0	1.0
Pore diameter (μm)	0.3	1.0
Specific area (m^{-1})	1.080×10^5	1.080×10^5
Electrolyte		
Thickness (μm)	10	10
Oxidant electrode		
Thickness (μm)	10	10
Porosity (%)	35	35
Tortuosity	3.0	3.0
Particle diameter (μm)	1.0	1.0
Pore diameter (μm)	0.3	1.0
Specific area (m^{-1})	1.080×10^5	1.080×10^5
Operating conditions		
Pressure (bar)	1.0	1.0
Temperature (K)	1023.15/1123.15/1223.15	1073.15
Inlet gas composition		
At the H_2 electrode channel	50%, 70% H_2O in H_2	50% H_2O + 50% H_2
At the O_2 electrode channel	21% O_2 in N_2 (air), pure O_2	21% O_2 + 79% N_2

In the case of the button-cell configuration, the equations for gas flow in the channels are not solved (unlike the case of planar configuration). Only the MEA (membrane-electrode assembly)/porous media is discretized in 1-D (along its axi-symmetric line). Hence, a boundary condition at the open electrode-channel interface is considered, which is nothing but the inlet species mass fractions. Consequently, the 2nd order reaction-diffusion equation is solved for species transport along the electrode's thickness, along with the supply of another boundary condition at the electrolyte-electrode interface. This boundary condition is equal to the species flux that is calculated based on the local current density. Since the equations in the gas channel are not solved, under isothermal conditions, one can assume that the employed button-cell model is independent of fuel dilution effects caused in the gas channels. Table 4.3 provides means for comparison between ASR values

obtained during DC characterization of the cell in the experiments [112] and the performed numerical simulations. One can note a good agreement between the two.

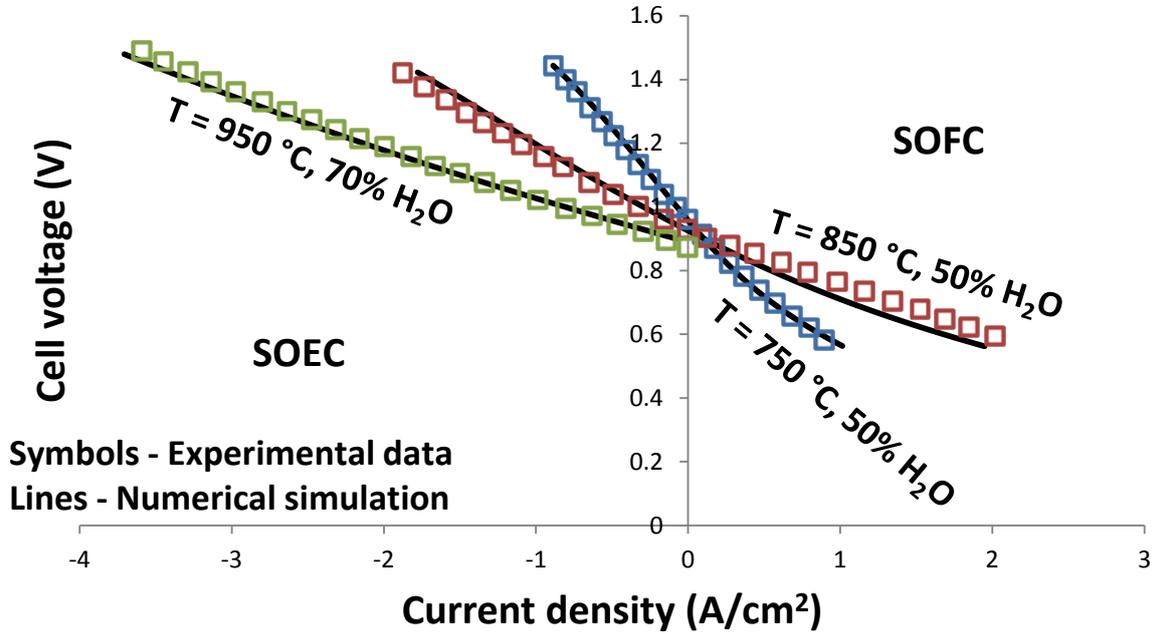


Figure 4.2: Comparison between numerical simulation and experimental data.

Table 4.3: Comparison of ASR values between simulation and experiment

Fuel composition	Temperature (°C)	ASR ($\Omega \cdot \text{cm}^2$) – Experiment		ASR ($\Omega \cdot \text{cm}^2$) – Numerical model	
		Electrolysis mode	Fuel cell mode	Electrolysis mode	Fuel cell mode
50% H ₂ O + 50% H ₂	750	0.55	0.41	0.548	0.4
50% H ₂ O + 50% H ₂	850	0.26	0.16	0.28	0.186
70% H ₂ O + 30% H ₂	950	0.17	-	0.159	-

In order to compare breakdown of polarization resistances obtained from AC characterization of the cell in the experiments [65] and the model used in the numerical simulations, results obtained from a small stimulus current of ~ 20 mA is compared to that attained at OCV. Alternatively, the charge transfer resistance R_{ct} can also be derived from the Butler-Volmer equation by taking the partial derivative of the current density i with respect to the activation overpotential. For the numerical simulations, the inlet fuel to the Ni/YSZ electrode is 25% H₂O + 75% H₂ while air is supplied to the LSM/YSZ electrode. Table 4.4 provides insight into the resistances obtained from numerical simulations. One can observe that it is in good agreement with the range in the aforementioned reference, giving the polarization resistances for the SOCs produced at DTU Energy conversion (former

Risø DTU). The conversion resistance can be neglected/minimized by providing sufficiently high flow rates at the inlets to minimize fuel/reactant dilution, although considering this effect can partake in making the model more robust.

Table 4.4: Breakdown of polarization resistances for the cell used in the model validation after consideration of electrochemical fit parameters

System Component	Resistance ($\Omega \cdot \text{cm}^2$)	
	T = 700 °C	T = 850 °C
$R_{\text{ct-LSM}}$ (O_2 electrode)	0.759	0.153
$R_{\text{ct-Ni}}$ (H_2 electrode)	0.348	0.0984
R_{ohmic} (electrolyte)	0.0532	0.0164
$R_{\text{Diffusion}}$	0.0222	0.0269

4.2 Thermal characteristics of the SOC during isothermal operation

The validated model is further employed for parametric analysis using data listed in Tables 4.1 and 4.2. The net heat flux q''_{net} is the sum of the ohmic and reaction heat flux [113], which are described as

$$q''_{\text{ohm}} = i^2 ASR = i(E_{\text{cell}} - E_{\text{rev}}) \quad (4.5)$$

$$q''_R = \frac{i}{2F} (T\Delta S) = \frac{i}{2F} (\Delta G - \Delta H_R) = i(E_{\text{rev}} - V_{\text{th}}) \quad (4.6)$$

respectively. In the electrolysis mode, one can notice that the net flux is negative for low operating current densities, approaches zero at thermo-neutral voltage (at $\sim 0.57 \text{ A/cm}^2$) and is positive at higher current densities. At low current densities, the net heat flux is negative due to the endothermic steam reduction reaction, whereas higher current densities correspond to excess production of heat. In the fuel cell mode of operation, all forms of heat flux are positive and increase with an increase in current density. Therefore, thermal management becomes important in order to maximize efficiencies, via conscious choice of optimum design for various configurations of steam electrolysis systems. This affects the delamination phenomena, i.e., detachment of the electrode layer from the electrolyte layer due to thermal expansion mismatch in SOECs, and influences local charge current density distributions. These phenomena are depicted in Fig. 4.3.

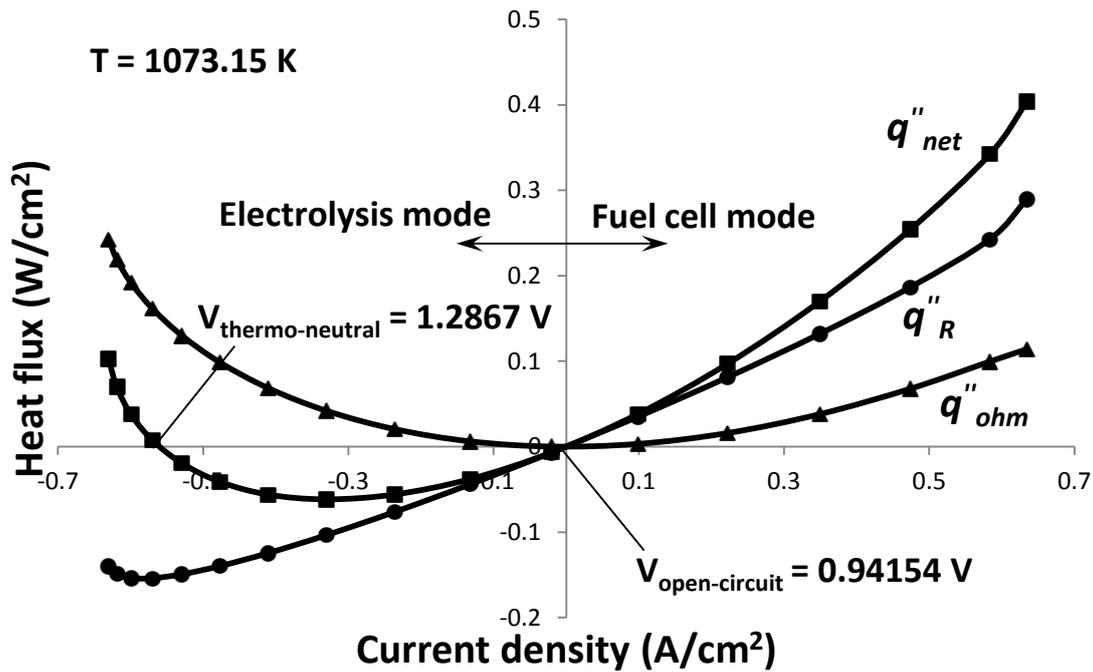


Figure 4.3: Thermal characteristics of a SOEC during isothermal operation.

4.3 Effect of operating temperature on the SOEC

Fig. 4.4 articulates the fact that higher operating temperatures result in decreased SOEC operating potentials. It is important to remember that the current densities are actually negative and only the magnitudes are considered for parametric analysis. One can observe that the activation and ohmic overpotentials increase with a decrease in temperature. Also, there is a stark difference in SOEC electrode activation losses between low and high temperatures. This can be attributed to the functional dependency of the exchange current density i_0 [71]. This decrease in overpotential losses translates to the attainment of higher current densities at a specified operating voltage. But, high temperature operation has two main disadvantages - (i) Cell degradation, and (ii) Cost of suitable materials. Thus, better thermal management techniques and/or materials that can operate at intermediate temperatures are required.

The effect of temperature on gas concentration distribution is shown in Fig. 4.5. The top and bottom panels represent the fuel and air channels, whereas the middle panels represent the porous media at the inlet, centre and exit positions (with respect to the gas channels). The height and width of the gas channels are 1 mm each. The length of the channels is 5 cm. The molar fraction of H_2 increases, and H_2O decreases, with axial distance. Accordingly, this change is reflected in the cathode. An increase in temperature improves reaction kinetics and decreases overpotential losses, thereby en-

hancing the performance of the cell. This increase in performance translates to the attainment of higher current densities at a specified voltage. Thus, one can attain higher gas-phase molar fractions of H_2 at the exit of the cathode channel. Furthermore, an increase in temperature causes only a marginal increase in gas-phase O_2 molar fraction in the air channel. It is important to note that the inlet gas velocities at the fuel and air channels are 0.35 m/s and 3.0 m/s, respectively. Lower inlet gas velocities entail greater dilution, which implies lesser availability of H_2O at the TPB. This increases the reversible cell potential and hence, the operating cell voltage increases at a specified current density.

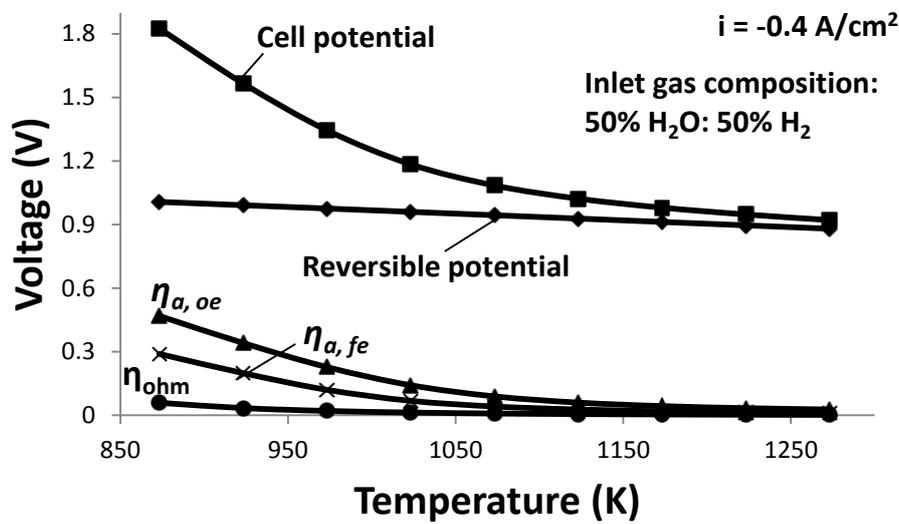


Figure 4.4: Effect of temperature on SOEC electrochemical characteristics.

4.4 Effect of steam content and current density on the SOEC

An increase in steam molar fraction has an effect of reducing the operating SOEC potential as shown in Fig. 4.6. Alternatively, one can obtain higher current densities with decreasing H_2/H_2O ratios, although an increase in current density implies higher activation losses. The reversible potential increases with increasing H_2/H_2O ratios. This increase in reversible potential leads to the attainment of lower current densities. As mentioned above, an increase in current density causes an elevation in the overpotentials of the system (Fig. 4.7). This increase in overpotentials is a direct consequence of the B-V equation. The reversible potential shows a minor increase of ~ 0.06 V between $i = 0$ A/cm² and $i = 1.0$ A/cm².

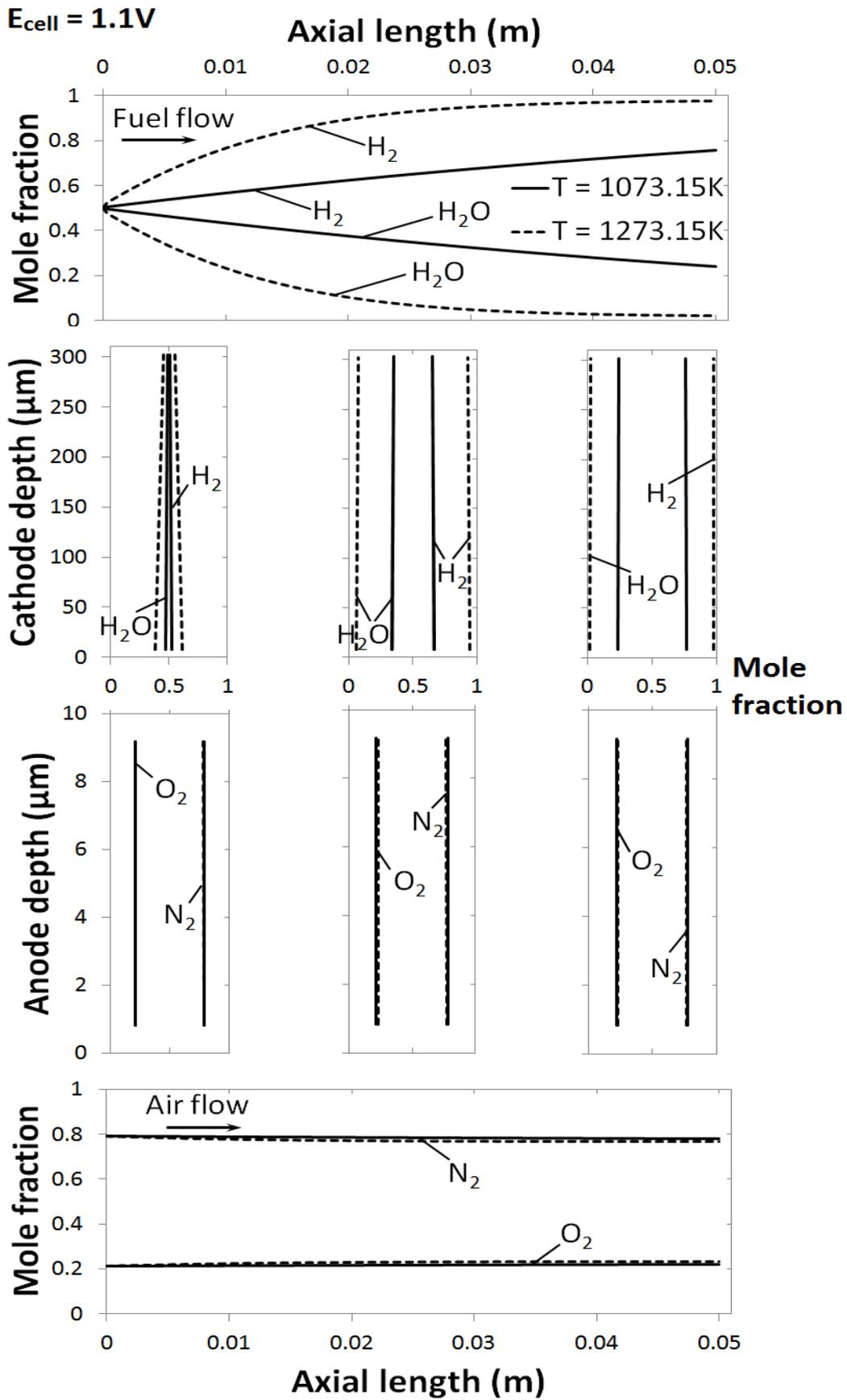


Figure 4.5: Effect of temperature on gas distribution in the cell.

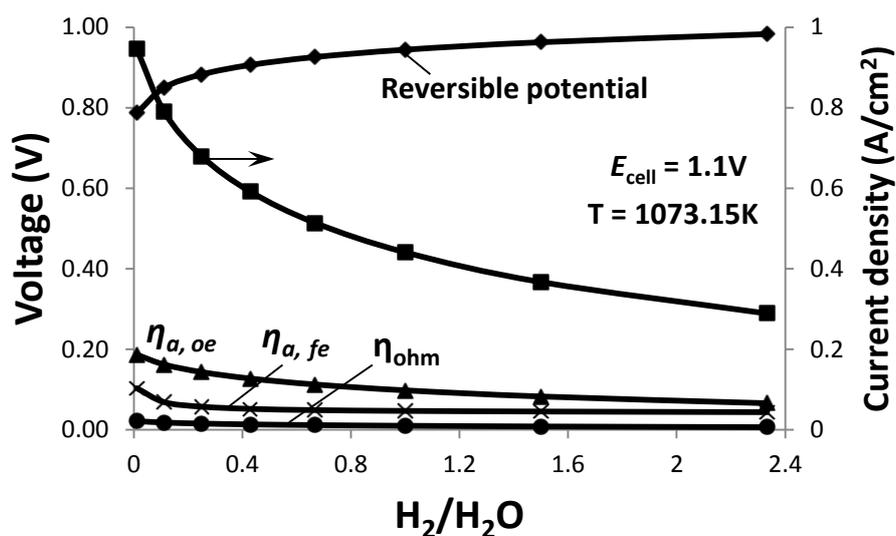


Figure 4.6: Effect of cathode inlet gas composition on SOEC electrochemical characteristics.

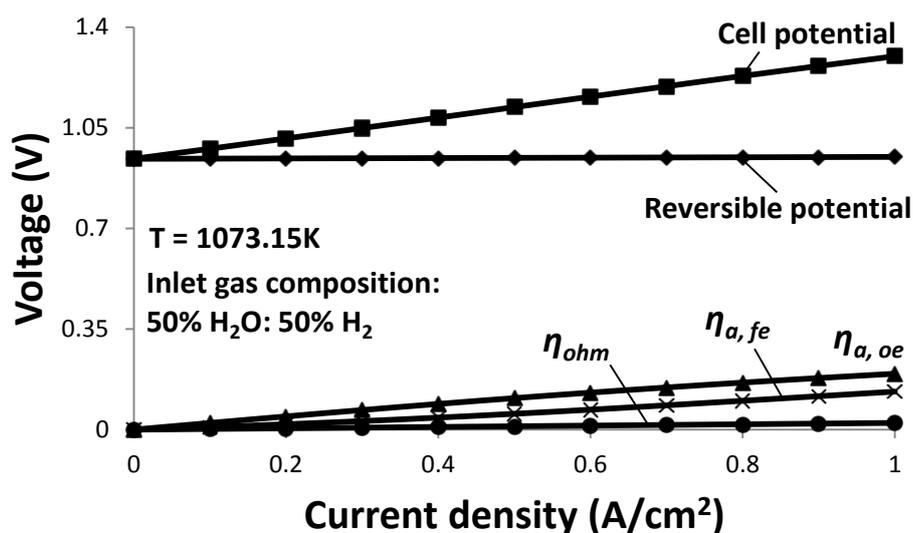


Figure 4.7: Effect of current density on SOEC electrochemical characteristics.

4.5 Adsorbed surface species distribution within the cathode

The impact of H_2/H_2O ratios on the coverage of various surface adsorbed species and intermediates, ~ 3 cm from the inlet, are shown in Fig. 4.8. The variations are shown at ~ 3 cm from the inlet, since all adsorbed species had qualitatively similar trends at all axial positions of the TPB. θ is the surface coverage fraction. Nickel is commonly used as cathode material due to its cost effectiveness. $H_{(s)}$ adsorbate concentration mainly governs the concentration of the uncovered $Ni_{(s)}$ surface, i.e., greater $H_{(s)}$ adsorbate coverage implies lower uncovered $Ni_{(s)}$ surface concentration. An increase in

H_2/H_2O ratio translates to lower concentrations of $H_{(s)}$ and $H_2O_{(s)}$, which show similar trends as compared to the species composition in the fuel channel. But, there is a significant difference in their magnitudes due to fast diffusion of H_2 in the porous media and negligible concentration overpotentials. Besides species composition in the gas channels, H_2O is constantly consumed by the electrochemical charge transfer reaction that produces H_2 at the TPB. The intermediate $OH_{(s)}$ and $O_{(s)}$ adsorbate coverages are found to decrease with an increase in H_2/H_2O ratio, and along the TPB. These coverages are a consequence of the dissociative adsorption of $H_2O_{(s)}$, though their magnitudes depend on the influence of operating conditions on position specific reaction rates. Additionally, H_2O also contributes to $O_{(s)}$ adsorbate generation. The gradients in concentrations of $OH_{(s)}$ and $O_{(s)}$ adsorbates are found to increase, along the axial TPB length of the cell, with increase in inlet steam molar fraction. Therefore, an increase in inlet steam molar fraction promotes the dissociative adsorption of H_2O . This in turn increases the electrochemical reaction rate, and also increases the local current density due to direct proportionality. Consequently, the SOEC operating potential is lowered.

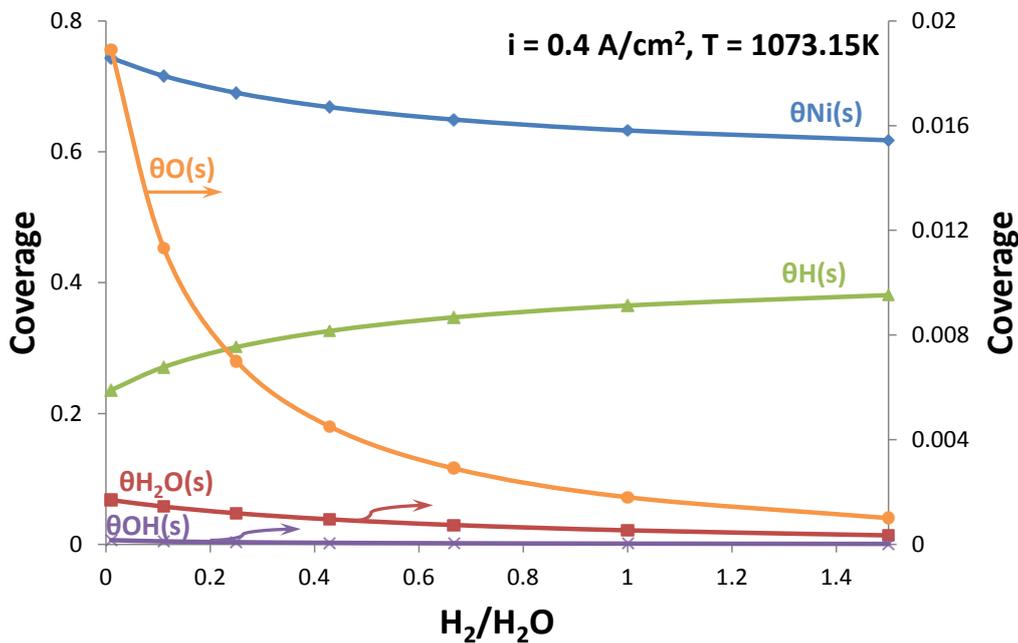


Figure 4.8: Effect of cathode inlet gas composition on various surface adsorbed species at the cathode TPB.

From section 4.3, it is seen that high temperatures play a beneficial role in terms of improving electrochemical characteristics of the SOEC system. In Fig. 4.9, we observe that the concentration of the uncovered $Ni_{(s)}$ surface increases with increasing temperature, even though molar fraction of H_2

increases in the gas channels. This is due to the fact that desorption reactions are favored with increase in temperature, leading to lower $H_{(s)}$ adsorbate coverage in the porous cathode. The decrease in $H_2O_{(s)}$ concentration with an increase in temperature is due to faster electrochemical consumption. The concentrations of the $OH_{(s)}$ and $O_{(s)}$ adsorbates show an increase, as higher temperatures can elicit the rate of surface chemical reactions based on different activation energies. This gives a more detailed insight into the interplay between surface adsorbed species and cell performance, along with logical predictions as to why higher temperatures lead to lower SOEC operating potentials along with higher gas-phase H_2 at the exit of the cathode channel.

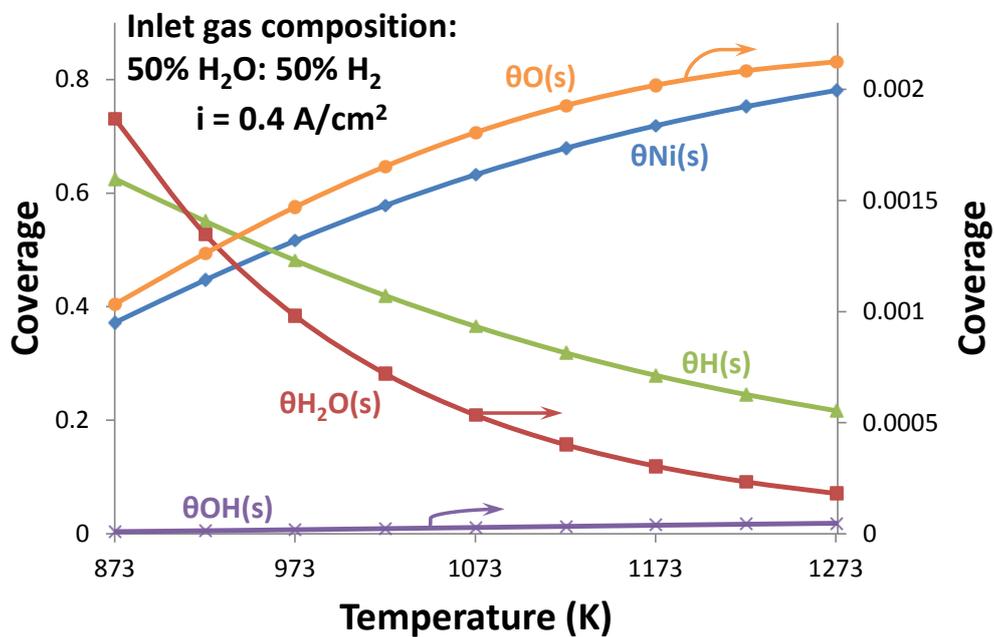


Figure 4.9: Effect of temperature on various surface adsorbed species at the cathode TPB.

The impact of cell voltage on various surface adsorbed species is relatively straightforward, and is represented by Fig. 4.10. In view of the fact that $H_{(s)}$ adsorbate concentration mainly governs the concentration of uncovered $Ni_{(s)}$ surface, one can notice the pattern of increased uncovered $Ni_{(s)}$ surface concentrations with decreased $H_{(s)}$ adsorbate concentration. Basically, an increase in cell voltage increases the electrochemical reaction rate at the TPB, which results in decreased $H_2O_{(s)}$ concentration and increased $H_{(s)}$ adsorbate concentration along the axial TPB length. Accordingly, the $OH_{(s)}$ and $O_{(s)}$ surface concentrations show similar trends as the $H_2O_{(s)}$ concentration.

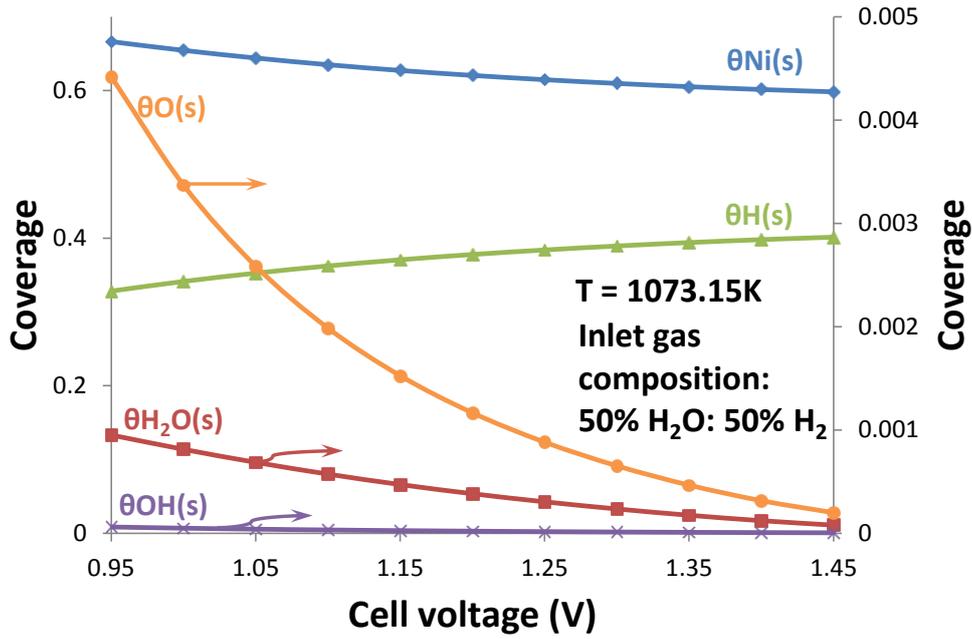


Figure 4.10: Effect of cell voltage on various surface adsorbed species at the cathode TPB.

4.6 Efficiency analysis of the SOEC

The overall hydrogen production efficiency of the system is given by [111]:

$$\eta_{overall} = \frac{LHV_{H_2}}{Q_{elec} + Q_{th}} = \frac{LHV_{H_2}}{\left[2F \left(\frac{E_{cell}}{\eta_{elec}} + \frac{(V_{th} - E_{cell})}{\eta_{th}} \right) \right]} \quad (4.7)$$

where Q_{elec} is the consumed thermal energy used for electricity generation, Q_{th} is the thermal energy required for the electrolysis process, η_{th} is the thermal utilization efficiency and η_{elec} is the electrical power generation efficiency. η_{elec} is the ratio between the electrical energy consumed in the electrolysis process (ΔG) and the consumed thermal energy from a primary energy source used for electricity generation (Q_{elec}). The voltage efficiency of the SOEC, which gives a measure of the energy lost through overpotential losses, can be described as:

$$\eta_{voltage} = \frac{E_{rev}}{E_{cell}} \quad (4.8)$$

From the system's perspective, the influence of operating cell voltage on the aforementioned efficiencies is portrayed in Fig. 4.11. It is interesting to note that the overall hydrogen production effi-

ciency and steam utilization rate show opposite trends. The hydrogen production efficiency increases with a decrease in steam utilization and cell voltage. At $\eta_{th} = 0.9$ and $\eta_{elec} = 0.52$, the hydrogen production efficiency decreases from $\sim 57\%$ at 0.95 V to $\sim 48\%$ at 1.45 V . This implies that, at low steam utilization rates, the system processes excess material (steam) that lowers the average Nernst potential, leading to the attainment of lesser cell voltages at a specified current density. This is a performance penalty. In contrast, operation at very high steam utilization rates lead to steam starvation, which translates to cell degradation and performance losses as well. Thus, it becomes important to consider a trade-off between hydrogen production rate and overall efficiency of the system from a practical standpoint. This occurs at about $\sim 1.1\text{ V}$, which is lower than the thermo-neutral voltage. One can notice that the hydrogen production efficiency decreases with a decrease in the electrical efficiency of the system ($\eta_{th} = 0.9$ is assumed for all cases). Furthermore, the voltage efficiency of the system decreases with an increase in voltage because of higher overpotential losses.

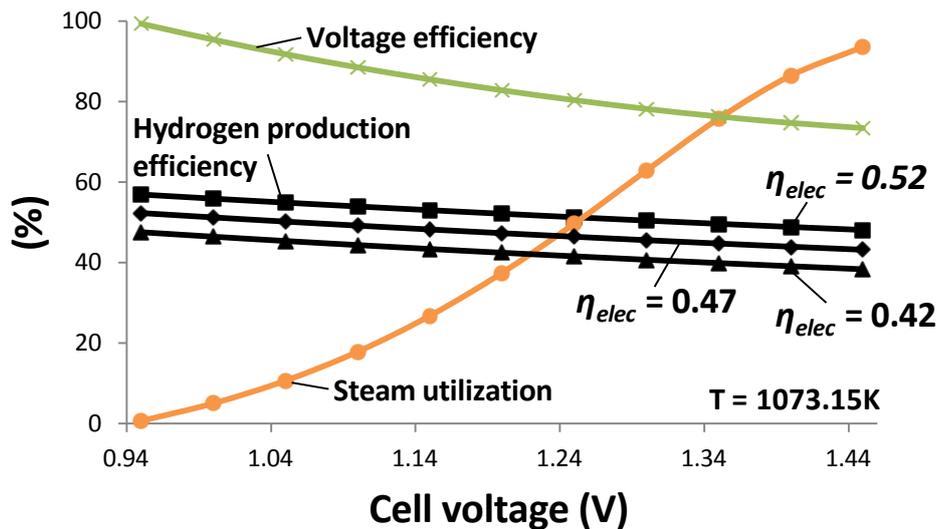


Figure 4.11: Efficiency analysis of the SOEC - Influence of operating cell voltage.

Fig. 4.12 gives insight into the advantageous effects of temperature and inlet steam molar fraction on the hydrogen production efficiency of the system. One can notice that an increase in temperature increases the overall efficiency of the system. At $H_2/H_2O = 0.2658$, the overall efficiency increases from $\sim 44\%$ at 873.15 K to $\sim 58\%$ at 1273.15 K . This can be attributed to improved electrochemical characteristics of the cell. Also, an increase in H_2/H_2O ratios leads to a decrease in overall efficiencies of the system. This is due to the fact that a reduction in inlet steam molar fraction raises the operating SOEC potential. At 1273.15 K , the overall efficiency increases from $\sim 55\%$ at H_2/H_2O

= 2.3333 to ~60 % at $H_2/H_2O = 0.0101$. The inlet gas velocity at the fuel channel, only for this case, is 0.7 m/s.

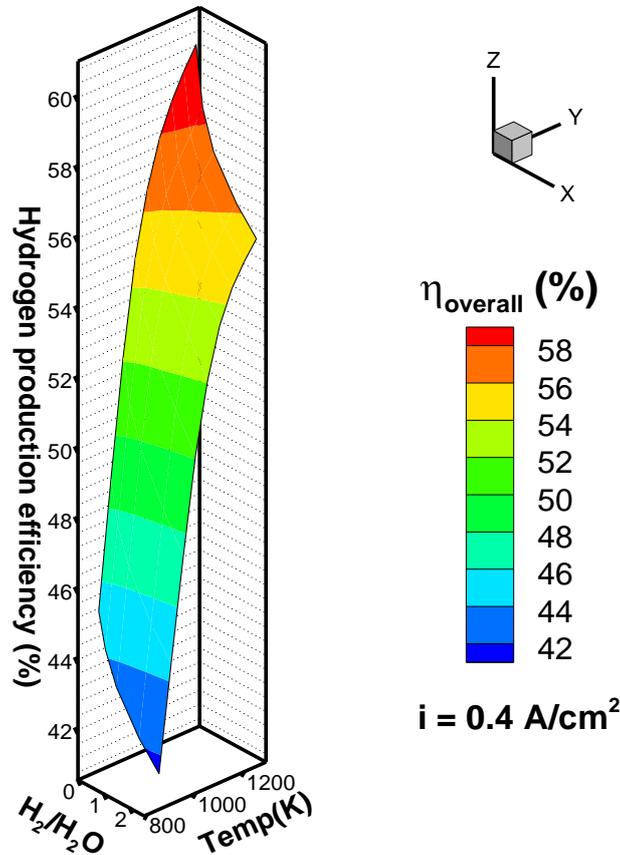


Figure 4.12: Efficiency analysis of the SOEC - Influence of temperature and cathode inlet gas composition.

4.7 Diffusion limitation behavior vs. micro-structural properties

It is well established that micro-structural parameters have a pronounced effect on the limiting current behavior. In Fig. 4.13, one can observe that even less than an order of magnitude change in pore diameter has a significant impact on diffusion limitation. This is due to the fact that the Knudsen diffusion coefficient is directly proportional to the pore radius. Lowering pore diameter produces similar trends to that of increasing tortuosity (to unrealistic values) and decreasing cathode inlet gas velocity by several orders of magnitude. Since the actual physical phenomena responsible for limiting current behavior is not well understood, we speculate that lowering pore diameter inhibits the reactants from reaching the TPB directly from the gas-phase and hence, bringing about a localized depletion zone. Replenishing existing reactants at the TPB turns harder. At higher current den-

sities, the electrochemical reaction rates are relatively higher, causing competition between product production and constant supply of reactant through the diffusion pathway. This can also be observed in the reversible potential characteristics, which increases from ~ 0.65 V at ~ 3.84 A/cm² (for $d_{\text{pore}} = 0.1$ μm) to ~ 0.903 V at ~ 3.84 A/cm² (when $d_{\text{pore}} = 0.5$ μm). This is significant as the reversible cell potential takes into account partial pressures of electrochemical reactants and products at the TPB. This effect can be countered by increasing/optimizing porosity, or via the usage of materials with lower physically realistic tortuosities (2.0–3.5) [114].

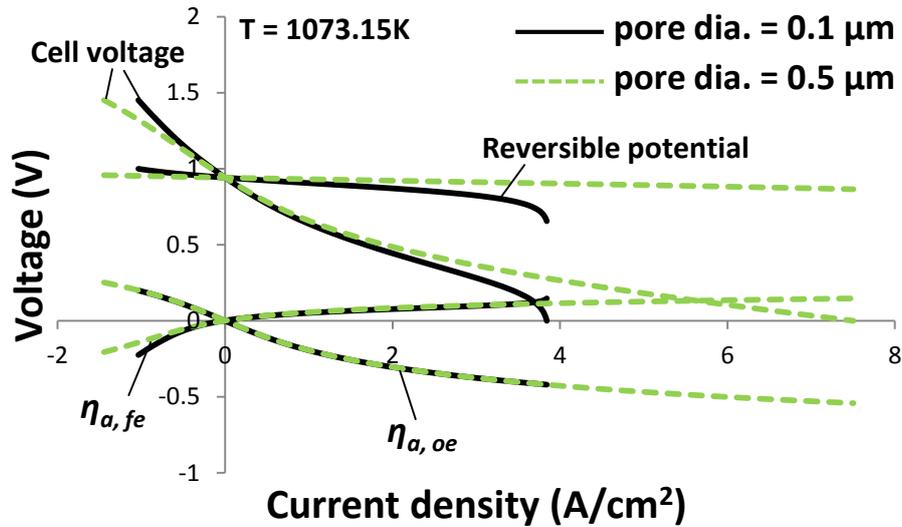


Figure 4.13: Effect of pore diameter on limiting current behavior.

4.8 Summary

A quasi-two-dimensional model to numerically study the performance of a Solid Oxide Electrolysis Cell (SOEC) is employed. The effects of temperature, H₂/H₂O and current density on the electrochemical characteristics of the SOEC system are investigated. High temperature plays a crucial and beneficial role in shaping efficiency, hydrogen production rate and performance of a SOEC system. At a specified voltage, low H₂/H₂O ratios lead to the attainment of higher current densities that are responsible for relatively higher overpotential losses. Also, low H₂/H₂O ratios prove to be advantageous from the perspective of overall hydrogen production efficiency. But, lower H₂/H₂O ratios translate to smaller steam utilization rates, which are not favorable from a practical standpoint. Thus, one must bear in mind an optimum trade-off between the efficiency, overpotentials, operating cell voltage and hydrogen production rate. The concentrations of surface adsorbed species - H₂O_(s), O_(s), H_(s) and OH_(s), at the TPB, are significantly affected by operating parameters and conditions.

Another interesting phenomenon in SOCs is the importance of micro-structural influence on the limiting current characteristics of the system. We demonstrate a case where the electrochemical behavior of the system is studied at two different pore diameters. A decrease in reversible potentials, at a specified current density, indicates product build-up at the TPB as opposed to steady supply of fresh reactants through the diffusion pathway. Therefore, further in-depth study on the effect of these parameters on concentration overpotentials of the system would give deeper understanding of the multi-physics phenomena at work, at limiting current. Nevertheless, a case is presented to better understand SOEC technology for performance and design optimization.

Chapter 5 On the production of synthesis gas in SOECs by co-electrolysis of steam/carbon dioxide

¹Solid-Oxide Electrolysis Cells (SOECs) are valued for their capacity to facilitate the production of hydrogen and syngas (H_2 , CO) as well as oxygen. In comparison to the multiple dissociative methods for hydrogen or syngas production, high temperature co-electrolysis of H_2O and CO_2 combines advantages such as fast reaction rates, lowered propensity towards carbon formation and reduced cell resistance via remarkably efficient use of heat and electricity [115]. The produced syngas can be further processed to generate liquid hydrocarbons (e.g. synthetic diesel) via Fischer-Tropsch synthesis, or be converted to methanol, dimethyl ether (DME) or methane via catalytic reactions. Thus, it is environmentally advantageous and technologically practical to supply the energy requirements of a SOEC with a sustainable yet renewable energy source (wind, solar etc.) or nuclear energy to lower the carbon footprint and limit greenhouse gas emissions. Nevertheless, proper economic assessment is necessary to underline the feasibility of such a complex process at the systems level [116]. This could further help shift focus towards alternative energy carriers, away from existing finite fossil fuel resources, due to environmental concerns.

There is a wide application potential for Solid-Oxide Cells (SOCs) due to its fully reversible nature and simplicity. The representation of the planar SOEC under consideration, in this study, is shown in Fig. 5.1. The electrolysis reactions that contribute to the production of H_2 and CO occur at the cathode three-phase boundary (TPB) via Eqs. 5.1 and 5.2, whereas the reverse water-gas shift (RWGS) reaction occurs in the porous cathode material via Eq. 5.3. Although the RWGS reaction shifts towards equilibrium over nickel catalysts under reaction conditions described by [117], there is speculation as to whether it is accompanied by electrochemical/electrolysis reactions to produce CO. If so, the degree of its influence also becomes important. The oxygen production takes place at the anode TPB sites via Eq. 5.4. This feature was used by NASA as a proposed means for

¹Parts of this chapter are taken from Menon et al. [62]. Copyright (2014), with permission from Elsevier.

supporting life in Mars via CO₂ electrolysis on Ni- and Pt- based cathodes [118].

At the cathode-electrolyte interface,



At the porous cathode sites,



At the anode-electrolyte interface,

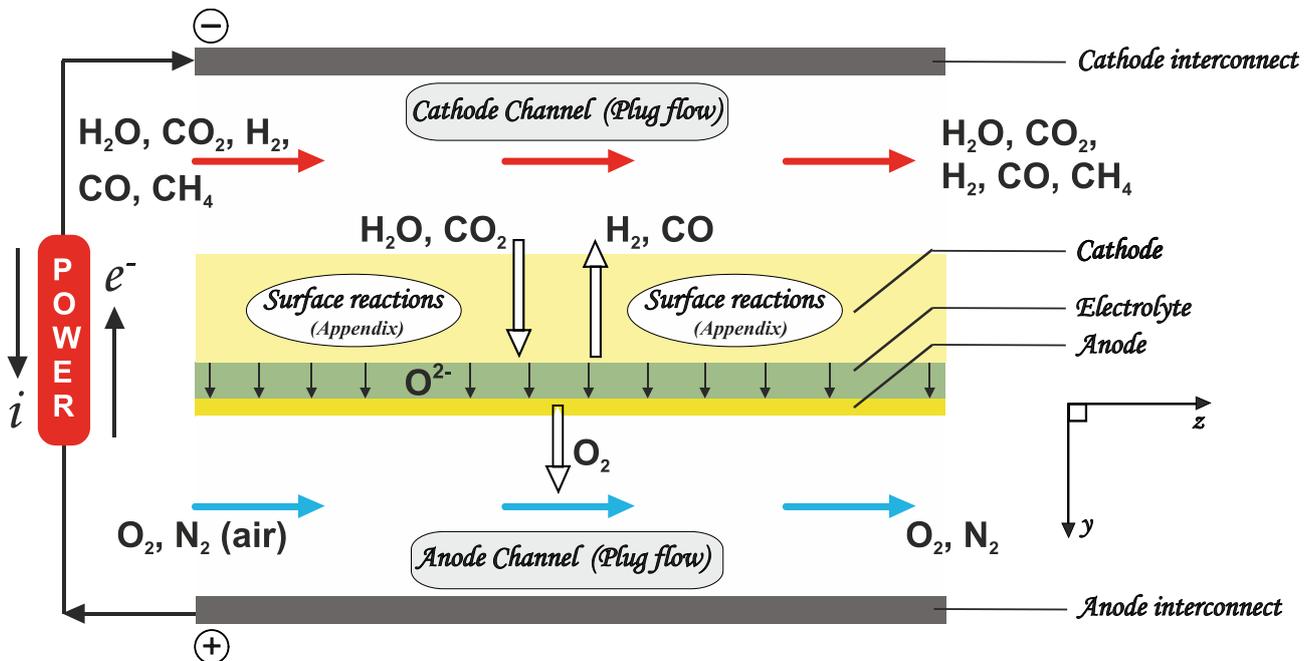


Figure 5.1: Schematic representation of a planar co-flow Solid Oxide Electrolysis Cell (SOEC).

where, the cathode is the fuel electrode and the anode is the oxidant electrode (opposite to the that of a SOFC).

In the present analysis, we apply an in-house mathematical model that combines mass transport, heterogeneous chemistry, porous media transport and electro-chemistry. The 1-D electrochemical button cell model is validated with two sets of experimental data. The first set is obtained from Ref. [65], and the second set of experiments was performed at EIFER (European Institute for Energy Research) [119]. Unlike approximations made in literature, modified B-V equations are considered for the reduction of both CO_2 and H_2O , by considering multi-step single electron transfer reactions. Additionally, the estimated electrochemical parameters are employed in the quasi 2-D model for parametric analysis. The thermo-catalytic chemistry is handled by a 42-step elementary heterogeneous reaction mechanism for Ni catalysts, which consists of 6 gas-phase species and 12 surface adsorbed species (listed in the Appendix). Reaction flow analysis is carried out in a perfectly mixed batch reactor, at OCV, to clearly understand the source of methane formation in the system. The code is available as a part of the DETCHEMTM software package [90].

5.1 Experimental setup

Two sets of experimental data are used to numerically validate the model. The first set of experiments was performed at DTU Energy conversion (former Risø DTU). The cell was composed of a NiO/YSZ porous support layer, NiO/YSZ fuel electrode, YSZ electrolyte and LSM/YSZ oxygen electrode whose thicknesses were 300 μm , 10-15 μm , 10-15 μm and 15-20 μm respectively. The inlet flow rate of pure oxygen to the LSM/YSZ electrode was 20 l/h for all experiments. Planar Ni/YSZ supported SOCs of $5 \times 5 \text{ cm}^2$, with an active electrode area of $4 \times 4 \text{ cm}^2$, were used in the experiments. The NiO in the Ni/YSZ electrode was reduced to nickel with hydrogen at 1000 °C, at start-up.

As described in Ref. [119], the SOC used in the second set of experiments performed at EIFER is procured from H. C. Starck (cell type ESC2). It is composed of a TZ3Y (3 mol % Y_2O_3 - stabilized ZrO_2) electrolyte ($50 \times 50 \text{ mm}^2$ area, 90 μm thick), NiO/GDC (gadolinium-doped ceria) anode ($40 \times 40 \text{ mm}^2$ area, 40 μm thick) and 8YSZ/LSM-LSM (8YSZ: 8 mol % Y_2O_3 -stabilized ZrO_2 , LSM: lanthanum strontium manganite) double-layer cathode ($40 \times 40 \text{ mm}^2$ area, 40 μm thick). Although the literature reports results carried out only at 860 °C, experiments pertaining to a temperature of 810 °C were also performed and used in this study. The ceramic cell housing used for cell testing at EIFER is schematically shown in Fig. 5.2. The current collection is achieved using a Ni-grid and

Ni-foam at the fuel electrode, while a Pt-grid is used at the oxidant electrode. Gas inlets and outlets are symmetrical. As a result, the MEA may be tested in both co-flow and counter-flow configurations. It should be noted, however, that the model validation is done using experimental data that was obtained with the latter configuration. The sealing of the fuel chamber relies on the smooth surfaces of the electrolyte layer and adjacent alumina frames. The air chamber is not sealed, but is always swept with 500 sccm air. A thermocouple is inserted through a drilled hole in the anode frame, and is located at about 5 mm under the central point of the cell. The cell temperature is thus obtained, which is usually different from the oven temperature. A bubbler humidifier is used to supply steam to the cell. The polarization curves (i - V curves) were recorded by ramping the current through the cell at 5 A min^{-1} from $i = 0 \text{ A}$.

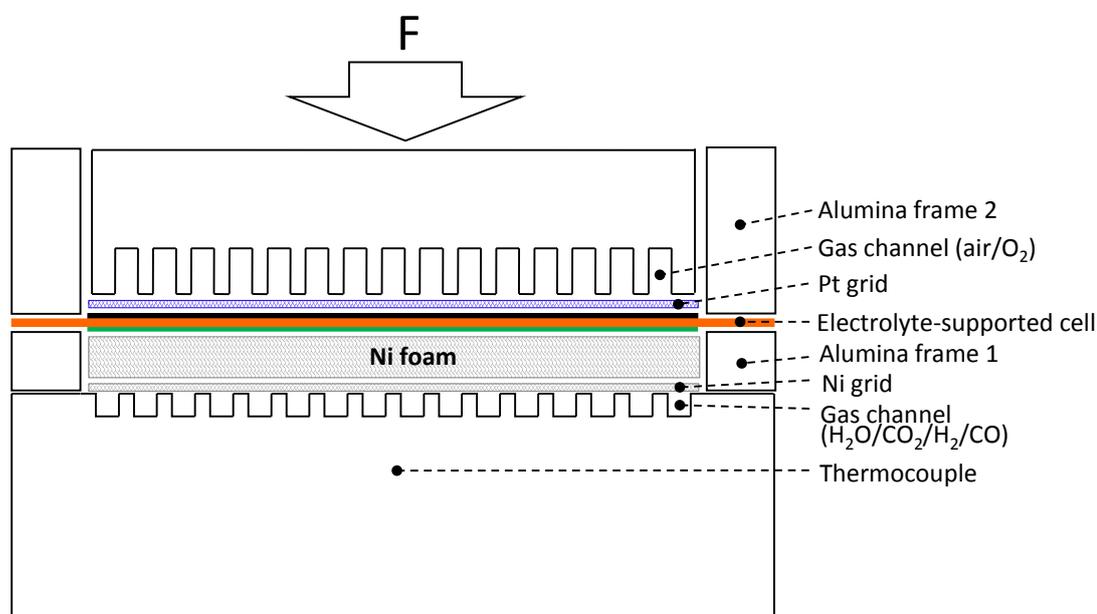


Figure 5.2: Schematic illustration of the ceramic cell housing at EIFER.

5.2 1-D electrochemical model

5.2.1 Model validation

The model is validated with the first set of experiments performed at DTU Energy conversion (former Risø DTU) [65]. According to the article, the authors elucidate on various loss mechanisms and reaction pathways involved in reversible SOCs via thorough DC and AC characterization (by Electrochemical Impedance Spectroscopy (EIS)) of the system. They studied electrochemical reduction and oxidation phenomena in $\text{H}_2\text{O}-\text{H}_2$, CO_2-CO and $\text{H}_2-\text{H}_2\text{O}-\text{CO}-\text{CO}_2$ mixtures to analyze the role of

the WGS/RWGS reaction. Fig. 5.3 portrays good agreement between numerical simulation results and experimental data, measured at 750 °C and 850 °C with an inlet gas composition of 25% H₂O: 25% CO₂: 25% CO: 25% Ar to the Ni/YSZ electrode. A leakage overpotential is considered in each of the potential balance Eqs. 2.30 and 2.31, as the experimentally measured OCV differs from the thermodynamically estimated one, and is formulated as

$$\eta_{leak} = \eta_{leak,max} \left(1 - \frac{i}{i_{max}}\right) \quad (5.1)$$

where i_{max} is the maximum current and a fit parameter. Here, we use $\eta_{leak,max} = 0.03, 0.02$ V and $i_{max} = 1.0$ A/cm². The calculated ASR values at 1.1 V are 0.287 Ω.cm² at 850 °C and 0.593 Ω.cm² at 750 °C. The ASR values correspond to the case where $\eta_{leak,max} = 0.02$ V. Firstly, electrochemical input parameters are determined, through model validation, by making individual fits for varying compositions of H₂O-H₂ and CO₂-CO at 750 and 850 °C [74]. After calibration, the model is then validated for H₂O-CO₂-H₂-CO mixtures. The electrochemical parameters used for reproducing the experimental data are listed in Table 5.1. The values of thicknesses of the electrodes and electrolyte, along with cell properties used in model validation are listed in Table 5.2. It is important to note that micro-structural properties are assumed to be within a realistic range, due to its unavailability in the aforementioned literature.

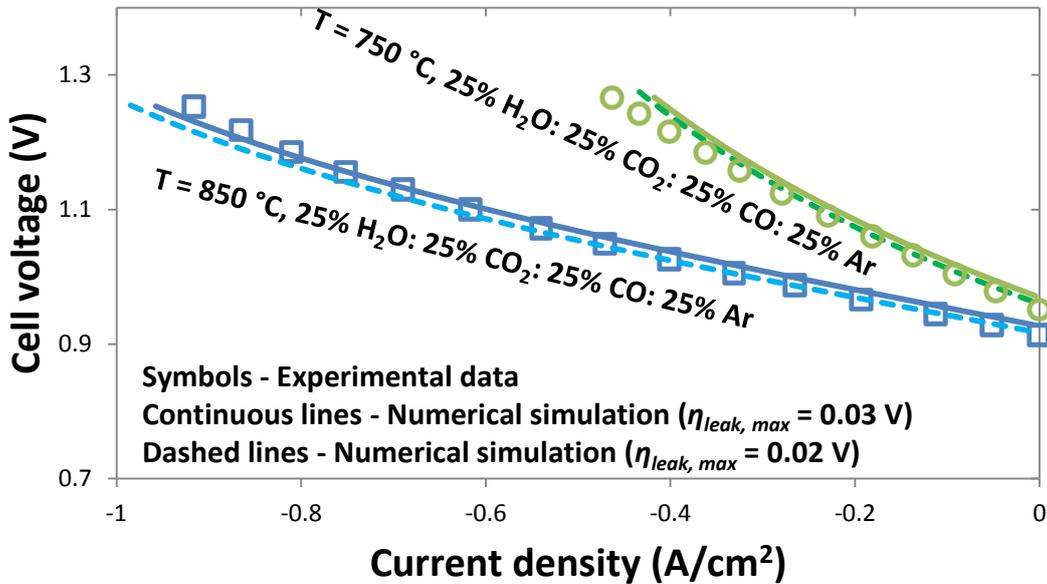


Figure 5.3: Comparison between numerical simulation and experiments from Ref. [65].

Table 5.1: Electrochemical model/input parameters for experiments done at DTU Energy conversion (former Risø DTU)^f

Property	H ₂ -H ₂ O	CO-CO ₂
Fuel electrode asymmetry factor (β_a)	0.7	0.5
Oxidant electrode asymmetry factor (β_a)	0.1	0.1
Exchange current density parameters		
Pre-exponential factor (k_i) (A/cm ²)	594113.87	16129714.99
Activation energy (E_i) (J/mol)	108.4×10^3	131.38×10^3
Pre-exponential for O ₂ production (k_{O_2}) (A/cm ²)	41783.22	
Activation energy for O ₂ production (E_{O_2}) (J/mol)	88.75×10^3	
Ionic conductivity (σ_0) (S/cm)	3.6×10^5	
Ionic conductivity (E_{el}) (J/mol)	80.0×10^3	

^f Fitted parameters

Table 5.2: Cell parameters and properties used for model validation/analysis

Parameter	Model Validation [65]	Model Validation (EIFER) [119]	Parametric analysis
Gas channels (planar)			
Length (cm)	-	-	5
Height (mm)	-	-	1
Width (mm)	-	-	1
Air inlet velocity (m/s)	-	-	2.0
Fuel inlet velocity (m/s)	-	-	0.3
Fuel electrode			
Thickness (μm)	315	40	315
Porosity (%)	35	35	35
Tortuosity	5.0	3.5	3.5
Particle diameter (μm)	1.0	2.5	2.5
Pore diameter (μm)	0.22	1.0	1.0
Specific area (m ⁻¹)	1.025×10^5	1.025×10^5	1.025×10^5
Electrolyte			
Thickness (μm)	15	90	15
Oxygen electrode			
Thickness (μm)	20	40	20
Porosity (%)	35	35	35
Tortuosity	5.0	3.5	3.5
Particle diameter (μm)	1.0	2.5	2.5
Pore diameter (μm)	0.22	1.0	1.0
Specific area (m ⁻¹)	1.025×10^5	1.025×10^5	1.025×10^5
Operating conditions			
Pressure (bar)	1.0	1.0	1.0
Temperature (°C)	750, 850	810, 860	800, 900
Inlet gas composition			
At the cathode	25% H ₂ O: 25% CO ₂ : 25% CO: 25% Ar	As per figure	As per figure
At the anode	pure O ₂	21% O ₂ + 79% N ₂ (air)	21% O ₂ + 79% N ₂ (air)
Leakage			
$\eta_{leak,max}$ (V)	0.02, 0.03	0.05	0
i_{max} (A/cm ²)	1.0	1.7	0

Further, a second set of experiments performed at EIFER is numerically simulated to facilitate model validation. In the experiments, electrolysis was carried out with the supply of H₂O-CO₂-H₂ mixtures to the NiO-GDC cathode and air to the 8YSZ/LSM-LSM double-layer anode. The experi-

ments were carried out at 810 and 860 °C with multiple cathode inlet gas compositions. Supplementary information about the setup can be found in section 3. It was observed that the ASR values for electrolysis in CO-CO₂ mixtures were only slightly higher than co-electrolysis in H₂O-CO-CO₂ mixtures. Also, the ASR values of the cell for co-electrolysis using H₂O-CO-CO₂ mixtures and electrolysis using H₂O-H₂ mixtures were nearly identical. Figs. 5.4a–5.4c show good agreement with experimental data. The model is also able to predict trends in limiting current density, along with experimentally observed ASR values. The electrochemical model parameters used for the reproduction of experimental data are given in Table 5.3, while details pertaining to cell properties can be found in Table 5.2. Additionally, the electrochemical parameters deduced from reproduction of experiments carried out at EIFER, from Table 5.3, are used for further parametric analysis.

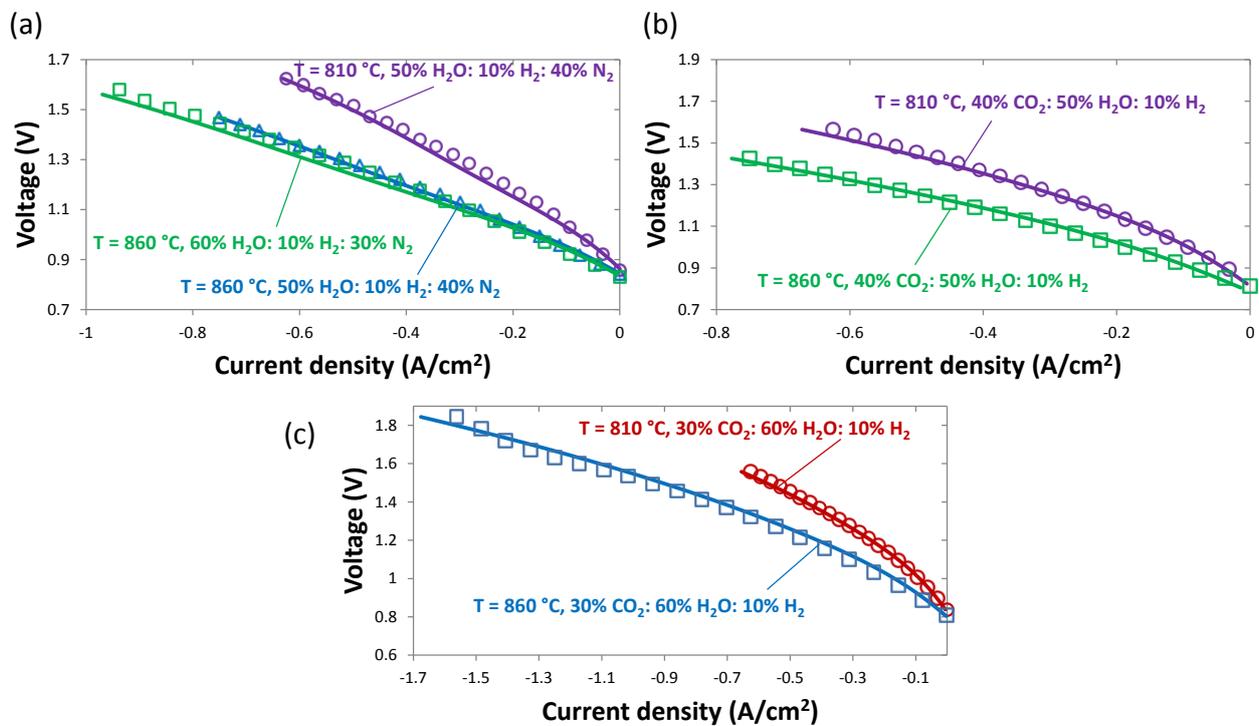


Figure 5.4: Comparison between numerical simulation and experiments from Ref. [119].

5.2.2 Effect of operating temperature on the SOEC

The effect of operating temperature on reversible cell potential and normalized net current density is shown in Fig. 5.5. The net reversible cell potential is given as

$$E_{rev} = E^0 + \frac{RT}{4F} \ln \left(\frac{p_{H_2,fe} p_{CO,fe} p_{O_2,oe}}{p_{H_2O,fe} p_{CO_2,fe}} \right) \quad (5.2)$$

It is interesting to note that the reversible cell potential decreases with increase in temperature, even though an increase in temperature elevates the electrochemical reaction rate leading to increased consumption and production of reactants and syngas, respectively. This rise is offset by the electromotive force at standard pressure E^0 , which decreases with a rise in temperature as the Gibbs free energy (ΔG) available to the system decreases, and the heat energy demand ($T\Delta S$) increases at higher temperatures. The current density increases with an increase in temperature due to a decrease in ohmic and activation overpotentials. It is important to remember that the current densities are actually negative and only the magnitudes are considered for parametric analysis.

Table 5.3: Electrochemical model/input parameters for experiments done at EIFER^f

Property	H ₂ -H ₂ O	CO-CO ₂
Fuel electrode asymmetry factor (β_a)	0.7	0.5
Oxidant electrode asymmetry factor (β_a)	0.3	0.45
Exchange current density parameters		
Pre-exponential factor (k_i) (A/cm ²)	178763.39	1480354.03
Activation energy (E_i) (J/mol)	108.4×10^3	131.38×10^3
Pre-exponential for O ₂ production (k_{O_2}) (A/cm ²)	88735.51	
Activation energy for O ₂ production (E_{O_2}) (J/mol)	122.5×10^3	
Ionic conductivity (σ_0) (S/cm)	3.6×10^5	
Ionic conductivity (E_{ei}) (J/mol)	80.0×10^3	

^f Fitted parameters

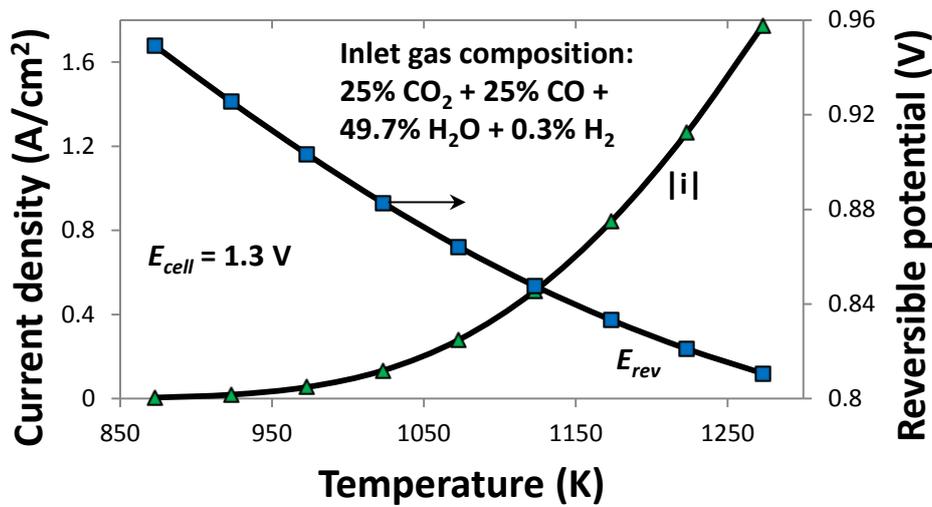


Figure 5.5: Effect of temperature on SOEC electrochemical characteristics.

5.2.3 Effect of micro-structural properties on the SOEC

The effect of micro-structural parameters on the performance of SOECs and species transport dispersion in the electrode are discussed in this section. Fig. 5.6 depicts the impact of pore size on the system. It can be noted that the current density obtained at a specified voltage increases with an increase in pore diameter. This is due to the direct dependence of the Knudsen diffusion coefficient (Eq. 2.80) and permeability (Eq. 2.79) on the pore size associated with the porous media. An increase in pore diameter enhances the Knudsen diffusion coefficient, thus making it easier for the reactants to diffuse in to the TPB. The permeability also increases with pore size. This decreases transport limitations within the electrode and enhances the net current density output. Simulations are performed by varying only the required fuel electrode/cathode micro-structural properties. The species composition is shown for $E_{cell} = 1.3$ V.

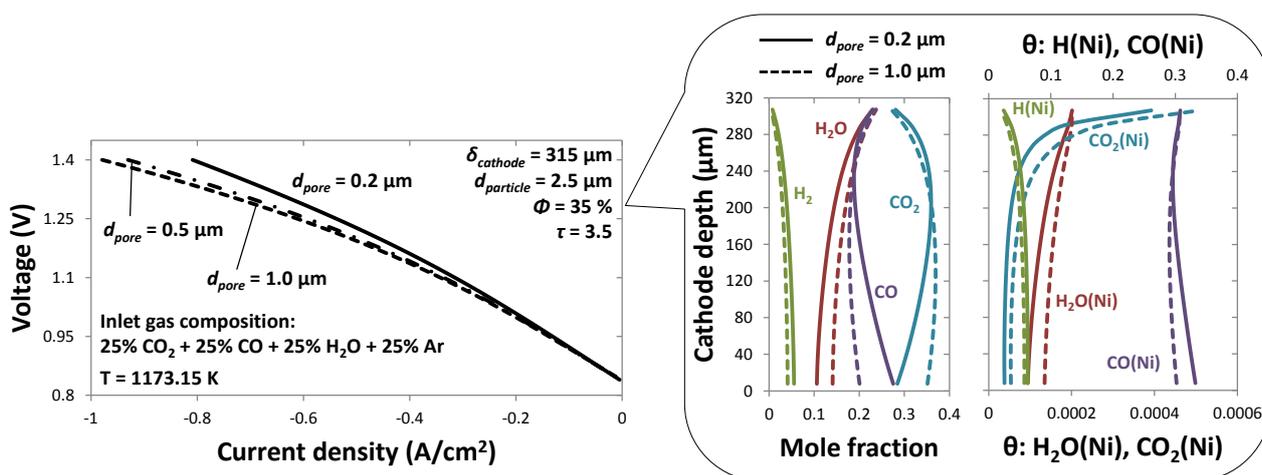


Figure 5.6: Effect of pore diameter on SOEC V-I characteristics and species distribution in the cathode.

Fig. 5.7 illustrates the impact of porosity on cell characteristics. Inevitably, the current density obtained at a specified voltage increases with an increase in porosity. This is because the concentration overpotential decreases, which facilitates species transport via increase in diffusion and permeability. Thus, there is decreased resistance to reactant transport. It can be seen that there are larger concentrations of electrochemical reactants at the TPB for $\phi = 50$ %, while the concentrations of products at the TPB are larger for $\phi = 20$ %. Thus, there is a trade-off between product build-up at the TPB and the steady supply of fresh reactants through the diffusion pathway, in determining optimum porosity for electrode materials. The surface coverage of electrochemical products is much higher than the surface coverage of reactants due to higher activation energies required for desorp-

tion. Similarly, one can predict the impact of tortuosity on cell V-I characteristics and electrode species distribution. An increase in tortuosity decreases the attainable current density at a specified voltage. This is because the reactants are required to travel through a longer tortuous path to reach the TPB, hence lowering the Knudsen diffusion coefficient and permeability. Thus, one can expect larger electrochemical product concentrations at the TPB for $\tau = 8.0$ as opposed to larger electrochemical reactant concentrations at the TPB for $\tau = 2.0$. Hence, replenishing the TPB with reactants turns harder with increasing tortuosities.

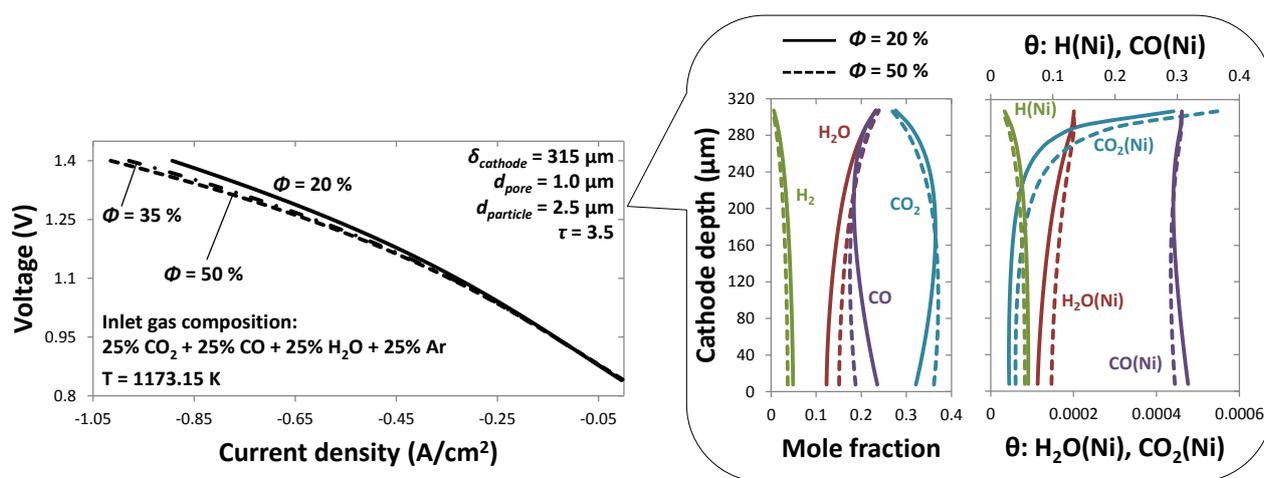


Figure 5.7: Effect of porosity on SOEC V-I characteristics and species distribution in the cathode.

5.3 1-D + 1-D co-flow planar SOEC

5.3.1 Effect of temperature and electrode thickness on the exit gas composition

Figure 5.8 demonstrates the impact of cathode thickness on the outlet gas composition of its corresponding channel. The inlet gas composition at the fuel channel is 25% H_2O : 25% CO_2 : 25% CO : 25% Ar , where as air is fed to the anode. It can be observed that the mole fraction of H_2 reaches a maximum at $\sim 200 \mu\text{m}$, while that of CO is highest at $\sim 20 \mu\text{m}$. This is due to the interplay between the electrochemical reactions at the fuel electrode TPB (utilization region), internal reforming (heterogeneous chemistry) zone and transport limitations within the porous electrode. Thinner cathodes result in an overlap between the electrochemical zone and the internal reforming zone, wherein the latter zone is limited by presence of shorter diffusion pathways to the former zone. The initial increase in H_2 mole fraction for thinner cathodes ($< \sim 200 \mu\text{m}$) is due to the presence of short diffusion pathways for H_2O to migrate to the electrochemical reaction zone. The mole fraction of CO still

decreases due to slower diffusion of heavier CO_2 and lower possibility for the RWGS reaction to occur. As the cathode thickness increases ($> \sim 200 \mu\text{m}$), the mole fractions of H_2 and CO decrease due to transport limitations leading to higher concentration overpotentials, despite the electrochemical zone having negligible influence on the steady-state species concentrations in the internal reforming zone. The concentration of CH_4 increases slightly with an increase in cathode thickness due to higher carbon coverage $C_{(\text{Ni})}$ within the porous electrode, close to the TPB, owing to a highly reducing atmosphere.

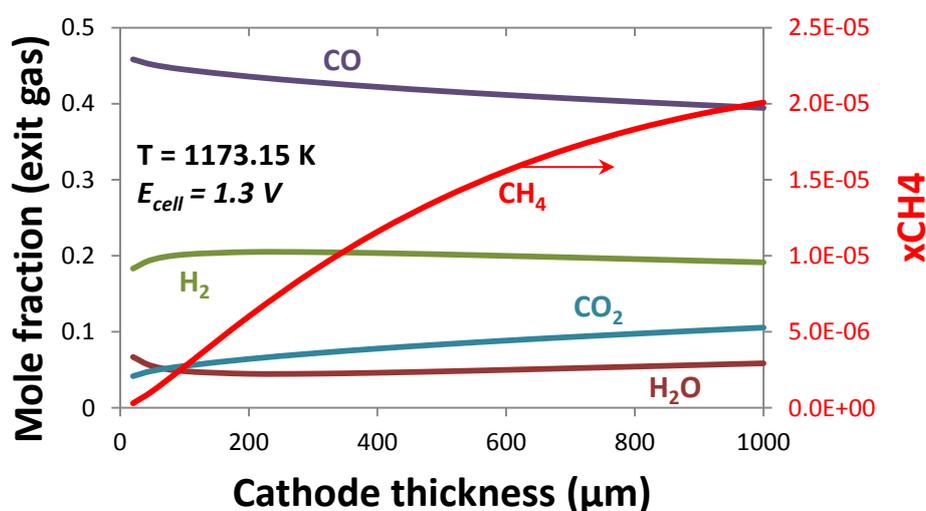


Figure 5.8: Dependence of cathode exit gas composition on its corresponding electrode thickness. Inlet cathode gas composition: 25% H_2O : 25% CO_2 : 25% CO : 25% Ar.

Figure 5.9 describes the influence of temperature on the exit gas composition obtained in the cathode channel. The general trend encompasses a decrease in the mole fraction of reactants, alongside an increase in that of products, with an increase in temperature. The electrochemical reaction rates are enhanced due to a reduction in irreversible losses, which lead to the attainment of higher current densities. The mole fraction of CO is greater than that of H_2 due to the contribution of both electrolysis and the RWGS reaction. Also, it is important to note that the input gas contains more carbon ($\text{CO} + \text{CO}_2$) than hydrogen atoms. On closer observation, one can notice an increase in H_2O mole fraction, and a decrease in H_2 mole fraction, for temperatures between ~ 873.15 and ~ 1050 K. This is due to the equilibrium between the WGS and RWGS reaction that is attained above ~ 873.15 K on Ni catalysts. The mole fraction of CH_4 decreases from ~ 873.15 to 1073.15 K, and then increases from ~ 1073.15 to 1273.15 K, though it is quite small. At lower temperatures, the Boudouard reaction along with the hydrogenation of elemental carbon $C_{(\text{Ni})}$ is favored. A highly reducing atmos-

phere contributes to CH₄ formation at higher temperatures, due to the presence of large concentrations of CO and H₂ [120].

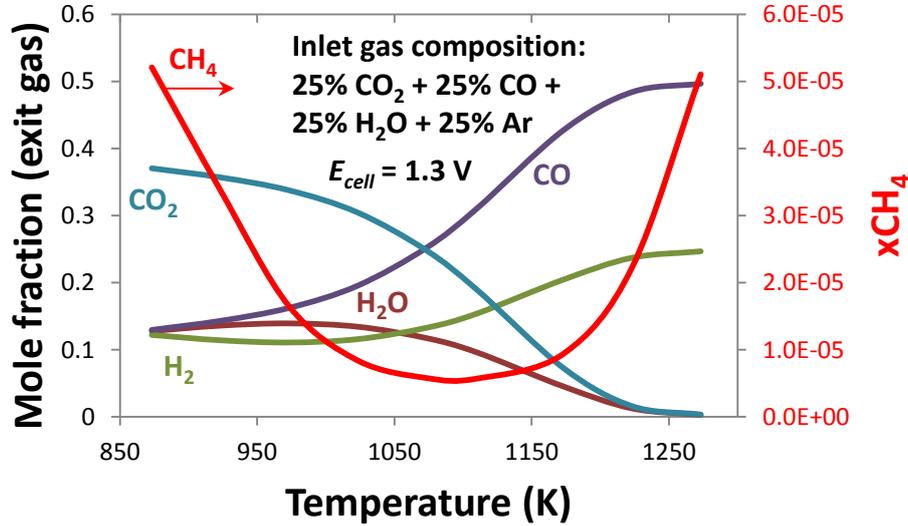


Figure 5.9: Dependence of cathode exit gas composition on temperature.

5.3.2 Effect of inlet gas velocity on the exit gas composition

Figure 5.10a explains the impact of inlet gas velocity, in the cathode channel, on SOEC performance parameters. The reactant utilization factor η_{R-U} is given by

$$\eta_{R-U} = 100 \times \left[1 - \frac{(\dot{n}_{H_2O} + \dot{n}_{CO_2})_{outlet}}{(\dot{n}_{H_2O} + \dot{n}_{CO_2})_{inlet}} \right] \quad (5.3)$$

The oxygen production factor η_{O-P} is defined as

$$\eta_{O-P} = 100 \times \left[\frac{(Y_{O_2})_{outlet}}{(Y_{O_2})_{inlet}} - 1 \right] \quad (5.4)$$

The reactant utilization factor decreases, while the oxygen production factor increases, with an increase in cathode inlet gas velocity. Thus, the amount of reactant available at the TPB increases, although the electrochemical reaction rate at a given voltage limits the amount of reactant that can be converted. This decreases the reversible cell potential (Eq. 5.2), which translates to the attainment of a higher normalized current density. As the electrochemical fluxes are directly proportional

to current density, higher concentrations of oxygen are obtained at the exit of the air channel. The variation in axial gas concentrations as a function of cathode inlet gas velocity can be seen in Fig. 5.10b. High inlet velocities lead to reactant wastage. Hence, a trade-off between syngas production rates and reactant utilization factors is necessary to avoid performance penalties and degradation.

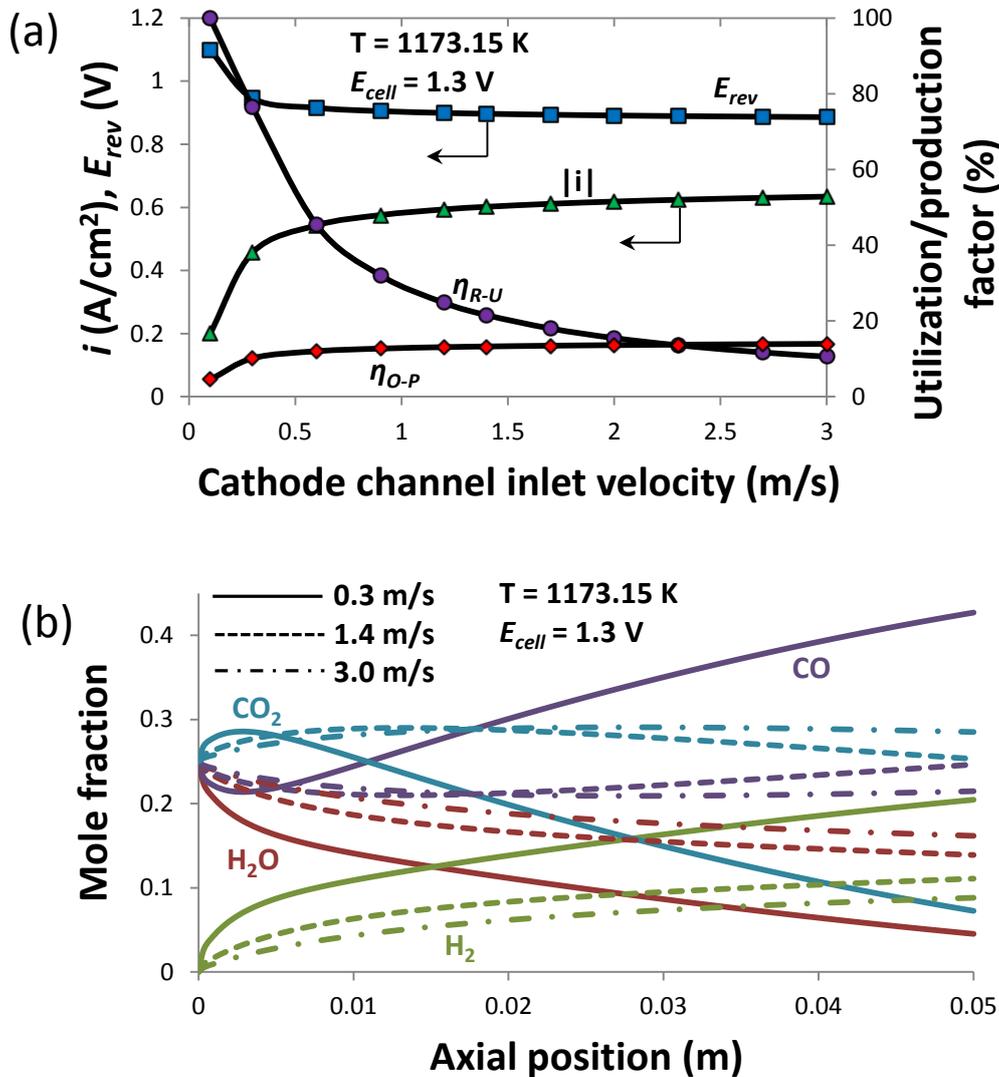


Figure 5.10: Influence of cathode inlet gas velocity on: (a) SOEC process parameters, and (b) the axial species composition in the cathode channel.

5.3.3 Type of electrolysis vs. species composition in the cathode and fuel channel

The effect of H_2O electrolysis (CO_2 electrolysis pathway is turned off) coupled with detailed chemistry, and $\text{H}_2\text{O}/\text{CO}_2$ co-electrolysis coupled with detailed chemistry, on the profiles of gas and surface species within the cathode and its corresponding channel are depicted in Fig. 5.11. The operat-

ing temperature and voltage are 1173.15 K and 1.3 V, respectively. The concentrations of products increase, while that of reactants decrease, as one moves towards the exit of the gas channel. The reactant utilization and syngas production rate are higher during co-electrolysis, which translates to similar trends within the cathode. The gas concentrations and surface coverages of relevant species are also illustrated at two positions - 0.5 and 4.5 cm from the inlet. The mole fraction of CH₄, although negligible, is higher during co-electrolysis as compared to the case involving only H₂O electrolysis. This can be attributed to higher carbon coverage C_(Ni) within the porous electrode, which increases in magnitude with increase in axial distance. Adsorbates - H_(Ni) and CO_(Ni) form the major species in the cathode, and decide the concentration of the uncovered Ni surface. Reaction flow analysis is performed, at OCV, to study methane production characteristics and kinetics during co-electrolysis.

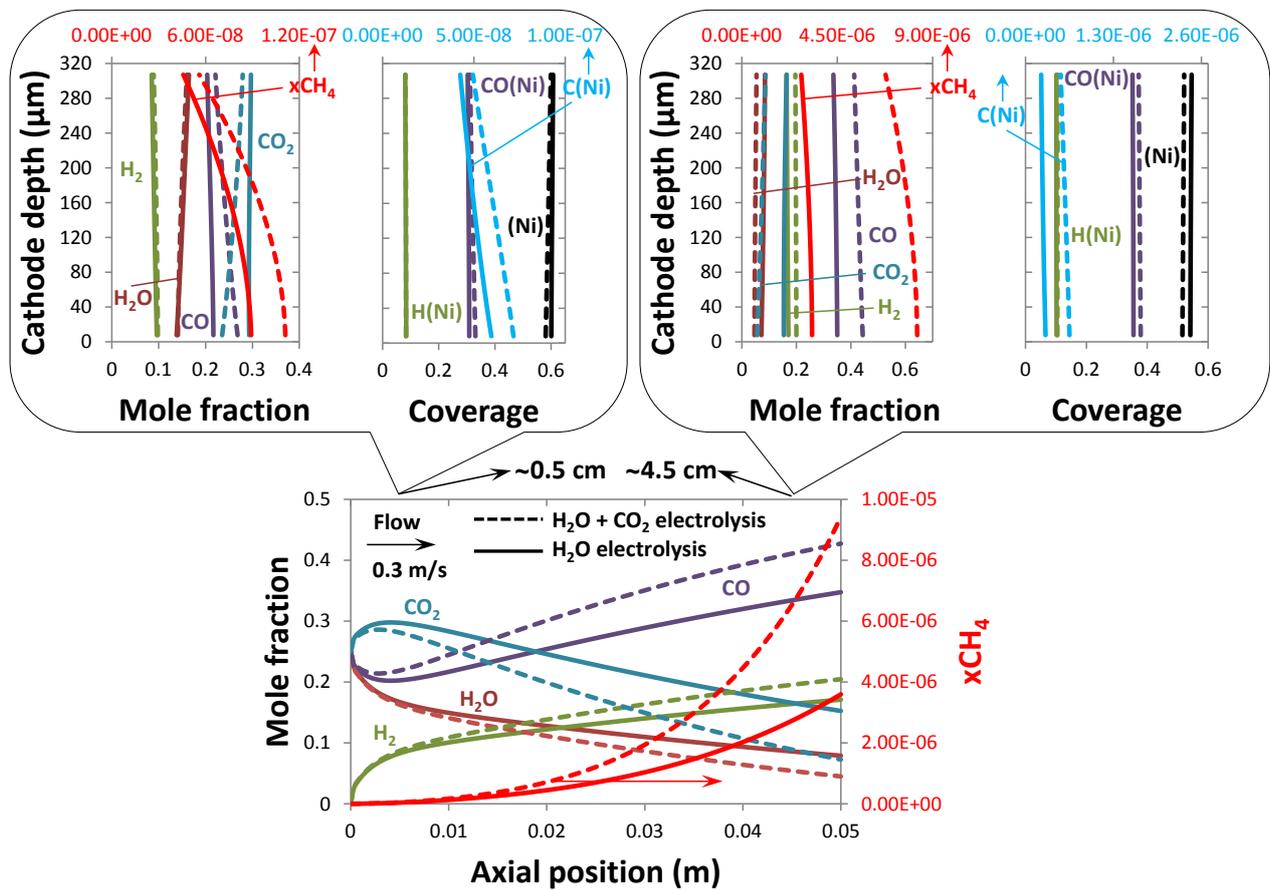


Figure 5.11: Importance of the type of electrolysis on species composition in the cathode and its corresponding channel. Inlet gas composition: 25% H₂O: 25% CO₂: 25% CO: 25% Ar.

5.4 Possible methane production reaction pathways

In this section, we study the kinetics of methane production and factors affecting it. There is existent speculation in literature about formation pathways and experimental data pertaining to the methanation process. In this study, we do not develop an additional model or mechanism, but perform reaction flow analysis and simulations using the surface reaction mechanism listed in the Appendix. A 0-D batch reactor model is used for the aforementioned analysis, whose equations and modeling approach are elucidated in Ref. [90]. The reactor is considered to operate at OCV, and does not account for electrochemistry. The input parameters for all simulations are Volume $V = 50 \text{ mm}^3$, $T = 923.15 \text{ K}$, $p = 1 \text{ bar}$ and $A_{\text{cat}} = 28.25 \times 10^{-04} \text{ m}^2$.

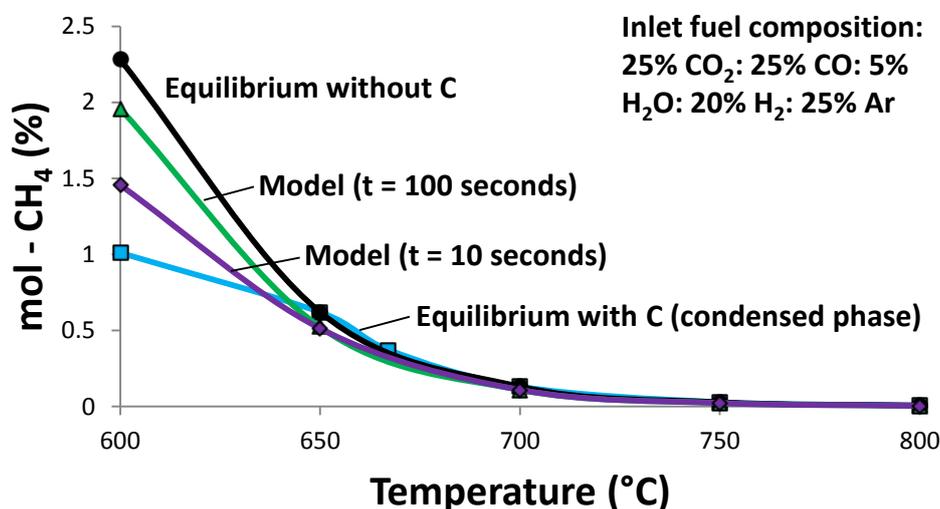


Figure 5.12: Effect of temperature on the composition of methane determined by equilibrium calculations and kinetics described by the surface reaction mechanism (fuel-B in Table 5.4).

Table 5.4: Fuel compositions considered for batch reactor model simulations

Fuel	xH ₂ %	xH ₂ O %	xCO %	xCO ₂ %	xAr %
A	40	-	40	5	15
B	20	5	25	25	25
C	20	25	25	25	5
D	40	-	25	25	10
E	40	-	5	40	15

Figure 5.12 portrays a comparison between the effect of temperature on the equilibrium composition of methane and on the kinetics described by the surface reaction mechanism. The equilibrium composition without elemental carbon results in much higher CH_4 mole fraction as compared to the batch model and the simulation considering equilibrium composition with elemental carbon. At low temperatures, the model predictions are close to equilibrium calculations without surface carbon, while at high temperatures, the model predictions are close to equilibrium calculations with surface carbon. The model profiles at two different times indicate compositions before and after steady-state. After ~ 35 seconds, steady-state concentration is reached. It is now established that the model is capable of capturing trends in CH_4 formation, although one requires improvement in the carbon model for accurate predictions. The equilibrium calculations are performed using the commercial software - HSC Chemistry v5.1, while the batch model runs on the module - DETCHEM^{BATCH} [90].

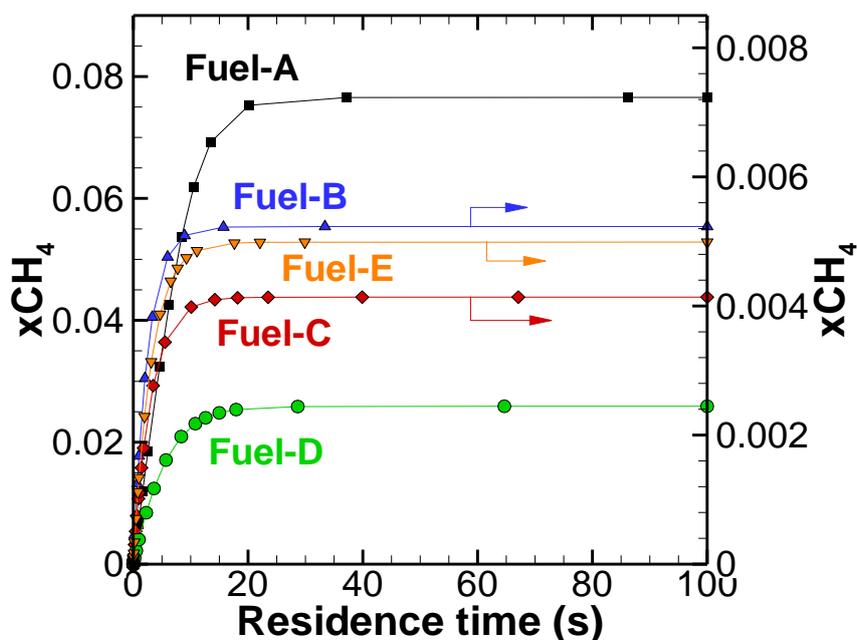


Figure 5.13: The variation of CH_4 mole fraction with residence time for various fuel compositions described in Table 5.4.

In Figure 5.13, one can notice the variation in CH_4 mole fraction as a function of residence time for various fuel compositions listed in Table 5.4. It can be observed that an increase in the amount of H_2O inhibits the formation of CH_4 . Adsorbed $\text{H}_2\text{O}_{(\text{Ni})}$ decomposes to $\text{H}_{(\text{Ni})}$ and $\text{OH}_{(\text{Ni})}$ via reaction R32 in the Appendix. The adsorbate $\text{OH}_{(\text{Ni})}$ further dissociates to $\text{H}_{(\text{Ni})}$ and $\text{O}_{(\text{Ni})}$. From the results of the reaction flow analysis, it is seen that a greater fraction of adsorbed carbon $\text{C}_{(\text{Ni})}$ is oxidized by $\text{O}_{(\text{Ni})}$ via reaction R35 and is a few orders of magnitude ($\sim 10^4$) higher than the contribution of reac-

tion R28 in the Appendix. An increase in CO_2 input concentration does not favor CH_4 production, as it demotes the formation of elemental carbon $\text{C}_{(\text{Ni})}$. The highest amount of CH_4 is obtained for fuel-A, which has the largest inlet concentration of H_2 and CO . Consequently, hydrogenation of $\text{C}_{(\text{Ni})}$ is strongly feasible in this case.

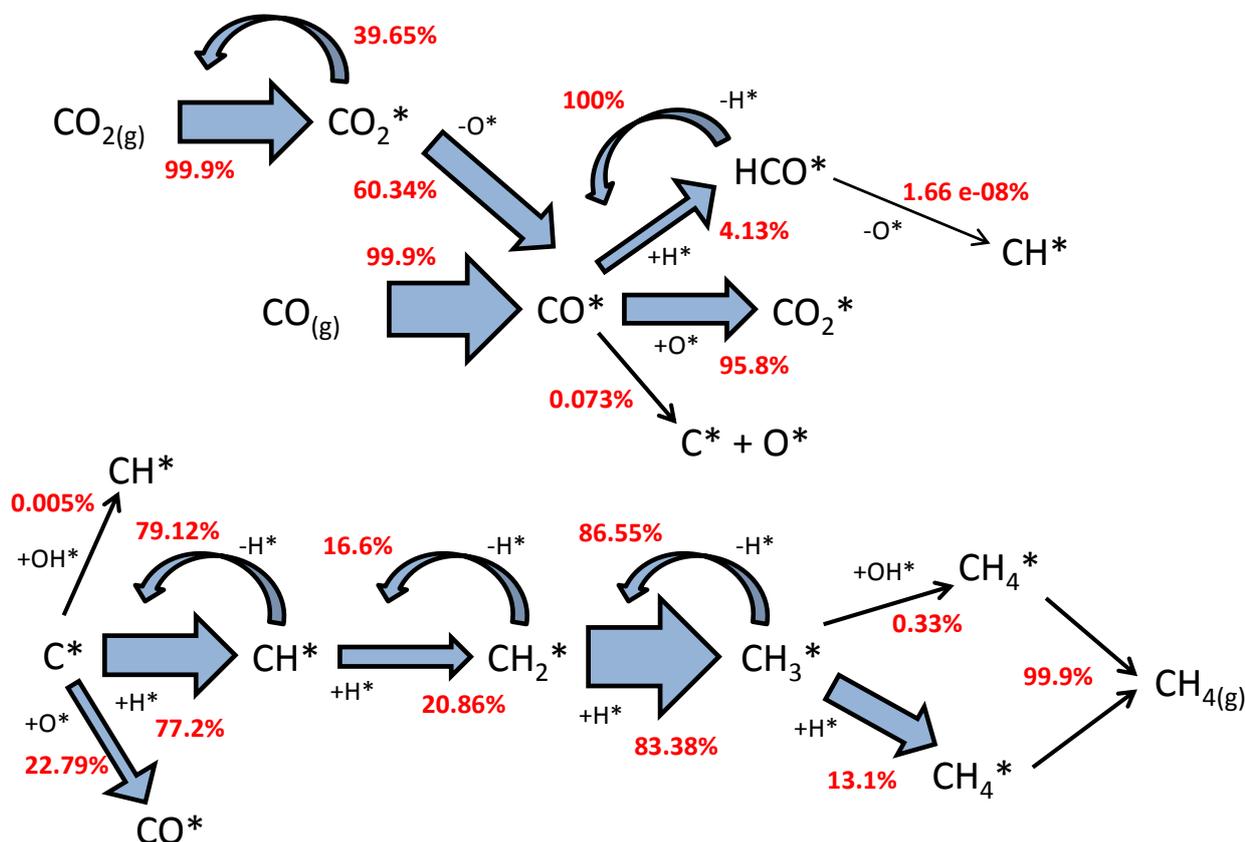


Figure 5.14: Reaction flow analysis diagram indicating species consumption/production for fuel - B in Table 5.4.

Furthermore, reaction flow analysis is carried out, for fuel-A and fuel-B in Table 5.4, to clearly understand the contribution of participating gas and surface species towards methane formation. In Fig. 5.14, the numbers beside the arrows indicate the amount of species converted. The desorption of adsorbate $\text{CO}_{(\text{Ni})}$ to gaseous CO is not considered so as to get the absolute scale of its contribution towards $\text{HCO}_{(\text{Ni})}$, $\text{CO}_{2(\text{Ni})}$ and $\text{C}_{(\text{Ni})}$ formation. In this case, the inlet fuel composition is 25% CO_2 : 5% H_2O : 20% H_2 : 25% CO : 25% Ar (fuel-B) and the residence time is 1.0 second. The majority of the adsorbate $\text{CO}_{(\text{Ni})}$ comes from the dissociation of $\text{CO}_{2(\text{Ni})}$ and adsorption of CO . The adsorbed $\text{CO}_{(\text{Ni})}$ then splits into adsorbates - $\text{HCO}_{(\text{Ni})}$, $\text{CO}_{2(\text{Ni})}$ and $\text{C}_{(\text{Ni})}$ through surface reactions. The adsorbate $\text{HCO}_{(\text{Ni})}$ has negligible contribution towards $\text{CH}_{(\text{Ni})}$ formation and is the unlikely path towards CH_4 formation. On the other hand, the surface carbon $\text{C}_{(\text{Ni})}$ undergoes hydrogenation,

through reaction R20 in the Appendix, to form $\text{CH}_{(\text{Ni})}$. This adsorbate $\text{CH}_{(\text{Ni})}$ reacts with $\text{H}_{(\text{Ni})}$ to form $\text{CH}_{2(\text{Ni})}$, which further reacts in the same manner to form $\text{CH}_{3(\text{Ni})}$ and then $\text{CH}_{4(\text{Ni})}$ through reactions R18, R16 and R14, respectively. Almost all of the adsorbed $\text{CH}_{4(\text{Ni})}$ desorbs to form CH_4 gas. This appears to be the more likely pathway leading to CH_4 formation.

In Figure 5.15, the same analysis is performed for an inlet fuel composition of 5% CO_2 : 40% H_2 : 40% CO : 15% Ar (fuel-A), while the residence time is 1.0 second. Here, one can notice a higher fraction of adsorbate $\text{CO}_{(\text{Ni})}$ dissociating to surface carbon $\text{C}_{(\text{Ni})}$ and adsorbed oxygen $\text{O}_{(\text{Ni})}$, thereby resulting in a higher mole fraction of CH_4 . Simulations performed with other fuel compositions in Table 5.4 also yield the same trend, even at higher residence times. In addition, the methanation process is also affected by the extent of pretreatment of the Ni catalyst by the oxidation and reduction process [121]. It was found that the NiO in the pretreated catalyst acted as a promoter and weakened the C–O bond to produce surface carbon that was easily hydrogenated, which led to the formation of more methane. Nevertheless, this study can be considered as a preliminary step towards understanding the complex methane production kinetics in a SOC system.

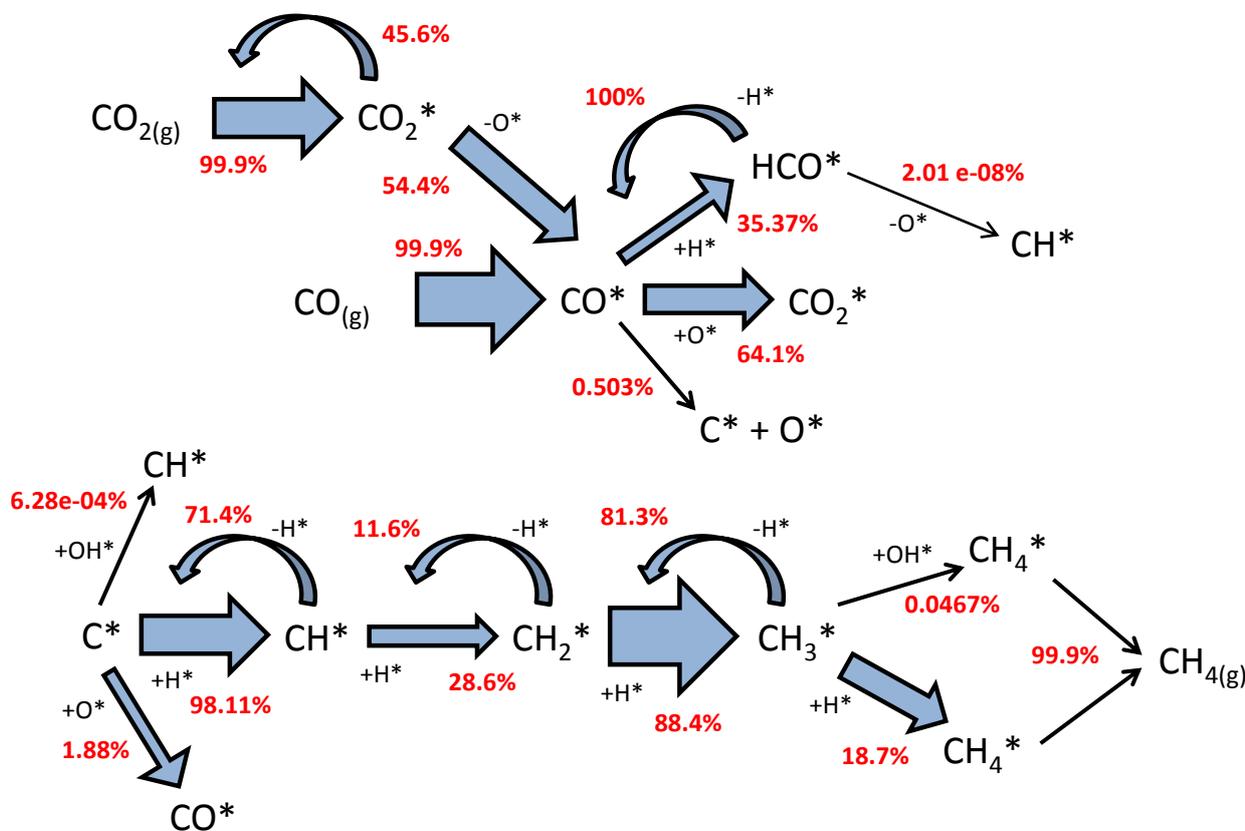


Figure 5.15: Reaction flow analysis diagram indicating species consumption/production for fuel - A in Table 5.4.

5.5 Summary

The analysis of high temperature co-electrolysis of H_2O and CO_2 , for syngas production, in a SOEC has been carried out using a 1-D electrochemical model and a 1-D + 1-D detailed model. The model is validated with experimental data from two sources. The electrochemical parameters determined from the experiments performed at EIFER are used for additional parametric analysis. A number of output parameters such as syngas production rate, current density, reversible cell potential and efficiency depend strongly on temperature. Micro-structural properties such as tortuosity, porosity and pore diameter tend to affect the SOEC electrochemical characteristics by controlling mass transport within the porous electrode, which in turn affects the concentration overpotentials of the system. High tortuosity, low porosity and low pore diameter result in product buildup at the TPB, denying facilitation for reactant replenishment via the diffusion pathway. Furthermore, the cathode inlet gas flow rate is found to have a significant impact on the operating SOEC current density and channel gas composition due to reactant dilution effects. Therefore, it is important to optimize inlet gas flow rates to minimize depletion, bearing in mind the trade-off with fuel utilization. It was found that the co-electrolysis process produced higher amounts of methane in the gas channel as opposed to the simulation that considered electrolysis of only H_2O with the CO_2 electrolysis pathway turned off at the TPB, for the specified inlet fuel composition, due to the production of higher amounts of reducing H_2 and CO in the system. Also, the former resulted in higher reactant utilization rates. Logical analysis using the surface reaction mechanism was carried out using a batch reactor model to study methane formation characteristics in the system at OCV. Through reaction flow analysis, it was established that reaction R20 in the Appendix (hydrogenation of surface carbon $\text{C}_{(\text{Ni})}$) was the more likely pathway towards CH_4 formation. Further work would involve investigation into the underlying charge transfer mechanisms of a SOEC during co-electrolysis, and methods to make the model more robust via reaction mechanism improvement, carbon model development, energy balance employment and implementation of an elementary approach for analyzing charge transfer kinetics instead of the conventional B-V approach. Nonetheless, the described model can be viewed as an initial approach towards clearly understanding the dynamics of a SOEC system.

Chapter 6 Investigating mass and heat transport in proton-conducting SOFCs

¹Fuel cells deliver an efficient approach for energy conversion via usage of chemical energy. Unlike low temperature fuel cells, high temperature SOFCs have enhanced kinetics and reduced resistivity of the solid electrolyte. Additionally, high temperatures also facilitate the usage of cheaper catalysts that allow direct internal reforming within the cell [45]. Direct internal reforming reduces system complexity and cost (lack of need for an external reforming unit) and promotes intrinsic thermal-coupling between endothermic and exothermic reactions within the cell. This coupling results in enhanced system efficiencies due to a shift in the reforming reaction towards hydrogen production for oxide-ion-conducting SOFCs, as steam is also produced via electrochemical reactions in the anode side. Furthermore, the produced carbon monoxide enables added hydrogen production via the water-gas shift reaction. However, some of the disadvantages of internal reforming over Ni/YSZ anodes include coking that leads to catalyst deactivation, and large thermal gradients that cause thermal mismatch/stress due to variable expansion rates of different materials [122, 123]. In the former case, carbon deposition/removal occurs through the disproportionation of carbon monoxide (Boudouard reaction), cracking of methane and oxidation of carbon, as listed in Table 2.3 [124].

The interplay of physico-chemical phenomena in SOFCs is complex. Modeling the system requires immense understanding of the coupled interactions at work. Traditional SOFCs employ an oxide-ion-conducting electrolyte, such as yttria-stabilized zirconia (YSZ), which facilitates the electrochemical production of H_2O at the anode three-phase boundary (TPB). There is a great deal of literature available on the modeling of these systems, ranging from simple 0-D electrochemical cells to quasi-2-D unit cells to complex 3-D stacks [125-127]. Oxide-ion-conducting SOFCs can also be operated in “reverse” mode at high temperatures as solid oxide electrolysis cells (SOECs) for the production of H_2 or H_2/CO by means of H_2O electrolysis or H_2O/CO_2 co-electrolysis, respectively [62, 79, 128]. Operation of SOFCs with proton-conducting electrolytes, such as $BaCeO_3$ -based ceramics, have emerged as systems that provide higher theoretical energy efficiencies than its oxide-

¹ Parts of this chapter are taken from Menon et al. [75].

ion-conducting counterpart due to higher average EMF under the same conditions [129, 130]. Here, the electrochemical production of H_2O occurs at the cathode three-phase boundary (TPB), which helps in exclusive utilization of H_2 in the fuel channel. Thus, unless the system is run with fuels other than pure hydrogen, the problem of gas separation at the exit of the fuel channel can be avoided. Also, direct recycling of the anode tail-gas to the inlet is possible.

The basic principle of a proton-conducting SOFC is the same as that of an oxide-ion-conducting SOFC, except for the type of ion conducted by the electrolyte. The representation of the planar SOFC under consideration, in this study, is shown in Fig. 6.1. Here, the anode is the fuel electrode and the cathode is the oxidant electrode.

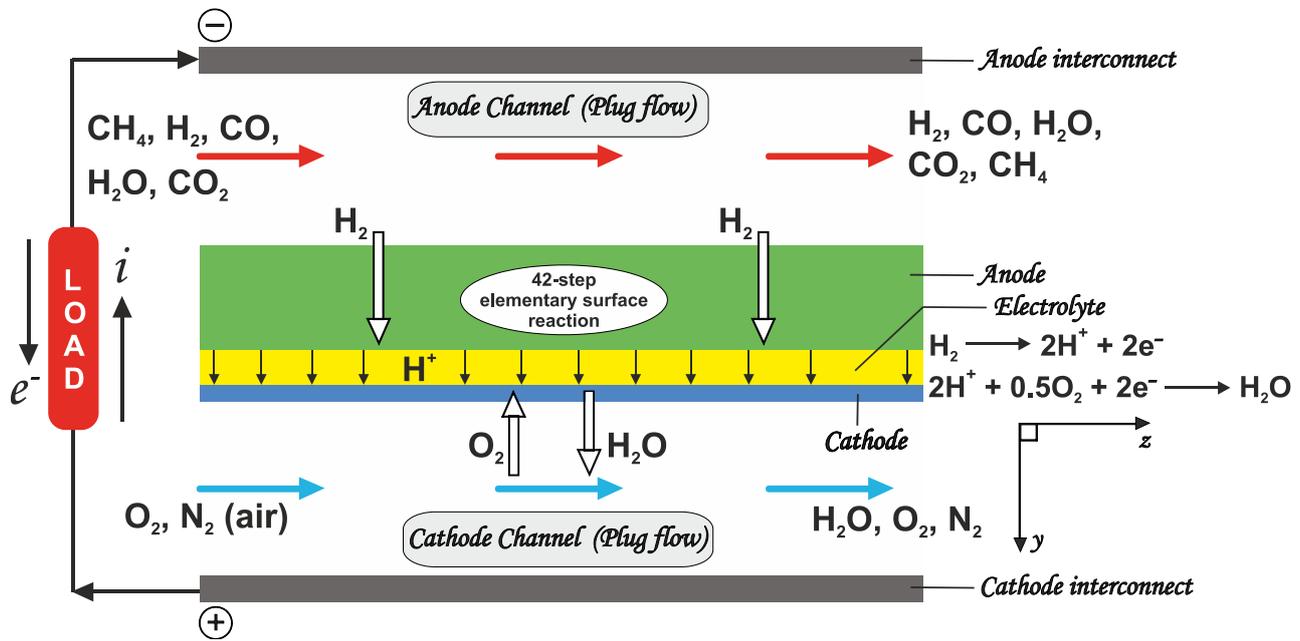


Figure 6.1: Schematic representation of a planar co-flow proton-conducting Solid Oxide Fuel Cell (SOFC).

In this chapter, the numerical model that accounts for coupled interactions between fluid flow, mass transport, heterogeneous chemistry, porous media transport, energy transport and electro-chemistry is applied to understand proton-conducting SOFCs. The detailed electrochemical model, comprising of non-linear B-V equations, is validated with two sets of experimental data [32, 34]. A modified B-V equation is derived to represent charge transfer at the anode/electrolyte interface, while a global B-V equation is used at the electrolyte/cathode interface. In addition, the estimated electrochemical parameters are employed in a quasi-2-D planar cell model for parametric analysis. The dependence of temperature distribution on cell voltage, cell length, specific catalytic area of the anode, and an-

ode zoning is illustrated. This analysis is also extended to investigate species transport within the whole cell. The main focus of this chapter is to provide a base model for future proton-conducting SOFC models employing fuels other than hydrogen and methane-based compositions.

6.1 Model validation and parametric analysis

A comparison between the simulated polarization curves and the first set of experimental data obtained from Ref. [32] is depicted in Fig. 6.2. In the experiments, the electrochemical characteristics of a single SOFC with a dense Sm-doped BaCeO₃ electrolyte (BaCe_{0.8}Sm_{0.2}O_{2.90} - BCSO) was studied. The anode and cathode were made of porous NiO-BCSO and Ba_{0.5}Sr_{0.5}Co_{0.8}Fe_{0.2}O₃-BCSO (BSCF-BCSO), respectively. Conductivities of BCSO at 773.15 K, 873.15 K and 973.15 K were 0.416 S/m, 0.662 S/m and 0.936 S/m, respectively. The cell was operated with humidified hydrogen (~3% H₂O) as fuel and pure oxygen as oxidant. Button cell simulations are used to reproduce experimental data and derive the electrochemical fit parameters, which are the pre-exponential factors and activation energies. At low current densities, the non-linearity of the V-I curves increases with decreasing temperature due to the dominance of activation losses. The model is in good agreement with experiments. The values of thicknesses of the electrodes and electrolyte, along with cell properties used in model validation are listed in Table 6.1. The electrochemical parameters used for reproducing the experimental data are shown in Table 6.2.

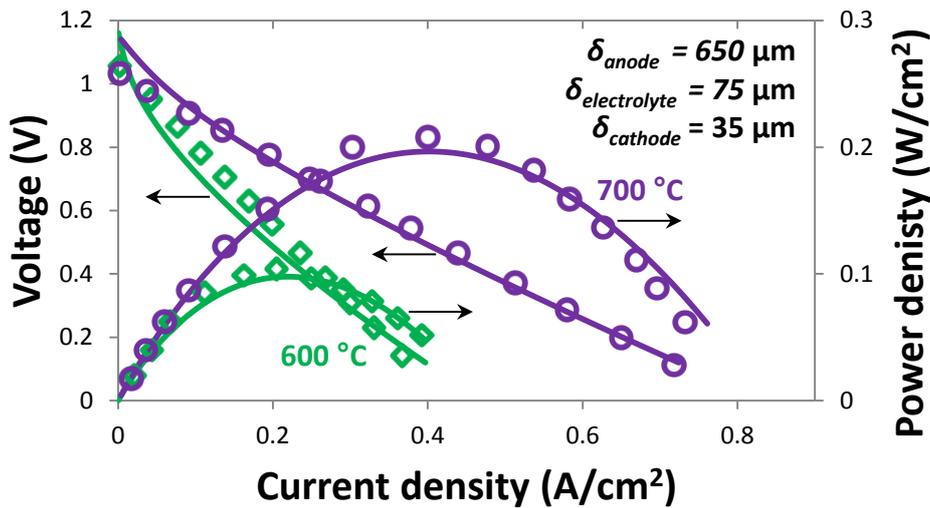


Figure 6.2: Model validation with experimental data obtained from Ref. [32].

The model is also validated with a second set of experiments from Ref. [34]. The anode, electrolyte and cathode were composed of Ni-BCY10, yttrium-doped barium cerate (BCY10 -

BaCe_{0.9}Y_{0.1}O_{2.95}) and Pr₂NiO_{4+δ}, respectively. The materials were chosen because of their good electrochemical and morphological properties, although electrode-electrolyte interfaces suffered from delamination post-operation. Ohmic resistances of the cell at 823.15 K, 873.15 K and 923.15 K were 2.38 Ω-cm², 1.84 Ω-cm² and 1.36 Ω-cm², respectively. The model is able to reproduce the experiments well, as shown in Fig. 6.3. The validated electrochemical model parameters are described in Table 6.3. The pre-exponential factors in Tables 6.2 and 6.3 are used as fit parameters, while the activation energies are taken from Ref. [131]. It is important to note that the microstructural properties are assumed to be within a realistic range for modern day cells.

Table 6.1: Cell parameters and properties used for model validation/analysis

Parameter	Model Validation [32]	Model Validation [34]	Parametric analysis (base case)
Gas channels (planar)			
Length (cm)	-	-	5, 7.5
Height (mm)	-	-	1
Width (mm)	-	-	1
Air inlet velocity (m/s)	-	-	2.5
Fuel inlet velocity (m/s)	-	-	0.3
Anode			
Thickness (μm)	650	850	500
Porosity (%)	35	35	35
Tortuosity	3.8	3.8	3.8
Particle diameter (μm)	2.5	2.5	2.5
Pore diameter (μm)	1.0	1.0	1.0
Specific area (m ⁻¹)	1.025×10 ⁵	1.025×10 ⁵	1.025×10 ⁵
Electrolyte			
Thickness (μm)	75	85	25
Cathode			
Thickness (μm)	35	50	30
Porosity (%)	35	35	35
Tortuosity	3.8	3.8	3.8
Particle diameter (μm)	2.5	2.5	2.5
Pore diameter (μm)	1.0	1.0	1.0
Specific area (m ⁻¹)	1.025×10 ⁵	1.025×10 ⁵	1.025×10 ⁵
Operating conditions			
Pressure (bar)	1.0	1.0	1.0
Temperature (°C)	600, 700	550, 600, 650	650 (air channel), 800 (fuel channel)
Inlet gas composition			
Fuel channel	3% H ₂ O + 97% H ₂	3% H ₂ O + 97% H ₂	20.37% CH ₄ + 32.2 % H ₂ + 13.67% CO + 0.87% CO ₂ + 32.89% H ₂ O
Air channel	3% H ₂ O + 97% O ₂	3% H ₂ O + 21% O ₂ + 76% N ₂	3% H ₂ O + 21% O ₂ + 76% N ₂
Thermal properties [45]			
λ _{anode}	-	-	1.86
λ _{electrolyte}	-	-	2.16
λ _{cathode}	-	-	5.84
C _{ps}	-	-	3515.75
ρ _s	-	-	452.63

Table 6.2: Electrochemical model/input parameters (Fig. 6.2)

Anode asymmetry factor (β_a)	0.5
Cathode asymmetry factor (β_c)	0.5
Exchange current density parameters	
Pre-exponential for H ₂ oxidation (k_{H_2}) (A/cm ²)	174919.71 ^f
Pre-exponential for O ₂ reduction (k_{O_2}) (A/cm ²)	58016.6 ^f
Activation energy for H ₂ oxidation (E_{H_2}) (J/mol)	100.0 × 10 ³
Activation energy for O ₂ reduction (E_{O_2}) (J/mol)	120.0 × 10 ³
Ionic conductivity (σ_0) (S/m)	339.34 × 10 ²
Ionic conductivity (E_{el}) (J/mol)	29.5 × 10 ³

^f Fitted with experimental data

Table 6.3: Electrochemical model/input parameters (Fig. 6.3)

Anode asymmetry factor (β_a)	0.5
Cathode asymmetry factor (β_c)	0.5
Exchange current density parameters	
Pre-exponential for H ₂ oxidation (k_{H_2}) (A/cm ²)	288176.65 ^f
Pre-exponential for O ₂ reduction (k_{O_2}) (A/cm ²)	528582.88 ^f
Activation energy for H ₂ oxidation (E_{H_2}) (J/mol)	100 × 10 ³
Activation energy for O ₂ reduction (E_{O_2}) (J/mol)	120 × 10 ³

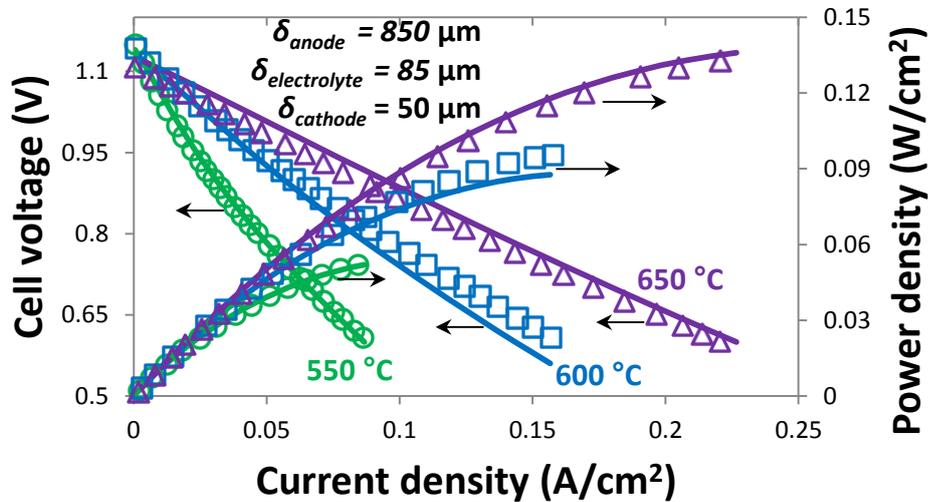
^f Fitted with experimental data

Figure 6.3: Model validation with experimental data obtained from Ref. [34].

In order to understand the multi-physics in a methane-fed proton conducting SOFC, simulations are carried out using the electrochemical model parameters listed in Table 6.2. All other relevant information for the parametric analysis is given in Table 6.1. The fuel is assumed to enter the fuel channel at 1073.15 K and 0.3 m/s, while air enters the air channel at 923.15 K and 2.5 m/s. These conditions represent the base case. Fig. 6.4 shows the temperature profiles of the fuel channel, solid (MEA) and the air channel, at $t \rightarrow 500$ s (steady-state distribution). The temperature profiles result

from the combination of heterogeneous chemical reactions in the anode, heat transfer between the channels and the solid, exothermic electrochemical reactions at the TPB, and ohmic heat produced by the resistances of the MEA materials. Close to the inlet section, the temperature in the fuel channel drops due to heat lost to the air channel, as air enters at lower temperature. This leads to a rise in temperature in the air channel. As one moves towards the exit of the gas channels, the temperature starts to increase due to heat released within the MEA. At steady-state, the temperatures in the gas channels approach the temperature of the solid. The multi-physics phenomena affecting temperature profiles in the cell will be discussed hereafter.

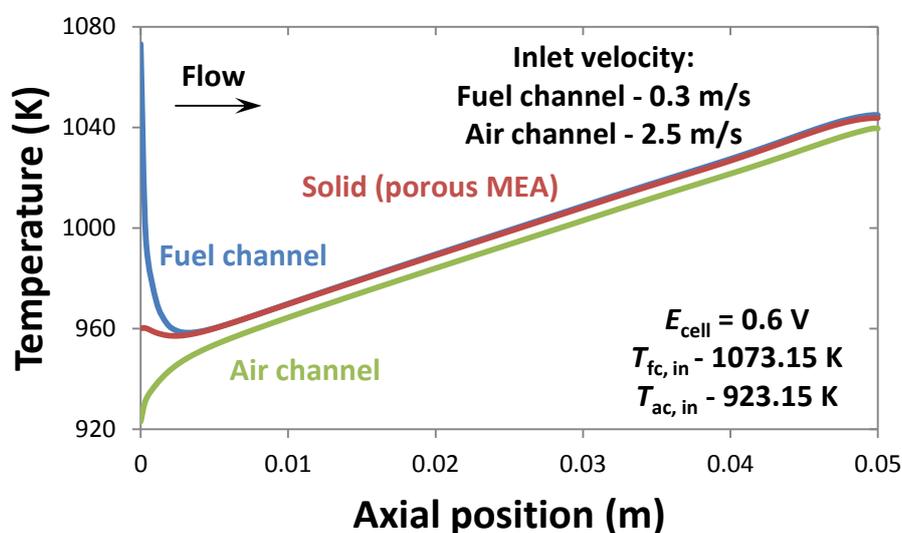


Figure 6.4: Temperature profiles within the fuel channel, air channel, and solid (MEA) along the length of the cell.

The variations in fuel channel temperature with length and cell voltage are shown in Fig. 6.5. All temperature profiles are shown at steady-state. When operated at OCV, the fuel channel continuously loses heat to the air channel by convection due to higher air inlet velocities. The fuel channel attains an exit temperature of ~ 941.4 K, due to the occurrence of the exothermic water-gas shift reaction. When a voltage of $E_{\text{cell}} = 0.6$ V is applied, there is a rise in fuel channel temperature after its initial drop. This can be attributed to the exothermic electrochemical reactions occurring at the TPB, which also produces ohmic heat. An increase in the length of the cell causes further increase in temperature due to higher electrochemical utilization of available hydrogen in the fuel channel. Theoretically, an increase in fuel utilization rate can lead to an increase in energy conversion efficiency.

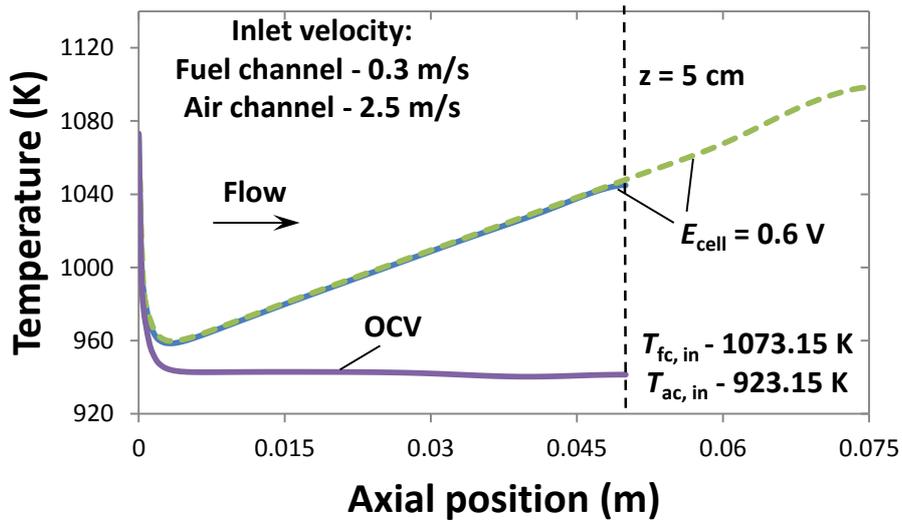


Figure 6.5: The effect of cell length and applied voltage on the temperature profile of the fuel channel.

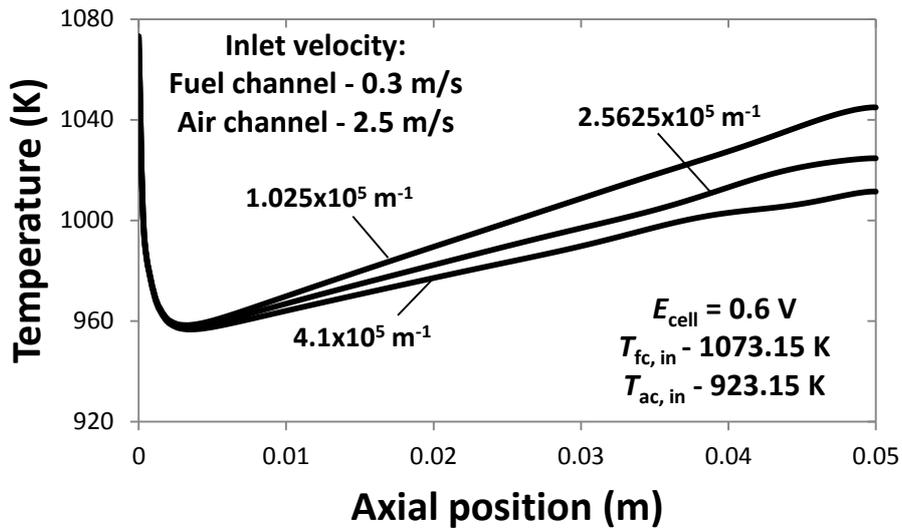


Figure 6.6: The effect of specific catalytic area on the temperature profile of the fuel channel.

The effect of specific catalytic area on fuel channel temperature is illustrated in Fig. 6.6. The characteristic initial temperature drop in the inlet region appears to be similar in magnitude for all the three specific areas. However, the temperature is lower for a catalyst with higher specific catalytic area, as one moves towards the exit of the fuel channel. In the first $\sim 1.5 \text{ cm}$ of the channel, H_2 and CO_2 production occurs through the exothermic water-gas shift reaction that leads to the consumption of H_2O and CO . But, the heat loss to the air channel dominates and hence, governs the early

drop in temperature. After ~ 1.5 cm, CH_4 and H_2O are consumed by the endothermic steam reforming process, as a result of which concentrations of H_2 and CO continue to increase. Nonetheless, exothermic electrochemical reactions dominate and govern the overall temperature rise, though higher specific areas can lead to more reforming, thereby decreasing the exit temperature.

The current density and reversible potential profiles, for both isothermal and non-isothermal cases, are depicted in Fig. 6.7. The isothermal temperature is taken to be equal to the temperature at the fuel channel inlet, i.e., 1073.15 K. In the non-isothermal case, the reversible potential increases close to the inlet due to the temperature drop in the solid. The combined effect of increasing solid temperature as well as fuel dilution causes the reversible cell potential to decrease towards the exit. However, in the isothermal case, the linear drop in reversible cell potential is only due to fuel dilution. The current density initially increases near the inlet, then decreases due to the temperature drop in the solid and continues to increase due to the rise in solid temperature, when operating non-isothermally. Current density seems to be a weak function of fuel dilution but a strong function of solid temperature. This phenomenon is similar to what happens in an oxide-ion-conducting SOFC when operated with humidified methane [45]. In the isothermal case, the current density simply varies as a function of hydrogen concentration in the fuel channel. Sufficient hydrogen is produced in the case considered here. An increase in the length of the fuel channel would further bring down the current density, due to enhanced hydrogen utilization.

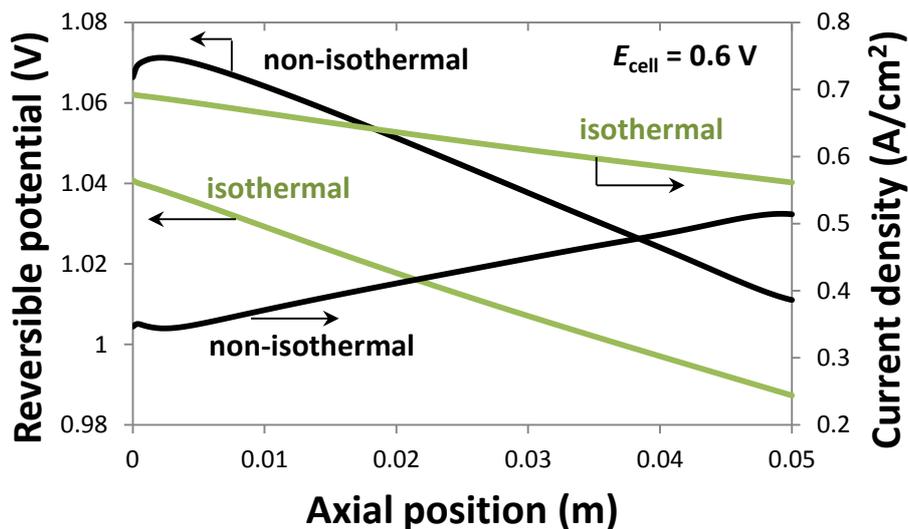


Figure 6.7: Reversible potential and current density for the cell operating at 0.6 V. The temperature for the isothermal case is 1073.15 K.

The axial variation of overpotential losses along the cell length is shown in Fig. 6.8, for both isothermal and non-isothermal operation. The cathode activation overpotential is higher than the anode activation and ohmic overpotentials. As expected, the ohmic overpotential varies as a function of current density and temperature.

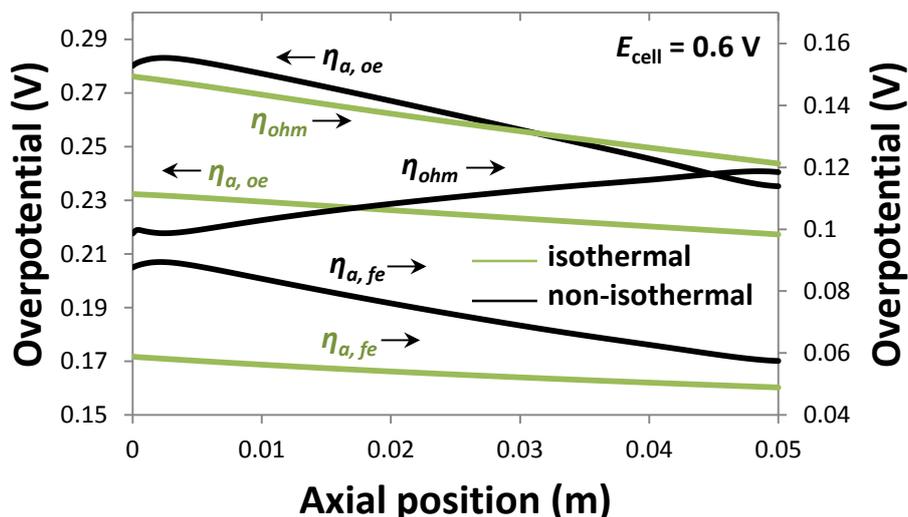


Figure 6.8: Overpotential losses as a function of axial position along the cell. The temperature for the isothermal case is 1073.15 K.

The axial species distribution resulting from the combination of thermo-catalytic chemical reactions and electrochemical fluxes in the anode is shown in Fig. 6.9, for the cell operating at OCV and 0.6 V. At OCV, species profiles proceed pre-dominantly through the equilibrium between the WGS/RWGS reactions. Due to the WGS reaction, the consumption of H_2O and CO , and the production of H_2 and CO_2 follow similar trends. The decrease in axial CH_4 concentration can be attributed to weak steam reforming that leads to the added production of H_2 and CO . Subsequently, the CO generates more CO_2 via the WGS reaction, as depicted by the axial profiles. A decline in the concentration of H_2 occurs, when a cell voltage of 0.6 V is applied, due to its electrochemical oxidation. We speculate that the initial rise in CH_4 axial concentration is due to the hydrogenation of surface carbon $\text{C}_{(\text{Ni})}$. The decrease in CH_4 axial concentration after ~ 3.25 cm is due to weak steam reforming that leads to a slightly higher concentration of CO_2 than CO (due to the WGS reaction) towards the exit. Predicting accurate surface carbon coverage is vital for the correct determination of OCVs [71]. The equilibrium composition at the exit of the fuel channel, at 1044.96 K, was found to be 1% CH_4 + 66.96% H_2 + 21.32% CO + 2.99% CO_2 + 7.73% H_2O . This shows slow reaction kinetics over the catalyst surface, which can be improved by increasing the specific catalytic area

and residence time of the gases in the fuel channel. The coverage of $C_{(Ni)}$ adsorbate is slightly higher at 0.6 V than at OCV, as shown in Fig. 6.10. The key global reaction that governs this phenomena involves the hydrogenation of CO ($CO + H_2 \leftrightarrow C + H_2O$). Also, it is important to bear in mind that the flux of H_2 towards the anode TPB rises with increasing current densities, while the amount of H_2O decreases due to its electrochemical formation on the cathode side. This promotes the hydrogenation of surface carbon by shifting its equilibrium towards product (CH_4) formation. Moreover, the above findings are specific to the inlet fuel composition used in this study.

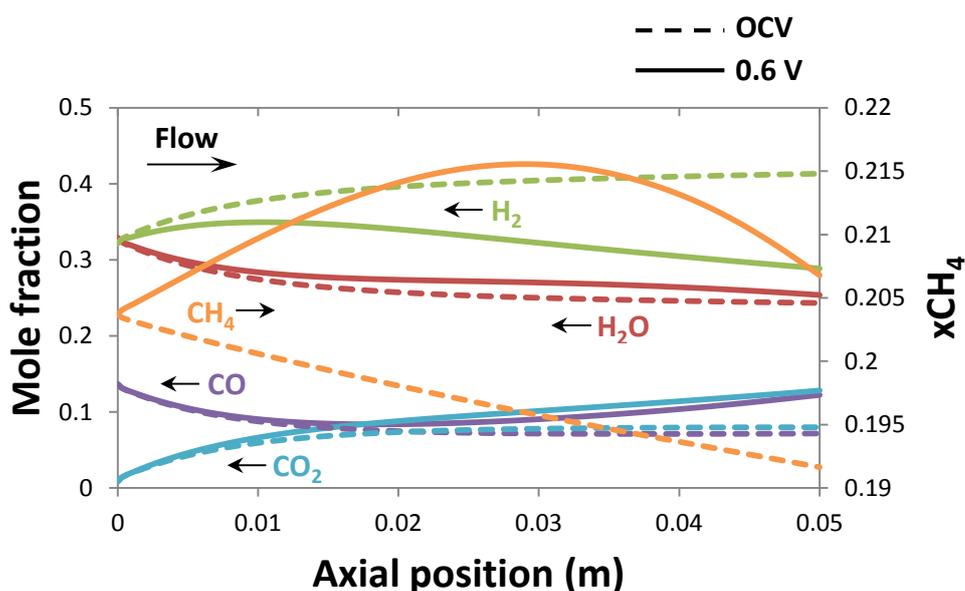


Figure 6.9: Gas-phase species distribution in the fuel channel along the length of the cell.

The gas concentrations of various species and surface coverages of major species within the anode at three different positions along the cell length are shown in Figs. 6.11–6.13. Fig. 6.11 describes this close to the inlet of the cell. The major adsorbates that determine the open surface coverage of the Ni catalyst are $CO_{(Ni)}$ and $H_{(Ni)}$. The trend in these coverages is similar to the concentration of its corresponding gas species in the anode. At $E_{cell} = 0.6$ V, the decrease in concentration of H_2 towards the TPB due to electrochemical consumption is offset by its production from the WGS reaction. This is reflected by decreasing H_2O and CO , and increasing CO_2 , concentrations towards the TPB away from the anode-channel interface. An interesting phenomenon to note in Figs. 6.12 and 6.13 is the increase in the concentration of adsorbate $H_{(Ni)}$ to a point where it exceeds the concentration of adsorbate $CO_{(Ni)}$, as one moves down the channel length. This can be attributed to current density which also drives the direction of the H_2 gas within the anode. One can note a more prominent de-

crease in H_2 gas concentration towards the TPB, with increasing axial length, due to an increasing current density profile along the axial length (Fig. 6.7).

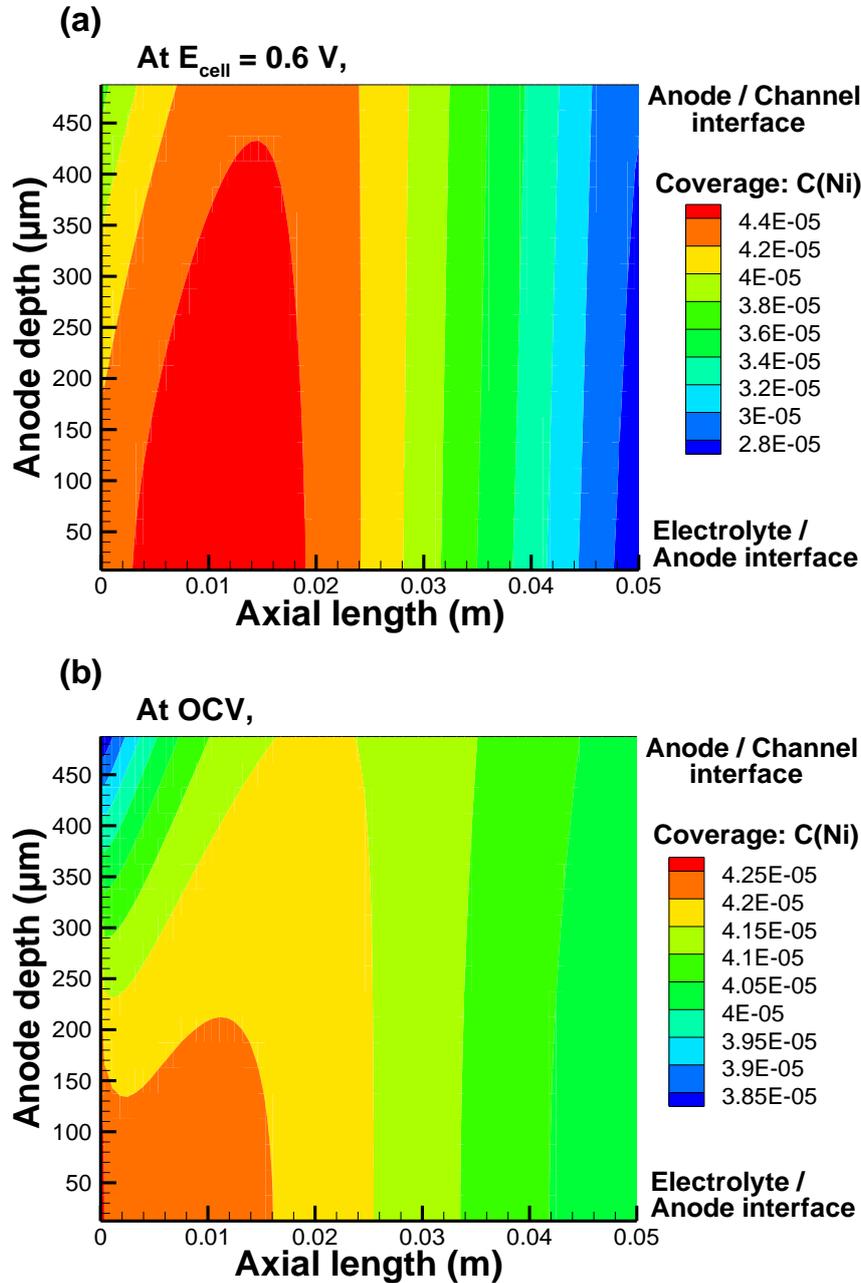


Figure 6.10: The influence of cell voltage on surface carbon coverage within the anode when operated at: (a) $E_{cell} = 0.6$ V, and (b) OCV.

However, this is not the case at OCV due to the absence of electrochemical flux. The amount of catalyst covered increases as we move towards the exit, although only marginally at OCV, due to higher surface coverage of adsorbate $CO_{(Ni)}$ and increasing surface coverage of adsorbate $H_{(Ni)}$. The gas composition of the air channel as a function of axial distance is described in Fig. 6.14. The mole

fractions of O_2 and N_2 decrease, while that of H_2O increases due to electrochemical reactions at the cathode TPB (Eqs. 2.6). The corresponding pattern is reflected in the cathode gas concentrations at three different axial locations of the air channel. The profiles at OCV act as a yardstick to measure deviation in species distribution when a voltage is applied.

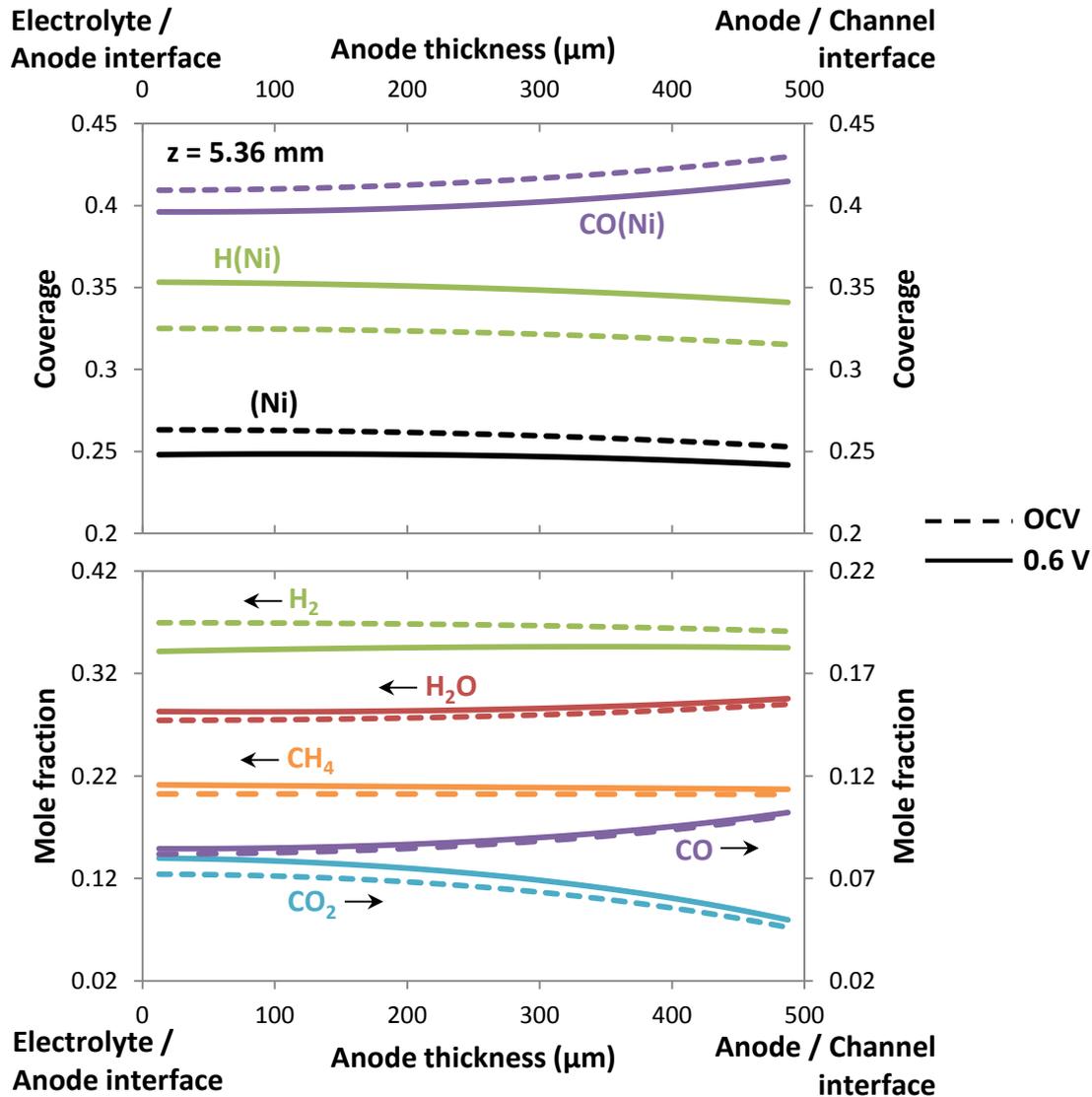


Figure 6.11: Species profiles and surface coverages within the anode near the reactor inlet ($z = 5.36$ mm). Top panel shows the surface coverage and bottom panel shows gaseous species profiles.

In order to understand the effect of catalyst zoning on temperature profiles in the cell, the anode is divided into four equal zones with increasing and decreasing specific catalytic areas as presented in Fig. 6.15. Case I represents a step decrease in specific area, while case II represents a step increase in specific area. The difference in exit temperatures between cases I and II is ~ 18.5 K. In the initial

~5.1 cm of the cell, case I has a lower temperature due to higher amount of methane consumed in the endothermic steam reforming process as compared to case II. After ~5.1 cm, case II has a lower temperature/higher temperature drop due to higher endothermic steam reforming rates as opposed to case I. Thus, the amount of H₂ and CO at the exit of the fuel channel is greater in case II, i.e., $\frac{x_{H_2, case I}}{x_{H_2, case II}} = 0.782$ and $\frac{x_{CO, case I}}{x_{CO, case II}} = 0.841$. However, the net output current density for both cases do not differ significantly from each other (~0.02 A/cm²) due to the lack of significant fuel depletion, and temperatures in both sections (before and after ~5.1 cm) balancing each other out.

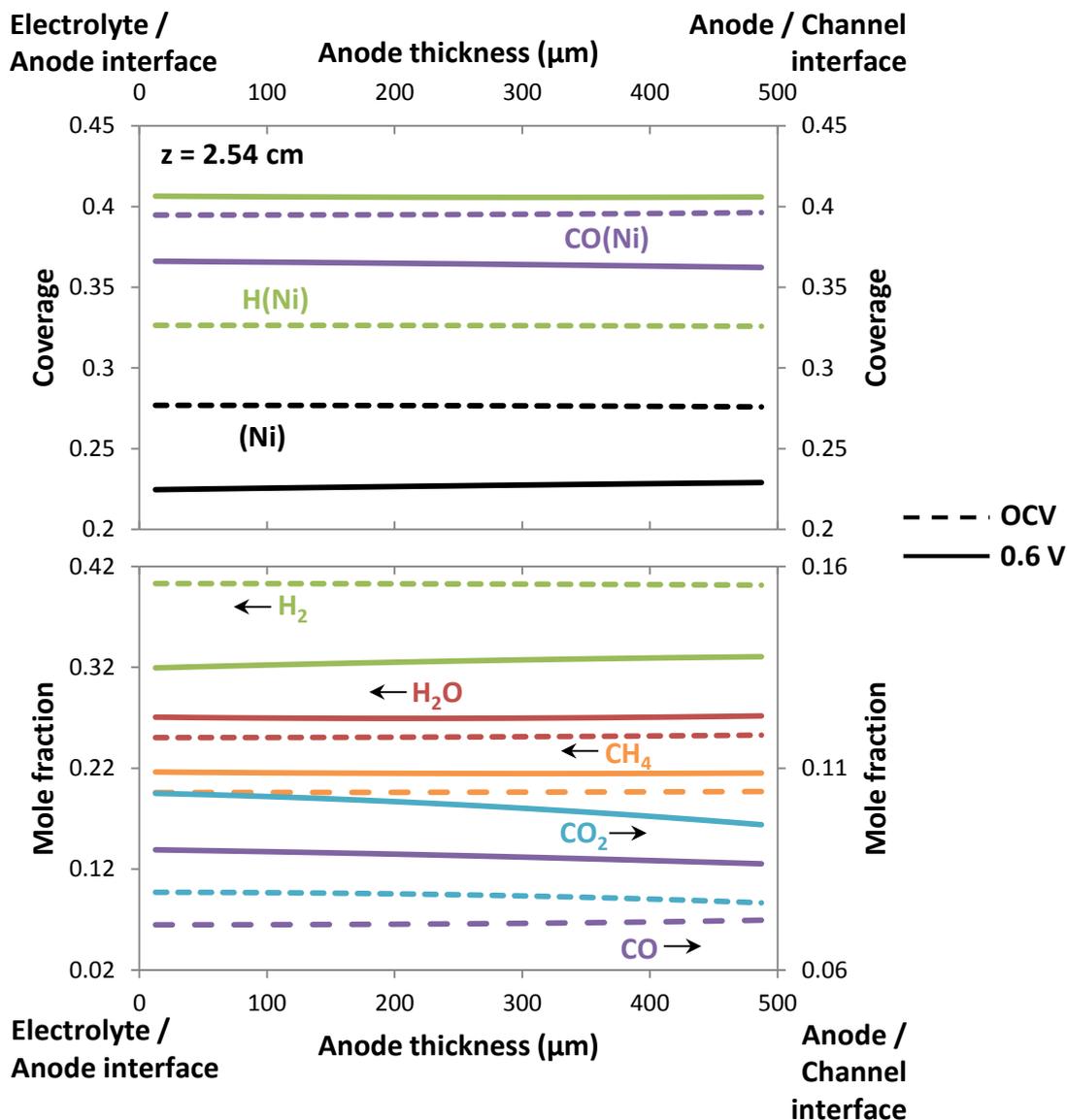


Figure 6.12: Species profiles and surface coverages within the anode halfway from the inlet ($z = 2.54$ cm). Top panel shows the surface coverage and bottom panel shows gaseous species profiles.

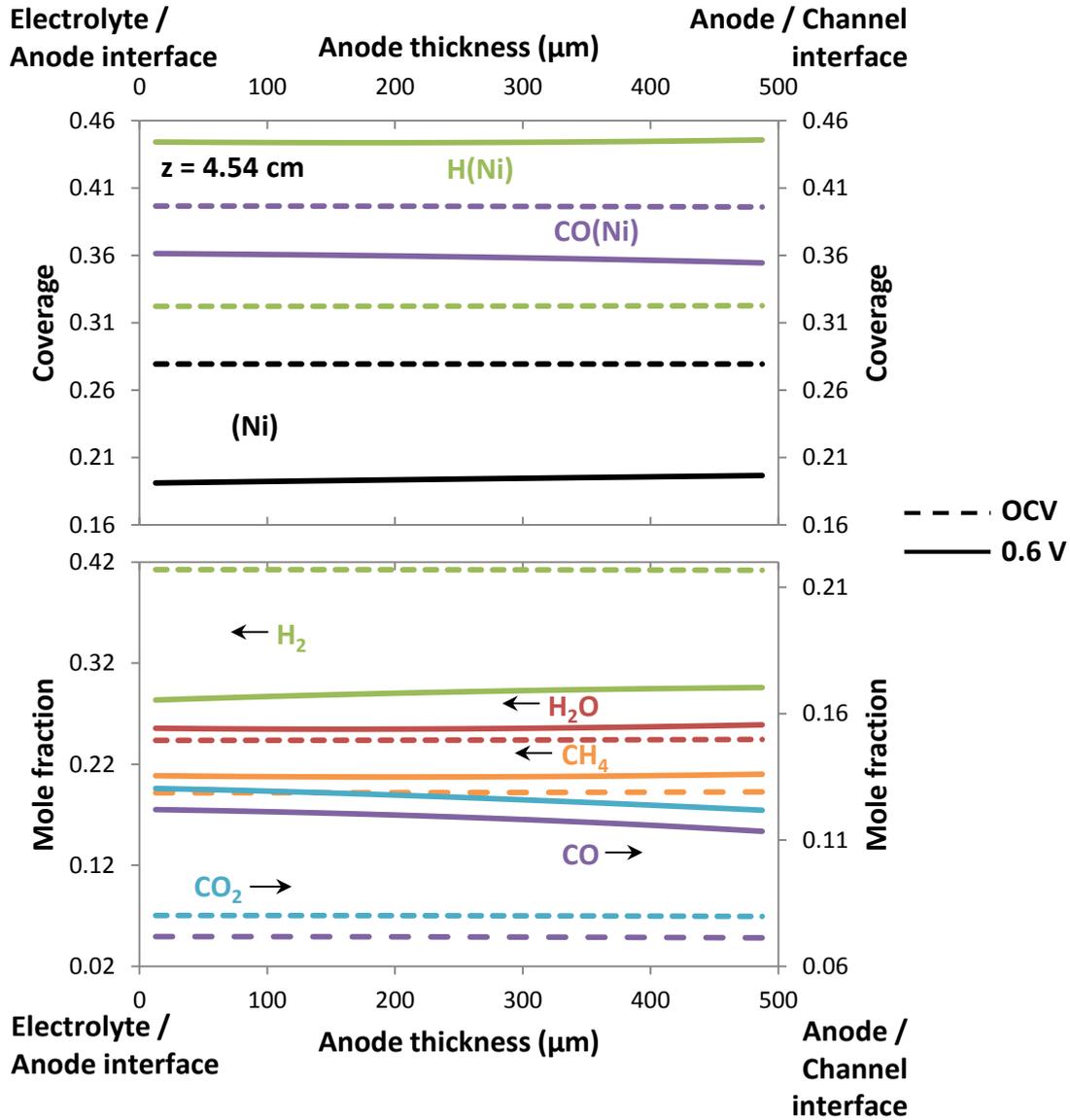


Figure 6.13: Species profiles and surface coverages within the anode near the reactor exit ($z = 4.54$ cm). Top panel shows the surface coverage and bottom panel shows gaseous species profiles.

The effect of different operating conditions on exit temperature of the solid (at steady-state) and electrochemical performance parameters are listed in Table 6.4. The base case (Table 6.1) is compared with three other cases: (1) inlet temperature at the air channel $T_{ac, in} = 873.15$ K, (2) inlet temperature at the fuel channel $T_{fc, in} = 1223.15$ K, and (3) inlet velocity at the fuel channel $v_{fc, in} = 2.5$ m/s. A predictable trend was observed for all the cases. A decrease in the inlet temperature of the gases at the air channel leads to a higher temperature drop in the porous MEA, which causes the attainment of a lower current density due to prominent overpotential losses. This is accompanied by low hydrogen and oxygen utilization in the gas channels. The power density of the cell can be im-

proved by raising the inlet gas temperature at the fuel channel, although this would include the supply of more heat energy to the system and steepen the temperature gradients. As expected, an increase in current density raises the electrochemical flux that leads to higher consumption of active species participating in charge transfer. Highest power density was obtained for case (3), which only involved raising the inlet velocity of gases at the fuel channel. This results in the highest solid temperature amongst the four cases. The utilization of electrochemically active H_2 is the least due to the dominance of the WGS reaction and higher supply of fuel at the inlet. Nevertheless, the oxygen consumption is the highest. Although the ohmic resistance of the electrolyte decreases with an increase in temperature, its overpotential is driven strongly by rising current densities.

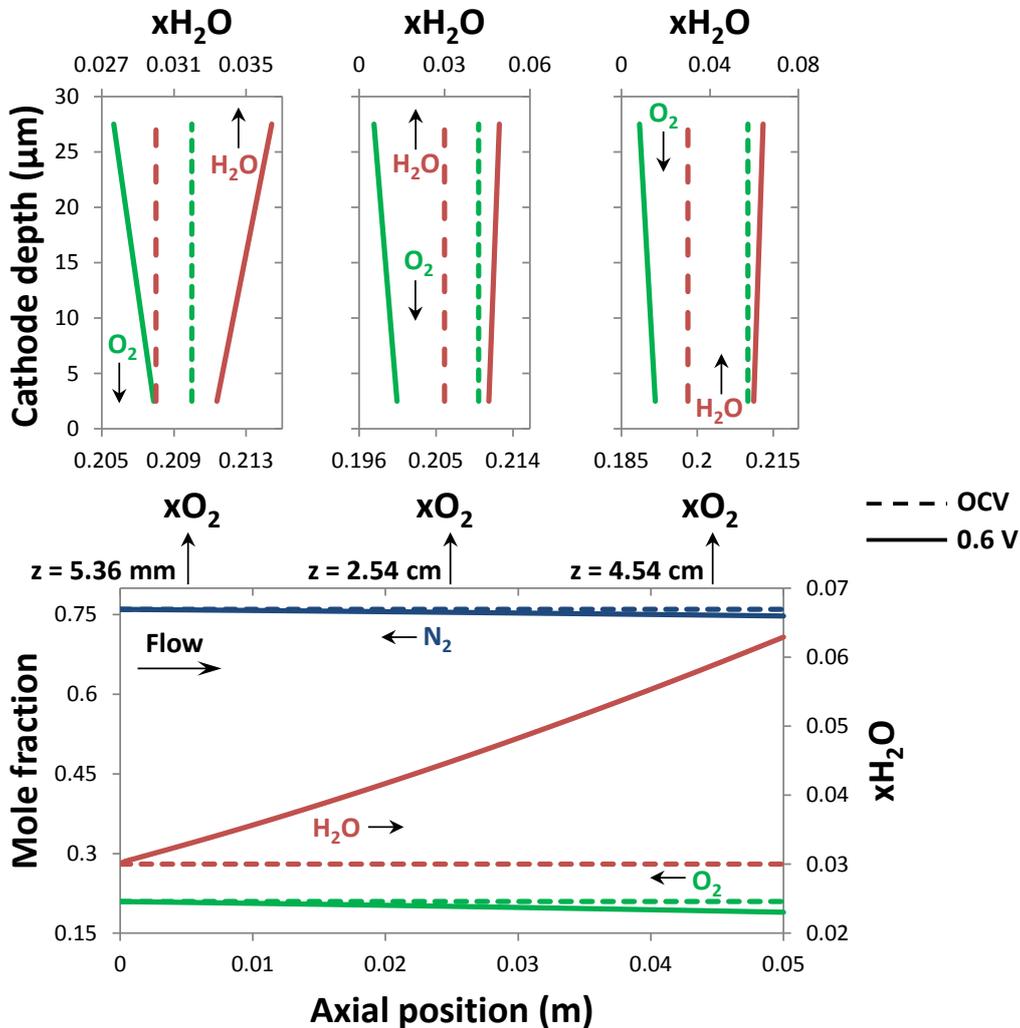


Figure 6.14: Gas-phase species distribution within the air channel and cathode, as a function of cell length. Top panels depict the gas concentrations within the cathode, while the bottom panel shows the gas concentrations in the air channel.

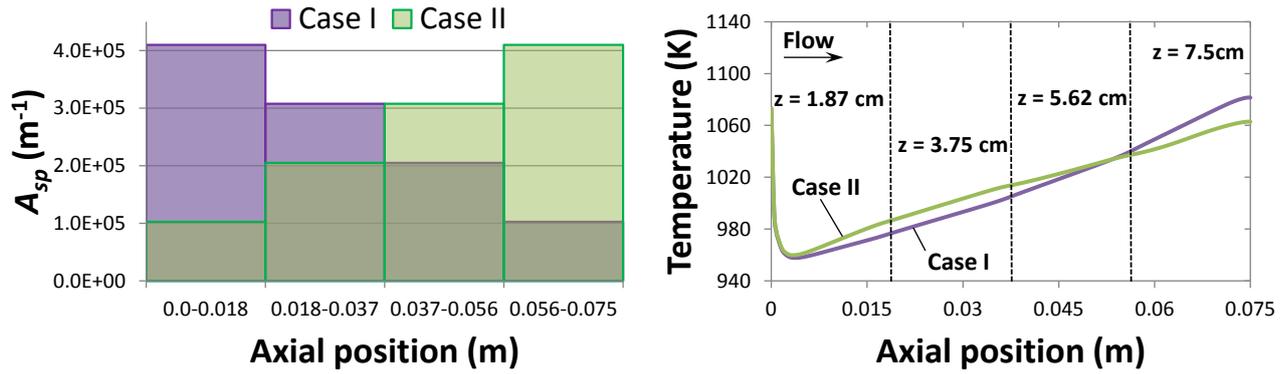


Figure 6.15: The effect of catalyst zoning on the temperature distribution in the fuel channel. The left panel shows two cases: (i) Case I represents a step-wise decrease in A_{sp} and, (ii) Case II represents a step-wise increase in A_{sp} . The right panel shows its impact on the temperature profiles in the fuel channel.

Table 6.4: Effect of operating conditions on system performance parameters.

Case	i (A cm ⁻²)	E_{rev} (V)	P_{out} (W cm ⁻²)	$\eta_{a,fe}$ (V)	$\eta_{a,oe}$ (V)	η_{ohm} (V)	T_s (K)	x_{H_2} % (at exit)	x_{O_2} % (at exit)
Base	0.4285	1.043	0.2571	0.073	0.2611	0.1105	1043.75	28.85	18.98
(1)	0.2858	1.065	0.1715	0.0927	0.2868	0.0869	970.34	29.15	19.71
(2)	0.4681	1.037	0.2809	0.0685	0.2534	0.116	1059.32	27.46	18.79
(3)	0.5593	1.029	0.3356	0.0608	0.2402	0.1286	1079.4	34.8	18.38

6.2 Summary

A numerical investigation of proton-conducting SOFCs with direct internal reforming has been carried out. The model is parameterized with two sets of experimental data to derive electrochemical parameters. Further parametric analysis is carried out to study the influence of operating conditions on mass and heat transport in the cell. It was found that the WGS reaction played an important role in driving temperature distributions in the cell. The air channel was mainly used to regulate temperature gradients, and for heat management purposes. The equilibrium between the WGS/RWGS reactions was found to dominate the occurrence of weak endothermic steam reforming. Since the electrochemical formation of H₂O occurs at the cathode side, further steam reforming of CH₄ is not possible unlike its oxide-ion-conducting counterpart. Moreover, slow chemical kinetics were exhibited under the used operating conditions. However, it should be noted that the findings were limited to the specific fuel composition used for this analyses. The effect of specific catalytic area and cell

voltage on temperature and species distribution in the system was also investigated. A qualitative study of the influence of cell voltage on surface carbon coverage shows its concentration to be the highest in the first half of the anode. Two different configurations of catalyst zoning in the anode does not result in a significant difference in temperature gradients, although it could be used to enhance cell efficiencies and fuel utilization rates. A brief analysis of the impact of fuel and air inlet conditions on the cell was conducted by keeping all other parameters constant. It was determined that a higher inlet velocity at the fuel channel results in higher current and power densities but lower fuel utilization rates and efficiencies. Better heat management configurations and innovative materials are important in enhancing performance and sustainability of the system. Future work could involve the qualitative comparison between the co-flow, counter-flow and cross-flow configurations to study heat generation/utilization in the cell. The electrochemical model used in this paper does not consider defect transport within the proton-conducting electrolyte. A detailed algorithm that describes the transport of multiple charge-carrying defects can be found in Ref. [132]. Nevertheless, the numerical model applied in this chapter can be considered as one of the first steps towards understanding the interplay between various physico-chemical phenomena in a proton-conducting SOFC.

Chapter 7 Summary and outlook

7.1 Accomplished results

A unified modeling framework was significantly extended and employed to study reversible oxide-ion-conducting and proton-conducting SOCs. These models covered dimensions ranging from 1-D to 3-D, and coupled heat and mass transport, gas-phase and heterogeneous chemistry, porous media transport, fluid mechanics, thermodynamics and electrochemistry. They were applied to investigate SOFC stacks, SOECs for hydrogen and syngas production, and proton-conducting SOFCs. Models for each of these applications were validated with relevant experiments, either from literature or collaborations with research laboratories, to deduce electrochemical parameters. Then, parametric analysis was carried out to answer pertinent questions facing the SOFC and SOEC communities.

Numerous SOFC stack models have been reported in literature. All of them carry out detailed simulations for every cell in the stack, leading to high computation time along with a restriction in the number of cells that can be simulated. In our 3-D model, a cluster agglomeration algorithm is employed to choose representative cells for detailed simulation by forming clusters based on local temperature profiles. All channels with the same temperature profiles were assumed to behave alike. This approach drastically reduced computational cost, and eased the constraint on the number of cells that could be simulated. Furthermore, simulations were carried out to study the transient behavior of this co-flow system running on a reformat fuel composition of 31.81% H₂ + 36.56% N₂ + 13.19% CO + 13.19% CH₄ + 2.23% CO₂ + 3.02% H₂O. The thermal response of the system was investigated for step-changes in current and voltage. The thermal response time of the stack during step-change in current from 0.3 to 0.4 A/cm² was found to be ~17 minutes. This was determined between the steady-state temperature distribution obtained at 0.3 A/cm² (before the introduction of step-change) and the steady-state temperature distribution obtained at 0.4 A/cm² (after the introduction of step-change). It was found that the response times were independent of whether a step-increase or a step-decrease in load was introduced, for a specified magnitude. Also, different thermal diffusivities of the solid structure material yielded different response times. Lower thermal diffusivities lead to faster response, and was postulated to be the reason behind disparities in re-

response times reported in literature. The response times were also studied for two different boundary conditions imposed on the stack: adiabatic and Neumann. The Neumann boundary condition considers a case where the stack is placed in a large enclosure, such that the external heat transfer coefficient is equal to $2 \text{ W/m}^2\text{K}$ (natural convection) and the thermal emissivity is 0.09. It was found that the response times did not differ much based on whether an adiabatic or Neumann condition was employed at the borders of the simulation domain. The model predicts temperature contours in the stack and in the gas channels of its individual cells. One of the limitations of the model was the difficulty in employing two or more sets of cells with different physical and thermal properties in the stack. All cells in the stack needed to have uniform physical and thermal properties.

SOFCs can be employed to carry out electrolysis of inlet feed by reversing the polarity of supplied current. This application was studied for two cases: (i) H_2O electrolysis, and (ii) $\text{H}_2\text{O}/\text{CO}_2$ co-electrolysis. In the case of H_2O electrolysis for hydrogen production, the 1-D button cell model was used to reproduce experimental data from literature. The numerical model was validated with V-I curves, ASR values, and the breakdown of polarization resistances obtained from experiments. The effect of temperature, inlet $\text{H}_2/\text{H}_2\text{O}$ ratios, and current density on the electrochemical performance parameters of the cell was investigated. An increase in temperature played a beneficial role by enhancing kinetics and electrochemical reaction rates, and by lowering ohmic resistances. As the overpotential losses decreased with an increase in temperature, at a specified current density, the operating cell potential also decreased. Due to this phenomena, rising temperatures also favored higher hydrogen production efficiencies. The overpotential losses increased with an increase in current density, which is also what happened when inlet $\text{H}_2/\text{H}_2\text{O}$ ratios were lowered. Nevertheless, low inlet $\text{H}_2/\text{H}_2\text{O}$ ratios generated high hydrogen production efficiencies due to an increase in electrochemical conversion of reactants. An efficiency analysis revealed that it is important to consider the trade-off between steam utilization rates and hydrogen production efficiencies. At low voltages, high hydrogen production efficiencies and low steam utilization rates were attained, while low hydrogen production efficiencies and high steam utilization rates were obtained at high operating voltages. Low operating voltages lead to reactant wastage and high voltages cause steam starvation leading to performance penalties and cell degradation. The trade-off between the two was found to occur at $\sim 1.1 \text{ V}$, which is lower than the thermo-neutral voltage. The concentrations of surface adsorbed species - $\text{H}_2\text{O}_{(\text{Ni})}$, $\text{O}_{(\text{Ni})}$, $\text{H}_{(\text{Ni})}$ and $\text{OH}_{(\text{Ni})}$, at the TPB, were significantly affected by operating parameters and conditions, and influenced cell performance. In addition, the electrochemical behavior of the system was demonstrated for two different fuel electrode pore diameters to understand the influence of micro-structural parameters on limiting current behavior. As the pore diameter is low-

ered, the reversible potential decreased due to product build-up at the TPB as opposed to steady supply of fresh reactants through the diffusion pathway.

In the case of H₂O/CO₂ co-electrolysis for syngas production, two sets of experimental data were used to validate the 1-D electrochemical button cell model. As in all cases, the electrochemical model was independent of the type of geometric structure. The reversible potential, current density and exit-gas composition of the cell varied as a strong function of temperature. The micro-structural parameters of the fuel electrode such as tortuosity, pore diameter and porosity were responsible for controlling the concentration overpotentials of the system. A variation in fuel electrode thickness to study the exit-gas composition using the quasi-2-D co-flow planar model helped in understanding the interaction between the electrochemical reactions at the TPB (utilization region), internal reforming (heterogeneous chemistry) zone and transport limitations within the porous electrode. For the given set of physical conditions, the exit mole fraction of H₂ reached a maximum when the fuel electrode thickness was ~200 μm, while that of CO was highest for a thickness of ~20 μm. The effect of temperature on exit-gas composition was also studied. At lower temperatures, it was found that the major contributor to the production of methane was the hydrogenation of surface carbon C_(Ni) that was produced via the Boudouard reaction. At high temperatures, the syngas production rates increased drastically to form a highly reducing atmosphere of H₂ and CO which also contributed to methane formation. It was found that the inlet gas velocity at the fuel channel was mainly responsible in determining the trade-off between syngas production and reactant utilization rates. In addition, co-electrolysis produced higher amounts of CH₄ in comparison to the simulation that considered electrolysis of only H₂O with the CO₂ electrolysis pathway turned off. This CH₄ production was due to higher surface carbon C_(Ni) coverage in the fuel electrode, as co-electrolysis led to the production of more H₂ and CO. Moreover, in order to understand the real source of methane formation, reaction flow analysis was carried out using a batch reactor model at OCV. Reaction flow analysis revealed that the dissociation of adsorbate CO_(Ni) into C_(Ni) and O_(Ni) was the major step towards surface carbon formation. Hydrogenation of surface carbon via C_(Ni) → CH_(Ni) → CH_{2(Ni)} → CH_{3(Ni)} → CH_{4(Ni)} was found to be the most likely pathway towards CH₄ formation. Almost 100% of the adsorbed CH_{4(Ni)} desorbed to form gaseous methane CH_{4(g)}.

Proton-conducting SOFCs offer an innovative way in lowering the high operating temperatures of conventional oxide-ion-conducting SOFCs. This is beneficial from the viewpoint of lowering material cost. 1-D button cell simulations were carried out to reproduce experimental data. The deduced electrochemical parameters were employed in the quasi-2-D co-flow planar cell model to perform

adiabatic simulations, and study mass and heat transport in the cell. The fuel composition employed was 20.37% CH_4 + 32.2 % H_2 + 13.67% CO + 0.87% CO_2 + 32.89% H_2O . For this specific fuel composition, the equilibrium between the WGS/RWGS reaction seemed to play a crucial role in determining species composition and temperature distributions in the cell. Steam reforming of CH_4 was weak due to electrochemical formation of H_2O on the oxidant electrode side, and due to slow reaction kinetics on the catalytic sites under the used operating conditions. Nevertheless, increasing specific catalytic area increased CH_4 conversion to syngas via steam reforming, and led to a temperature drop in the cell. The consequences of dividing the fuel electrode into four zones with different specific catalytic areas are studied for two profiles: (i) step decrease in specific area, and (ii) step increase in specific area. The exit gas temperature at the fuel channel (at steady-state) for case (i) exceeded that of case (ii) by ~ 18.5 K. The impact of fuel and air channel inlet conditions on cell performance was investigated. It was determined that the simulation which had the highest inlet velocity at the fuel channel generated highest current and power densities but lower fuel utilization rates and efficiencies. Thus, the numerical framework presented in this thesis is computationally inexpensive, and can be used as an efficient tool for performance and design optimization.

7.2 Future work

In this thesis, the described models assume micro-structural properties to be within a reasonable range for modern day cells. In order to overcome this assumption, one can use image analysis techniques by processing a series of 2-D images for microstructural characterization, or use Focused Ion Beam (FIB) and Scanning Electron Microscopy (SEM) combined with image processing, to reconstruct the 3-D structure of the electrodes [133-135]. These methods generate information that can be used for direct numerical simulations, or as an input to other computationally efficient multi-scale models. The scope of this thesis is restricted to fuels such as hydrogen, carbon monoxide and methane. The modeling framework permits the usage of other fuels as well. Development of multi-step surface reaction mechanisms for fuels such as bio-gas, ammonia, hydrogen sulfide, ethanol, ethane, propane, butane etc. on Ni catalysts is a challenging task, but offers tremendous potential in clearly understanding the multi-physics of the cell [136-138]. A direct flame type solid oxide fuel cell (DFFC) is a prospective source for electricity generation due to its fuel flexibility [139]. Models describing this type of cell are scarce in literature. Our current modeling framework supports the detailed chemistry occurring in this system, and can be extended to model it. Future work could involve the qualitative comparison between the co-flow, counter-flow and cross-flow configurations to study heat generation/utilization in the cell.

Appendix

A. Surface reaction mechanism over Ni-based electrodes

Heterogeneous surface reaction mechanism [52]

	REACTION	A ^a (cm, mol, s)	E _a ^a (kJ/mol)	β ^a [-]
R1	H ₂ + 2 Ni(s) → 2 H(s)	1.000·10 ^{-02b}	0.0	0.0
R2	2 H(s) → 2 Ni(s) + H ₂	2.545·10 ⁺¹⁹	81.21	0.0
R3	O ₂ + 2 Ni(s) → 2 O(s)	1.000·10 ^{-02b}	0.0	0.0
R4	2 O(s) → 2 Ni(s) + O ₂	4.283·10 ⁺²³	474.95	0.0
R5	CH ₄ + Ni(s) → CH ₄ (s)	8.000·10 ^{-03b}	0.0	0.0
R6	CH ₄ (s) → CH ₄ + Ni(s)	8.705·10 ⁺¹⁵	37.55	0.0
R7	H ₂ O + Ni(s) → H ₂ O(s)	1.000·10 ^{-01b}	0.0	0.0
R8	H ₂ O(s) → H ₂ O + Ni(s)	3.732·10 ⁺¹²	60.79	0.0
R9	CO ₂ + Ni(s) → CO ₂ (s)	1.000·10 ^{-05b}	0.0	0.0
R10	CO ₂ (s) → CO ₂ + Ni(s)	6.447·10 ⁺⁰⁷	25.98	0.0
R11	CO + Ni(s) → CO(s)	5.000·10 ^{-01b}	0.0	0.0
R12	CO(s) → CO + Ni(s)	3.563·10 ⁺¹¹	111.27-500 _{CO(s)}	0.0
R13	CH ₄ (s) + Ni(s) → CH ₃ (s) + H(s)	3.700·10 ⁺²¹	57.7	0.0
R14	CH ₃ (s) + H(s) → CH ₄ (s) + Ni(s)	6.034·10 ⁺²¹	61.58	0.0
R15	CH ₃ (s) + Ni(s) → CH ₂ (s) + H(s)	3.700·10 ⁺²⁴	100.0	0.0
R16	CH ₂ (s) + H(s) → CH ₃ (s) + Ni(s)	1.293·10 ⁺²³	55.33	0.0
R17	CH ₂ (s) + Ni(s) → CH(s) + H(s)	3.700·10 ⁺²⁴	97.10	0.0
R18	CH(s) + H(s) → CH ₂ (s) + Ni(s)	4.089·10 ⁺²⁴	79.18	0.0
R19	CH(s) + Ni(s) → C(s) + H(s)	3.700·10 ⁺²¹	18.8	0.0
R20	C(s) + H(s) → CH(s) + Ni(s)	4.562·10 ⁺²²	161.11	0.0
R21	CH ₄ (s) + O(s) → CH ₃ (s) + OH(s)	1.700·10 ⁺²⁴	88.3	0.0
R22	CH ₃ (s) + OH(s) → CH ₄ (s) + O(s)	9.876·10 ⁺²²	30.37	0.0
R23	CH ₃ (s) + O(s) → CH ₂ (s) + OH(s)	3.700·10 ⁺²⁴	130.1	0.0
R24	CH ₂ (s) + OH(s) → CH ₃ (s) + O(s)	4.607·10 ⁺²¹	23.62	0.0
R25	CH ₂ (s) + O(s) → CH(s) + OH(s)	3.700·10 ⁺²⁴	126.8	0.0
R26	CH(s) + OH(s) → CH ₂ (s) + O(s)	1.457·10 ⁺²³	47.07	0.0
R27	CH(s) + O(s) → C(s) + OH(s)	3.700·10 ⁺²¹	48.1	0.0

R28	$C(s) + OH(s) \rightarrow CH(s) + O(s)$	$1.625 \cdot 10^{+21}$	128.61	0.0
R29	$H(s) + O(s) \rightarrow OH(s) + Ni(s)$	$5.000 \cdot 10^{+22}$	97.9	0.0
R30	$OH(s) + Ni(s) \rightarrow H(s) + O(s)$	$1.781 \cdot 10^{+21}$	36.09	0.0
R31	$H(s) + OH(s) \rightarrow H_2O(s) + Ni(s)$	$3.000 \cdot 10^{+20}$	42.7	0.0
R32	$H_2O(s) + Ni(s) \rightarrow H(s) + OH(s)$	$2.271 \cdot 10^{+21}$	91.76	0.0
R33	$OH(s) + OH(s) \rightarrow H_2O(s) + O(s)$	$3.000 \cdot 10^{+21}$	100.0	0.0
R34	$H_2O(s) + O(s) \rightarrow OH(s) + OH(s)$	$6.373 \cdot 10^{+23}$	210.86	0.0
R35	$C(s) + O(s) \rightarrow CO(s) + Ni(s)$	$5.200 \cdot 10^{+23}$	148.1	0.0
R36	$CO(s) + Ni(s) \rightarrow C(s) + O(s)$	$1.354 \cdot 10^{+22}$	$116.12 \cdot 500_{CO(s)}$	-3.0
R37	$CO(s) + O(s) \rightarrow CO_2(s) + Ni(s)$	$2.000 \cdot 10^{+19}$	$123.6 \cdot 500_{CO(s)}$	0.0
R38	$CO_2(s) + Ni(s) \rightarrow CO(s) + O(s)$	$4.653 \cdot 10^{+23}$	89.32	-1.0
R39	$CO(s) + H(s) \rightarrow HCO(s) + Ni(s)$	$4.019 \cdot 10^{+20}$	132.23	-1.0
R40	$HCO(s) + Ni(s) \rightarrow CO(s) + H(s)$	$3.700 \cdot 10^{+21}$	$0.0 + 500_{CO(s)}$	0.0
R41	$HCO(s) + Ni(s) \rightarrow CH(s) + O(s)$	$3.700 \cdot 10^{+24}$	95.8	-3.0
R42	$CH(s) + O(s) \rightarrow HCO(s) + Ni(s)$	$4.604 \cdot 10^{+20}$	109.97	0.0

Total surface site density $\Gamma = 2.66 \times 10^{-09}$ mol/cm²

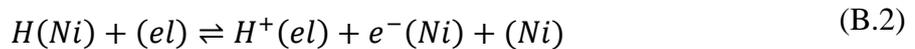
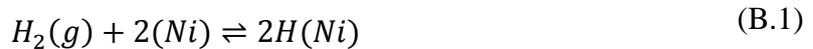
^a Arrhenius parameters for the rate constant is written as: $k = AT^\beta \exp(-E_d/RT)$

^b Sticking coefficient

** (s) or (Ni) represents a single site on the active catalytic surface

B. Modified B-V equation derivation for H-SOFCs

The Appendix serves to provide details about the derivation of the modified Butler-Volmer equation from the following elementary reaction steps considered for the electrochemical oxidation of H₂ at the anode-electrolyte three phase boundary (TPB),



Reaction B.1 describes the dissociative adsorption of gas-phase hydrogen, H₂(g), into two empty active sites on the Ni surface, (Ni). For the charge-transfer step, as illustrated in reaction B.2, the H₂ spillover mechanism is assumed in accordance with the general consensus in the literature. The adsorbed atomic hydrogen, H(Ni), vacates its Ni site, (Ni), and spills over to the electrolyte to release a proton in the electrolyte, H⁺(el), and an electron in the Ni anode, e⁻(Ni).

Assuming the charge-transfer step to be rate limiting, the fast adsorption-desorption reaction proceeds to equilibrium. Therefore, from the law of mass action,

$$K_1 = \frac{\theta_H^2}{p_{H_2} \theta_{Ni}^2} \quad (\text{B.3})$$

where K_1 is the equilibrium constant, θ_H and θ_{Ni} are the site fractions or surface coverages of adsorbed hydrogen and empty active sites on the Ni surface and p_{H_2} is the partial pressure of hydrogen at the TPB. For the charge-transfer reaction, the rate is dependent on both the surface coverages of the reacting species and the potential difference between the electrode and the electrolyte, E_a . Therefore, the current density, i , for the rate-limiting step is given by

$$i = l_{TPB} F \left[k_{2,a} \theta_H \exp\left(\frac{\beta_{2,a} F E_a}{RT}\right) - k_{2,c} \theta_{Ni} \exp\left(\frac{-\beta_{2,c} F E_a}{RT}\right) \right] \quad (\text{B.4})$$

where l_{TPB} is the TPB length, F is the Faraday constant, $k_{2,a}$ and $k_{2,c}$ are the reaction rate constants in the anodic and cathodic direction respectively, $\beta_{2,a}$ and $\beta_{2,c}$ are the anode and cathode charge transfer coefficients, R is the universal gas constant and T is the cell temperature. It is assumed here that there is no change in the site vacancies in the electrolyte, (el), and H^+ ion concentrations at the TPB. Consequently, the surface coverages in the electrolyte are neglected in Eq. B.4.

Noting that $\beta_{2,a} + \beta_{2,c} = 1$, at equilibrium, when the forward reaction rate equals the backward reaction rate (i.e. $i = 0$), the equilibrium potential difference, E_a^{eq} , is given by

$$\exp\left(\frac{F E_a^{eq}}{RT}\right) = \frac{1}{K_2} \frac{\theta_{Ni}}{\theta_H} \quad (\text{B.5})$$

where the equilibrium constant $K_2 = \frac{k_{2,a}}{k_{2,c}}$. Substituting Eq. B.5 in Eq. B.4 leads to the Butler-Volmer form for current density,

$$i = i_0 \left[\exp\left(\frac{\beta_{2,a} F \eta_a}{RT}\right) - \exp\left(\frac{-\beta_{2,c} F \eta_a}{RT}\right) \right] \quad (\text{B.6})$$

where the exchange current density,

$$i_0 = l_{TPB} F k_{2,a} \theta_H \exp\left(\frac{\beta_{2,a} F E_a^{eq}}{RT}\right) \quad (\text{B.7})$$

and the anodic activation overpotential is defined as

$$\eta_a = E_a - E_a^{eq} \quad (\text{B.8})$$

The expression for exchange current density can be further simplified by raising Eq. B.5 on both sides by $\beta_{2,a}$ and substituting the result in Eq. B.7:

$$i_0 = \frac{l_{TPB} F k_{2,a}}{K_2^\beta} \theta_H^{1-\beta_{2,a}} \theta_{Ni}^{\beta_{2,a}} \quad (\text{B.9})$$

Now, by definition, the site fractions on the Ni anode surface must sum up to unity:

$$\theta_H + \theta_{Ni} = 1 \quad (\text{B.10})$$

Substituting Eq. B.10 in Eq. B.3 and defining $K_1 = 1/p_{H_2}^*$, θ_H and θ_{Ni} can be expressed in terms of the gaseous partial pressures of hydrogen,

$$\theta_H = \frac{(p_{H_2}/p_{H_2}^*)^{1/2}}{1 + (p_{H_2}/p_{H_2}^*)^{1/2}} \quad (\text{B.11})$$

and,

$$\theta_{Ni} = \frac{1}{1 + (p_{H_2}/p_{H_2}^*)^{1/2}} \quad (\text{B.12})$$

Here, the parameter $p_{H_2}^*$ is obtained from a balance between adsorption and desorption rates of H on Ni at equilibrium,

$$\gamma_0 \sqrt{\frac{RT}{2\pi W_{H_2}}} \frac{p_{H_2}}{RT} \theta_{Ni}^2 = A_{des} \exp\left(\frac{-E_{des}}{RT}\right) \theta_H^2 \Gamma^2 \quad (\text{B.13})$$

which yields

$$p_{H_2}^* = p_{H_2} \left(\frac{\theta_{Ni}}{\theta_H}\right)^2 = A_{des} \exp\left(\frac{-E_{des}}{RT}\right) \frac{\Gamma^2}{\gamma_0} \sqrt{2\pi W_{H_2} RT} \quad (\text{B.14})$$

where $\Gamma = 2.6 \times 10^{-9} \text{ mol/cm}^2$, the pre-exponential factor $A_{des} = 5.59 \times 10^{19} \text{ cm}^2 \text{ mol}^{-1} \text{ s}^{-1}$, sticking coefficient for H_2 adsorption $\gamma_0 = 0.01$, the activation energy $E_{des} = 88.12 \text{ kJ/mol}$, and W_{H_2} is the molecular weight of H_2 .

Finally substituting Eqs. B.11 and B.12 in Eq. B.9, and grouping the leading constants in Eq. B.9 into a single parameter, the exchange current density can be expressed as

$$i_0 = i_{\text{H}_2}^* \frac{(p_{\text{H}_2}/p_{\text{H}_2}^*)^{(1-\beta_{2,a})/2}}{1 + (p_{\text{H}_2}/p_{\text{H}_2}^*)^{1/2}} \quad (\text{B.15})$$

The first term, $i_{\text{H}_2}^* \left(= \frac{l_{\text{TPBF}} k_{2,a}}{K_2^\beta} \right)$, is a constant for a given electrode microstructure and is a function of temperature only. It is adjusted to fit the measured fuel cell performance. The second term which shows how the exchange current density depends on the partial pressures of the reactant, divulges the apparent reaction order of the charge transfer reaction. For $\beta_{2,a} = 0.5$, Eq. B.15 reduces to

$$i_0 = i_{\text{H}_2}^* \frac{(p_{\text{H}_2}/p_{\text{H}_2}^*)^{1/4}}{1 + (p_{\text{H}_2}/p_{\text{H}_2}^*)^{1/2}} \quad (\text{B.16})$$

References

- [1] C. F. Schönbein, "Further experiments on the current electricity excited by chemical tendencies, independent of ordinary chemical action," *The London and Edinburgh Philosophical Magazine and Journal of Science*, vol. 12, pp. 311-317, 1838.
- [2] C. F. Schönbein, "On the voltaic polarization of certain solid and fluid substances," *The London and Edinburgh Philosophical Magazine and Journal of Science*, vol. 14, pp. 43-45, 1839.
- [3] W. R. Grove, "On voltaic series and the combination of gases by platinum," *The London and Edinburgh Philosophical Magazine and Journal of Science*, vol. 14, pp. 127-130, 1839.
- [4] W. R. Grove, "On a gaseous voltaic battery," *The London, Edinburgh and Dublin Philosophical Magazine and Journal of Science*, vol. 21, pp. 417-420, 1842.
- [5] A. Kromp, "Model-based interpretation of the performance and degradation of reformato fueled solid oxide fuel cells," Ph.D. Dissertation, Institut für Werkstoffe der Elektrotechnik (IWE), Karlsruher Institut für Technologie (KIT), Karlsruhe, 2013.
- [6] W. Vielstich, A. Lamm, and H. A. Gasteiger, *Handbook of fuel cells: Fundamentals, technology, applications*, 1st ed. New York: Wiley, 2003.
- [7] S. C. Singhal and K. Kendal, *High Temperature and Solid Oxide Fuel Cells: Fundamentals, design, applications*, 1st ed. Amsterdam: Elsevier Science, 2003.
- [8] V. M. Janardhanan, "A detailed approach to model transport, heterogeneous chemistry, and electrochemistry in solid-oxide fuel cells," Ph.D. Dissertation, Institut für Technische Chemie und Polymerchemie (ITCP), Universität Karlsruhe (TH), Karlsruhe, 2007.
- [9] J. B. Goodenough, "Ceramic technology: Oxide-ion conductors by design," *Nature*, vol. 404, pp. 821-823, 2000.

-
- [10] F. Lefebvre-Joud, G. Gauthier, and J. Mougin, "Current status of proton-conducting solid oxide fuel cells development," *Journal of Applied Electrochemistry*, vol. 39, pp. 535-543, 2009.
- [11] K. D. Kreuer, "Proton-conducting oxides," *Annual Review of Materials Research*, vol. 33, pp. 333-359, 2003.
- [12] N. P. Brandon, S. Skinner, and B. C. H. Steele, "Recent advances in materials for fuel cells," *Annual Review of Materials Research*, vol. 33, pp. 183-213, 2003.
- [13] E. P. Murray, T. Tsai, and S. A. Barnett, "A direct-methane fuel cell with a ceria-based anode," *Nature*, vol. 400, pp. 649-651, 1999.
- [14] J. Hanna, W. Y. Lee, Y. Shi, and A. F. Ghoniem, "Fundamentals of electro- and thermochemistry in the anode of solid-oxide fuel cells with hydrocarbon and syngas fuels," *Progress in Energy and Combustion Science*, vol. 40, pp. 74-111, 2014.
- [15] Y. Jiang and A. V. Virkar, "Fuel composition and diluent effect on gas transport and performance of anode-supported SOFCs," *Journal of The Electrochemical Society*, vol. 150, pp. A942-A951, 2003.
- [16] J. Liu and S. A. Barnett, "Operation of anode-supported solid oxide fuel cells on methane and natural gas," *Solid State Ionics*, vol. 158, pp. 11-16, 2003.
- [17] Y. Lin, Z. Zhan, J. Liu, and S. A. Barnett, "Direct operation of solid oxide fuel cells with methane fuel," *Solid State Ionics*, vol. 176, pp. 1827-1835, 2005.
- [18] Z. Shao, J. Mederos, W. C. Chueh, and S. M. Haile, "High power-density single-chamber fuel cells operated on methane," *Journal of Power Sources*, vol. 162, pp. 589-596, 2006.
- [19] T. Hibino, A. Hashimoto, M. Yano, M. Suzuki, and M. Sano, "Ru-catalyzed anode materials for direct hydrocarbon SOFCs," *Electrochimica Acta*, vol. 48, pp. 2531-2537, 2003.
- [20] S. Park, J. M. Vohs, and R. J. Gorte, "Direct oxidation of hydrocarbons in a solid-oxide fuel cell," *Nature*, vol. 404, pp. 265-267, 2000.
- [21] Z. Zhan and S. A. Barnett, "An octane-fueled solid oxide fuel cell," *Science*, vol. 308, pp. 844-847, 2005.

- [22] Z. Zhan and S. A. Barnett, "Operation of ceria-electrolyte solid oxide fuel cells on iso-octane-air fuel mixtures," *Journal of Power Sources*, vol. 157, pp. 422-429, 2006.
- [23] L. Yang, Y. Choi, W. Qin, H. Chen, K. Blinn, M. Liu, *et al.*, "Promotion of water-mediated carbon removal by nanostructured barium oxide/nickel interfaces in solid oxide fuel cells," *Nat Commun*, vol. 2, p. 357, 2011.
- [24] B. A. Boukamp, "Fuel cells: The amazing perovskite anode," *Nat Mater*, vol. 2, pp. 294-296, 2003.
- [25] E. Maguire, B. Gharbage, F. M. B. Marques, and J. A. Labrincha, "Cathode materials for intermediate temperature SOFCs," *Solid State Ionics*, vol. 127, pp. 329-335, 2000.
- [26] S. P. S. Badwal, R. Deller, K. Foger, Y. Ramprakash, and J. P. Zhang, "Interaction between chromia forming alloy interconnects and air electrode of solid oxide fuel cells," *Solid State Ionics*, vol. 99, pp. 297-310, 1997.
- [27] Z. Shao and S. M. Haile, "A high-performance cathode for the next generation of solid-oxide fuel cells," *Nature*, vol. 431, pp. 170-173, 2004.
- [28] Y. Lin, R. Ran, Y. Zheng, Z. Shao, W. Jin, N. Xu, *et al.*, "Evaluation of $\text{Ba}_{0.5}\text{Sr}_{0.5}\text{Co}_{0.8}\text{Fe}_{0.2}\text{O}_{3-\delta}$ as a potential cathode for an anode-supported proton-conducting solid-oxide fuel cell," *Journal of Power Sources*, vol. 180, pp. 15-22, 2008.
- [29] J. W. Fergus, "Metallic interconnects for solid oxide fuel cells," *Materials Science and Engineering: A*, vol. 397, pp. 271-283, 2005.
- [30] N. E. T. Laboratory and U. S. D. o. Energy, *Fuel Cell Handbook*, 7 ed.: University Press of the Pacific, 2005.
- [31] T. Hibino, A. Hashimoto, M. Suzuki, and M. Sano, "A solid oxide fuel cell using Y-doped BaCeO_3 with Pd-loaded FeO anode and $\text{Ba}_{0.5}\text{Pr}_{0.5}\text{CoO}_3$ cathode at low temperatures," *Journal of The Electrochemical Society*, vol. 149, pp. A1503-A1508, 2002.
- [32] P. Ranran, W. Yan, Y. Lizhai, and M. Zongqiang, "Electrochemical properties of intermediate-temperature SOFCs based on proton conducting Sm-doped BaCeO_3 electrolyte thin film," *Solid State Ionics*, vol. 177, pp. 389-393, 2006.

- [33] Q. Ma, R. Peng, Y. Lin, J. Gao, and G. Meng, "A high-performance ammonia-fueled solid oxide fuel cell," *Journal of Power Sources*, vol. 161, pp. 95-98, 2006.
- [34] G. Taillades, J. Dailly, M. Taillades-Jacquin, F. Mauvy, A. Essouhmi, M. Marrony, *et al.*, "Intermediate Temperature Anode-Supported Fuel Cell Based on BaCe_{0.9}Y_{0.1}O₃ Electrolyte with Novel Pr₂NiO₄ Cathode," *Fuel Cells*, vol. 10, pp. 166-173, 2010.
- [35] J. Dailly, M. Marrony, G. Taillades, M. Taillades-Jacquin, A. Grimaud, F. Mauvy, *et al.*, "Evaluation of proton conducting BCY10-based anode supported cells by co-pressing method: Up-scaling, performances and durability," *Journal of Power Sources*, vol. 255, pp. 302-307, 2014.
- [36] I. Riess, "On the single chamber solid oxide fuel cells," *Journal of Power Sources*, vol. 175, pp. 325-337, 2008.
- [37] A. Sciacovelli and V. Verda, "Entropy generation analysis in a monolithic-type solid oxide fuel cell (SOFC)," *Energy*, vol. 34, pp. 850-865, 2009.
- [38] H. Zhu and R. J. Kee, "Two-dimensional model of distributed charge transfer and internal reforming within unit cells of segmented-in-series solid-oxide fuel cells," *Journal of Power Sources*, vol. 196, pp. 7654-7664, 2011.
- [39] O. Yamamoto, "Solid oxide fuel cells: Fundamental aspects and prospects," *Electrochimica Acta*, vol. 45, pp. 2423-2435, 2000.
- [40] A. B. Stambouli and E. Traversa, "Solid oxide fuel cells (SOFCs): A review of an environmentally clean and efficient source of energy," *Renewable and Sustainable Energy Reviews*, vol. 6, pp. 433-455, 2002.
- [41] A. Lashtabeg and S. J. Skinner, "Solid oxide fuel cells-A challenge for materials chemists?," *Journal of Materials Chemistry*, vol. 16, pp. 3161-3170, 2006.
- [42] B. Zhu, "Solid oxide fuel cell (SOFC) technical challenges and solutions from nano-aspects," *International Journal of Energy Research*, vol. 33, pp. 1126-1137, 2009.
- [43] R. M. Heck, R. J. Farrauto, and S. T. Gulati, *Catalytic air pollution control: Commercial technology*, 3rd ed. Hoboken, New Jersey: Wiley, 2009.

-
- [44] H. S. Fogler, *Elements of chemical reaction engineering*, 4th ed. Upper Saddle River, New Jersey: Pearson Education Inc., 2006.
- [45] V. M. Janardhanan and O. Deutschmann, "Numerical study of mass and heat transport in solid-oxide fuel cells running on humidified methane," *Chemical Engineering Science*, vol. 62, pp. 5473-5486, 2007.
- [46] J. R. Rostrup-Nielsen, J. Sehested, and J. K. Nørskov, "Hydrogen and synthesis gas by steam- and CO₂ reforming," in *Advances in Catalysis*. vol. Volume 47, ed: Academic Press, 2002, pp. 65-139.
- [47] M. L. Toebes, J. H. Bitter, A. J. van Dillen, and K. P. de Jong, "Impact of the structure and reactivity of nickel particles on the catalytic growth of carbon nanofibers," *Catalysis Today*, vol. 76, pp. 33-42, 2002.
- [48] K. H. Delgado, "Surface Reaction Kinetics for Oxidation and Reforming of H₂, CO, and CH₄ over Nickel-based Catalysts," Ph.D. Dissertation, Institut für Technische Chemie und Polymerchemie (ITCP), Karlsruher Institut für Technologie (KIT), Karlsruhe, 2014.
- [49] J. M. Klein, Y. Bultel, S. Georges, and M. Pons, "Modeling of a SOFC fuelled by methane: From direct internal reforming to gradual internal reforming," *Chemical Engineering Science*, vol. 62, pp. 1636-1649, 2007.
- [50] E. Achenbach and E. Riensche, "Methane/steam reforming kinetics for solid oxide fuel cells," *Journal of Power Sources*, vol. 52, pp. 283-288, 1994.
- [51] F. P. Nagel, T. J. Schildhauer, S. M. A. Biollaz, and S. Stucki, "Charge, mass and heat transfer interactions in solid oxide fuel cells operated with different fuel gases—A sensitivity analysis," *Journal of Power Sources*, vol. 184, pp. 129-142, 9/15/ 2008.
- [52] L. Maier, B. Schädel, K. Herrera Delgado, S. Tischer, and O. Deutschmann, "Steam reforming of methane over nickel: Development of a multi-step surface reaction mechanism," *Topics in Catalysis*, vol. 54, pp. 845-858, 2011.
- [53] E. S. Hecht, G. K. Gupta, H. Zhu, A. M. Dean, R. J. Kee, L. Maier, *et al.*, "Methane reforming kinetics within a Ni-YSZ SOFC anode support," *Applied Catalysis A: General*, vol. 295, pp. 40-51, 2005.

- [54] W. Y. Lee, J. Hanna, and A. F. Ghoniem, "On the predictions of carbon deposition on the nickel anode of a SOFC and its impact on open-circuit conditions," *Journal of The Electrochemical Society*, vol. 160, pp. F94-F105, 2013.
- [55] C. Y. Sheng and A. M. Dean, "Importance of gas-phase kinetics within the anode channel of a solid-oxide fuel cell," *The Journal of Physical Chemistry A*, vol. 108, pp. 3772-3783, 2004.
- [56] D. W. Blaylock, T. Ogura, W. H. Green, and G. J. O. Beran, "Computational investigation of thermochemistry and kinetics of steam methane reforming on Ni(111) under realistic conditions," *The Journal of Physical Chemistry C*, vol. 113, pp. 4898-4908, 2009.
- [57] O. Deutschmann (Editor), *Modeling and simulation of heterogeneous catalytic reactions: From the molecular process to the technical system*. Weinheim, Germany: Wiley-VCH Verlag GmbH & Co. KGaA, 2011.
- [58] R. J. Kee, M. E. Coltrin, and P. Glarborg, *Chemically reacting flow: Theory and practice*, 1st ed. Hoboken, New Jersey: John Wiley & Sons, Inc., 2003.
- [59] D. Chan, S. Tischer, J. Heck, C. Diehm, and O. Deutschmann, "Correlation between catalytic activity and catalytic surface area of a Pt/Al₂O₃ DOC: An experimental and microkinetic modeling study," *Applied Catalysis B: Environmental*, vol. 156–157, pp. 153-165, 2014.
- [60] V. M. Janardhanan, V. Heuveline, and O. Deutschmann, "Three-phase boundary length in solid-oxide fuel cells: A mathematical model," *Journal of Power Sources*, vol. 178, pp. 368-372, 2008.
- [61] W. G. Bessler, J. Warnatz, and D. G. Goodwin, "The influence of equilibrium potential on the hydrogen oxidation kinetics of SOFC anodes," *Solid State Ionics*, vol. 177, pp. 3371-3383, 2007.
- [62] V. Menon, Q. Fu, V. M. Janardhanan, and O. Deutschmann, "A model-based understanding of solid-oxide electrolysis cells (SOECs) for syngas production by H₂O/CO₂ co-electrolysis," *Journal of Power Sources*, vol. 274, pp. 768-781, 2015.

-
- [63] A. M. Sukeshini, B. Habibzadeh, B. P. Becker, C. A. Stoltz, B. W. Eichhorn, and G. S. Jackson, "Electrochemical oxidation of H₂, CO, and CO/H₂ mixtures on patterned Ni anodes on YSZ electrolytes," *Journal of The Electrochemical Society*, vol. 153, pp. A705-A715, 2006.
- [64] C. Stoots, J. O'Brien, and J. Hartvigsen, "Results of recent high temperature coelectrolysis studies at the Idaho National Laboratory," *International Journal of Hydrogen Energy*, vol. 34, pp. 4208-4215, 2009.
- [65] S. D. Ebbesen, R. Knibbe, and M. Mogensen, "Co-electrolysis of steam and carbon dioxide in solid oxide cells," *Journal of The Electrochemical Society*, vol. 159, pp. F482-F489, 2012.
- [66] H. Zhu, R. J. Kee, V. M. Janardhanan, O. Deutschmann, and D. G. Goodwin, "Modeling elementary heterogeneous chemistry and electrochemistry in solid-oxide fuel cells," *Journal of The Electrochemical Society*, vol. 152, pp. A2427-A2440, 2005.
- [67] B. de Boer, "SOFC anode: Hydrogen oxidation at porous nickel and nickel/zirconia electrodes," Ph.D. Dissertation, University of Twente, Netherlands, 1998.
- [68] M. Vogler, "Elementary kinetic modelling applied to solid oxide fuel cell pattern anodes and a direct flame fuel cell system," Ph.D. Dissertation, Universität Heidelberg, Heidelberg, 2009.
- [69] G. Narasimhaiah and V. Janardhanan, "Modeling CO₂ electrolysis in solid oxide electrolysis cell," *Journal of Solid State Electrochemistry*, vol. 17, pp. 2361-2370, 2013.
- [70] G. Tao, K. R. Sridhar, and C. L. Chan, "Study of carbon dioxide electrolysis at electrode/electrolyte interface: Part I. Pt/YSZ interface," *Solid State Ionics*, vol. 175, pp. 615-619, 2004.
- [71] V. M. Janardhanan and O. Deutschmann, "CFD analysis of a solid oxide fuel cell with internal reforming: Coupled interactions of transport, heterogeneous catalysis and electrochemical processes," *Journal of Power Sources*, vol. 162, pp. 1192-1202, 2006.

- [72] A. C. Co, S. J. Xia, and V. I. Birss, "A kinetic study of the oxygen reduction reaction at LaSrMnO₃-YSZ composite electrodes," *Journal of The Electrochemical Society*, vol. 152, pp. A570-A576, 2005.
- [73] J. Aicart, J. Laurencin, M. Petitjean, and L. Dessemond, "Experimental validation of two-dimensional H₂O and CO₂ co-electrolysis modeling," *Fuel Cells*, vol. 14, pp. 430-447, 2014.
- [74] V. Menon, V. M. Janardhanan, and O. Deutschmann, "Modeling of solid-oxide electrolyser cells: From H₂, CO Electrolysis to co-electrolysis," *ECS Transactions*, vol. 57, pp. 3207-3216, 2013.
- [75] V. Menon, A. Banerjee, J. Dailly, and O. Deutschmann, "Numerical analysis of mass and heat transport in proton-conducting SOFCs with direct internal reforming," *Applied Energy* (*accepted*), 2015.
- [76] F. He, T. Wu, R. Peng, and C. Xia, "Cathode reaction models and performance analysis of Sm_{0.5}Sr_{0.5}CoO_{3-δ}-BaCe_{0.8}Sm_{0.2}O_{3-δ} composite cathode for solid oxide fuel cells with proton conducting electrolyte," *Journal of Power Sources*, vol. 194, pp. 263-268, 2009.
- [77] L. Zhao, B. He, J. Gu, F. Liu, X. Chu, and C. Xia, "Reaction model for cathodes cooperated with oxygen-ion conductors for solid oxide fuel cells using proton-conducting electrolytes," *International Journal of Hydrogen Energy*, vol. 37, pp. 548-554, 2012.
- [78] R. Peng, T. Wu, W. Liu, X. Liu, and G. Meng, "Cathode processes and materials for solid oxide fuel cells with proton conductors as electrolytes," *Journal of Materials Chemistry*, vol. 20, pp. 6218-6225, 2010.
- [79] V. Menon, V. M. Janardhanan, and O. Deutschmann, "A mathematical model to analyze solid oxide electrolyzer cells (SOECs) for hydrogen production," *Chemical Engineering Science*, vol. 110, pp. 83-93, 2014.
- [80] E. A. Mason and A. P. Malinauskas, *Gas transport in porous media: The dusty-gas model*. New York: Elsevier, 1983.
- [81] R. Krishna, "A simplified procedure for the solution of the dusty gas model equations for steady-state transport in non-reacting systems," *The Chemical Engineering Journal*, vol. 35, pp. 75-81, 1987.

-
- [82] R. Suwanwarangkul, E. Croiset, M. W. Fowler, P. L. Douglas, E. Entchev, and M. A. Douglas, "Performance comparison of Fick's, dusty-gas and Stefan–Maxwell models to predict the concentration overpotential of a SOFC anode," *Journal of Power Sources*, vol. 122, pp. 9-18, 2003.
- [83] J. Bear, *Dynamics of fluids in porous media*. New York: American Elsevier, 1972.
- [84] V. M. Janardhanan, V. Heuveline, and O. Deutschmann, "Performance analysis of a SOFC under direct internal reforming conditions," *Journal of Power Sources*, vol. 172, pp. 296-307, 2007.
- [85] V. Menon, V. M. Janardhanan, S. Tischer, and O. Deutschmann, "A novel approach to model the transient behavior of solid-oxide fuel cell stacks," *Journal of Power Sources*, vol. 214, pp. 227-238, 2012.
- [86] L. L. Raja, R. J. Kee, O. Deutschmann, J. Warnatz, and L. D. Schmidt, "A critical evaluation of Navier–Stokes, boundary-layer, and plug-flow models of the flow and chemistry in a catalytic-combustion monolith," *Catalysis Today*, vol. 59, pp. 47-60, 2000.
- [87] R. E. Hayes and S. T. Kolaczkowski, *Introduction to catalytic combustion*, 1st ed. Amsterdam: Gordon and Breach Science Publishers, 1997.
- [88] A. Pramuanjaroenkij, S. Kakaç, and X. Yang Zhou, "Mathematical analysis of planar solid oxide fuel cells," *International Journal of Hydrogen Energy*, vol. 33, pp. 2547-2565, 2008.
- [89] P. Deufhard, E. Hairer, and J. Zugck, "One-step and extrapolation methods for differential-algebraic systems," *Numerische Mathematik*, vol. 51, pp. 501-516, 1987.
- [90] O. Deutschmann, S. Tischer, S. Kleditzsch, V. M. Janardhanan, C. Correa, D. Chatterjee, *et al.* (2012). *DETCHEMTM software package, 2.4 ed.* Available: <http://www.detchem.com/>
- [91] S. Tischer and O. Deutschmann, "Recent advances in numerical modeling of catalytic monolith reactors," *Catalysis Today*, vol. 105, pp. 407-413, 2005.
- [92] C. Bao, Y. Shi, C. Li, N. Cai, and Q. Su, "Multi-level simulation platform of SOFC–GT hybrid generation system," *International Journal of Hydrogen Energy*, vol. 35, pp. 2894-2899, 2010.

-
- [93] D. Cocco and V. Tola, "Use of alternative hydrogen energy carriers in SOFC–MGT hybrid power plants," *Energy Conversion and Management*, vol. 51, p. 623, 2010.
- [94] A. Traverso, L. Magistri, and A. F. Massardo, "Turbomachinery for the air management and energy recovery in fuel cell gas turbine hybrid systems," *Energy*, vol. 35, pp. 764-777, 2010.
- [95] Z. Yu, J. Han, X. Cao, W. Chen, and B. Zhang, "Analysis of total energy system based on solid oxide fuel cell for combined cooling and power applications," *International Journal of Hydrogen Energy*, vol. 35, pp. 2703-2707, 2010.
- [96] M. Santin, A. Traverso, and L. Magistri, "Liquid fuel utilization in SOFC hybrid systems," *Applied Energy*, vol. 86, pp. 2204-2212, 2009.
- [97] P.-H. Lin and C.-W. Hong, "Cold start dynamics and temperature sliding observer design of an automotive SOFC APU," *Journal of Power Sources*, vol. 187, pp. 517-526, 2009.
- [98] H. Timmermann, W. Sawady, R. Reimert, and E. Ivers-Tiffée, "Kinetics of (reversible) internal reforming of methane in solid oxide fuel cells under stationary and APU conditions," *Journal of Power Sources*, vol. 195, pp. 214-222, 2010.
- [99] Y. H. Chan, T. S. Zhao, R. Chen, and C. Xu, "A self-regulated passive fuel-feed system for passive direct methanol fuel cells," *Journal of Power Sources*, vol. 176, pp. 183-190, 2008.
- [100] A. Lindermeir, S. Kah, S. Kavurucu, and M. Mühlner, "On-board diesel fuel processing for an SOFC–APU—Technical challenges for catalysis and reactor design," *Applied Catalysis B: Environmental*, vol. 70, pp. 488-497, 2007.
- [101] B. Tu, Y. Dong, M. Cheng, Z. Tian, and Q. Xin, "IT-SOFC operated with catalytically processed methane fuels," in *Studies in Surface Science and Catalysis*. vol. Volume 167, M. S. Fábio Bellot Noronha and S.-A. Eduardo Falabella, Eds., ed: Elsevier, 2007, pp. 43-48.
- [102] O. Deutschmann and S. Tischer, "Modellierung und Simulation chemischer Reaktoren," Lecture series, Karlsruher Institut für Technologie (KIT), Karlsruhe, 2012.
- [103] E. Ivers-Tiffée, A. Weber, K. Schmid, and V. Krebs, "Macroscale modeling of cathode formation in SOFC," *Solid State Ionics*, vol. 174, pp. 223-232, 2004.

-
- [104] E. Achenbach, "Response of a solid oxide fuel cell to load change," *Journal of Power Sources*, vol. 57, pp. 105-109, 1995.
- [105] V. Menon, V. M. Janardhanan, S. Tischer, and O. Deutschmann, "Internal multi-physics phenomena of SOFC with direct internal reforming," *ECS Transactions*, vol. 57, pp. 2475-2484, 2013.
- [106] J. Li, G.-Y. Cao, X.-J. Zhu, and H.-Y. Tu, "Two-dimensional dynamic simulation of a direct internal reforming solid oxide fuel cell," *Journal of Power Sources*, vol. 171, pp. 585-600, 2007.
- [107] E. Achenbach, "Three-dimensional and time-dependent simulation of a planar solid oxide fuel cell stack," *Journal of Power Sources*, vol. 49, pp. 333-348, 1994.
- [108] X. Xue, J. Tang, N. Sammes, and Y. Du, "Dynamic modeling of single tubular SOFC combining heat/mass transfer and electrochemical reaction effects," *Journal of Power Sources*, vol. 142, pp. 211-222, 2005.
- [109] M. Ni, M. K. H. Leung, and D. Y. C. Leung, "Technological development of hydrogen production by solid oxide electrolyzer cell (SOEC)," *International Journal of Hydrogen Energy*, vol. 33, pp. 2337-2354, 2008.
- [110] J. S. Herring, J. E. O'Brien, C. M. Stoots, G. L. Hawkes, J. J. Hartvigsen, and M. Shahnam, "Progress in high-temperature electrolysis for hydrogen production using planar SOFC technology," *International Journal of Hydrogen Energy*, vol. 32, pp. 440-450, 2007.
- [111] L. Mingyi, Y. Bo, X. Jingming, and C. Jing, "Thermodynamic analysis of the efficiency of high-temperature steam electrolysis system for hydrogen production," *Journal of Power Sources*, vol. 177, pp. 493-499, 2008.
- [112] S. H. Jensen, P. H. Larsen, and M. Mogensen, "Hydrogen and synthetic fuel production from renewable energy sources," *International Journal of Hydrogen Energy*, vol. 32, pp. 3253-3257, 2007.
- [113] J. E. O'Brien, "Thermodynamic considerations for thermal water splitting processes and high temperature electrolysis," in *Proceedings of the 2008 International Mechanical*

Engineering Congress and Exposition, Boston, Massachusetts, USA, October 31 - November 6, 2008.

- [114] V. M. Janardhanan and O. Deutschmann, "Modeling diffusion limitation in solid-oxide fuel cells," *Electrochimica Acta*, vol. 56, pp. 9775-9782, 2011.
- [115] C. Graves, S. D. Ebbesen, M. Mogensen, and K. S. Lackner, "Sustainable hydrocarbon fuels by recycling CO₂ and H₂O with renewable or nuclear energy," *Renewable and Sustainable Energy Reviews*, vol. 15, pp. 1-23, 2011.
- [116] Q. Fu, C. Mabilat, M. Zahid, A. Brisse, and L. Gautier, "Syngas production via high-temperature steam/CO₂ co-electrolysis: An economic assessment," *Energy & Environmental Science*, vol. 3, pp. 1382-1397, 2010.
- [117] J. Wei and E. Iglesia, "Isotopic and kinetic assessment of the mechanism of reactions of CH₄ with CO₂ or H₂O to form synthesis gas and carbon on nickel catalysts," *Journal of Catalysis*, vol. 224, pp. 370-383, 2004.
- [118] K. R. Sridhar and B. T. Vaniman, "Oxygen production on Mars using solid oxide electrolysis," *Solid State Ionics*, vol. 93, pp. 321-328, 1997.
- [119] Q. Fu, J. Dailly, A. Brisse, and M. Zahid, "High-temperature CO₂ and H₂O electrolysis with an electrolyte-supported solid oxide cell," *ECS Transactions*, vol. 35, pp. 2949-2956, 2011.
- [120] Y. Tao, S. D. Ebbesen, and M. B. Mogensen, "Carbon deposition in solid oxide cells during co-electrolysis of H₂O and CO₂," *Journal of The Electrochemical Society*, vol. 161, pp. F337-F343, 2014.
- [121] S. H. Kim, S.-W. Nam, T.-H. Lim, and H.-I. Lee, "Effect of pretreatment on the activity of Ni catalyst for CO removal reaction by water-gas shift and methanation," *Applied Catalysis B: Environmental*, vol. 81, pp. 97-104, 2008.
- [122] B. C. H. Steele, "Fuel-cell technology: Running on natural gas," *Nature*, vol. 400, pp. 619-621, 1999.
- [123] A. Nakajo, Z. Wuillemin, J. Van herle, and D. Favrat, "Simulation of thermal stresses in anode-supported solid oxide fuel cell stacks. Part I: Probability of failure of the cells," *Journal of Power Sources*, vol. 193, pp. 203-215, 2009.

-
- [124] C. M. Finnerty, N. J. Coe, R. H. Cunningham, and R. M. Ormerod, "Carbon formation on and deactivation of nickel-based/zirconia anodes in solid oxide fuel cells running on methane," *Catalysis Today*, vol. 46, pp. 137-145, 1998.
- [125] S. A. Hajimolana, M. A. Hussain, W. M. A. W. Daud, M. Soroush, and A. Shamiri, "Mathematical modeling of solid oxide fuel cells: A review," *Renewable and Sustainable Energy Reviews*, vol. 15, pp. 1893-1917, 2011.
- [126] D. Bhattacharyya and R. Rengaswamy, "A review of solid oxide fuel cell (SOFC) dynamic models," *Industrial & Engineering Chemistry Research*, vol. 48, pp. 6068-6086, 2009.
- [127] V. M. Janardhanan and O. Deutschmann, "Modeling of solid-oxide fuel cells," *Zeitschrift fur Physikalische Chemie*, vol. 221, pp. 443-479, 2007.
- [128] M. A. Laguna-Bercero, "Recent advances in high temperature electrolysis using solid oxide fuel cells: A review," *Journal of Power Sources*, vol. 203, pp. 4-16, 2012.
- [129] A. K. Demin, P. E. Tsiakaras, V. A. Sobyenin, and S. Y. Hramova, "Thermodynamic analysis of a methane fed SOFC system based on a protonic conductor," *Solid State Ionics*, vol. 152-153, pp. 555-560, 2002.
- [130] A. Demin and P. Tsiakaras, "Thermodynamic analysis of a hydrogen fed solid oxide fuel cell based on a proton conductor," *International Journal of Hydrogen Energy*, vol. 26, pp. 1103-1108, 2001.
- [131] P. Costamagna, A. Selimovic, M. Del Borghi, and G. Agnew, "Electrochemical model of the integrated planar solid oxide fuel cell (IP-SOFC)," *Chemical Engineering Journal*, vol. 102, pp. 61-69, 2004.
- [132] R. J. Kee, H. Zhu, B. W. Hildenbrand, E. Vøllestad, M. D. Sanders, and R. P. O'Hayre, "Modeling the steady-state and transient response of polarized and non-polarized proton-conducting doped-perovskite membranes," *Journal of The Electrochemical Society*, vol. 160, pp. F290-F300, 2013.
- [133] J. R. Wilson, W. Kobsiriphat, R. Mendoza, H.-Y. Chen, J. M. Hiller, D. J. Miller, *et al.*, "Three-dimensional reconstruction of a solid-oxide fuel-cell anode," *Nature Materials*, vol. 5, pp. 541-544, 2006.

- [134] J. Joos, T. Carraro, A. Weber, and E. Ivers-Tiffée, "Reconstruction of porous electrodes by FIB/SEM for detailed microstructure modeling," *Journal of Power Sources*, vol. 196, pp. 7302-7307, 2011.
- [135] A. Lanzini, P. Leone, and P. Asinari, "Microstructural characterization of solid oxide fuel cell electrodes by image analysis technique," *Journal of Power Sources*, vol. 194, pp. 408-422, 2009.
- [136] B. V. R. S. N. Prasad and V. M. Janardhanan, "Modeling Sulfur Poisoning of Ni-Based Anodes in Solid Oxide Fuel Cells," *Journal of The Electrochemical Society*, vol. 161, pp. F208-F213, 2014.
- [137] S. Appari, V. M. Janardhanan, S. Jayanti, L. Maier, S. Tischer, and O. Deutschmann, "Micro-kinetic modeling of NH₃ decomposition on Ni and its application to solid oxide fuel cells," *Chemical Engineering Science*, vol. 66, pp. 5184-5191, 2011.
- [138] S. Appari, V. M. Janardhanan, R. Bauri, S. Jayanti, and O. Deutschmann, "A detailed kinetic model for biogas steam reforming on Ni and catalyst deactivation due to sulfur poisoning," *Applied Catalysis A: General*, vol. 471, pp. 118-125, 2014.
- [139] H. Kronemayer, D. Barzan, M. Horiuchi, S. Suganuma, Y. Tokutake, C. Schulz, *et al.*, "A direct-flame solid oxide fuel cell (DFFC) operated on methane, propane, and butane," *Journal of Power Sources*, vol. 166, pp. 120-126, 2007.

Curriculum Vitae

Personal details

Name	Vikram Menon
Date of Birth	28 th May, 1988
Place of Birth	Chennai, India
Nationality	Indian
Marital Status	Single

Education

Karlsruhe Institute of Technology, School of Mechanical Engineering (Karlsruhe, Germany)

May 2011 – Mar 2015 Doctoral candidate, Mechanical Engineering
Dissertation: "A model-based understanding of reversible oxide-ion-conducting and proton-conducting solid oxide fuel cells (SOFCs)"
Ph.D. Advisors: Prof. Olaf Deutschmann, Prof. Ulrich Maas

Columbia University, School of Engineering and Applied Science (New York, USA)

Sept 2009 – Feb 2011 Master of Science (M.S.), Mechanical Engineering
Research topic: CFD analysis of shock wave phenomena in pipes/cylinders, i.e., shock tubes
M.S. Advisors: Prof. Pejman Akbari, Prof. Daniel Attinger
GPA: 3.87/4.00

SASTRA University, School of Mechanical Engineering (Tanjore, India)

July 2005 – May 2009 Bachelor of Technology (B.Tech.), Mechanical Engineering
Project: Research internship at Bernstein AG, R&D, Germany
GPA: 9.42/10.00; Award: Dean's list scholarship (top 2%), 2005-2008

D.A.V. Senior Secondary School, Central Board of Secondary Education (Chennai, India)

June 1991 – May 2005 Completion certificate, equivalent to high school diploma
Score: 91% in X grade & 90% in XII grade

Research Experience

May 2011 – Mar 2015 **Karlsruhe Institute of Technology, Institute for Chemical Technology and Polymer Chemistry** (Karlsruhe, Germany)

Prof. Olaf Deutschmann - PI*Ph.D. student*

Feb 2013 – July 2013

Steinbeis GmbH für Technologietransfer (STZ 240 Reaktive Strömungen)*Scientific Consultant*

Sept 2009 – Sept 2010

Columbia University, Department of Mechanical Engineering (New York, USA)**Prof. Pejman Akbari - PI***Research Assistant*

Sept 2008 – Jan 2009

Bernstein AG, R&D, Germany**Mr. Dieter Mönnicke, Manager, R&D - PI***Research Intern*

Academic Achievements and Awards

May 2011 – Mar 2015

Helmholtz Research School *Energy Related Catalysis* Fellowship (KIT, Germany).

July 2005 – May 2008

Dean's list scholarship - top 2% out of approximately 3000 students (SASTRA University, India).

July 2005 – May 2009

- **Subject topper** in 10 courses, out of approximately 240 students (SASTRA University, India).

- **Department topper** during the 1st, 2nd & 4th semester of bachelor's degree (SASTRA University, India).

List of Publications and Conference Proceedings

- [1] Vikram Menon, Aayan Banerjee, Julian Dailly, Olaf Deutschmann, "Numerical analysis of mass and heat transport in proton-conducting SOFCs with direct internal reforming", **Applied Energy** (accepted).
- [2] Vikram Menon, Qingxi Fu, Vinod M. Janardhanan, Olaf Deutschmann, "A model-based understanding of solid-oxide electrolysis cells (SOECs) for syngas production by H₂O/CO₂ co-electrolysis", **Journal of Power Sources** 274 (2015) 768–781.
- [3] Vikram Menon, Vinod M. Janardhanan, Olaf Deutschmann, "A mathematical model to analyze solid oxide electrolyzer cells (SOECs) for hydrogen production", **Chemical Engineering Science** 110 (2014) 83–93.
- [4] Vikram Menon, Vinod M. Janardhanan, Steffen Tischer, Olaf Deutschmann, "Internal multi-physics phenomena of SOFC with direct internal reforming", **ECS Trans.** 57 (2013) 2475–2484.
- [5] Vikram Menon, Vinod M. Janardhanan, Olaf Deutschmann, "Modeling of solid-oxide electrolyser cells: from H₂, CO electrolysis to co-electrolysis", **ECS Trans.** 57 (2013) 3207–3216.
- [6] Vikram Menon, Vinod M. Janardhanan, Steffen Tischer, Olaf Deutschmann, "Modeling and experi-

mental validation of SOFC operating on reformat fuel", Proceedings of the 10th European Solid Oxide Fuel Cell Forum, pp. 18-146–18-157 (2012).

- [7] Vikram Menon, Vinod M. Janardhanan, Steffen Tischer, Olaf Deutschmann, "A novel approach to model the transient behavior of solid-oxide fuel cell stacks", **Journal of Power Sources** 214 (2012) 227–238.
- [8] Vikram Menon, Steffen Tischer, Olaf Deutschmann, "A novel approach to model solid-oxide fuel cell stacks", 9th Symposium on Fuel Cell/Battery Modeling and Experimental Validation (ModVal 9), Book of Abstracts, pp. 89–90 (2012).

List of Conference Contributions

- [1] Vikram Menon, Qingxi Fu, Olaf Deutschmann, "A model-based understanding of solid-oxide electrolysis cells: from hydrogen to syngas production", 11th European SOFC Forum (Lucerne, Switzerland), 01.07–04.07.2014 (**Poster**).
- [2] Vikram Menon, Vinod M. Janardhanan, Olaf Deutschmann, "Modeling of solid-oxide electrolyser cells: from H₂, CO electrolysis to co-electrolysis", 13th International Symposium on Solid Oxide Fuel Cells/SOFC-XIII (Okinawa, Japan), 06.10.2013–11.10.2013 (**Poster**).
- [3] Vikram Menon, Vinod M. Janardhanan, Steffen Tischer, Olaf Deutschmann, "Internal multi-physics phenomena of SOFC with direct internal reforming", 13th International Symposium on Solid Oxide Fuel Cells/SOFC-XIII (Okinawa, Japan), 06.10.2013–11.10.2013 (**Oral**).
- [4] Vikram Menon, Vinod M. Janardhanan, Steffen Tischer, Olaf Deutschmann, "Efficiency analysis of a solid oxide electrolysis cell (SOEC) for hydrogen production", Jahrestreffen Reaktionstechnik 2013 (Würzburg, Germany), 06.05–08.05.2013 (**Poster**).
- [5] Vikram Menon, Vinod M. Janardhanan, Steffen Tischer, Olaf Deutschmann, "Transient three-dimensional mathematical modeling of high density solid oxide electrolysis cell (SOEC) stacks", 5th International Conference on Fundamentals & Development of Fuel Cells/FDFC 2013 (Karlsruhe, Germany), 16.04–18.04.2013 (**Poster**).
- [6] Vikram Menon, Vinod M. Janardhanan, Steffen Tischer, Olaf Deutschmann, "Multi-scale analysis of solid-oxide electrolysis cells for hydrogen production", 528. Wilhelm and Else Heraeus-Seminar (Bad Honnef, Germany), 24.03–27.03.2013 (**Poster**).
- [7] Vikram Menon, Vinod M. Janardhanan, Steffen Tischer, Olaf Deutschmann, "Modeling and experimental validation of solid oxide electrolysis cells for hydrogen production", 10th Symposium on Fuel

Cell/Battery Modeling and Experimental Validation/ModVal 10 (Bad Boll, Germany), 19.03–20.03.2013 (**Oral**).

- [8] Vikram Menon, Vinod M. Janardhanan, Olaf Deutschmann, "Conversion of natural gas to electrical power by direct internal reforming in solid-oxide fuel cells", 10th Natural Gas Conversion Symposium/NGCS 10 (Doha, Qatar), 02.03–07.03.2013 (**Poster**).
- [9] Vikram Menon, Vinod M. Janardhanan, Olaf Deutschmann, "A mathematical model to analyse solid oxide electrolysis cells (SOEC) for syngas production", Mathematics in Chemical Kinetics and Engineering/MaCKiE 2013 (Chennai, India), 04.02–06.02.2013 (**Oral**).
- [10] Vikram Menon, Vinod M. Janardhanan, Steffen Tischer, Olaf Deutschmann, "Dynamic three-dimensional modeling of solid-oxide fuel cell stacks", 22nd International Symposium on Chemical Reaction Engineering/ISCRE 22 (Maastricht, The Netherlands), 02.09–05.09.2012 (**Poster**).
- [11] Vikram Menon, Vinod M. Janardhanan, Steffen Tischer, Olaf Deutschmann, "Modeling and experimental validation of SOFC operating on reformat fuel", 10th European SOFC Forum (Lucerne, Switzerland), 26.06–29.06.2012 (**Poster**).
- [12] Vikram Menon, Vinod M. Janardhanan, Steffen Tischer, Olaf Deutschmann, "A novel approach to model solid-oxide fuel cell stacks", 9th Symposium on Fuel Cell/Battery Modeling and Experimental Validation/ModVal 9 (Sursee, Switzerland), 02.04–04.04.2012 (**Oral**).
- [13] Vikram Menon, Steffen Tischer, Olaf Deutschmann, "Transient three-dimensional modeling of solid-oxide fuel cell stacks: coupling of mass and heat transfer with electro-catalytic and thermo-catalytic reactions", 45th Annual Meeting of the German Catalysis Society (Weimar, Germany), 14.03–16.03.2012 (**Poster**).
- [14] Vikram Menon, Steffen Tischer, Olaf Deutschmann, "Transient three-dimensional modeling of solid-oxide fuel cell stacks", 45th Annual Meeting of the German Catalysis Society (Weimar, Germany), Workshop - "Electrochemistry in Catalysis: Experiment and Theory", 14.03–16.03.2012 (**Oral**).